Residual Stress Evaluation and Modelling at the Micron Scale

Department of Engineering Science

Enrico Salvati
Trinity College

Supervised by
Professor Alexander M. Korsunsky

A thesis submitted for the degree of

Doctor of Philosophy

Trinity 2017

Abstract

The presence of residual stresses in engineering components may significantly affect damage evolution and progression towards failure. Correct evaluation of residual stress is of crucial importance for assessing mechanical components, predicting response and ensuring reliability. For example, when failure occurs due to cyclic loading, the underlying damage begins at the nano-, and then micro-scale. It is clear that improving engineering reliability at the micro-scale requires the ability to evaluate residual stress and mechanical properties at the appropriate scale.

The key objective of the thesis is to advance the understanding and practice of residual stress evaluation at the micro-scale, and to examine the implications and applications that follow. Significant effort was devoted to the evaluation of two aspects of the relatively novel FIB-DIC micro-ring-core experimental technique: assessing the effects of Ga-ion damage and the quantification of uncertainty in stress evaluation due to unknown crystal orientation.

FIB-DIC micro-ring-core milling was then used alongside with synchrotron XRD to study residual stress effects on fatigue crack growth propagation rate following the occurrence of overload or underload. The effects of the two principal mechanisms of crack retardation following an overload, residual stress and crack closure, were separated by testing samples at different loading ratios. Whilst, the acceleration after an underload was studied using validated non-linear FEM analyses.

Conceptual focus was placed on the macro-micro-nano residual stress decomposition into Type I, II & III according to scale and, detailed examination was conducted experimentally and numerically. In the context of shot-peening surface treatment, residual stresses were modelled using a novel eigenstrain-based modelling procedure for arbitrarily shaped components. Furthermore, a fine scale characterisation was performed of the recast layer produced by EDM, with particular attention paid to the residual stress.

The investigations presented in this thesis open new perspectives for the assessment of material reliability. Improved failure prediction models will be elaborated based on the insights obtained in the present study.

Acknowledgements

A doctoral thesis is often described as a solitary endeavour; however the long list that follows definitely demonstrates the contrary.

Above all, I want to express gratitude to my supervisor Professor Alexander Korsunsky. It has been an honour to be one of his DPhil students. He has been supportive since the days I began working in his group. He has consistently stimulated and encouraged me to push beyond the limits of what I thought I could accomplish. I have been continuously inspired by his wit and creativity, and surely he has conveyed his passion for the research and what I would call in Italian, his "*sete di conoscenza*" (thirst for knowledge). I hope we will have another opportunity to work together again in the future.

My deepest appreciation goes to my beautiful girlfriend Maria, for her care, love and constant support. She has been always supportive during tough times, even in the difficult situation of long-distance relationship. I am fortunate to have such a wonderful person to call my partner.

I would also like to express my gratitude to my parents Giuseppe and Rosanna, and my brothers Antonio and Roberto for their consistent guidance, support and encouragement. Words cannot express the gratitude that I have for all that you have given to me. I know that none of this would have been possible without your continual belief in my potential. What I have done, I have done also to make you proud. Words of appreciations also go to the other members of the family.

I am grateful to all my old-standing friends from Italy, particularly to the guys of the "Centro Senza Conservanti" of Mirabello, the former class mates and friends I met at the University of Ferrara and even older-standing friends from Arenabianca. I cannot forget also to thank all those special people I have met during my time in Oxford, with a special thanks to all the members of the Oxford University Greek Society.

My thanks must also go to my colleagues who have helped me over the past few years. Especially during the sleepless nights on beamtime, collaborating together to overcome challenging scientific and technical problems or simply sharing a pint after a tough day of work. Thanks to all the former and current members of the AMK group: Alexander Lunt, Hongjia Zhang, Ricky Siqi, Chryssa Papadaki, Léon Romano Brandt, Tan Sui, Mahmoud Mousavi, Bohang Song, Fatih Uzun, Lifeng Ma, Guanhua Sun, André de Carvalho and Juliana de Martins. It was a memorable experience to work with them.

My special gratitude goes to the two main European Synchrotron Facilities, Diamond Light Source (United Kingdom) and European Synchrotron Radiation Facility (France), for their “vital” Beamtime allocations. I have received outstanding support from the scientists working in these facilities, I particular I would like to extend my thanks to Igor Dolbnya, Andrew Malandain, Annette Kleppe, Dominik Daisenberg, Ian Pape and Didier Wermeille.

Special thanks goes to my former supervisors at the time I was employed in the University of Ferrara, Professors Paolo Livieri and Roberto Tovo.

In addition I must thank the European Commission for funding me through the FP7 ISTRESS project throughout the first 2.5years of my doctorate.

I am deeply grateful to all the wonderful people who collaborated to the ISTRESS project. Thanks to all the European partners from: University of Roma Tré, Friedrich-Alexander-University of Erlangen-Nürnberg, NPL, ETH, Tescan, Bosh, University of Brescia and Fraunhofer-Gesellschaft. To all the inspiring and fruitful discussions during the several meetings all over Europe.

I would very much like to thank Dr. Xu Song, Soon Kai Fong and Tea-Sung Jun for providing me samples and pieces of key advices.

My thanks go to all the member of the Department of Engineering Science. Special thanks to Rodolfo M.N. Fleury, Robert J.H. Paynter, Kalin Dragnevski, Richard Duffin and his team.

Finally I would like to thank my examiners for taking the time to read my thesis. I look forward to meet with for discussing my work.

Selected Publications

Some of the work reported in this thesis has been either published or under consideration in the following papers.

Journal Articles:

1. **E. Salvati**, A.M. Korsunsky. *Depth-resolved analysis of the composition, grain orientation and residual stress associated with the white layer formed in an Al alloy due to wire EDM primary and finishing cuts. (**Under review**).*
2. **E. Salvati**, L.R. Brandt, C. Papadaki, H. Zhang, D. Wermeille, A.M. Korsunsky. *Density Change and Intrinsic Eigenstrain Within Amorphous Layer on Si Generated by Ga+ Focused Ion Beam Milling. (**Under review**).*
3. **E. Salvati**, A.M. Korsunsky. *Macro- and micro-scale analysis of Type I, II and III residual stresses using FIB-DIC micro-ring-core milling*. (2017) International Journal of Plasticity.
4. **E. Salvati**, A.J.G. Lunt, S. Ying, T. Sui, H.J. Zhang, C. Heason, G. Baxter, A.M. Korsunsky. *Eigenstrain Reconstruction of Residual Strains in an Additively Manufactured and Shot Peened Nickel Superalloy Compressor Blade*. (2017) Computer Methods in Applied Mechanics and Engineering. *Volume 320, 15 June 2017, Pages 335–351*
5. **E. Salvati**, H. Zhang, K. S. Fong, X. Song, A. M. Korsunsky. *Separating Plasticity-Induced Closure and Residual Stress Contributions to Fatigue Crack Retardation Following an Overload.* (2016) Journal of Mechanics and Physics of Solids. Volume 98, January 2017, Pages 222–235
6. A. M. Korsunsky, J. Guénolé, **E. Salvati**, T. Sui, M. Mousavi, A. Prakash, E. Bitzek. *Quantifying eigenstrain distributions induced by focused ion beam damage in silicon*. Materials Letters 185 (2016) 47–49.
7. **E. Salvati**, T. Sui, H. Zhang, A. J.G. Lunt. K. S. Fong, X. Song, A. M. Korsunsky. *Elucidating the Mechanism of Fatigue Crack Acceleration Following the Occurrence of an Underload.* (2016) Advanced Engineering Materials. Volume 18, Issue 12, Pages 2076–2087

8. **E. Salvati**, S. O'Connor, T. Sui, D. Nowell, A.M. Korsunsky. *A Study of Overload Effect on Fatigue Crack Propagation Using EBSD, FIB-DIC and FEM Methods. (2016)* Engineering Fracture Mechanics. Volume 167, November 2016, Pages 210–223
9. **E. Salvati**, T. Sui, A. M. Korsunsky. *Uncertainty quantification of residual stress evaluation by the FIB–DIC ring-core method due to elastic anisotropy effects*. International Journal of Solids and Structures, Volume 87, 1 June (2016), Pages 61-69
10. **E. Salvati**, T. Sui, A. J.G. Lunt, A. M. Korsunsky. *The effect of eigenstrain induced by ion beam damage on the apparent strain relief in FIB-DIC residual stress evaluation*. Materials & Design, Volume 92, 15 February (2016), Pages 649-658.

Conference proceedings:

1. **E. Salvati**, H. Zhang, K. S. Fong, R.J.H. Paynter, X. Song, A. M. Korsunsky. *Fatigue and Fracture behaviour of AZ31b Mg alloy plastically deformed by Constrained Groove Pressing in the Presence of Overloads*. 21st European Conference on Fracture, ECF21, 20-24 June 2016, Catania, Italy. Structural Integrity Procedia (2016).
2. **E. Salvati**, S. O'Connor, D. Nowell, A.M. Korsunsky. *EBSD Investigation of Fatigue Crack Propagation Past a Crack Closure Due to Overload*. The 5th International Conference on Crack Paths (CP 2015). Ferrara, Italy, 16-18 September, (2015).
3. **E. Salvati**, M. Benedetti, T. Sui, A. M. Korsunsky. *Residual Stress Measurement on Shot Peened Samples Using FIB-DIC.* SEM 2015 Conference. Costa Mesa, CA, USA. June 8-11th (2015).
4. **E. Salvati**, A. J.G. Lunt, T. Sui and A. M. Korsunsky. *An Investigation of Residual Stress Gradient Effects in FIB-DIC Micro-Ring-Core Analysis*. IMECS Conference. Hong Kong. 18-20 March (2015).
5. **E. Salvati**, T. Sui, S. Ying, A. J.G. Lunt, A. M. Korsunsky. *On the Accuracy of Residual Stress Evaluation from Focused Ion Beam DIC (FIB-DIC) Ring-core Milling Experiments*. Proc. of the 5th Int. Conf. on Nanotechnology: Fundamentals and Applications Prague, Czech Republic, August 11-13, (2014) Paper No. 265

Table of Contents

Abbreviations

AFM	Atomic Force Microscopy
ALM	Additive Layer Manufacturing
CGP	Constrained Groove Pressing
CP-FEM	Crystal Plasticity – Finite Element Method
CT	Compact Tension
DIC	Digital Image Correlation
EBSD	Electro Discharge Machining
EDM	Electron BackScattered Diffraction
EDS	Energy Dispersive Spectroscopy
FCGR	Fatigue Crack Growth Rate
FEM	Finite Element Method
FIB	Focused Ion Beam
GIS	Gas Injection System
HAZ	Heat Affected Zone
IP	Integration Point
LE	Leading Edge
LEFM	Linear Elastic Fracture Mechanics
MC	Main Cut
MD	Molecular Dynamics
MP	Middle Position
ODF	Orientation Distribution Function
OL	Overload
PDF	Probability Distribution Function
RS	Residual Stress
SEM	Scanning Electron Microscopy
SIF	Stress Intensity Factor
SP	Shot Peening
SXRPD	Synchrotron X-Ray Powder Diffraction
TC	Trim Cut
TE	Trailing Edge
UL	Underload
WL	White Layer
XRD	X-Ray Diffraction
XRR	X-Ray Reflectivity

List of Figures

List of Tables

1. Introduction

1.1. General background

The design of structures, vehicles and machines must achieve cost-effectiveness in combination with the required level of performance, while at the same time guaranteeing the safety and durability of operation. Generally, the necessary condition for safe and reliable design of mechanical components and assemblies is expressed in terms of stress criteria that must not exceed the material and structural strength. The stress state within the material or a solid body is not completely determined by the external loads present. In fact, as a consequence of the manufacturing and processing history, residual stresses arise may exert significant influence on the evolution of damage and progression towards failure. Residual stresses are those stresses that are "locked-in" within the object, and persist even in the absence of active loading. These stresses are self-equilibrating, in the sense that regions of tensile and compressive stresses exist within solid bodies with traction-free boundary conditions, or in any case under zero force and moment resultants. Residual stresses may develop as a consequence of inelastic internal processes, but in the final state may be thought of as an elastic response to incompatible local strains within the component, for example, due to non-uniform plastic deformation. As a consequence of the presence of these incompatible inelastic strains, the surrounding material region must deform elastically to preserve continuity, thereby creating residual stresses that in turn must satisfy equilibrium. For example, the residual stress distribution through the thickness of a plate that undergoes plastic deformation by bending can exist without an external load. The tensile stresses balance the compressive stresses in a way that both force and momentum sums are nullified.

All manufacturing processes may create residual stresses and, depending upon the problem length-scale, these may be accounted for in the design process. Further, stresses can also develop during the service life of a manufactured component. When in service, residual stresses may combine with the stresses caused by external loading and contribute to failure. When the residual stress is of compressive nature, it is generally well-known to confer benefits for fatigue life. The presence of compressive residual stress combined with alternating cyclic stresses has the effect of reducing the mean stress. As became known from the pioneering studies conducted by Goodman [1] more than a century ago, the diminution of the mean stress value leads to the enhancement of fatigue life. However, controlling residual stress during manufacturing is extremely difficult, and in many cases it is impossible to achieve the most desired distribution, or remove them altogether. Welding process is an example where tensile residual stresses frequently arise within the finished component, with the consequent detrimental consequences for the component performance. These types of stresses can be called *uncontrolled* residual stress. On the other hand, a number of well-established techniques are available for the introduction of compressive residual stresses by localised plastic deformation (e.g. shot peening, hole expansion, deep rolling), and these can be called *controlled* residual stresses.

Figure 1. Images from the Viareggio train derailment (Italy). a) Capsized carriages and detached wheel sets [2]. b) Detail of the axle failure due to fatigue [3]

The Viareggio accident was the derailment of a freight train and subsequent fire which occurred on 29 June 2009 in a railway station at Viareggio, Lucca, a city in central Italy's Tuscany region. An illustration is provided in Figure 1(a). Twenty-six people were injured, and as of 22nd December 2009, 32 people were confirmed as having died [4]. As it is possible to see from Figure 1(b), mechanical failure occurred at the fillet of one of the train axles. The presence of striations at the fractured surface provided an overwhelming proof that failure was of fatigue origin. The fatigue failure mechanism involves the first stage during which the material accumulates damage locally due to the cyclic loads acting until a crack nucleates, usually from the component surface. The second stage of component damage is associated with the subsequent propagation of the nucleated crack until it reaches a critical length and size, at which point the third stage occurs when the component collapses in a rapid manner. As well as other mechanical components subject to cyclic loadings, train axles are commonly mechanically treated at the surface by deep rolling [5] with the purpose of introduce a compressive residual stress state at locations where stress concentrations are expected. It is then clear that the Viareggio disaster was trigged by either a deficiency in the design process or lack of adequate scheduled inspections. In any case, it is clear that the application of more profound knowledge of the interplay between the stress state (including residual stress), material processing and material properties (such as fatigue crack propagation and fracture toughness) could have prevented the loss of many lives.

The current state-of-art mechanical design rules only account for the residual stress evaluated at the macroscopic scale, i.e. stresses obtained by averaging over gauge volumes some millimetres in size. Such length-scales are representative of the entire volume where material damage occurs, as assumed in many successful approaches to fatigue durability prediction [6-14]. Nevertheless, particularly for high- and very-high-cycle fatigue (HCF and VHCF), material damage accumulation that leads to crack nucleation begin to occur at the grain level. In such cases, the adoption of a macro-scale approach to the evaluation of residual stress is not sufficient for reliable assessment of material life. The evaluation of residual stress at smaller scales is required to improve dramatically the quality of predictions where classical approaches lack in accuracy. Considerations may be made on the basis of approaches to design against fatigue that are similar to the existing large scale/continuum methodologies, yet modifications must be introduced to consider characteristic lengths ranging down to a few micrometres. In recent decades, the advent of miniaturised micro-mechanical systems (MEMS & NEMS) [15-18] has motivated researchers and designers to explore material strength characteristics at the micron- and even nano-scales. It is evident that when reliable *(micro) structural integrity* is sought, the characterisation of material microstructures and intrinsic stresses at the appropriate length scale is of vital importance.

For the purpose of distinguishing residual stresses across the scales, classification approaches are conventionally used. This classification distinguishes residual stress according to the length scale at which they are averaged. Type I, II and III stress types refer respectively to the residual stresses at the macroscopic scale, stress variations present from grain to grain (*intergranular*), and fine scale gradients that can be found within a single grain (*intragranular*).

As far as the experimental evaluation of residual stress is concerned, a number of well-established techniques are nowadays available, particularly when dealing with type I stresses. One class of techniques is based on the use of X-rays. This method has been used with increasing success to extract strain measures from the atomic arrangements perceived at the appropriate scales [19]. The great advantage of these X-ray based methods is their non-invasive nature, meaning that strains can be measured with good accuracy and without inducing damage into the probed material. Recent developments have been enabling the probing of strain at ever smaller scales. Such down-scaling of residual stress measurement resolution can be achieved by using micro-focused X-ray beams, but usually requires special preparation techniques for thin samples (~100nm).

Another family of residual stress measurement techniques relies on the material strain relief phenomena. The introduction of a cut in a material that contains residual stress gives rise to deformation in the vicinity as a consequence of stress redistribution that results in strain modification. Several sub-categories of this family of techniques exist. In contrast with X-ray scattering techniques, these methods are invasive. However, they lead to *absolute* residual stress estimates, whereas X-ray stress evaluation requires the knowledge of the unstrained reference material condition. With the recent advent of microscopic manipulation tools, the stress relief based techniques have been developed down to the (sub)micron-scale. One such approach is the FIB-DIC micro-ring-core method that has opened up a new range of possibilities for residual stress evaluation at high spatial resolution [20, 21], enabling probing residual stresses at all scales, including Type (I, II & III).

With the advent of the numerical methods for thermo-mechanical deformation modelling, it is possible to simulate numerous manufacturing processes and treatments. The applications of these methods is widely reported in literature as case studies, including welding [22, 23], shot peening [24-26], cold rolling [27-30], cold hole expansion [31-33] etc. Numerical modelling can also be a very useful tool for the parametric study of the process parameters [34-36]. Although this approach provides accurate simulation of the interactions occurring between the workpiece and the tool, and is thus very useful for understanding the residual stress origins, the computational effort and the amount of history-dependent and temperature-dependent material property information remains a major challenge.

As mentioned earlier, residual stresses must be self-equilibrating. It is thereby of great importance that agreement is sought between experimental measurements and the model to underpin their validity. A computationally lean and inexpensive approach to experimental data interpretation and sample state modelling is offered by the eigenstrain method [37, 38]. Eigenstrain-based methods have been successfully implemented both analytically and numerically for the modelling of various surface treatment and manufacturing processes that involve plastic deformation [39-42]. The fundamental of the method is the prescription of an inelastic strain (eigenstrain) distribution within the object that is characteristic of the plastic deformation induced by the process itself. As a consequence of such perturbation of the body equilibrium due to the eigenstrain, the stress balance can be re-established only upon the generation of a residual elastic strain field. The corresponding field of internal forces associated with this eigenstrain distribution is in fact the residual stress. In the current study, eigenstrain methodology is used extensively to model residual stress states across the scales.

1.2. Aim and scope of the current research

The current state-of-the-art in residual stress research presents several gaps that require further investigation. There is a number of aspects that require better understanding and further development, ranging from improvements in experimental techniques to the application of those technique to relevant case-studies. In recent years, scientific research in the field of mechanics of materials has been focused on the study of fundamental mechanisms at the micro- and nano- scales. These studies require high resolution equipment for manipulation, machining, imaging and characterisation.

Amongst the experimental techniques used for measurements of residual stress at the micro-scale, the sole one known to the author that is capable of providing the quantification of specific components of the absolute residual stress tensor at the micro- to nano-scales is the FIB-DIC micro-ring-core method. This technique has the potential to resolve residual stresses at the spatial resolution better than 1μm in all classes of materials, independently of whether they are crystalline or amorphous. Moreover, the FIB-DIC method is likely to become one of the most cost-effective ways of assessing Type I, II and III residual stresses in materials. However, as it was recognised at the beginning of the present doctorate project that several aspects required further study in order to make the methodology reliable and applicable to a wider range of materials. These aspects were related to the effect of FIB milling on the stress state of the target material and the formulation of good practice approaches for dealing with microstructured polycrystalline materials. These key improvements of the FIB-DIC technique formed a significant part of research presented in this thesis, along with the demonstrations of the application of the FIB-DIC ring-core technique to a number of practical situations that require experimental insight into the residual stress state variation at the micron scale.

As highlighted in the introduction, residual stress may exert significant influence on the onset and progress towards failure in mechanical components, particularly under cyclic loading. Fatigue, for example, is the single largest cause of failure in metals, estimated to be responsible for approximately 90% of all metallic component failure events; whilst polymers and ceramics are also susceptible to this type of failure [43]. The lack of fundamental quantitative insight into the mechanisms of failure evolution is the cause of this high percentage of failures due to fatigue. Another theme of the present work concerns the attempt to shed some light onto this problem, particularly for the case of cracks propagating in metallic materials or components. It is common knowledge that fatigue crack propagation rate (FCGR) is influenced by a large number of factors, although only few of them make a prominent contribution [43, 44]. Fatigue crack growth rate is known to be strongly dependent on the occurrence of crack closure, e.g. due to crack tip plasticity, and on the sign and severity of residual stress field in the vicinity of the crack tip. The role of these two mechanisms in crack propagation and how they are affected by the loading history remained unclear to a large extent, and was deemed worth investigating here. Improved understanding of the contributions to FCGR will lead to the formulation of more precise models for the prediction of safe lifetime of critical components. In this study, several experimental techniques were employed with the purpose of studying these mechanisms, namely, FIB-DIC ring-core milling, synchrotron X-ray powder Diffraction, EBSD, etc.

When dealing with polycrystalline materials, the evaluation of residual stress at the (sub) micron-scale turns out to be particularly challenging. The challenge arises from the fact that material grains typically show discrepancies in the intrinsic mechanical response, due mainly to the elastic and plastic anisotropy, and grains interaction effects. In turns out, in particular, that plastic strains introduced by the manufacturing and thermo-mechanical processing produce non-uniform oscillatory micro-scale residual stress fields. With the aim of refining the accuracy and completeness of experimental assessment of these stresses, systematic investigations were conducted of selected representative problems for this class of materials. For instance, the analysis of residual stress generated by shot peening, Electrical Discharge Machining (EDM) cutting and material bending was conducted and critically discussed in the context of a multi-scale approach to the problem, using continuum macroscale FEM and grain level Crystal-Plasticity FEM (CP-FEM) analyses.

Another field that deserves further attention concerns the modelling of residual stress. The use of eigenstrain theory has experienced fast growth in recent years, particularly in the context of its application for numerical simulations using FEM [45-47]. Nevertheless, significant limitations remain, especially when the objects of study possess complex geometries that cannot be readily described as equipotential surfaces defined by continuous functions. This shortcoming in the classical modelling methods provided the basis for developing a new modelling methodology. Accordingly, the aim of the final chapter of the present thesis was the consideration of particular cases in eigenstrain modelling where adequate methods could not be found in the literature. In this case eigenstrain modelling was used to simulate the residual stress states in a sample that could be approximately defined by extruded two-dimensional geometry, namely, an additively manufactured and shot peened compressor blade of a civil aeroengine.

1.3. Thesis Overview

Structurally, apart from the introductory (Chapter 1, Chapter 2) and summarising (Chapter 6), the thesis contains three main sections identified as Chapter 3, Chapter 4 and Chapter 5, that are respectively devoted to the developments of the FIB-DIC micro-ring-core method, the study of crack propagation under complex fatigue loading (in the presence of single overload/underload), and the study of residual stresses in polycrystalline materials, including the eigenstrain modelling aspect.

The first study of the FIB-DIC method focuses on the uncertainty quantification analysis in residual stress evaluation in polycrystalline materials. As described in the first part of Chapter 3, the effect of the local grain level elastic anisotropy is accounted for the first time, and the uncertainty in this parameter is assessed with the purpose of quantifying the attending errors in the residual stress evaluation. Furthermore, statistical analysis is presented aimed at evaluating the probability density function of residuals stress values where the underlined crystal orientation is unknown, and estimating the uncertainty error that arises from this effect. In the second part of Chapter 3, particular attention was paid to the study of the inelastic strain (eigenstrain) induced by Gallium ion implantation during FIB milling process within the shallow near-surface region where material amorphisation is also known to take place. From simple qualitative reasoning it is clear that when the depth of affected material becomes comparable with the FIB-DIC gauge volume, this FIB damage effect on the residual stress evaluation may be no longer negligible. Experimental tests, accompanied by Molecular Dynamics (MD) simulations were performed with the purpose of quantifying the eigenstrain magnitude and its extent within the affected region. Final aim of the FIB-induced effect study was the definition of a critical lower bound micro-ring-core dimension (diameter) above which this effect can be neglected.

Chapter 4 is focused on the application of the FIB-DIC method, alongside with other experimental techniques to shed light on the problems in mechanics for which the role of residual stress at the micro-scale is particularly significant. Attention is focused on answering one of the long-standing questions in fatigue fracture mechanics: to what extent the *residual stress* and *plasticity-induced crack closure* affect the crack propagation in presence of Overload and/or Underload applied following crack propagation under constant amplitude loading. Results obtained by combining several experimental techniques (i.e. synchrotron-based XRD, FIB-DIC, DIC, FEM, mechanical testing) are presented alongside validated non-linear FEM models. In particular, the first part of this Chapter is devoted to the study of Overload effect and the discrimination of the two principal contributing mechanisms (i.e. residual stress and plasticity-induced crack closure) to crack retardation. The second part focuses on the study of the Underload effect in terms of the acceleration of fatigue crack growth rate. The influence of the loading history *prior* to the occurrence of the Underload was revealed.

Finally, Chapter 5 explores a number of applications where the newly developed FIB-DIC techniques and other well-established methods were employed to obtain insights into deformation behaviour, especially in polycrystalline materials. The first part deals with the residual stress field arising from shot peening applied to samples having different notches severities (radii). Eigenstrain-based predictions of the residual stress fields are also presented. A second case-study concerns the characterisation of the brittle, so-called white-layer (WL) that develops during cutting of metallic samples by means of EDM (electrical discharge machining). Detailed microstructural and residual stress analyses of the WL are shown and discussed along with the implications of these findings. The third part reports the newly developed methodology for prescribing eigenstrain distributions in samples of arbitrary shape. A practical example of the application of this method is considered. A study of residual stress arising as a consequence of additive manufacturing and shot peening of an aeroengine compressor blade is presented, illustrating the strength and accuracy of this method. Finally, the FIB-DIC method and numerical simulation are used to study the stress state arising in a polycrystalline sample subjected to inelastic bending. The discrimination of residual stress across the scales is presented, in accordance with the definition residual stress into Type I, II and III. The statistical distribution of stress at the grain level is described by collecting the experimental measurements and performing comparison with macroscopic (continuum FEM) and microscopic (CP-FEM) predictions.

The concluding Chapter overviews the key points of my doctoral study, and discusses the implications that they have for the research and applied problems. Finally, ideas for possible further study are given.

2. Scientific Background

2.1. Residual Stress

2.1.1. The Origins of Residual Stress

Residual stress is usually generated when engineering materials are subjected to manufacturing operations that involve thermal and mechanical processing. The processes may also be classified into solidification (e.g. casting), shaping (forging, rolling, stamping, extrusion), thermal (heat treatment, hot isostatic pressing), material removal (machining) or joining (e.g. welding, soldering, diffusion bonding). An important class of processes concerns additive manufacturing which may combine many of the features of other processes. For example, powder bed selective laser melting, apart from melting itself, also involves solidification, thermal treatment, and micro-scale joining processes.

The mechanisms that give rise to residual stress formation can be described with reference to Figure 2. For illustration, consider the initial condition of a coating (shown in green) to have the same length as the substrate (shown in blue), L_0. Let us now assume that, at some point, the coating undergoes elongation due to plastic deformation inducing a change in its "natural" length from L_0 to L_1. Now, in order to join the two elements, i.e. attach the coating to the substrate, the coating must shrink elastically. In order to balance the internal forces and moments, the substrate must also be elongated elastically. In simple terms, compressive residual stresses will arise in the coating and at the same time tensile residual stress will develop in the substrate. Furthermore, the entire assembly must undergo bending to ensure that moment balance is also satisfied. This simple example illustrates the way in which plastic strains give rise to accompanying elastic strain fields that satisfy equilibrium and compatibility requirements simultaneously.

Whenever a more complex realistic processing operation is considered, residual stress can be thought to originate in a similar manner, whereby an inelastic deformation (often referred to as *eigenstrain*) gives rise to accommodating elastic strains that restore continuity (compatibility) and maintain the equilibrium of forces (and moments) via the presence of residual stresses.

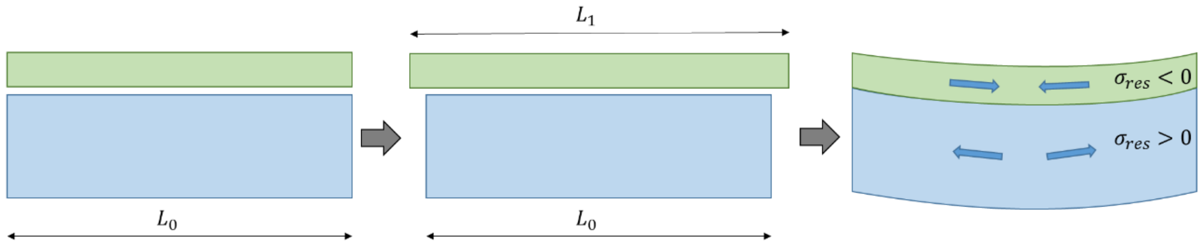

Figure 2 Schematic illustration of residual stress formation

Let us consider a material that is subjected to heat treatment and does not show any change in crystal structure during the process. The cooling step of any heat treatment develops a gradient of temperature within the material due to the different cooling rates occurring at the surface and in the inner regions of the material. Since elevated temperatures generally reduce the yield stress of materials, non-uniform cooling is accompanied by plastic flow and permanent shape changes in the hotter interior regions. On the other hand, the cooler outer region tends to contract ahead of the core which experiences compression, whilst the outer regions find themselves in tension. It is important to note that plastic flow is typically controlled to the greatest extent by the deviatoric part of the stress tensor, meaning that the evolution of plastic strains is dependent on the sample shape and the direction of local thermal gradients. After cooling is completed, material surface that has seen less plastic flow typically remains in compression, with the core sustaining tension.

However, not all materials will have compressive residual stress at the outer regions following this process. If phase transformation occurs during cooling process, the resulting residual stress may be highly dependent on the extent of transformation strain, e.g. volume expansion/contraction, or shear. An example is given by steels that undergo the phase transformation from austenite to martensite during quenching. Indeed, the volume expansion due to the formation of martensite at the material surface may result in the surface being subject to tensile residual stress after cooling to room temperature. The nature of residual stress after heat treatment may be further modified by means of annealing at moderate temperatures.

Other manufacturing processes also considerably affect the final material residual stress state. An example is a material forming operation such as cold rolling. Due to the friction at the interface between the work piece surface and the rollers, the surface tend to undergo greater amount of deformation than the inner material. Therefore, compressive residual stress may be introduced at the surface, and tensile stress in the inner regions in order to achieve the balance of internal forces in the sheet metal after processing.

Amongst other manufacturing processes that generate residual stress it is worth dwelling on welding as an important example. During welding, only a localised region within the material undergoes melting. The molten material tends to reduce in volume during solidification, but at the same time the surrounding solid material provides a constraint for this volume change, giving rise to tensile residual stresses within or near the weld. Alongside with the detrimental effect of tensile residual stress in the vicinity of the weld, the final product may contain internal defects and microstructural changes, and have overall distortion that may compromise the mechanical and geometric tolerances and thus the functionality of the assembly. Once again, thermo-mechanical post-weld heat treatments are used to overcome partially these issues.

In general, compressive residual stresses are preferable at the surface of mechanical components, since they prevent crack formation and propagation, and may increase hardness and reduce wear rate. Numerous techniques have been developed to introduce compressive residual stresses in final products. One of the most used and well-established technique is shot-peening. In this process, high speed shot particles fired at the sample surface cause local plastic deformation within a shallow surface layer. Similarly to the illustration in Figure 2, the material lying at greater depths does not undergo plastic deformation, and provides constraint for the surface layers undergoing in plane expansion. This gives rise to high compressive residual stresses at the surface. In accordance with the force/moment balance requirement, tensile residual stress develop in the core. If the thickness of the product is large enough compared to the depth of plastic deformation, then the tensile residual stresses are distributed through large enough thickness to result in low stress magnitude.

Examples of all manner of residual stress arising in production are shown in Figure 3. The left column illustrates typical residual stresses generated at the macro-scale, while the right column shows a few examples of residual stress arising at the grain-scale. Detailed classification of residual stress will be presented in the next section.

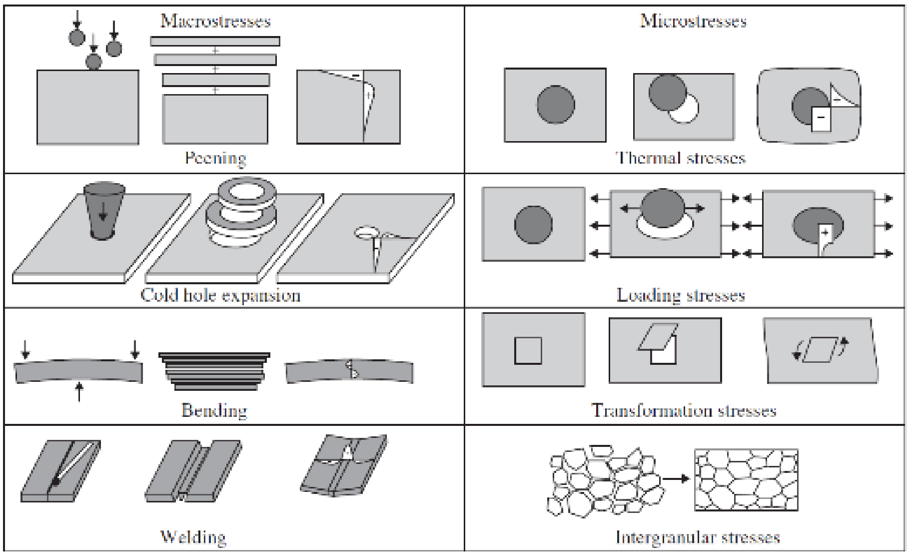

Figure 3 Examples of some typical ways in which residual stresses are created in engineering materials. Reproduced with permission from [48] .

It is important to highlight that in some cases residual stresses may change their magnitude and sometimes even their sign when engineering component is in service, e.g. during fatigue. For example, in low cycle bending fatigue residual stress may change sign each half cycle [49]. Moreover, residual stress may change sign even in shot-peened components loaded in fatigue with positive R-ratios (i.e. tension-tension). As a general rule, attention must be paid to cyclic processes which induce inelastic deformation, because these tend to modify the distribution of eigenstrains that serve as the origins of residual stress.

2.1.2. Classification

Residual stress is a quantity of great complexity, not only due to its inherent tensorial nature, but also because of the dependence on the scale of consideration. The very definition of stress as a component of internal force per cross-sectional area introduces the concept of scale: the choice of the linear dimension to which this definition refers immediately defines the inherent resolution of subsequent consideration. Notably, this also contains an element of non-locality: the operation involved in the definition of stress amounts to averaging over a chosen cross-sectional area, implying that oscillations on the finer scale are deliberately ignored. Instead, the value obtained is assumed to be distributed uniformly over the entire domain. Note that a similar argument applies to the definition of strain that is linked to an initial reference length that defines the scale of consideration.

The natural limit to these definitions arises from the atomic structure of matter: once the characteristic dimension of the analysis becomes comparable with the interatomic distance (be it in crystalline or amorphous solid), the underlying 'graininess' of matter commands that bonding forces are taken into consideration in place of 'smeared' continuum description. An interesting set of challenges then arises in determining the extent to which continuum theories are capable of capturing correctly the mechanical interactions that play out at those shortest length scales. Seeking answers to these questions has been a persistent theme in nano-scale materials science and technology, and both bottom-up and top-down approaches have been pursued. Notable work in this field has been linked to the interpretation of Molecular Dynamics (MD) simulation results in terms of continuum stresses and strains [50, 51].

As long as the scale of consideration remains above the scale of several interatomic distances, i.e. a few nanometres, the possibility of interrogating internal forces and deformation using classical continuum definitions of stress and strain remains valid and relevant [52]. It has been shown in various studies that tiny volumes of material as small as 3-4 atoms along the edge obey the classical laws of continuum mechanics, provided a correction is made for the surface energy effects that become significant at these scales [53].

In the context of residual stresses this means that consideration can be conducted across the scales, from nanometric to microscopic to macro-scale. In relation to the underlying microstructure of polycrystalline solids this subject has been the focus of interest of several authors since the 1960's, with notable contributions made by Macherauch [54], Pintschovius [55], Niku-Lari [56] et al. It was probably Macherauch who introduced the classification of residual stresses according to scale into Type I, II and III. Referring to the conceptual illustration of this classification in Figure 3 (from [56]), we note that the separation of stresses into these three types is additive, namely:

$$\sigma^{RS} = \sigma^{RS,I} + \sigma^{RS,II} + \sigma^{RS,III} \tag{1}$$

This classification is of great importance both from the viewpoint of historical developments in residual stress analysis and evaluation methodology, and in terms of adopting correct approach and interpretation based in current research. Figure 4 illustrates that each subsequent stress term refers to the *deviation* from the previous at the finer scale: Type II stresses refer to the extent to which the grain average value of residual stress differs from the macroscopic trend of Type I long range stresses, while

Type III is the intragranular deviation of nanoscale stress from the grain average level. Type III stresses are of particular conceptual importance, since they may be directly associated with material defects, such as vacancies, voids, precipitates, inclusions, slip bands, dislocation pile-ups, etc. Although such straightforward association is not possible for Type II and Type I stresses, it is clear that these stresses arise due to aggregation of nano-scale defects that cause micro-scale mismatch in the thermal and mechanical properties between different distinct phases present within the material (Type II) or to macro-scale inhomogeneity associated with inelastic deformation history, e.g. bending, forging, machining, etc.

The present model is closely related to another well-known model widely accepted by the scientific community, the so-called Mughrabi composite model [9, 10]. Its basic idea is that the presence of dislocation distributions within a crystal makes it display some aspects of dual-phase (or multi-phase, in general) material behaviour that contains “hard” regions and “soft” regions. This model can be thought of as the combination of material unit cells, or representative volume elements (RVE’s) containing walls of high dislocation density (hard region) around the cell core region of low dislocation density (soft region). As well as the description discussed above, the Mughrabi composite model also introduces built-in long-range internal stresses. Considering the material configuration after loading, the model predicts high and low magnitudes of residual stress, respectively in the hard and soft regions. It is then evident that the smallest scale considered in the model determines the RS types referred to in terms of the grain level (e.g. intra- vs inter-).

All of these processes and sources of residual stress can be conveniently generalised based on the previously mentioned scale-independent concept of *eigenstrain* that refers to any inelastic process, including phase transformation, plastic deformation, etc. The development of eigenstrain theory [47, 57-59] led to the formulation of direct and inverse problems that allow, respectively, the calculation of residual stress from the underlying intrinsic eigenstrain distribution, or the determination of unknown eigenstrain distribution based on residual stress known at a number of probe points.

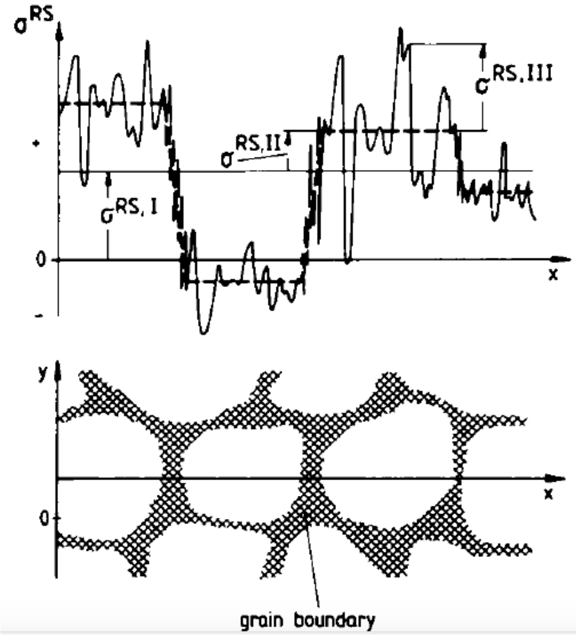

Figure 4 Illustration of the multi-scale nature of residual stresses in polycrystals [56].

Accurate and reliable residual stress (RS) evaluation is a critical pre-requisite step for understanding and predicting engineering component behaviour and failure. Quantification of the magnitude and orientation and fine scale variation of locked-in internal forces has great utility for a wide range of applications, from the impact of ion radiation on thin films to the interaction between residual and applied stresses in the failure mode of high-pressure components.

Type II and III stresses are usually neglected when dealing with the study of the structural integrity of mechanical components having characteristic dimensions of the order of tens of millimetres. Nevertheless, it is evident that mechanical failure originates at the grain level, where intra-granular stress plays a crucial role. Particularly when cyclic loading is applied, regions within grains that contain tensile RS are more prone to damage accumulation in the form of slip or twinning, subsequent formation of defects and micro-voids that lead to crack nucleation and propagation. A relevant example can be the dwell fatigue failure which is a well-known failure mechanism experienced in aero-engine discs. This type of failure manner is thought to be highly influenced by the presence of very localised residual stress arising by the interaction between hard and soft grains during cycling [60], giving rise eventually to facet formations followed by crack nucleation.

For these reasons, the knowledge and understanding of Type III RS has the potential to improve dramatically the accuracy of mechanical failure prediction. From the practical point of view, precise point-wise RS simulation within material microstructure remains rather prohibitive due to the large computational effort required. On the other hand, a statistical approach to the problem may provide an improvement in terms of accounting for the influence of RS distribution on the onset and development of failure processes.

Whilst the evaluation methods of Type I residual stress have advanced to the stage when industry level standards have been available for a few decades, until recently intergranular (Type II) and intragranular residual stresses (Type III) continued to be discussed and described mostly at the conceptual level. This is due to the insurmountable difficulties of their practical evaluation at the appropriate scale and resolution. Experimental stress evaluation techniques are inextricably linked to a certain length scale, the so-called gauge volume, within which the interaction between the probe and the solid material in question is played out.

2.1.3. Measurement techniques

In terms of the experimental techniques available for RS evaluation, attention must be paid to the effective gauge volume and nature of measurement. It is important to make a further classification of RS analysis techniques into three principal approaches:

I. *Non-destructive*. Physical analysis methods allow RS evaluation via the quantification of small variations in structural or physical parameters e.g. the evaluation of interplanar atomic lattice spacing by diffraction, or changes in molecular bond stiffness by spectroscopy. The wide range of experimental methods includes high resolution optical techniques, Raman spectroscopy analysis of diamond-like coatings [61, 62] and a multitude of X-ray diffraction techniques for the analysis of intergranular stresses [63-66] .High resolution Electron Back Scatter Diffraction (HR-EBSD) has also made significant advances, and provides a powerful means of determining the lattice strains at resolutions ranging from sub-micron scale in back-scattered geometry to a few nm in transmission. In the last decade ever increasing levels of EBSD sensitivity have been achieved through the improvement of interpretation procedures [67]. Accurate intragranular lattice mis-orientation and quantitative RS analysis is now possible to quantify small changes in diffraction patterns (HR-EBSD) [68, 69]. An example of recent relevant work is the analysis of intragranular stress/strain distribution around an inclusion [70]. Non-destructive methods rely on the quantification of the relative changes in the measured parameters, and require comparison with a reference. The accuracy of these techniques is therefore limited by the precision to which reliable reference values can be determined. However, this approach cannot be applied to amorphous materials or heavily deformed crystals, due to the degradation of Kikuchi scattering patterns.

II. *Destructive*. The introduction of traction-free surfaces by sample sectioning induces stress redistribution and strain relief in the surrounding material. In this respect the approach is most closely related directly to the conventional definition of stress. The quantification of strain or displacement caused by the relief of tractions at the sectioned surface can be used in combination with numerical modelling to back-calculate the residual stresses originally present in the material. Experimental techniques that rely upon this approach include the slitting and contour method, with typical resolution in the range of fractions of a millimetre being achievable [71, 72].

III.*Semi-destructive*. The introduction of localised stress relief through hole-drilling or core milling can be used to quantify the magnitude of stress at a particular location within a sample [73, 74], whilst introducing minimal disturbance to its overall state. Similarly to the destructive techniques, the quantification of the strain change induced at the surface enables back-calculation of the residual stresses originally present. Traditional semi-destructive techniques are capable of resolving stress at the resolution of ~1 mm laterally, and at a depth resolution of ~0.03 mm. The idea of obtaining a minimally destructive probe of local RS using a ring-core geometry is not new: it goes back to the pioneering work of Wolf in the early 1970’s [75]. The need for probing RS at smaller scales pushed researchers to develop procedures that involve finer tools for material removal [21, 76]. The nano-scale Focused Ion Beam (FIB) [77] ring-core milling, in combination with Digital Image Correlation (DIC) has been developed to quantify RS in a precisely defined micro-scale gauge volume. Comparison with Finite Element (FE) simulation is used to relate the strain relief to the pre-existing RS state. FIB-DIC, as the method has become to be known in short, provides a conceptually appealing mechanistic approach to RS evaluation on the scale from a few microns to sub-micron, and thus lends itself naturally to the application for the study of inter- and intra-granular residual stresses (Type II and Type III).

2.2. Experimental techniques for residual stress measurement

2.2.1. FIB-DIC ring-core

Amongst the various techniques adapted to the measurement of residual stress at the micron scale, the Focused Ion Beam – Digital Image Correlation (FIB-DIC) ring-core method is particularly versatile and adaptable [78-85]. This method may be considered as a semi-destructive technique that is analogous to the macro-scale ring-core method, and it is based on the measurement of material relief after cutting [75]. The difference stems from the fact that FIB is adopted as the milling tool for the material removal, and SEM is used for imaging the resulting surface, rather than employment of strain gauges. In the course of the milling process a circular trench is machined around the central "island", or micro-pillar. The variation of surface strain in the course of this procedure is monitored using high resolution imaging by means of a SEM (Figure 5).

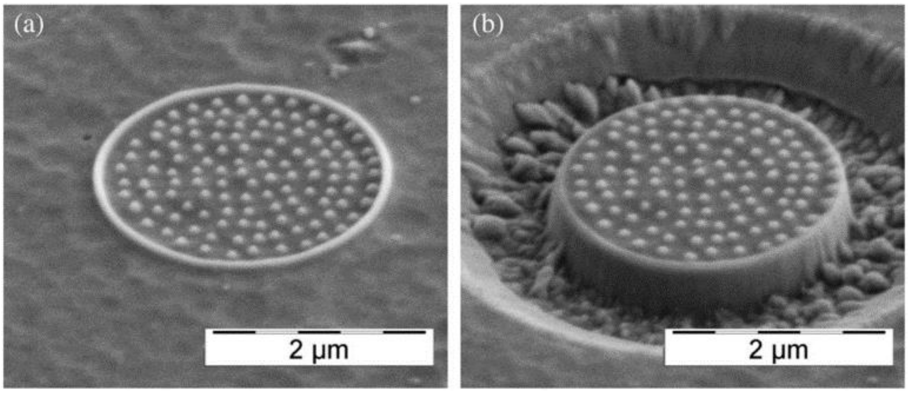

Figure 5 SEM images of the ring-core (a) prior and (b) after milling. [84]

DIC software is used to determine the displacement field, and to compute the strain increment. The apparent strain relief evolution as a function of milling depth is plotted, the profile is fitted with a "master curve" function [21] derived from FEM modelling. This procedure allows robust estimation of the residual strain present at the same location prior to milling. The analysis of the strain components, in at least three different in-plane directions, provides enough information for the reconstruction of the complete in-plane strain state [21] (Figure 6).

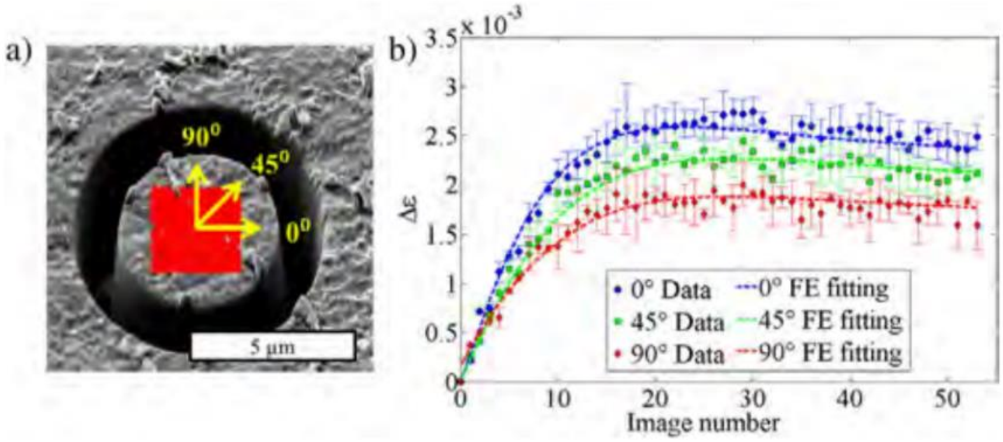

Figure 6 (a) SEM image showing DIC marker placement on the core centre (red). (b) Strain relief curves obtained as function of the milling depth in the 0, 45 and 90 degrees orientations. [21]

If the object of study contains gradients of residual stress within a shallow layer of size comparable with that of the ring-core, other approaches need to be utilised for the evaluation of the depth stress evolution. The most used and widely accepted technique for residual stress depth profiling relies on the use of an integral method firstly developed by Schajer [86-90]. Although this calculation method was developed specifically for the macro-scale version of the ring-core method, recently it was applied also in the FIB-DIC micro-ring-core version successfully [78].

Other, alternative geometries have been proposed by several researchers for the analysis of residual stress by monitoring the strain relief. Especially when higher depth sensitivity is needed and only one component of residual stress is required, the so-called double slot [91] (Figure 7(a)) and the single slit [92] (Figure 7(b)) geometries can be used. Similarly to the ring-core geometry, the relief strain that manifests at the material surface is interpreted through numerical modelling.

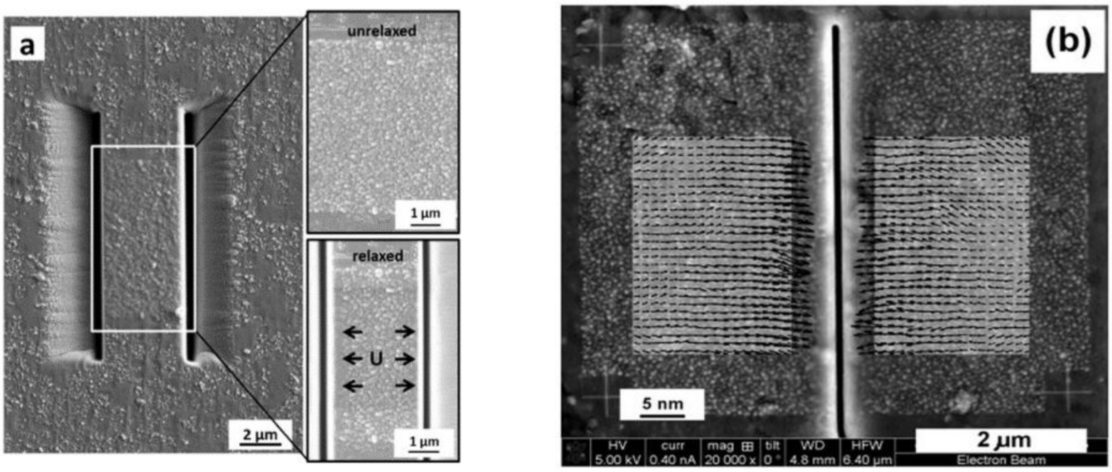

Figure 7 Uni-axial residual stress relief (a) Double slit [91] and (b) single slit [92] geometries.

Furthermore, these geometries are sometimes used for the evaluation of two stress components of even the full in-plane tensor. In the first instance, the double slot milling process can be performed multiple times for different orientations (Figure 8(a)). This configuration enables the assessment of one component of strain relief during the first double slot machining and the perpendicular component by relieving the residual stress in along the corresponding direction.

In contrast to the ring-core method that analyses the strain relief occurring in the core defined by the surrounding trench, the conventional hole drilling geometry analyses the strain field in the outer region close to the central hole (Figure 8(b)) [92].

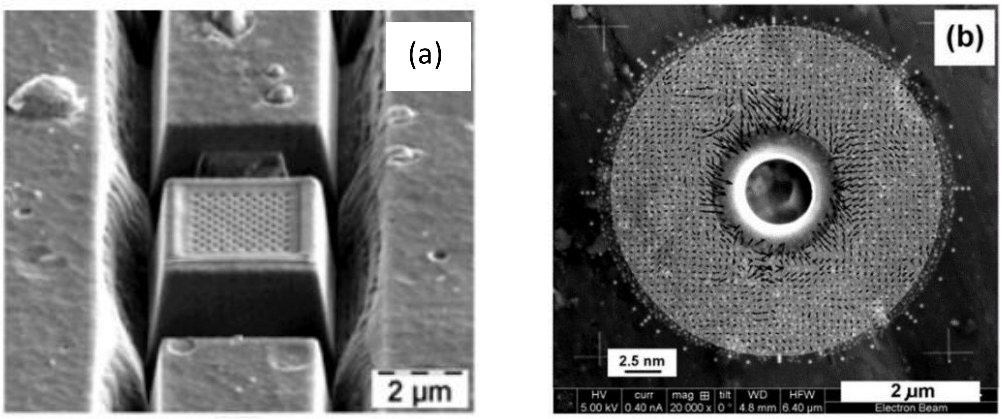

Figure 8 (a) Four slot [93] and (b) hole drilling [94] geometries examples

The principal limitation of these micro-scale approaches is given by the fact that they rely on the strain relief induced in relatively large surface regions (typically 5 times the ring core dimension) [82].

The residual stress field in this region is altered by the milling itself. This may limit their applicability for high-resolution spatially resolved analysis.

Two options arise for attaining this objective, namely, sequential milling or parallel milling of features on the sample surface [83]. A schematic of these two approaches is shown in Figure 9; sequential milling involves the incremental determination of residual stress in islands placed at regular intervals (left of Figure 9), whereas parallel milling requires simultaneous milling of multiple features in a contiguous array (right of Figure 9).

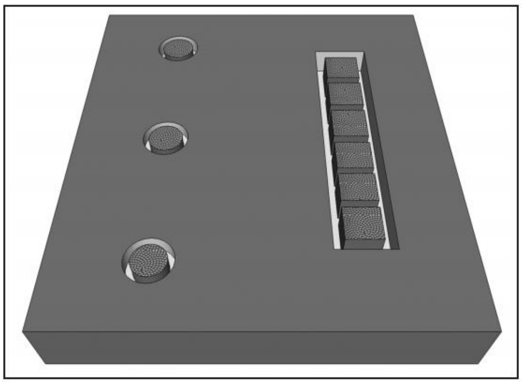

Figure 9 Schematic representation of the sequential (left) and parallel (right) approaches. [83]

2.2.2. X-ray Powder Diffraction

Diffraction techniques are widely employed for the study of engineering component formed by crystalline material. This technique is characterised by high versatility and precision, and non-destructive nature. Back in 1912, Max von Laue was the first to show that when X-rays interact with crystalline materials, they undergo diffraction, i.e. scatter in a highly structured way. A concise and convenient mathematical description of the relationship the between incident beam wavelength, interplanar lattice spacing and the scattering angle was proposed by Braggs in the form of the famous law. The development of appropriate instruments to make use of these relationships followed, from laboratory diffractometers to large particle accelerators, such as synchrotrons and neutron spallation sources.

There are several advantages that make X-ray diffraction favourable over other techniques in the context of residual stress evaluation:

- Residual stress can be evaluated in an entirely non-invasive manner making possible the assessment over the entire product life.
- The probed volume of material (gauge volume) can be defined flexibly due to the possibility of selecting beam spot size and energy.
- When high flux is available (Synchrotron based X-ray Diffraction), short time data acquisition can be performed enabling the measurement of *in situ* and time-dependent processes, e.g. phase transformation, heat treatments etc.

Although XRD stress analysis can be performed by means of lab-based X-ray sources, 3rd generation synchrotron facilities offer extremely high brilliance that in turn provides increased penetration depths and better insight into the bulk characteristics of the sample. Synchrotron radiation is based on the acceleration and injection of a small packet of charged particles (usually electrons) into a polygonal path. The accelerated beam travels close to the speed of light and is being continuously bent through magnets that contain the beam within the closed trajectory. The beam deflection process generates photonic radiation that covers a broad spectrum of wavelengths including X-rays. Otherwise, insertion of devices known as wigglers or undulators into the beam path can produce a sinusoidally varying magnetic field which generates constructive interference at the desired frequency.

High resolution analysis is facilitated by further refining the incident beam followed by accurate focusing. Optical methods have been developed to reduce the beam spot on the sample, e.g. Fresnel zone plate (FZP) or compound refractive lenses (CRL) that focus the incident radiation. However, one of the most versatile approaches is the use of Kirkpatrick-Baez (KB) mirrors which reflect and focus a broad range of energies present in the incident radiation in the vertical and horizontal planes down to (sub) micron size.

In the application to polycrystalline materials, the mode of X-ray analysis commonly employed is called X-ray Powder Diffraction (XRPD). XRPD is typically performed using a monochromatic beam, which is defined as having a single characteristic wavelength with small bandwidth. A monochromator is typically used to select the desired wavelength from the broad spectrum of incoming radiation produced by the synchrotron. The choice of wavelength is highly dependent upon the capabilities of the beamline and the X-ray absorption characteristics of the sample under investigation. This particular

XRD technique is widely employed not only for the analysis of residual stress, but is also used for phase identification and texture analysis. An example of diffraction pattern is shown in Figure 10. This pattern is characterised by the presence of peaks that are associated with certain families of atomic planes. The analysis of peak shift or shape modification is able to provide quantitative or qualitative information regarding the internal lattice strain modification (peak shift), permanent deformation (peak broadening) and density of atoms in the structure (peak intensity). The characteristic peak modifications are illustrated in Figure 10.

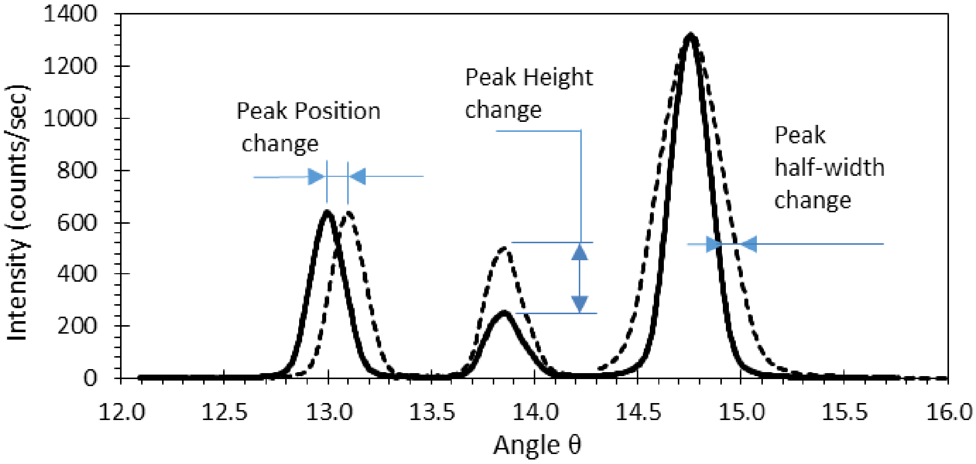

Figure 10 Characteristics of the diffraction peaks

For a given lattice plane, Bragg's law provides a way to relate the d-spacing with the half scattering angle (2θ):

$$n\,\lambda = 2d^{hkl}\sin\theta \tag{2}$$

Here n is an integer (1,2,3,…), λ is the radiation wavelength, d^{hkl} is the interplanar distance between planes of Miller indices (hkl), and θ is the angle that the incident beam makes with the lattice planes (also known as Bragg's angle). Using this elegant law allows to retrieve the beam angle of incidence at which atomic planes produce the most intense reflection of the electromagnetic radiation. As far as the residual stress analysis is concerned, the fundamental principle used for stress/strain analysis relies on the quantitative evaluation of the distance between lattice planes, d-spacing. The lattice plane spacing can be easily retrieved using the Bragg's law (2) once the diffraction pattern is acquired (peak centre position in terms of Bragg's angle θ) using radiation of known wavelength λ. Therefore, for a given lattice plane hkl, the lattice strain along the direction h can be determined using

$$\varepsilon_i^{hkl} = \frac{d_i^{hkl} - d_i^{hkl}}{d_i^{hkl}} \tag{3}$$

For successful collection of powder diffraction data, thousands of crystallites need to be simultaneously irradiated within the gauge volume. This implies that the grain size of the polycrystalline substrate must be significantly smaller than the focal spot size of the incident beam.

Assuming that the sample is untextured i.e. has no preferred crystallographic orientation, the irradiated crystallites are randomly orientated and therefore the Bragg condition can be equally well achieved for any given azimuthal angle (ω). The resulting diffraction is observed in the form Debye-Scherrer cones with half opening angles ($2\theta_1^{hkl}$, $2\theta_2^{hkl}$,…) corresponding to differing lattice spacings (d_1^{hkl}, d_2^{hkl},…) as shown in Figure 11.

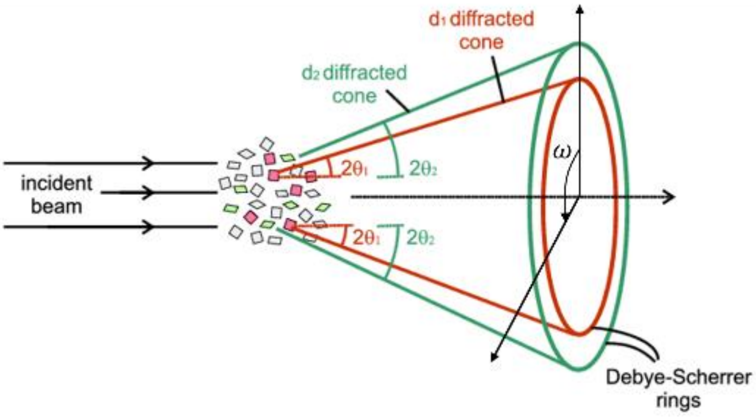

Figure 11 Schematic representation of the diffraction cones (Debye-Scherrer)[95]

XRPD can be performed using transmission mode, reflection mode or either a grazing incidence arrangements. In grazing incidence diffraction, the sample is arranged such that the incident beam is offset by ≈3−5° from the surface of the sample. This approach is highly effective in the analysis of thin films and coatings as it probes the near-surface characteristics of the sample, however, due to the geometric elongation of the focal spot, it only provides insight into the in-plane characteristics in a single orientation. In contrast with this arrangement, transmission mode XRPD considers the incident radiation aligned with the sample plane normal, permitting the collection of a through-sample average. Typically, a 2D detector is placed downstream from the sample in order to record the diffraction patterns corresponding to a particular cross section of the Debye-Scherrer cones. This geometry furnishes insight into the in-plane structural variation, and can be used to provide information about crystallographic preferred orientation through the variation in diffracted intensity as a function of azimuthal angle (texture analysis).

As will be illustrated in this study, the processing of 2D diffraction data is typically performed using software such as FIT2D [96]. This software is mostly used for sample-to-detector distance calibration and allows precise determination of the equivalent 1D diffraction patterns, such as shown in Figure 10.

Peak centre determination can be based on single peak fitting in order to obtain estimates for the height, peak width and peak centre parameters. Diffraction peaks are typically best described by a convolution between the Gaussian and Lorentzian distributions but, a simple and effective approximation to this is the Gaussian distribution:

$$f(\theta,\omega) = Ae^{-\frac{(\theta-B)^2}{2C^2}} \tag{4}$$

where A is the peak height, B is the peak centre and C is the peak half-width parameter. Confidence intervals of each fitting can be retrieved by least squares analysis for each parameter, which is critical to the strain error estimation.

2.2.3. X-ray reflectivity

X-ray reflectivity (XRR) technique is particularly suitable for the study of very thin layers (from few to tens nm).This technique relies on the analysis of the intensity of specular X-ray reflection as a function of the varying incident angle [94, 97]. The typical setup adopted in this type of experiment is shown by the scheme in Figure 12.

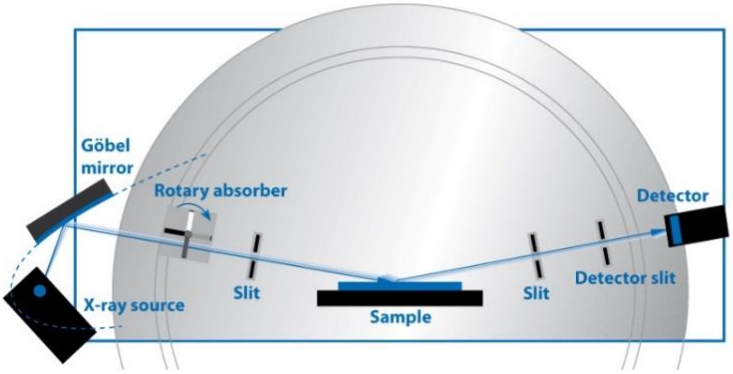

Figure 12 Typical setup of an XRR experiment [98]

Refractive index for a given X-ray energy has value smaller than unity and it can be written as:

$$n = 1 - \delta - i\beta \tag{5}$$

where δ and β denote, respectively, the real part related to the phase velocity, and β the imaginary part related to absorption and also called the extinction coefficient. The β parameter is related to the linear absorption coefficient μ as follows:

$$\beta = \frac{\mu\lambda}{4\pi} \tag{6}$$

where λ the X-ray wavelength.

Coefficient δ depends on the X-ray wavelength and the layer density. A useful formula relates this parameter with the critical angle above which the incident X-ray beam penetrate the sample due to refraction:

$$\Theta_c = \sqrt{2\delta} \tag{7}$$

Once the incidence angle Θ passes the critical value, the presence of electron density variation with depth below the sample surface in the form of a single or multiple layers leads to interference that manifests itself in the oscillatory dependence of reflected beam intensity on the incidence angle. This oscillation is a function of d, the thickness of distinct layer(s), and the depth variation of the refractive index. In the case of a single distinct layer film the oscillation of the reflected intensity I can be described as follows:

$$I \propto \cos\left(\frac{4\pi d}{\sqrt{\sin^2(\Theta - 2\delta)}}\right) \tag{8}$$

Further multipliers need to be incorporated in the above expression to account for the decay with the incident and scattering angles, but the above equation captures the modulation trend. By fitting an equation incorporating the oscillatory dependence described by (8) to experimental data, the layer thickness can be determined. In cases when multi-layer systems are being studied, the use of non-linear least-squares fitting is necessary.

2.2.4. EBSD

EBSD is an extensively used technique for the microstructural and crystallographic characterisation. It can be employed to study any crystalline or polycrystalline material provided the analysed surface is relatively flat and not affected by large plastic deformation. Typically it is used to explore microstructures, revealing texture, defects, grain morphology and deformation. It can be combined with complementary techniques, such Energy Dispersive Spectroscopy (EDS) within the SEM for phase discrimination at high spatial resolution (~0.2μm). Such high resolution allows discrimination of small misorientations that may occur in a single grain which are related to the plastic strains present in single grains (and hence Type III residual stresses). Misorientation can be also used for the production of qualitative strain maps.

Back in 1928, Nishikawa and Kikuchi were the first scientists to discover the fundamental diffraction phenomenon on which EBSD is based. They witnessed for the first time the diffraction patterns produced by illuminating a crystalline sample surface with a 50keV electron beam at grazing angle of 6°. These patterns are nowadays known as Kikuchi patterns (Figure 13(a)).

Modern EBSD experiments are commonly conducted within a SEM chamber. The relatively large range of electron beam energies offered by SEM makes this system extremely versatile. The SEM chamber is equipped with an EBSD detector containing usually a phosphor screen, compact lens and low light CCD camera, as schematically illustrated in Figure 13(b). Commercially available EBSD systems typically come with one of two or more different CCD cameras: for fast measurements the CCD chip has a native resolution of 640×480 pixels; for slower, and more sensitive measurements, the CCD chip resolution can go up to 1600×1200 pixels. For texture and orientation measurements, the diffraction patterns are binned in order to reduce their size and reduce computational times. Modern EBSD systems can index patterns at up to 1800 patterns / second. This enables very rapid and rich microstructural maps to be generated. High-resolution detectors possess higher sensitivity that allows the analysis of the diffraction pattern in more detail. Recently, it has become possible to exploit the information contained in high-resolution patterns thanks to the development of the so-called HR-EBSD technique [67-69]. By analysing the small angular changes (~0.006°) in the Kikuchi patterns, this technique provides measurements of residual elastic strain and lattice rotation with very high precision, enabling the measurement of strain with a precision of $1x10^{-4}$.

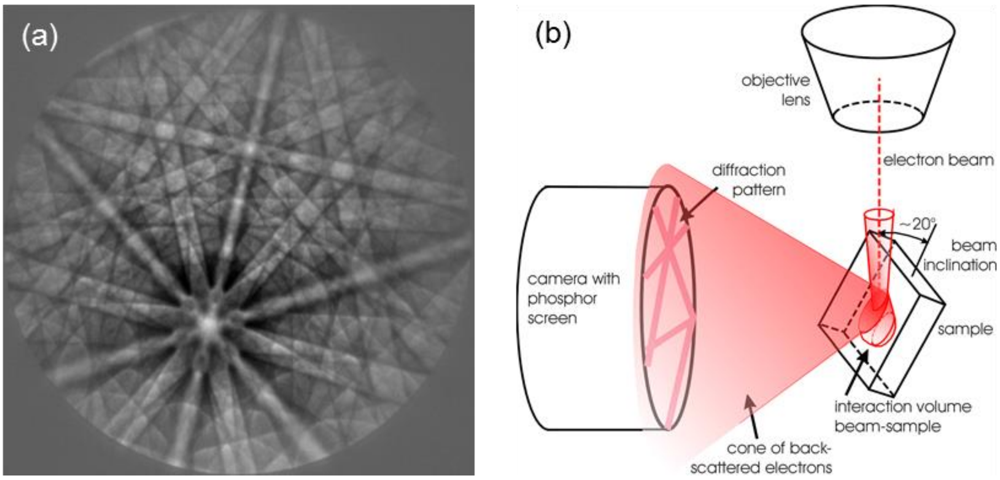

Figure 13 (a) EBSD pattern example and (b) Geometric setup [99]

2.3. Fatigue Crack Propagation

Developments of cracks in a body may occur due to the presence of either a monotonic or cyclic external loading. In the most common scenario of crack growth, a small flaw that is initially present develops into a crack and subsequently grows until it reaches a critical value at which the component may fail by brittle fracture.

There are the types of loading that a crack can experience, as Figure 14 illustrates. Mode I loading, where the principal load is applied normal to the crack plane and tends to open the crack. Mode II corresponds to in-plane shear loading. The last is Mode III that refers to out-of-plane shear. A cracked body can be loaded in any one of these modes, or a combination of two or three modes.

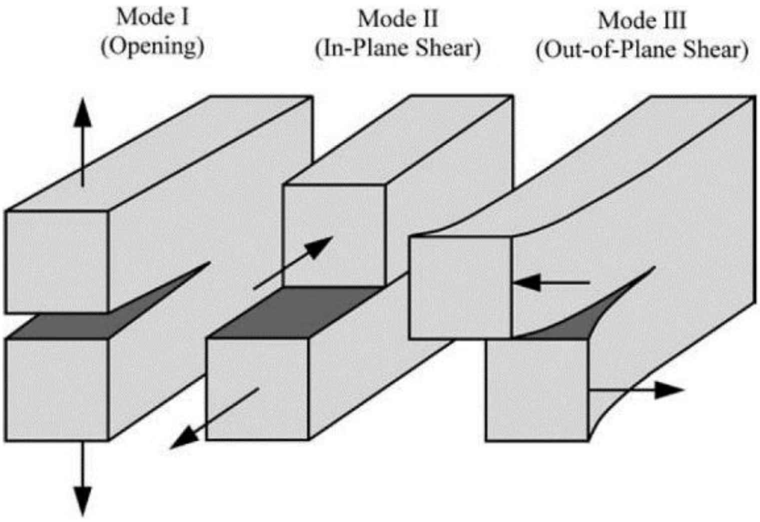

Figure 14 The modes of loading that a crack can be subjected to [100]

2.3.1. Stress Intensity Factor

The analysis of crack growth in engineering components is usually conducted considering the concept of Stress Intensity Factor (SIF), K. This approach is part of the discipline called Linear Elastic Fracture Mechanics (LEFM) and assumes that the material is homogenous and linearly elastic.

SIF is a quantity that describes quantitatively the severity of the stress fields ahead of the crack tip. For example, if the crack is subjected to Mode I loading, the in-plane components of stress can be described mathematically by equations (9) (with reference to Figure 15):

$$\begin{aligned}
\sigma_{xx} &= \frac{K_I}{\sqrt{2\pi r}}\cos\left(\frac{\theta}{2}\right)\left[1-\sin\left(\frac{\theta}{2}\right)\sin\left(\frac{3\theta}{2}\right)\right] \\
\sigma_{yy} &= \frac{K_I}{\sqrt{2\pi r}}\cos\left(\frac{\theta}{2}\right)\left[1+\sin\left(\frac{\theta}{2}\right)\sin\left(\frac{3\theta}{2}\right)\right] \qquad (9) \\
\tau_{xy} &= \frac{K_I}{\sqrt{2\pi r}}\cos\left(\frac{\theta}{2}\right)\sin\left(\frac{\theta}{2}\right)\cos\left(\frac{3\theta}{2}\right)
\end{aligned}$$

The set of equations (9) only reports the leading terms of an expansion series; higher order terms are usually neglected. As it is possible to note from (9), all expressions contain a leading term that is proportional to $1/\sqrt{r}$. As $r \rightarrow 0$, the leading term approaches infinity and gives rise to a singularity. Obviously, in the real case the stress field at the crack tip is not singular: if the stress combination exceeds the yielding condition, material plastic deformation occurs, and less steep gradient of stress is experienced. The region that undergoes to plastic deformation is usually called *plastic zone*. Nevertheless, LEFM is still widely used for crack growth prediction because it relies on the assumption that the conditions within the plastic zone are fully determined by the surrounding elastic field, that is, the *K-field*.

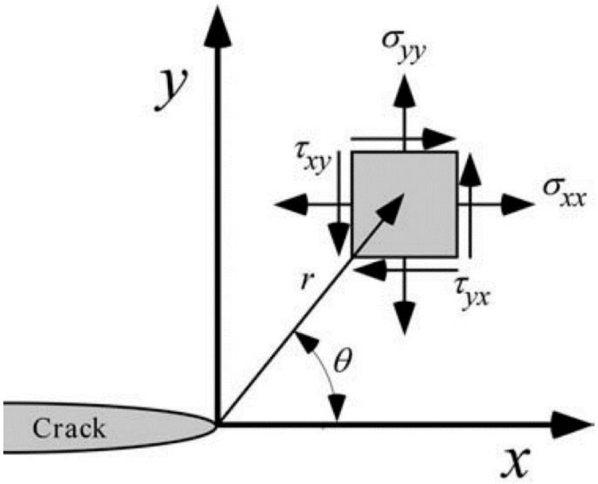

Figure 15 Definition of the coordinate axis ahead of the crack tip [100]

Depending on the geometry of the body, SIF can be evaluated at any instant of the crack propagation stage upon knowledge of the actual applied load as:

$$K = F\, S\, \sqrt{\pi\, a} \tag{10}$$

Where F is a dimensionless function of geometry, S is the nominal load and a is the crack length.

This calculation methodology can be also used when stress field induced by external loads or residual deformations follows a specific profile. In this case, the weight functions approach is usually employed, and it describes the SIF as:

$$K(a) = \int_0^a \sigma_z(x)\ m(x, a)\, dx \tag{11}$$

Here, a is the crack length, $\sigma_z(x)$ is the stress distribution along the crack bisector and $m(x, a)$ is the weight function.

2.3.2. J-integral

Amongst the few parameters available for fracture characterisation, J-integral has become particularly popular. According to Rice [101], this parameter can be applied to non–linear materials by idealising the elastic-plastic deformation as non-linear elastic. This means that the stress may follow a non-linear relationship with the strain but the process is assumed to be fully reversible. In contrast with the SIF approach, the use of J-integral extends fracture characterisation well beyond the limits of validity of LEFM. In the same work, Rice showed how that the non-linear energy release rate J could be written as a path-independent line integral. Further studies [102, 103] also demonstrated that J uniquely characterises the stress and strains at the crack tip in non-linear materials.

However, in the particular case of linear elastic materials, the relationship between SIF and J-integral is:

$$J = \frac{K_I^2}{E^I} \tag{12}$$

Here K_I is the Mode I SIF and E^I represents the elastic properties of the material depending on whether the problem is plane stress or plane strain, as shown below:

$$\begin{aligned} E^I &= E && \text{Plane Stress} \\ E^I &= \frac{E}{(1-\nu^2)} && \text{Plane Strain} \end{aligned} \tag{13}$$

Considering an arbitrary counter clockwise path Γ around the tip of a crack as illustrate in Figure 16 Arbitrary contour around the tip of a crack [100] Figure 16, the J-integral is given by:

$$J = \int_\Gamma \left(w\,dy - T_i \frac{du_i}{dx} ds\right) \tag{14}$$

Where w is the strain energy density, T_i is the component of the traction vector, u_i is the displacement vector component and ds is the length increment along the contour Γ.

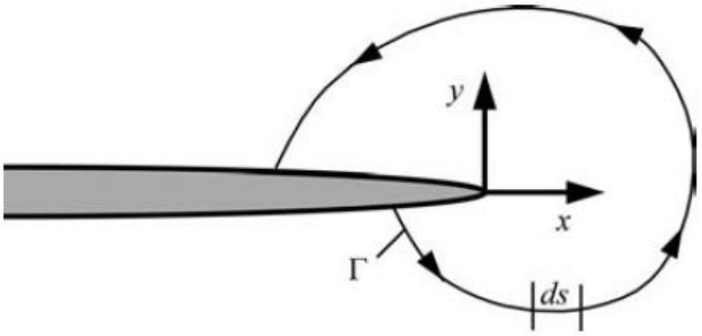

Figure 16 Arbitrary contour around the tip of a crack [100]

In the case of fatigue crack propagation, Downing and Begley [104] first proposed the use of the cyclic J-integral as a parameter which correlates with the crack growth rate, da/dN.

The material ahead of a growing fatigue crack experiences cyclic elastic-plastic loading. Therefore, the material deformation can be characterized by the stress range Δs_{ij} and the strain range Δe_{ij} in a given cycle. Considering a loading branch of the stress-strain curve, where the stresses and strains have initial values s_{ij} and e_{ij}, and increase to s_{ij} and e_{ij}. It is possible to define a J -like integral as follows:

$$\Delta J = \int_{\Gamma} \left(\psi(\Delta\varepsilon_{ij})\, dy - \Delta T_i \frac{d\Delta u_i}{dx} ds \right) \tag{15}$$

Note that ψ represents the stress work per unit volume performed during loading, rather than the stress work in a complete cycle.

The use of the cyclic J integral, as a crack driving force parameter, increases the accuracy in describing the stress state ahead of the crack tip for materials in which sample sizes are too small and for which the assumptions of Linear Elastic Fracture Mechanics (LEFM) do not hold.

2.3.3. Fatigue Crack Growth Behaviour

The crack growth behaviour can be described by the relationship between the Fatigue Crack Growth Rate (FCGR), usually expressed as da/dn, and a crack driving force, D. Depending on the specific case, in the present thesis two expressions for crack driving forces were considered, namely, SIF and J-integral. A more generic relationship may take into account also the loading ratio R. The overall relationship can be written as

$$\frac{da}{dn} = f(D) \tag{16}$$

If SIF and R are thought to determine the crack driving force, this formulation can be written as:

$$\frac{da}{dn} = f(\Delta K, R) \tag{17}$$

In the early 60’s, Paris discovered an empirical formulation that is able to describe the FCGR correctly at intermediate values of ΔK [105]. This fairly well-accepted formulation is now known as Paris’ law:

$$\frac{da}{dn} = C(\Delta K)^m \tag{18}$$

where C and m are material constants.

Similarly, Dowling and Begley [104] applied the J-integral formulation to fatigue crack growth under large-scale yielding condition where LEFM fails in predicting the FCGR. The same power-law expression could be formulated:

$$\frac{da}{dn} = C(\Delta J)^m \tag{19}$$

(It is worth noting that in cyclic loading fatigue problem, the fundamental quantities that relates to the stress acting at the crack tip must be expressed in terms of range, e.g. ΔK for the SIF approach, and ΔJ for the J-integral approach).

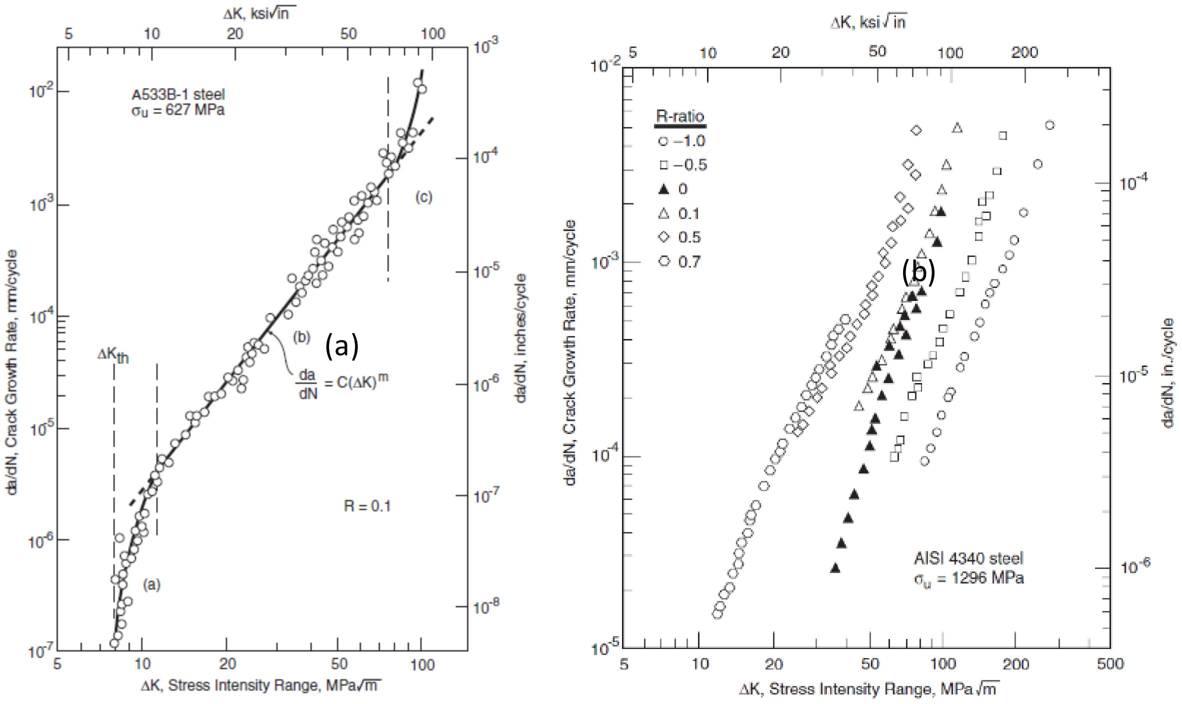

Figure 17 (a) Fatigue crack growth rate over a wide range of SIF for a ductile steel [106, 107]. (b) Effect of R-ratio on Crack Growth Rate [107, 108].

In Figure 17, examples of experimental FCGR plots are shown. In particular, Figure 17(a) shows the region of ΔK where the Paris' law is valid, i.e. after the crack propagation early stage and before the imminent ductile static failure. The same type of diagram can be constructed also by means of the cyclic J-integral ΔJ and the same region can be identified. Figure 17(b) shows also the effect of R-ratio on the FCGR. As it is possible to see, higher values of R shift the Paris' curve towards smaller SIF ranges. It is important to note also that the slope m of these curves is almost the same independently from the magnitude of R.

In literature, many formulations can be found that attempt to account for the loading ratio and fatigue history. However, it is very important to pay attention to situations where the loading history is characterised by variable amplitude loading. Indeed, non-linear mechanisms (e.g. plasticity induced crack closure and residual stress ahead of the crack tip) are highly dependent on the loading history and may lead to unexpected FGCR behaviour. One of the purposes of the present thesis was to try to shed some light onto the effect of these non-linear mechanisms on FCGR

2.3.4. Factors that Influence Fatigue Crack Growth Rate

In recent decades a great deal of effort has been devoted by the research community to understanding fatigue crack growth behavior in mechanical components subjected to arbitrary amplitude loading variable amplitude loading) [109-111]. No agreement has emerged so far regarding the best approach to crack growth prediction under this loading mode [112], due to the difficulties in understanding the exact role of plasticity-induced crack closure [113], residual stress generated ahead the crack tip [114] and other mechanisms [115-118] that control crack propagation.

Recently, a multi-parameter characterisation of the elastic stress field around a crack contained within a plastic enclave was proposed by James et. ali [119], aimed at capturing the relevant factors that influence the fatigue crack propagation. This approach claims that a realistic elastic stress distributions representing crack wake contact and the compatibility-induced shear stresses acting at the elastic–plastic boundary can be modelled; essentially treating the crack as a plastic inclusion in an elastic body. The model lies on definition of a modified stress intensity factor perpendicular to the crack plane, called K_F, which drives crack growth in an analogous fashion to K_I. The shielding effect of the plastic enclave is accounted for via two new stress intensity factors, an interfacial shear stress intensity factor, K_S, and a retarding stress intensity factor, K_R.

A single anomalous load encountered during constant amplitude fatigue test can be thought of as the simplest case of variable amplitude loading. Material response under variable amplitude fatigue can therefore be initially explored through the analysis of a single Overload (OL), single Underload (UL) or their combination (e.g. OL-UL).

In recent years, publications devoted to this topic largely concerned cases of OL [120, 121]. The Fatigue Crack Growth Rate (FCGR) retardation effect due overload has been known for almost fifty years. The causes of such retardation have been imputed to various phenomena that take place during the occurrence of the overload, such as residual stress generation, plastic deformation and the consequent plasticity-induced crack closure, and work hardening. However, no clear consensus has been reached regarding the relative significance of these mechanisms [122-126].

Crack closure is a mechanism active in the wake of the crack that is caused by the plastic deformation-induced modification of the crack flank geometry [127]. Crack closure effect may be operative during crack propagation even in the absence of overload, but becomes particularly significant once an overload has been applied. As the crack tip moves forward past the overload-affected region, during the unloading part of the cycle crack flanks come into contact prior to the cyclic load reaching its minimum value. This results in a lower effective range of crack opening displacement and crack tip stress intensity factor. It is important to note that in the case of overload, closure causes crack retardation only when crack face contact occurs in the wake of the growing crack. As the crack tip moves sufficiently far away, the closure effect becomes negligible. Conversely, if crack arrest is observed immediately after the overload, no crack closure can be present until re-nucleation or propagation takes place. This effect has been subject of numerous studies in the past, and its contribution to crack retardation is widely accepted.

The region of heavy plastic deformation ahead of the crack tip gives rise to a region of compressive residual stress. The occurrence of an overload amplifies this compressive residual stress significantly. It is well known that the presence of compressive residual stress ahead of the crack tip impedes propagation due to the local reduction of the mean stress during fatigue cycling. In the last decade the proliferation of new experimental microscopic techniques (X-ray diffraction, DIC and the FIB ring-core method) [128-130] enabled direct spatially resolved evaluation of residual stress, and better understanding of its evolution during the relevant phases of propagation in the presence of an overload.

Crack closure and compressive residual stress are not the only mechanisms thought to be involved in crack retardation. Indeed, other causes may appear and play their role depending on the loading condition and material behaviour. In the last decades, many authors have directed effort at the understanding of the conditions when these additional effects may arise.

Crack tip blunting is another retardation mechanism [131]: extensive plastic flow at the crack tip may modify the geometry leading to the consequent crack blunting. The resulting crack tip displays behaviour similar to a rounded notch where finite stress concentration is observed, instead of stress intensification observed at a crack tip. Under such circumstances the fatigue crack growth rate (FCGR) is reduced in comparison with the steady-state conditions. The extreme version of this scenario corresponds to the situation when the crack is blunted to such an extent that a new nucleation site appears at a different location from the previous tip. Crack branching or kinking that takes place in this case is another mechanism that contributes to crack retardation [116, 132]. Change in the crack growth direction and/or the creation of small secondary cracks lead to the redistribution of stresses around the crack tip which, in turn, reduces the crack driving force and causes retardation.

Another view of the crack propagation process is to assume that the material ahead of the crack tip through which crack advances experiences cyclic loading, damage and localised failure, giving rise to a connected crack. Depending on the material properties and deformation history, strain hardening may play its role in controlling the crack growth rate. Material hardening generally reduces the ductility of the material with a consequent reduction in the resistance to crack propagation [133]. The general consequence of this effect is to accelerate the fatigue crack growth rate (FCGR). However, in terms of the overall significance for FCGR this may be considered of limited, secondary importance. Unlike plasticity-induced crack closure and the residual stress that exert direct strong influence on FCGR, secondary effects of the kind enumerated above may only become prominent for specific and particular combinations of material properties, microstructure and overload ratio.

On the other hand, when an UL is applied, observations show either crack growth acceleration, or no detectable disturbance in the FCGR [134-136]. This crack acceleration effect was noted in pipelines subjected to varying internal pressure [137]. It has been noted [135] that crack acceleration is likely to be manifested in cases where the baseline fatigue loading is positive, i.e. positive loading ratio R. Furthermore, higher crack acceleration occurs at higher baseline loading ratio [138]. In addition, the extent of such acceleration, if present, is dependent on the material cyclic hardening behaviour and the magnitude of UL with respect to the steady-state cyclic load.

Using reasoning similar to that used for the analysis of OL, it is possible to anticipate that the main causes of the UL effect may be two contributions: Residual stress ahead of the crack tip and plasticity-induced crack closure.

2.4. Eigenstrain modelling

Eigenstrain theory is based on the description of the inelastic strain distribution that gives rise to residual stress. Permanent ('frozen-in') strain that is termed *eigenstrain* describes shear, shrinkage or dilatation induced by an arbitrary inelastic process that may be associated with phase transformation, temperature change, plastic deformation, etc.

The total strain within a solid can always be decomposed additively into the irreversible and reversible parts. The former part is the permanent inelastic strain (eigenstrain ε^*), whilst the latter part corresponds to the elastic strain, ε_{el}:

$$\overline{\overline{\varepsilon_{tot}}} = \bar{\bar{\varepsilon}}^* + \overline{\overline{\varepsilon_{el}}} \tag{20}$$

In most cases, the presence of an eigenstrain distribution within a body means that an elastic strain field is required to maintain strain compatibility. It is important to note that this elastic strain field is subject to further mathematical requirements: the generalised Hooke's law that imposes the linear relationship between the elastic strain and stress within the body means that the elastic strain must be *statically admissible*, i.e. correspond to an equilibrated stress field. If no external tractions are applied to the body, then the aforementioned tensor fields are referred to as *residual elastic strain* (r.e.s.) and *residual stress*, respectively.

The eigenstrain method has already been adopted widely for modelling residual stress at various scales and fields of application. An important field of eigenstrain analysis concerns inclusions in elastic solids for which a whole range of fundamental solutions are available [139-141], notably for Eshelby ellipsoidal inclusions, cuboidal inclusions, etc. Eigenstrain-based analytical solutions have also been presented for residual stress distributions within a plate subjected to shot peening [41, 142] and a hollow tube subjected to autofrettage [42].

In cases where the geometry of the problem cannot be described using an analytical formulation, numerical methods can be utilised. Since real mechanical components are usually geometrically complex, the Finite Element Method (FEM) is widely employed. Within the framework of FEM it is convenient to introduce arbitrary eigenstrain fields into the model using pseudo-thermal strain expressed in terms of a temperature change ΔT and a tensor of thermal expansion coefficients $\bar{\bar{\alpha}}$. Then:

$$\bar{\bar{\varepsilon}}^* = \bar{\bar{\alpha}}\,\Delta T \tag{21}$$

The thermal expansion coefficient tensor $\bar{\bar{\alpha}}$ contains six independent components and allows the description of all possible eigenstrain states. The prescription of the thermal expansion coefficient tensor at the totality of the Integration Points (IP) of the FEM model, in combination with the application of a uniform temperature change, furnishes an entirely flexible description of the eigenstrain field with the help of a user subroutine to define $\bar{\bar{\alpha}}$. Once the known eigenstrain distribution is prescribed, the one step solution of the thermo-elastic problem follows which returns the residual elastic strain distribution, and with it the associated residual stress distribution that is self-equilibrated by construction.

The evaluation of the elastic strain field when the imposed eigenstrain is known is called the *direct problem.* An example of a direct problem is the Eshelby treatment of an ellipsoidal inclusion [143], whereby uniform eigenstrain distribution is imposed within an ellipsoidal domain (inclusion), and the inner and outer elastic strain and stress fields are determined.

It is worth mentioning that the inelastic deformation (eigenstrain), produced by a mechanical treatment, if known because evaluated through a simple case, this can be transferred to more complex geometries. This was firstly introduced by Korsunsky [57] and named *Principle of Transferability of Eigenstrain*.

On the other hand, if the elastic strain is known and the eigenstrain the generated it is sought, this is called *inverse problem.* This is the case where experimental evidence provides information regarding the elastic strain field and thus the reconstruction of the eigenstrain that induced that elastic strain change is evaluated. In the past years, this procedure has been widely performed to several relevant engineering case such as: shot peening [144], including in the context of Crystal Plasticity [45], friction stir welding [145], phase transformation [146], etc.

The eigenstrain method turns out to be a very efficient way to simulate residual stress fields and check consistency of experimental results. And so, extensively implemented in the present thesis.

3. FIB-DIC Developments

3.1. Uncertainty quantification FIB–DIC ring-core method due to elastic anisotropy effects

3.1.1. Introduction and background

Experimental techniques capable of attaining micron resolution provide a measure of displacements or strains, followed by stress calculation using the generalised Hooke's law. Whilst the uncertainty of strain or displacement measurement can be quantified using experimental error analysis methods, the stress calculation introduces further uncertainties that require quantification. In a single grain within an aggregate, the local crystal structure may have a dramatic effect on the stress state due to the orientation of the grain itself and of its neighbouring grains with the respect of external loading. A complex relationship exists between global and local stress-strain states that reflects the accommodation taking place during elastoplastic deformation of a polycrystal, leading to simultaneous attainment of stress equilibrium and strain compatibility [143, 147]. The models in the literature that simulate the local stress evolution [148, 149] share a common need for direct experimental validation, emphasising the requirement for correct stress evaluation at the intra-granular level. Engineering reliability and durability analysis for design e.g. against creep or high cycle fatigue conventionally uses criteria based on stresses, rather than strains. For isotropic materials the stress calculation can be readily performed using the combination of only two elastic parameters: Young's Modulus E and Poisson's Ratio ν. The aim of this section is to present and to evaluate the extension of the residual stress calculation in the FIB-DIC ring-core method for the case when the material is anisotropic, and possesses cubic symmetry. The results show that the uncertainty of residual stress evaluation at the inter- and/or intragranular level depends on the material's degree of anisotropy, and that for materials with high anisotropy factor the knowledge of grain orientation is mandatory.

The computational background to the analysis of relief strains in the FIB-DIC micro-ring-core experiments, such as illustrated in Figure 18(a), has been presented in a series of papers [78, 82, 150]. The central idea of the method that has been validated through extensive numerical modelling is that the surface of the micro-pillar undergoes the change from initial residual elastic strain to the final strain-free state that arises after sufficiently deep milling (to the depth of the order of the pillar diameter, or greater [76]. Therefore, simple inversion of the sign of the perceived strain relief during milling provides a means of determining the pre-existing residual strain. The FIB-DIC ring-core method [83] allows simultaneous evaluation of three components of surface in-plane relief strains ($\Delta\varepsilon_{11}, \Delta\varepsilon_{22}, \Delta\varepsilon_{12}$) (and hence the residual elastic strains) in the laboratory (global) Cartesian system (Figure 18(b)), The three out-of-plane strain components ($\varepsilon_{33}, \varepsilon_{13}, \varepsilon_{23}$) are not measured in this configuration. However, it can be assumed that the traction-free surface condition prevails, so that the three out-of-plane stress components vanish in the initial state ($\sigma_{33} = \sigma_{13} = \sigma_{23} = 0$). This additional boundary condition allows the out-of-plane residual strain to be also found.

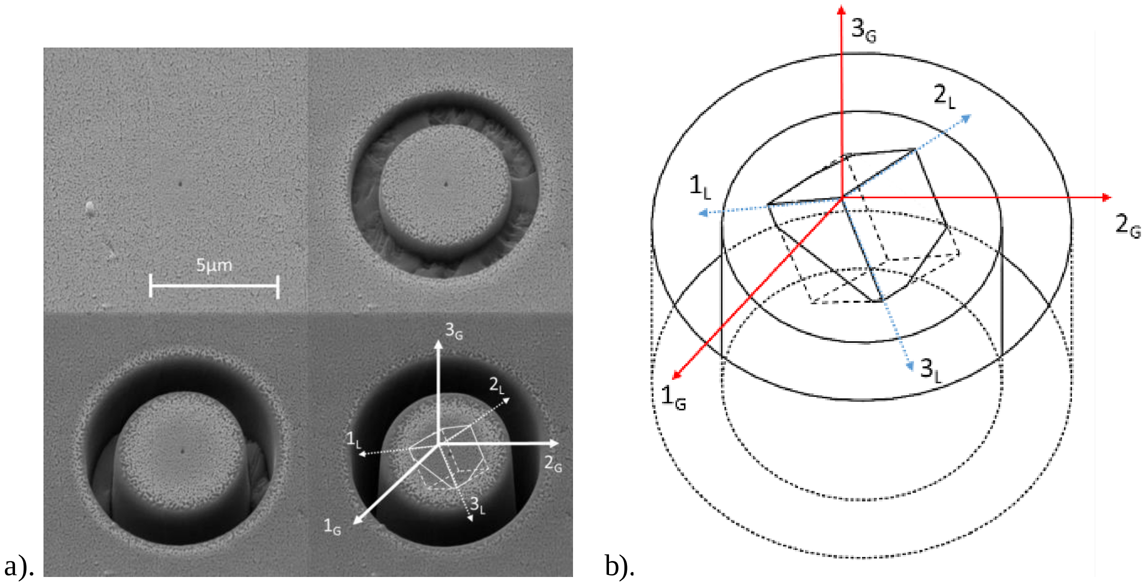

Figure 18 Cartesian Coordinate System definition at the ring core. The axes 1 and 2 denotes the in-plane coordinates and the axis 3 the out-of-plane coordinate. (a) Illustration of the evolution of the micro-scale ring-core geometry during Focused Ion Beam (FIB) milling. The diameter of the central pillar is 5µm. (b) Coordinate systems defined as global (G) (associated with laboratory axes) and local (L) (associated with sample crystal axes) for a single crystal micro-pillar.

Assuming the grain orientation at the milling location and the elastic properties of the material (stiffness matrix) to be known, a compact analytical procedure can be elaborated for the calculation of the full local stress tensor. To aid the algebraic manipulations, to ensure their correctness and to enable direct use of the resulting expressions for numerical calculation, the procedure is implemented using

Mathematica package. Arbitrary materials with cubic symmetry can be considered, with varying degrees of elastic anisotropy. For cubic materials this property of the material can be characterised by a single parameter known as the Zener anisotropy factor [151]. For illustration, Ni-base superalloy is taken as an example of a highly anisotropic crystal, in which the ratio of Young's moduli in the stiffest and most compliant directions is of the order of 2.5. Single crystal silicon is taken as a moderate case for which this ratio is ~1.6. Finally, Al and its alloys are considered as materials that have properties close to isotropic material, with the ratio of stiffnesses ~1.2.

Once the procedure is established and validated, sensitivity analysis is performed to assess the extent to which errors in stress evaluation arise from the ignorance of the underlying crystal orientation, if the assumption of isotropic equivalent stiffness for bulk polycrystal is used. Different strain states are considered, and calculations are carried out for n=8000 instances of randomly distributed grain orientations described by the three Euler angles; this number is thought to be sufficiently high to accurately describe the statistical distribution. Since the selection of Euler angles encompasses the complete range of possibilities, and describes a uniform distribution in the orientation space, this gives unbiased statistical evaluation. The results serve as the basis for uncertainty quantification of stress evaluation using this approach.

The practical implementation and application of the method is illustrated using a set of experimental data for residual stresses in a cross-section of an aeroengine turbine blade made from a Ni-base superalloy, a material with a high Zener anisotropy factor. A comparison of the stresses computed is presented assuming correct anisotropic elastic properties against the results obtained assuming that the material is isotropic, and assess the findings.

3.1.2. Tensor and 6-vector matrix representation

Let us first define a Cartesian coordinate system that will be referred to as local, or crystal system of axes, associated with the cubic unit cell of the material. Also, a global, or laboratory system of axes are defined. In absence of grain rotation, the local system is coincident with the global. In this global system, the x_3 axis is associated with the normal to the sample surface and the x_1 and x_2 axes are associated with suitable mutually orthogonal directions parallel to the sample surface, e.g. the fast and slow scan directions within the SEM system. The graphical representation of these definitions is shown in Figure 18 in which the coordinate systems are distinguished by the subscript L for the local system, and G for global system. In the derivation below all quantities referring to a specific system have appropriate subscripts.

According to the Bunge notation [152], the general rotation between two arbitrary orientations of a crystal can be defined by means of the three Euler angles $(\varphi_1, \Phi, \varphi_2)$. Figure 18(a) illustrates this definition in which the rotation applied to a cubic crystal, initially aligned with the global axes, in order to bring it into alignment with the actual orientation of the local, or crystal axes. Firstly, rotation by the angle φ_1 is applied around axis x_1 , then the rotation by the angle Φ is applied around the new rotated axis $\tilde{x}_3$, and finally the third rotation by the angle φ_2 is applied around the new axis x_1'. The resulting coordinate system is referred to as local, and is associated with the crystal axes denoted x_1', x_2', x_3'.

The matrix that describes the transformation of a vector from a given coordinate system to another one rotated by an angle α_3 around the x_3 axis is given by

$$\overline{\boldsymbol{v}'} = \overline{\overline{\boldsymbol{R}(\alpha_3)}}\,\overline{\boldsymbol{v}}, \quad \overline{\overline{\boldsymbol{R}(\alpha_3)}} = \begin{pmatrix} \mathrm{Cos}[\alpha_3] & \mathrm{Sin}[\alpha_3] & 0 \\ -\mathrm{Sin}[\alpha_3] & \mathrm{Cos}[\alpha_3] & 0 \\ 0 & 0 & 1 \end{pmatrix} \tag{22}$$

Rotation matrices for other angles and axes are obtained by permutation of rows and columns. For example, for the first Euler angle φ_1 the matrix has the form:

$$\overline{\overline{\boldsymbol{R}(\varphi_1\ )}} = \begin{pmatrix} 1 & 0 & 0 \\ 0 & \mathrm{Cos}[\varphi_1] & \mathrm{Sin}[\varphi_1] \\ 0 & -\mathrm{Sin}[\varphi_1] & \mathrm{Cos}[\varphi_1] \end{pmatrix} \tag{23}$$

The matrix $\overline{\overline{\boldsymbol{R}}}$ that describe the sequence of rotations with respect to different axes is given by the product of rotation matrices for different axes and angles is given by the product of matrices:

$$\overline{\overline{\boldsymbol{R}}} = \overline{\overline{\boldsymbol{R}(\varphi_1, \Phi, \varphi_2\ )}} = \overline{\overline{\boldsymbol{R}(\varphi_2\ )}}\,.\,\overline{\overline{\boldsymbol{R}(\Phi\ )}}\,.\,\overline{\overline{\boldsymbol{R}(\varphi_1\ )}} \tag{24}$$

In the Bunge notation this rotation matrix $\overline{\overline{\boldsymbol{R}}}$ from the global to the local coordinate system is expressed explicitly as follows:

$$\overline{\overline{\boldsymbol{R}}} = \begin{pmatrix} \mathrm{Cos}[\varphi_1]\mathrm{Cos}[\varphi_2] - \mathrm{Cos}[\Phi]\mathrm{Sin}[\varphi_1]\mathrm{Sin}[\varphi_2] & \mathrm{Cos}[\varphi_2]\mathrm{Sin}[\varphi_1] + \mathrm{Cos}[\varphi_1]\mathrm{Cos}[\Phi]\mathrm{Sin}[\varphi_2] & \mathrm{Sin}[\varphi_2]\mathrm{Sin}[\Phi] \\ -\mathrm{Cos}[\varphi_2]\mathrm{Cos}[\Phi]\mathrm{Sin}[\varphi_1] - \mathrm{Cos}[\varphi_1]\mathrm{Sin}[\varphi_2] & \mathrm{Cos}[\varphi_1]\mathrm{Cos}[p]\mathrm{Cos}[\Phi] - \mathrm{Sin}[\varphi_1]\mathrm{Sin}[\varphi_2] & \mathrm{Cos}[\varphi_2]\mathrm{Sin}[\Phi] \\ \mathrm{Sin}[\varphi_1]\mathrm{Sin}[\Phi] & -\mathrm{Cos}[\varphi_1]\mathrm{Sin}[\Phi] & \mathrm{Cos}[\Phi] \end{pmatrix} \tag{25}$$

Tensor transformation between the global and local coordinate axes systems (indicated by the subscripts *G* and *L* respectively) is accomplished by pre- and post-multiplication by the rotation matrix and its transpose. For example, for the stress tensor the transformation is expressed as:

$$\overline{\overline{\boldsymbol{\sigma_L}}} = \overline{\overline{\boldsymbol{R}}}\ \overline{\overline{\boldsymbol{\sigma_G}}}\ \overline{\overline{\overline{\boldsymbol{R^T}}}} \tag{26}$$

Exactly the same transformation applies to the strain tensor defined in the consistent tensorial form, $\varepsilon_{ij} = \frac{1}{2}\left(\frac{\partial u_i}{\partial x_j} + \frac{\partial u_j}{\partial x_i}\right)$:

$$\overline{\overline{\boldsymbol{\varepsilon_L}}} = \overline{\overline{\boldsymbol{R}}}\ \overline{\overline{\boldsymbol{\varepsilon_G}}}\ \overline{\overline{\overline{\boldsymbol{R^T}}}} \tag{27}$$

Since the reverse rotation matrix is described by $\overline{\overline{\overline{\boldsymbol{R^{-1}}}}} = \overline{\overline{\overline{\boldsymbol{R^T}}}}$, the backward rotation is expressed as:

$$\overline{\overline{\boldsymbol{\varepsilon_G}}} = \overline{\overline{\overline{\boldsymbol{R^T}}}}\ \overline{\overline{\boldsymbol{\varepsilon_L}}}\ \overline{\overline{\boldsymbol{R}}} \tag{28}$$

The relationship between strains and stresses in linear elasticity is expressed in the form of the generalised Hooke's law. The elastic properties are described by the stiffness tensor $\widetilde{\boldsymbol{C}}$, or its reciprocal compliance tensor $\tilde{\boldsymbol{S}}$, where the tilde sign denotes the fourth order tensor:

$$\overline{\overline{\boldsymbol{\sigma_L}}} = \widetilde{\boldsymbol{C}}:\overline{\overline{\boldsymbol{\varepsilon_L}}}, \qquad \overline{\overline{\boldsymbol{\varepsilon_L}}} = \tilde{\boldsymbol{S}}:\overline{\overline{\boldsymbol{\sigma_L}}} \tag{29}$$

In practice these relationships are reported in the literature for different materials in reference to the Cartesian crystal axes associated with the lattice unit cell. However, not only is the fourth order tensor notation somewhat unwieldy, it also does not take into account explicitly the general symmetry properties of stiffness and compliance coefficients. For this reason elasticity relations are usually reported in the form of matrices using the 6-vector Voigt notation for stresses and strains [153]:

$$\overline{\boldsymbol{\varepsilon}} = (\varepsilon_{11}, \varepsilon_{22}, \varepsilon_{22}, 2\varepsilon_{23}, 2\varepsilon_{13}, 2\varepsilon_{12}), \quad \overline{\boldsymbol{\sigma}} = (\sigma_{11}, \sigma_{22}, \sigma_{33}, \sigma_{23}, \sigma_{13}, \sigma_{12}). \tag{30}$$

Using this basis, and adopting the notation $\gamma_{ij} = 2\varepsilon_{ij}$ for shear strains ($i \neq j$), the relationship between strain and stress for a general anisotropic material with respect to the local coordinate system is written using the 6×6 *compliance matrix* as follows:

$$\begin{pmatrix} e_{11} \\ e_{22} \\ e_{33} \\ g_{23} \\ g_{13} \\ g_{12} \end{pmatrix}_G = \begin{pmatrix} S_{11} & S_{12} & S_{13} & S_{14} & S_{15} & S_{16} \\ S_{12} & S_{22} & S_{23} & S_{24} & S_{25} & S_{26} \\ S_{13} & S_{23} & S_{33} & S_{34} & S_{35} & S_{36} \\ S_{14} & S_{24} & S_{34} & S_{44} & S_{45} & S_{46} \\ S_{15} & S_{25} & S_{35} & S_{45} & S_{55} & S_{56} \\ S_{16} & S_{26} & S_{36} & S_{46} & S_{56} & S_{66} \end{pmatrix}_G \begin{pmatrix} s_{11} \\ s_{22} \\ s_{33} \\ t_{23} \\ t_{13} \\ t_{12} \end{pmatrix}_G \tag{31}$$

or in short:

$$\bar{\boldsymbol{\varepsilon}}_{\boldsymbol{L}} = \bar{\bar{\boldsymbol{S}}}\bar{\boldsymbol{\sigma}}_{\boldsymbol{L}} \tag{32}$$

Note the single overbar indicating the vector notation for stresses and strains, and the double overbar indicating the fact that compliance is described by the square matrix. The inverse form of this relationship may also be written using the stiffness matrix:

$$\bar{\boldsymbol{\sigma}}_{\boldsymbol{L}} = \bar{\bar{\boldsymbol{C}}}\,\bar{\boldsymbol{\varepsilon}}_{\boldsymbol{L}}, \qquad \bar{\bar{\boldsymbol{C}}} = \bar{\bar{\boldsymbol{S}}}^{-\mathbf{1}} \tag{33}$$

The compact nature of the 6-vector notation brings with it significant advantages, but also leads to some complications. Firstly, the stiffness and compliance matrices under coordinate system rotation no longer obey the simple rules derived from simple 3-vector rotation. Furthermore, the introduction of the coefficient 2 for shear strains destroys the similarity of description for stress and strain 6-vectors, so that the rotation rules for these two fundamental quantities are no longer the same. As a consequence, the transformation rules for the stiffness and compliance matrices are complex, counter-intuitive, and are likely to contain errors if derived by hand and transcribed to and from a printed page. This may be the reason why, to the best of the authors' knowledge, these transformation rules have not been widely reported in the literature.

Modern capabilities of data storage and transmission and the combination of symbolic and numeric manipulation suggest that the most rational means for these algorithms to be derived and made available to the reader is in the form of computer code. To this end we present the implementation of these procedures in a Mathematica® notebook that is made available to the reader as Supplementary Material alongside the present article.

The algorithm implemented in the code is as follows:

1. Tensor rotation matrix $\bar{\bar{\boldsymbol{R}}}$ is computed symbolically using eq. (24) in terms of the trigonometric functions of the Euler angles.
2. Component-wise definitions are introduced for the stress tensor $\bar{\bar{\boldsymbol{\sigma}}}$ and the strain tensor $\bar{\bar{\boldsymbol{\varepsilon}}}$.
3. In preparation for the use of Voigt 6-vector notation, definitions of the stress vector $\bar{\boldsymbol{\sigma}}$ and the strain vector $\bar{\boldsymbol{\varepsilon}}$ are introduced in terms of the same components, including the factor 2 for shear strains.
4. The 'forward' stress tensor transformation from the global to the local coordinate axes is computed symbolically using eq. (45).

5. Using the command for determining the coefficients of vector components in a given expression, six coefficients of six distinct components of the original stress tensor are determined for the six distinct stress components of the transformed tensor.

6. The results are assembled into a '6-stress forward rotation matrix' $\overline{\overline{\boldsymbol{R_\sigma}}}$ that accomplishes the following linear operation:

$$\overline{\boldsymbol{\sigma_L}} = \overline{\overline{\boldsymbol{R_\sigma}}}\ \overline{\boldsymbol{\sigma_G}} \tag{34}$$

7. The above six steps are repeated in order to obtain the symbolic expression for the '6-strain forward rotation matrix' that accomplishes the following linear operation:

$$\overline{\boldsymbol{\varepsilon_L}} = \overline{\overline{\boldsymbol{R_\varepsilon}}}\ \overline{\boldsymbol{\varepsilon_G}} \tag{35}$$

8. It is noted, and verified, that in a similar way the '6-stress inverse rotation matrix' $\overline{\overline{\boldsymbol{R_\sigma^{-1}}}}$ and the '6-strain inverse rotation matrix' $\overline{\overline{\boldsymbol{R_\varepsilon^{-1}}}}$ can be derived, and that they are given by the matrix inverses of their 'forward' counterparts:

$$\overline{\boldsymbol{\sigma_G}} = \overline{\overline{\boldsymbol{R_\sigma^{-1}}}}\,\overline{\boldsymbol{\sigma_L}}, \qquad \overline{\boldsymbol{\varepsilon_G}} = \overline{\overline{\boldsymbol{R_\varepsilon^{-1}}}}\ \overline{\boldsymbol{\varepsilon_L}}. \tag{36}$$

9. The transformation rules for the stiffness and compliance 6×6 matrices are derived in the following form:

$$\overline{\boldsymbol{\sigma_G}} = \overline{\overline{\boldsymbol{R_\sigma^{-1}}}}\,\overline{\boldsymbol{\sigma_L}} = \overline{\overline{\boldsymbol{R_\sigma^{-1}}}}\,\overline{\overline{\boldsymbol{C}}}\,\overline{\boldsymbol{\varepsilon_L}} = \overline{\overline{\boldsymbol{R_\sigma^{-1}}}}\,\overline{\overline{\boldsymbol{C}}}\,\overline{\overline{\boldsymbol{R_\varepsilon}}}\,\overline{\boldsymbol{\varepsilon_G}} \tag{37}$$

and therefore:

$$\overline{\overline{\boldsymbol{C_G}}} = \overline{\overline{\boldsymbol{R_\sigma^{-1}}}}\,\overline{\overline{\boldsymbol{C}}}\,\overline{\overline{\boldsymbol{R_\varepsilon}}} \tag{38}$$

Here subscript *G* denotes that the stiffness matrix is now referred to the global axes.

10. Similar reasoning leads to the expression for the compliance matrix referred to the global axes:

$$\overline{\overline{\boldsymbol{S_G}}} = \overline{\overline{\boldsymbol{R_\varepsilon^{-1}}}}\,\overline{\overline{\boldsymbol{S}}}\,\overline{\overline{\boldsymbol{R_\sigma}}} \tag{39}$$

The resulting formulae run to many lines which will not be transcribed here. Instead, the reader is referred to Supplementary Materials for a chance to test the derived transformation rules, and verify their validity.

3.1.3. Application of transformation for stress determination in FIB-DIC data

In the previous section the expressions were derived in symbolic form for the stiffness and compliance tensors in the global coordinate system after rotation of a material volume with cubic elastic symmetry by an arbitrary set of Euler angles. Since these expressions are obtained within a symbolic and numerical computational framework, a further step can be made towards statistical analysis of stress interpretation in situations that involve anisotropic elasticity calculations.

In the case of FIB-DIC ring-core method, the gauge volume at the milling location lies at the free surface. We therefore make the assumption that, in the residually stressed state prior to milling, the deformed state corresponds to plane stress. It may be noted further that numerical experiments demonstrate that greatest contribution to the overall strain change during ring-core milling (~70%) is made by the residual stress at depths less than one third of the core diameter [154]. Therefore, the out-of plane stress components are ignored in the analysis of materials stress state:

$$\sigma_{33} = \tau_{13} = \tau_{23} = 0 \tag{40}$$

The in-plane strain components present in the residually stressed state at the measurement location are found from the experimentally measured relief strains during FIB-DIC ring-core procedure. Therefore, the overall strain-stress relationship written in the global axes as:

$$\begin{pmatrix} \varepsilon_{11} \\ \varepsilon_{22} \\ \varepsilon_{33} \\ \gamma_{23} \\ \gamma_{31} \\ \gamma_{12} \end{pmatrix}_G = \begin{pmatrix} S_{11} & S_{12} & S_{13} & S_{14} & S_{15} & S_{16} \\ S_{12} & S_{22} & S_{23} & S_{24} & S_{25} & S_{26} \\ S_{13} & S_{23} & S_{33} & S_{34} & S_{35} & S_{36} \\ S_{14} & S_{24} & S_{34} & S_{44} & S_{45} & S_{46} \\ S_{15} & S_{25} & S_{35} & S_{45} & S_{55} & S_{56} \\ S_{16} & S_{26} & S_{36} & S_{46} & S_{56} & S_{66} \end{pmatrix}_G \begin{pmatrix} \sigma_{11} \\ \sigma_{22} \\ 0 \\ 0 \\ 0 \\ \tau_{12} \end{pmatrix}_G \tag{41}$$

is reduced to:

$$\begin{pmatrix} \varepsilon_{11} \\ \varepsilon_{22} \\ \gamma_{12} \end{pmatrix}_G = \begin{pmatrix} S_{11} & S_{12} & S_{16} \\ S_{12} & S_{22} & S_{26} \\ S_{16} & S_{26} & S_{66} \end{pmatrix}_G \begin{pmatrix} \sigma_{11} \\ \sigma_{22} \\ \tau_{12} \end{pmatrix}_G \tag{42}$$

For compactness this relationship can be written as:

$$\overline{\boldsymbol{\varepsilon_G}^*} = \overline{\overline{\boldsymbol{S_G}^*}}\ \overline{\boldsymbol{\sigma_G}^*} \tag{43}$$

Here $\overline{\varepsilon_G{}^*}$ is the reduced 3-vector of in-plane strain components extracted from the FIB-DIC ring-core measurements, $\overline{\overline{S_G{}^*}}$ is the reduced 3×3 compliance matrix, and $\overline{\sigma_G{}^*}$ is the 3-vector of stress containing only the in-plane components. The inversion of (43) allows the unknown 3-vector $\overline{\sigma_G{}^*}$ to be found as:

$$\overline{\boldsymbol{\sigma_G}^*} = \overline{\overline{\boldsymbol{S_G}^*}}^{-1}\ \overline{\boldsymbol{\varepsilon_G}^*} \tag{44}$$

The stress 6-vector $\overline{\boldsymbol{\sigma}}$ in the global system is now completely known. Therefore, its back-substitution in eq.(41) allows the determination of the unmeasured out-of-plane strain components ε_{33}, γ_{23}, γ_{13}.

3.1.4. Uncertainty quantification of stress determination from ring-core data

Procedure and examples

The residual stress evaluated using FIB-DIC and the subsequently adopted mathematical procedure described above can now be applied to the analysis of single crystals with anisotropic elastic properties. A statistical analysis of the results of residual stress determination can be conducted. In the present study we consider a set of $n = 8000$ cubic crystals of randomly and evenly distributed orientation. Since the output given of FIB-DIC ring-core method is the set of three in-plane strains, in this analysis we consider three representative cases: (a) uniaxial strain state; (b) equi-biaxial strain state where the two normal components of strain are non-zero and equal, while the shear strain is zero, and (c) a strain state for which one normal strain is twice the magnitude of the other, whilst the shear strain is zero.

For materials with cubic structure the generalised Hooke's law takes the form:

$$\begin{pmatrix} \sigma_{11} \\ \sigma_{22} \\ \sigma_{33} \\ \tau_{23} \\ \tau_{31} \\ \tau_{12} \end{pmatrix}_L = \begin{pmatrix} C_{11} & C_{12} & C_{12} & 0 & 0 & 0 \\ C_{12} & C_{11} & C_{12} & 0 & 0 & 0 \\ C_{12} & C_{12} & C_{11} & 0 & 0 & 0 \\ 0 & 0 & 0 & C_{44} & 0 & 0 \\ 0 & 0 & 0 & 0 & C_{44} & 0 \\ 0 & 0 & 0 & 0 & 0 & C_{44} \end{pmatrix}_L \begin{pmatrix} \varepsilon_{11} \\ \varepsilon_{22} \\ \varepsilon_{33} \\ \gamma_{23} \\ \gamma_{31} \\ \gamma_{12} \end{pmatrix}_L \qquad (45)$$

The influence of the degree of anisotropy on stress determination from FIB-DIC ring-core measurements of relief strain can now be probed for any cubic material for which the stiffness coefficients are known in the above matrix. In order to illustrate the effect of anisotropy on the apparent computed residual stress, three materials were chosen. The first choice is Ni-base superalloy which is known to display significantly high anisotropy. The second is single crystal silicon which has moderate degree of anisotropy. Finally, an example of cubic material that is almost isotropic is aluminium and its alloys. In accordance with eq.(45), the stiffness matrix of each crystal can be described using only three independent coefficients C_{11}, C_{12} and C_{44}. The stiffness coefficients can be found in the literature [155] for Ni-base superalloy IN718 that was also the material studied in [156]. The elastic stiffness coefficients for Si and Al were also taken from the literature [157].

Since three parameters needed to describe the most general case of elasticity of cubic symmetry materials, there is one additional stiffness coefficient that arises compared to the isotropic case. The degree of elastic anisotropy for cubic structure materials is described quantitatively by the Zener anisotropy factor:

$$A = \frac{2C_{44}}{(C_{11} - C_{12})} = \frac{2(S_{11} - S_{12})}{S_{44}} \tag{46}$$

The anisotropy factor assumes the value of unity for isotropic material (e.g. W). The deviation from this value represents the degree to which the crystal stiffness in a particular direction varies with orientation.

We wish to compare the stress values obtained taking into account the effect of anisotropy and the stress value that would arise on the basis of the assumption of materials isotropy. The use of highly local FIB-DIC micro-ring-core probes makes this consideration directly relevant in the context of polycrystalline alloys which in the absence of texture (preferred crystal orientation) can be thought of as macroscopically isotropic agglomerates [158]. The equivalent isotropic elastic properties of the polycrystalline IN718 were taken from sources [155, 159] in the literature, along with those for polycrystalline Si and Al [160].

The table below reports the stiffness coefficients and anisotropy factor values for single crystals in the local coordinates associated with the lattice unit cell, together with Young's modulus and Poisson's ratio for untextured polycrystals.

Material	C_{11} [MPa]	C_{12} [MPa]	C_{44} [MPa]	A	E_{poly} [MPa]	ν_{poly}
IN718	234600	145400	126200	2.83	206000	0.29
Si	166000	64000	80000	1.57	160000	0.22
Al	108000	61000	29000	1.23	71000	0.33

Table 1 Elastic stiffness coefficients of selected materials with cubic elastic symmetry

Results

The calculations of the stress from given input strains were carried out following the procedure described above for a collection of 8000 uniformly distributed random crystal orientations. For the purpose of representation, the numerical results were normalized with respect to one particular stress component, namely, σ_{11}, that was computed based on the isotropic material assumption. The results are reported in the histogram graphs shown in Figure 19.

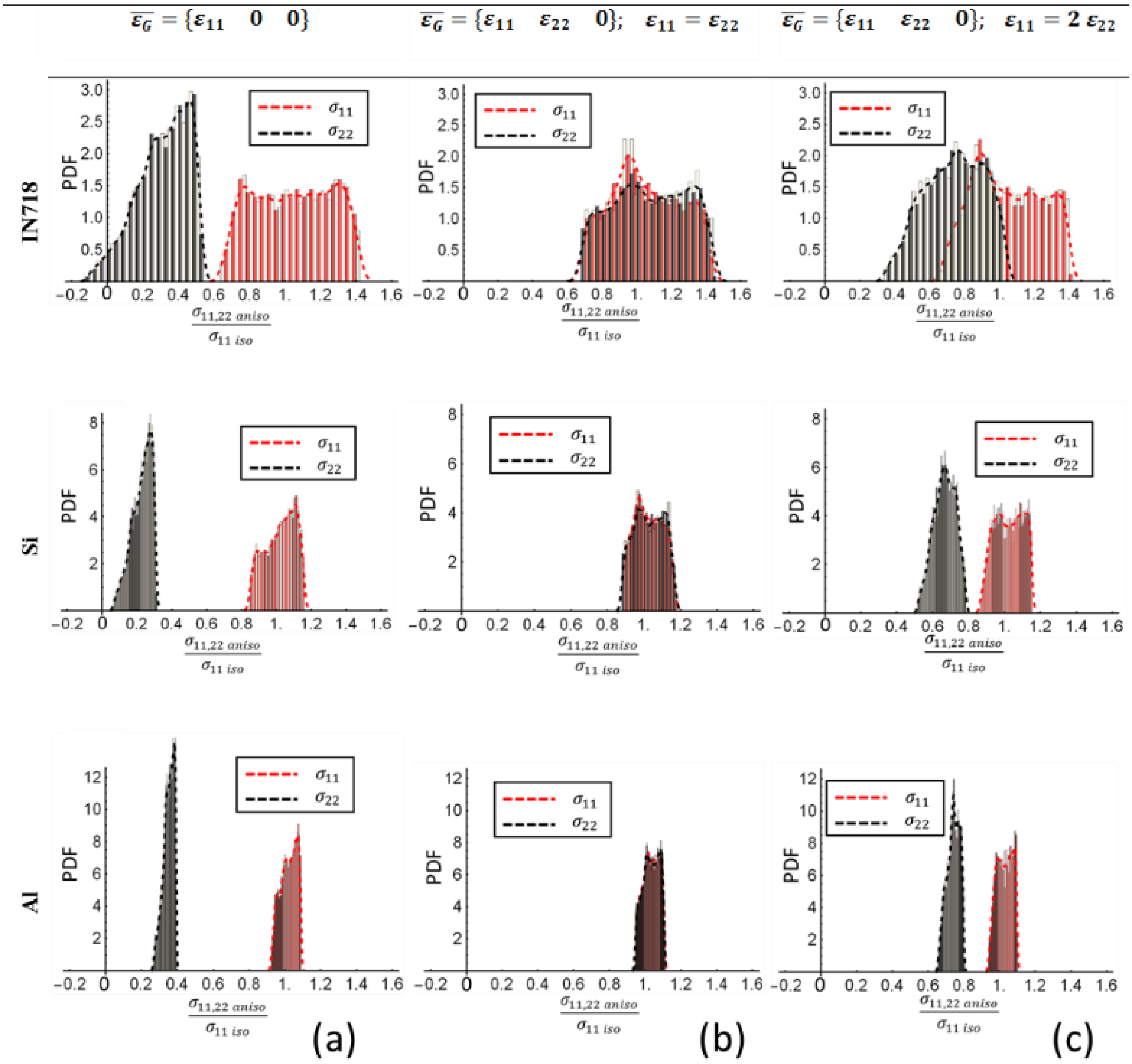

Figure 19 Probability Distribution Functions (PDF) of the evaluated stresses σ11 and σ22 in case of anisotropic material for IN718, Si and Al materials. a) Uniaxial strain state. b) Equibiaxial strain state c) Non-equibiaxial strain state

The table below reports the statistical measures of the results obtained in terms of mean value, median and the 95% confidence interval.

Mat.	CASE	$\left(\frac{\sigma_{11,anis}}{\sigma_{11,iso}}\right)_m$	$\left(\frac{\sigma_{22,anis}}{\sigma_{11,iso}}\right)_m$	$\left(\frac{\sigma_{11,anis}}{\sigma_{11,iso}}\right)_m$	$\left(\frac{\sigma_{22,anis}}{\sigma_{11,iso}}\right)_m$	$\left(\frac{\sigma_{11,anis}}{\sigma_{11,iso}}\right)_{St.Dev.}$	$\left(\frac{\sigma_{22,anis}}{\sigma_{11,iso}}\right)_{St.Dev.}$	$\beta_{\sigma_{11,an}}$	$\beta_{\sigma_{22,an}}$
Ni	***a***	1.048	0.312	1.052	0.332	0.212	0.143	±0.40	±0.90
	b	1.055	1.075	1.036	1.073	0.197	0.210	±0.36	±0.38
	c	1.052	0.742	1.038	0.751	0.195	0.166	±0.36	±0.44
Si	***a***	1.021	0.085	1.032	0.237	0.085	0.056	±0.16	±0.49
	b	1.023	1.027	1.019	1.027	0.076	0.079	±0.15	±0.15
	c	1.022	0.666	1.023	0.669	0.076	0.060	±0.15	±0.18
Al	***a***	1.021	0.351	1.024	0.356	0.044	0.029	±0.08	±0.16
	b	1.032	1.033	1.033	1.034	0.044	0.044	±0.08	±0.08
	c	1.027	0.740	1.028	0.743	0.043	0.035	±0.08	±0.08

Table 2 Statistical results. The value of β indicates the 95% confidence interval

Discussion

The histograms show very significant spread of actual stress values around the value obtained using the simplifying assumption of material isotropy. The mean normalized stress component σ_{11} corresponds to unity. Furthermore, the mean value of the σ_{22} component in all cases corresponds to the isotropic polycrystal's Poisson's ratio.

As expected, the material with the highest anisotropy factor (IN 718) displays the broadest distribution of stress values. In fact, the uniaxial strain example shows the values of σ_{11} computed using the correct anisotropic relations a spread in the range that deviates by approximately ±0.40 from the mean isotropic value. In the case of silicon and aluminium the range half-width drops to around 0.16 and 0.08, respectively. It is worth noting that under the uniaxial strain state, the component of in-plane stress σ_{22} that is perpendicular to the applied strain direction may assume a negative value. This behavior is only observed in materials with a high anisotropy factor.

The equibiaxial strain state analysis confirms further that the spread of values is consistent with the anisotropy factor, i.e. the materials that display higher degree of anisotropy also show greater spread.

Regarding the third example of strain state, the observation that can be made is that in this case the stress component showing the highest magnitude does not always correspond to the component of strain with the highest magnitude. Therefore, particular care must be taken in interpreting the principal stress and orientation at a given location within the sample, if the underlying grain orientation is not known.

In general, the case that gives the widest range of stress value distribution is the uniaxial one, providing a basis for the ‘worst case scenario’ conservative estimation.

3.1.5. Experimental illustration

Experimental procedure

In this section an illustration of the relevance of the developed procedure is provided using a case study. A polished section of a component made from the Ni-base superalloy IN718 was carefully polished to avoid the introduction of additional residual stresses. The section was first ground using the 320 grit grinding paper. This was followed by grinding with papers of increasing grit size up to 4000 grit to improve the surface finish, and to remove the consequence of the previous step. Polishing of the surfaces was then performed using 0.1 µm diamond suspension. In total, ten FIB-DIC ring-core markers were milled on the surface along a straight line. The spacing was not uniform and ranged from 0.05mm for the points in the central zone, and 0.10mm for the points at the ends. The milling configuration is illustrated in Figure 20, superimposed over the EBSD map that indicates grain orientation. The EBSD map was acquired following the milling procedure in order to determine the underlying crystal orientation at each milling location, with three triplets of Euler angles obtained at each position.

The milling procedure was performed using the ring-core procedure with a 5µm inner diameter and the trench width of 1µm. The FIB parameters used for the milling were: ion beam energy of 30 keV and ion beam current of 0.17nA. The milling process was subdivided into 50 incremental steps. At each step a high magnification SEM image was acquired at 5keV electron beam energy and 260nA electron current.

The two directions indicated in Figure 20 were assumed to be principal, and DIC analysis was performed for the strain components along these directions. As last step for the determination of relief strains, the DIC strain-depth curve was fitted with the master curve as described in [150].

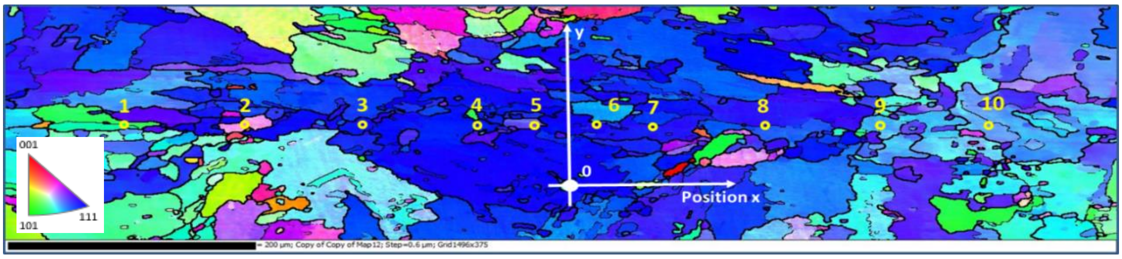

Figure 20 EBSD Inverse Pole Figure map and milling point locations

Results

The spatially resolved profile of residual stress under isotropic material behaviour assumption was reconstructed, and is plotted in Figure 21. The preceding uncertainty analysis allowed the error to be induced that arises by ignoring the anisotropy, and using isotropic assumptions. This is represented in the graph using the upper and lower dotted profiles that delimit the 95% confidence interval. The direct comparison of results obtained taking into account the correct anisotropic elastic behaviour of the material is also reported in the Figure 21. The expected prevalent compressive residual stress state was found in the material, in both *x* and *y* directions, as is apparent from Figure 21.

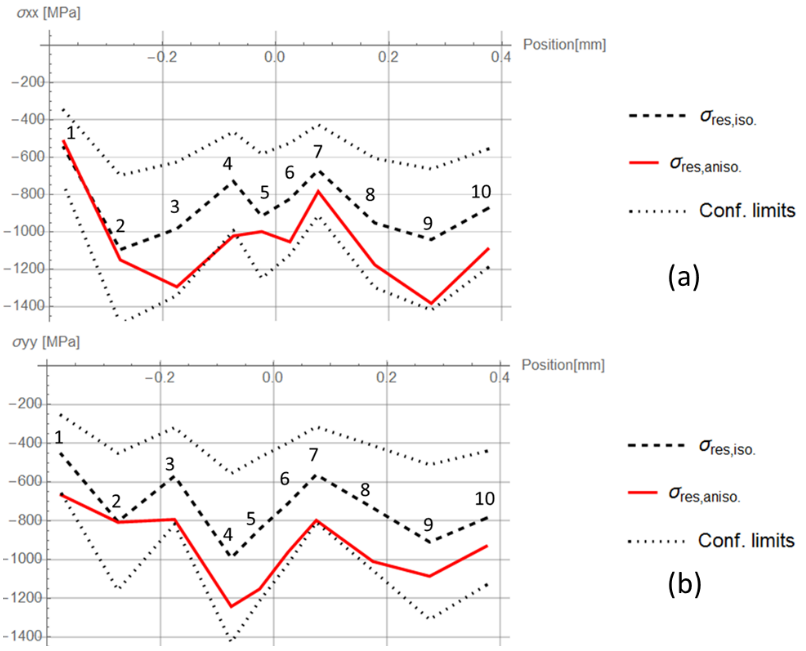

Figure 21 Residual stress profiles and comparison between hypothesis of Isotropic and Anisotropic material. The region within the two dotted lines represents the confidence interval in which the stress value may lie considering anisotropy at 95% confidence interval. . a) Component of residual stress in x direction $\sigma_{res,xx}$. *b) Component of residual stress in y direction* $\sigma_{res,yy}$.

Discussion

The consideration of the trends in the spatial variation of stresses computed using the isotropic and anisotropic assumptions reveals close similarity between the two approaches. The magnitude of the stresses, however, displays large deviations. The stress component in the *x* direction shows the greatest deviation from the isotropic calculation at the milling point n. 9. At this position the value given by the anisotropic elasticity calculation differs from the isotropic computation by about 33%. For the orthogonal direction of stress (the *y* component), the largest difference is observed at point no.4, where the offset is close to 25%.

Comparing the experimental results shown here with the examples from the previous section, the case closest to the experimental situations discussed here is the one illustrated in Figure 19(c). In this example the strain state is non-equibiaxial, and the uncertainty due to ignoring the underlying anisotropy effect is ±38% for this material (IN718). The plot shows the limits of the 95% confidence interval indicating the upper and lower bounding stress values. Once the orientation is known, as in the presented example, the stress can be calculated more precisely, and the result is shown in Figure 21. The result lies within the expected range of variation predicted on the basis of isotropy assumption and uncertainty quantification. It is worth noting that the experimental results, corrected by accounting the actual local elastic properties, lie predominantly in the region beneath the mean value (isotropic). This effect can be promptly explained by observing that the majority of the experimental points lie in grains showing approximatively the same orientation, as shown in Figure 20. Therefore, it was expected that the account of anisotropy would have produced consistent shift in terms of lower or higher values with the respect of the mean.

3.1.6. Conclusion

The analysis of statistical variation and uncertainty of stress evaluation using FIB-DIC ring-core analysis in combination with anisotropic elasticity calculations has been presented. The widest range of stress values obtains in the instance when the state of strain is close to uniaxial.

As expected, the material with the highest anisotropy factor (IN 718) gives the broader distribution of possible stress. In the uniaxial strain state example it was found that the σ_{11} stress component could take values in a range centred around the isotropic calculation, but may deviate from this value by as much as ±40%. In the case of silicon and aluminium the largest deviation drops to around ±16% and ±8%, respectively.

An experimental illustration was provided that showed the application of the procedure to the situation when EBSD technique provides the knowledge of grain orientation at the measurement location. The results obtained are consistent with the expectations based on the statistical analysis of uncertainty.

3.2. The effect of eigenstrain induced by ion beam damage on the apparent strain relief in FIB-DIC residual stress evaluation

3.2.1. Introduction

Focused Ion beam (FIB) has become an established technique for the sample preparation at the micron- and nano-scale [161]. The main areas of application are materials science (energy, structural and functional materials), biology, coatings technology, micro-electronics, as well as many other fields. FIB allows both surface imaging and modification, i.e. the removal and/or deposition of material. Material removal is typically accomplished by bombarding the target surface with Ga^+ ions that cause the spallation of secondary ions from the sample surface.

However, the ion beam–sample interaction can lead not only to the removal of material, but also to the alteration of the defect state and/or the stress state within the target material. Alteration of residual stress state within the target material is thought to be mainly the consequence of defect, dislocation and void evolution [162]. As discussed in [163], the damage accumulation process can be subdivided into three regimes. The first, which corresponds to a low ion fluence, is associated with a small implantation region and generates small and isolated defects. In this regime, a linear relationship has been observed between the strain generated and the volume defect density. The onset of loss of crystallinity is encountered at the second regime. At this stage the density of defects increases, and larger defects arise from combination. In the third regime amorphisation is predominant, and since the introduction of eigenstrain in the crystal/amorphous structure occurs, the measurement of strain is thought to be affected significantly in the second and third regimes.

The interaction between the Ga ion beam and the target material can be studied by means of simulation, e.g. using SRIM code [164] or molecular dynamics (MD) [165]. MD has been extensively used to investigate a vast range of materials processes. The simulation of Ga ion bombarding Si surface [166] and [167] provided quantitative predictions of the distribution of implanted Ga ions within the Si host material, and the accompanying atomic displacements of Si atoms. A recent study has shown that the consequences of Ga ion implantation during FIB milling can be reduced by means of Focused Electron Beam Induced Etching [168].

Samples that have the geometry showing a high ratio of FIB-milled surface to the overall volume are likely to be more strongly affected. For example, it is known that the preparation of samples for transmission electron microscopy (TEM) using FIB may introduce artefacts on the surface that degrades the quality of the acquired image [169] and [170]. In micromechanics, the use of micro- and nano-pillar as samples for local compression testing has become widely used [171] and [172]. These specimens have the shape of short cylinders with dimensions that can vary from a few hundreds to thousands of nanometres in diameter. Therefore, in a number of situations the material deformation effects that accompany FIB milling cannot be neglected. Studies on copper [173] using TEM and Auger Electron Spectroscopy (AES) have shown that during FIB milling a thin amorphous layer (~ 50 nm) is formed in which both dislocation activity and solution hardening are inhibited. Beneath the amorphous layer, produced in this way, dislocation pile-up is generated, suggesting that even in the absence of additional loading some stress evolution and inelastic deformation take place. Increasing dislocation density causes changes in the mechanical properties, typically by way of either solid solution or precipitation strengthening. As a consequence, the stress required to cause plastic deformation of the pillar is increased in comparison with what would be measured for a similarly shaped "pristine" pillar. However, dislocation dynamics simulations [174] of the affected layers and their deformation suggest that, for pillar sizes in excess of 1μm, the local hardening effect of the overall pillar deformation response is negligible. The thickness of the implanted layer and the depth affected by material property modification are functions of the ion beam incidence angle. The effect of FIB milling was studied on samples containing high residual stress induced by nanoindentation [175]: the morphology of indentation cracks was found to change depending on the location of milling. These observations provide supporting evidence for internal stress change due to FIB milling.

A pillar-like geometry is also the result of a classical FIB-DIC ring-core measurements. For this reason, it is important to take into account the above considerations concerning the effect of FIB-induced damage on the apparent stress state of the feature. Previous studies of the effect of FIB milling on material state took into account exclusively the surface effects, as well as dislocation generation and consequent material hardening. For the purpose of measuring the intrinsic elastic strain present within the sample prior to its evaluation using the FIB-DIC approach, the knowledge of additional stresses and apparent strains induced by FIB milling is required. Ga ion damage leading to amorphisation and crystal distortion is certain to cause strain modification. Furthermore, when the technique resolution is pushed towards smaller scale, when the pillar diameter reaches the order of magnitude of the FIB-affected zone, the effect on the apparent residual stress may become dominant, having substantial impact on the reliability of the measured value.

In first analysis performed in this study we employed the synchrotron X-ray Reflectivity technique to study the amorphous layer generated in a single crystal Silicon material due to Ga-ion beam exposure at small grazing angle. The thickness and the density of the amorphous layer were extracted by the analysis of the reflectivity curve.

Experimental quantification of the residual stress induced by FIB milling was then conducted by analysing the cantilever deflection (curvature) due to the presence of an external non-symmetric layer containing eigenstrain induced by FIB. The experiment was carried out on a commercial silicon AFM cantilever and the beam deflection observed using Scanning Electron Microscopy (SEM). The application of eigenstrain and beam bending theories allowed analytical evaluation of the intrinsic strain profile (eigenstrain) generated by FIB damage. The solution was validated by comparison with the one obtained by Finite Element Method (FEM) simulation.

An alternative way for the abstraction of the eigenstrain induced by FIB irradiation was provided by the analysis of the stress field simulated by means of Molecular Dynamics numerical modelling. With this end we adopted a hybrid approach MD/FEM. Eventually, the eigenstrain profile obtained served as input for the simulation of the tested Si cantilever with the purpose of validating its correctness.

The validated eigenstrain profile was then used for the FEM simulation of some putative residual strain profiles that are likely to be induced by FIB milling. Multiple conditions, in terms of the depth of the FIB-affected layer, were considered in order to provide parametric evaluation of the influence of FIB damage effect on the perceived residual stress. The approach presented here allowed defining material-specific geometric parameters (e.g. the minimum pillar diameter) to ensure that the FIB-induced effects remain negligible so that FIB-DIC method is used accurately for residual stress evaluation; for Si material. Obviously, the calculation framework presented can be generalised for any kind of crystalline material enabling accurate assessment of FIB induced effect when FIB-DIC is employed.

3.2.2. X-ray reflectivity FIB affected layer characterisation

In this study, synchrotron X-ray Reflectivity (XRR) was employed to interrogate the amorphous layer that arises following the exposure of Silicon single crystal sample to Ga$^+$ ion irradiation. X-ray reflectivity (XRR) technique is particularly suitable for the study of very thin layers (from few to tens nm).This technique relies on the analysis of the intensity of specular X-ray reflection as a function of the varying incident angle [176, 177]. The typical setup adopted in this type of experiment is shown by the scheme in Figure 22.

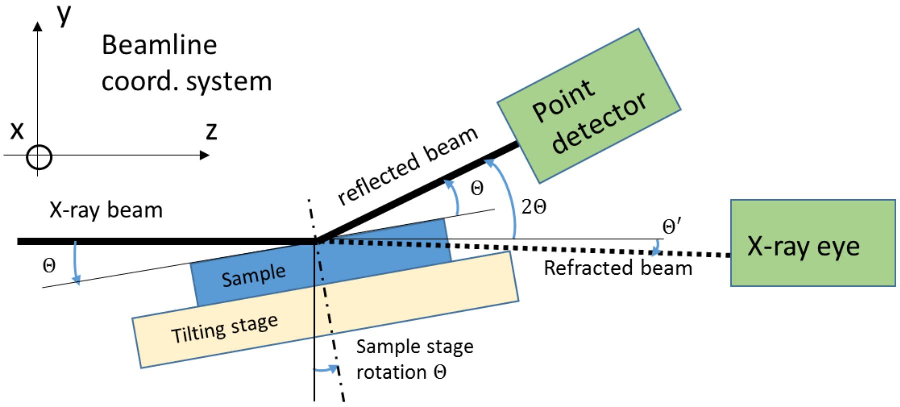

Figure 22 Schematic diagram of XRR setup

FIB milling was performed at the grazing angle of 10°. This low angle is chosen to reflect the conditions experienced by the sample material during surface polishing milling [13]. A single crystal Silicon sample was exposed to the FIB at the energy of 30keV until the thickness of material removed reached 0.2μm.

The XRR experiment was conducted on the BM28 - XMaS beamline at the European Synchrotron Radiation Facility (ESRF, Grenoble, France). A good X-ray beam energy compromise in terms of good intensity and good resolution of the pattern periodicity was found at 12.4keV. The beam size was set to 0.5mm in width (parallel to sample surface) and 0.2mm in height (in the direction close to the sample normal).

The sample was mounted on a diffractometer to allow precise alignment of the centre of rotation and to allow fine angular movements. For the detailed data collection of the reflection, an Avalanche Photodiode Detector (APD) KF16 with 5 mm×5 mm sensitive area was mounted on the diffractometer arm.

GenX software package was used to perform the fitting of experimental curves using a non-linear least-squares algorithm. In order to achieve adequate agreement between the fit and experimental data, the amorphous layer was thought to be composed from two layers distinct in terms of density (and hence refractive index). Whilst assuming a single layer did not lead to satisfactory agreement, using two layers provided sufficient flexibility to obtain a good match to the observed profile. The thickness of each sub-layer was considered to be a fitting parameter sought by the software as part of the refinement. Moreover, it was found that an additional surface layer had to be introduced to achieve the match that represented the SiOx phase arising from the exposure of Si amorphous layer to air.

Minimising the error between the fitted curve and the experimental data led to the results illustrated in Figure 23(a). The fit is shown by the continuous bold curve, and the experimental data by open markers. In order to show the details of the fitting, a close-up of the plot in Figure 23(a) is reported in Figure 23(b)

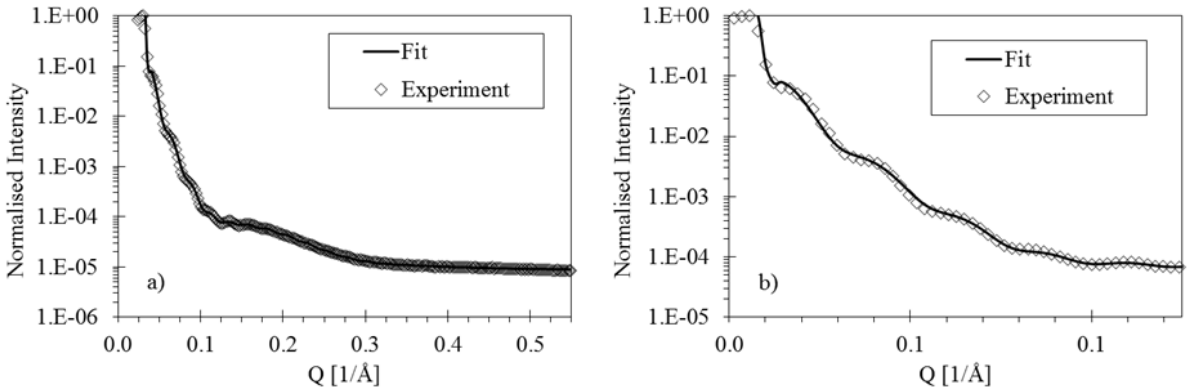

Figure 23 XRR profiles. a) Experimental intensity profiles for Ga-ion treated samples (open symbols), and fitting using GenX (continuous line). b) Magnified plot at low momentum transfer Q.

The relevant parameters that produced the best fit are summarised in Table 3. For the sake of convenience, material density is expressed as % change from the pristine Si condition.

Layer	*Thickness [nm]*	*Density change $\Delta\rho$*	*Roughness [nm]*
SiO_x	*2.8*	-	*0.6*
1st Si amorphous	*19.5*	*-10.0%*	*2.3*
2nd Si amorphous	*3.7*	*1.7%*	*0.4*

Table 3 The abstracted layer properties.

The overall thickness of the amorphous layer was found to be ~23 nm. This value corresponds to the sum of thicknesses of the two layers. To test the correctness of this conclusion, more complex analysis was carried out assuming a three-layer structure; however, the results came out very similar, and a similar overall thickness of ~23nm provided the best fit. Since the oscillation period is captured correctly by the fit, the error in the total thickness determination is likely to be small. The principal conclusion we draw is that the total thickness of the affected layer is consistent with the literature reports of the results obtained using TEM [178]. Furthermore, there is agreement between this depth of amorphisation and the predictions of molecular dynamics simulations reported previously [179].

Further observations concern the two-layer structure model. As seen in the previously reported experimental evidence [178] from through-thickness TEM imaging, no sharp interfaces are present within the affected layer. This is a further indication that the interfaces are not atomically flat, but rather correspond to diffuse transitions. In fact, the 2nd modelled Si layer can be thought as the diffuse interface itself between amorphised material and the unaffected material lying beyond this depth. Further insight into this “fuzzy interface” transition region can be obtained by noting that the interface roughness between the 1st and the 2nd layer is comparable to the thickness of the 2nd layer itself. The resulting density variation obtained from the analysis suggests that the layer modified by the ion beam interaction is itself inhomogeneous, characterised by significant changes with depth within the ~23nm range from the surface. Figure 24 illustrates the reconstructed density change $\Delta\rho$ with respect to the density of the parent (pristine) material.

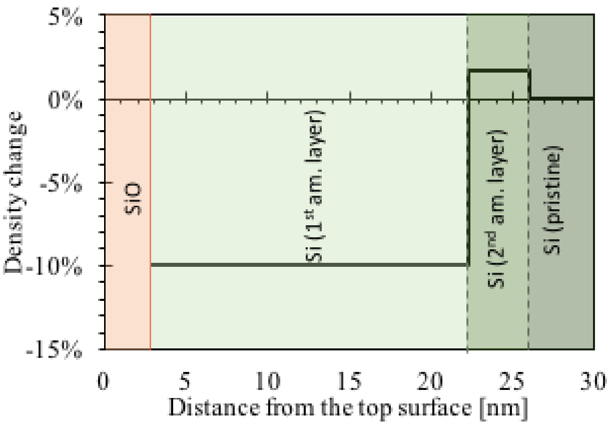

Figure 24 Relative density change within the layer affected by the ion beam.

Changes in the density detailed above are associated with (although not only) the inelastic deformation that can be thought of as linked with the transformation strain, or eigenstrain. In response to the introduction of this inelastic misfit, residual elastic strains arise in the sample in order to maintain overall compatibility, but also to ensure stress equilibrium [180].

In view of the predictions of various simulation tools that identify the possibilities of lattice damage, crystal fragmentation and amorphisation, it can be surmised that that process of ion interaction with the sample surface can be viewed in three stages. In Stage I the highly energetic Ga ions penetrate the surface of the Si crystal, travel at speeds when the probability of interaction with the lattice is relatively low, resulting in the presence of the very superficial layer of ~4-5nm thickness in which the density shows little change from the bulk value. Since oxidation is likely to affect similar thickness of material, it is difficult to distinguish between these two processes. In Stage II, having lost some energy, Ga ions slow down further and cause some damage at depths ~5-20nm. In this layer a decrease in density is observed (by up to 10%), corresponding to material swelling that accompanies the increase in the lattice defect population. Finally, in Stage III, at depths of ~20-25nm, Ga ions come to stop, and a mild increase in density is observed in our experiments.

3.2.3. Experimental evaluation of Eigenstrain induced by FIB

In order to estimate the amount of residual strain in the affected layer, we devised an experiment that makes use of flexible beam geometry and the measurement of curvature and deflection. The presence of a non-uniform residual stress profile, across the beam section, induces beam bending that ensures that the equilibrium of force and moment and the compatibility of total strain are satisfied simultaneously within the framework of Kirchhoff plane section kinematics. The measured radius of curvature can be correlated with the eigenstrain induced by the FIB ion damage within the beam cross section. The curvature measurement method has been successfully applied in the past for the quantification of residual stress profiles in thin coatings and films [181] and [182].

Atomic Force Microscope (AFM) cantilevers are slender, flexible and nearly residual stress-free micro-mechanical components. These properties of AFM cantilevers have been used previously for the determination of residual stresses generated by nickel film deposition by electroplating [183]. Our experiment is based on the observation of the cantilever deflection due to the eigenstrain introduced by FIB milling in a thin layer of material after Ga ion damage during material removal.

The angle of incidence of the ion beam on the target surface plays an important role in determining the nature of the damage cascade within the material, along with the severity and depth of the induced eigenstrain field. In most residual stress evaluation techniques that rely on material removal by FIB milling normal to the sample surface, such as the micro-ring-core FIB-DIC, the blind hole micro-drilling and the FIB slitting methods, a small incidence angle (of the order of few degrees) is formed between the ion beam and the affected surface of the remaining material wall, e.g. a micro-pillar. Although this minimises the amount of FIB implantation, some ions are deflected and implanted deep within the material. Since the purpose of this study is to provide a conservative limit on the FIB-induced eigenstrain effect, in the present experimental assessment we consider the case of normal incidence at the angle of 90°, that can be assumed to correspond to the worst case scenario. The eigenstrain effect quantification that is obtained as a result can be considered conservative.

Experimental procedure

The cantilever used for the present experiment was a silicon AFM probe provided by Asylum Research® of type AC240TS. The main reason for choosing this sample was the absence of any coating layers on any side, the fact that no other sources of residual stress are present within the sample, and the only effect considered is that of ion beam damage and the attendant amorphisation. The micro-beam length and the dimensions of its trapezoidal cross section are depicted in Figure 25. In order to improve the accuracy of graphical evaluation of the beam curvature, a relatively large extent of the cantilever top surface (150µm) was exposed to Ga ion bombardment.

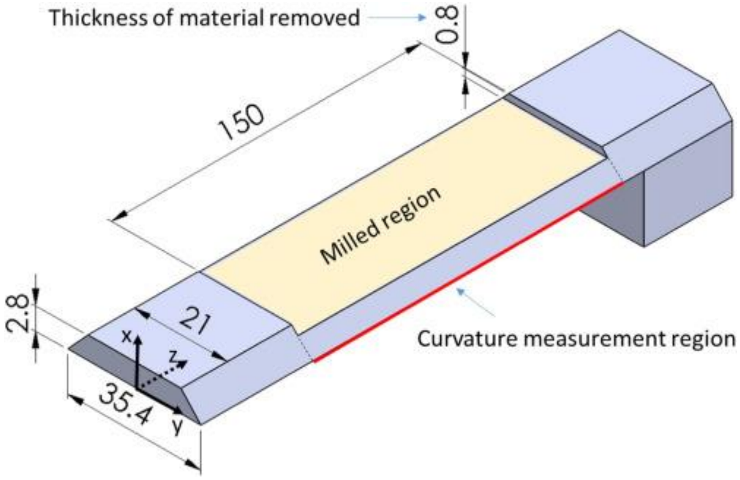

Figure 25 Schematic representation of the cantilever geometry and its dimensions. Units in micrometres

The experimental procedure consisted of the acquisition of a high resolution lateral (edge-on) image of the undeformed beam using Scanning Electron Microscope (SEM). This was followed by tilting the cantilever to align its normal with the axis of the ion beam column that is inclined at 55° to the SEM column. A thin layer was then milled at the upper surface of the cantilever using FIB energy of 30 keV and ion beam current of 0.17nA, as depicted in Figure 25. The cantilever was then again tilted so that it was viewed laterally (edge-on) by the SEM, and the thickness of the material layer removed was measured as 0.8µm. High resolution SEM imaging was also used to determine the cantilever deflection which serves as input in the analytical eigenstrain calculation (Figure 26). Supplementary images were taken for the purpose of observing the surface roughness after milling procedure and obtaining reliable measurement of the thickness of material removed.

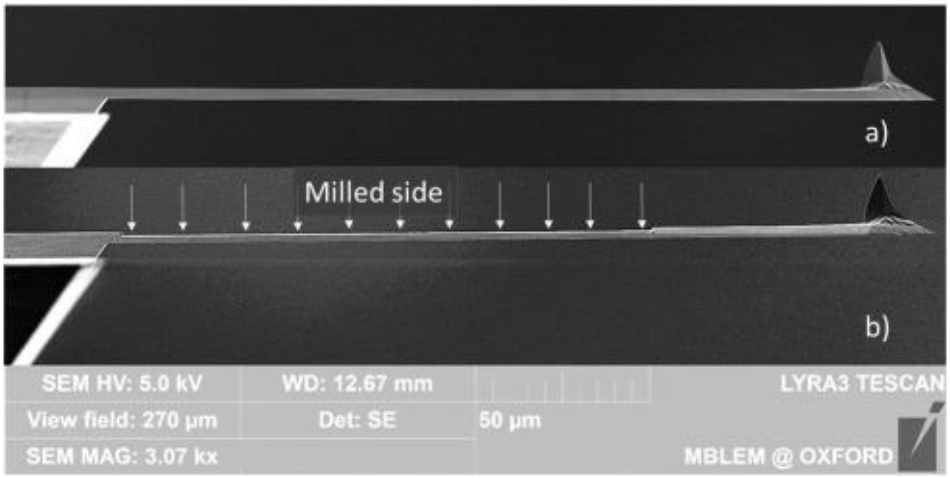

Figure 26 SEM images of the cantilever lateral view. a) Prior milling. b) After milling.

Eigenstrain profile determination

The characterisation of the residual elastic strain induced by the presence of a thin damaged and amorphised layer can be performed by coupling the eigenstrain theory with the bending theory within an analytical formulation. This procedure has been presented and discussed in some detail by Korsunsky [184] and [41].

Determining the eigenstrain distribution requires an assumption to be made regarding its profile and depth-wise extent. Some recent work has shown interesting characteristics of the amorphous damage layer generated in silicon after FIB milling using Ga ion milling [185]. The residual stress profile generated by ion beam damage shows a peak close to the surface followed by a steep gradient. Simulation also predicts a possible change in the sign of residual strain, and its decay to zero value with increasing depth. The results indicate that the sign of permanent strain due to ion damage may change between positive and negative depending on the depth below the surface, ion energy, and angle of incidence. We note, however, from previous analyses of eigenstrain-induced residual stresses, that the strain caused remotely by ion implantation is sensitive only to the integral properties of the profile, as discussed below. This allows us to proceed by reasoning that to the first approximation the eigenstrain profile can be represented by a half-Gaussian peak function. The depth extent of the damaged and amorphised layer after ion bombarding at 30keV of energy used in the present experiment reported in the literature corresponds to W=20nm. We use this parameter to set the Gaussian profile width for the eigenstrain profile. Considering the cantilever occupying the region $0<x<h$, we describe the eigenstrain distribution below the surface $x=h$ in the form

equation:

$$\varepsilon_{eig}^{*}(x) = \varepsilon_{max}^{*}\, e^{-\frac{(x-h)^2}{2W^2}} \tag{47}$$

The calculation procedure involves the determination of the linearly varying total axial strain within the beam that is given by the sum of the elastic and inelastic strain (eigenstrain):

$$\varepsilon_{tot}(x) = \varepsilon_{eig}^{*}(x) + \varepsilon_{el}(x) = a + \frac{bx}{h} \tag{48}$$

The linear variation of the total strain conforms to the strain compatibility requirement for beam bending, whilst the presence of two parameters a and b allows the force and moment balance equations to be satisfied. Simple geometric analysis of the strain variation within the beam shows that the relationship between the b parameter and the beam curvature is given by:

$$\frac{1}{\rho} = \frac{\mathrm{d}\varepsilon}{\mathrm{d}x} = \frac{b}{h} \tag{49}$$

The beam curvature was measured by direct image superposition and comparison of the SEM images taken at the two significant geometrical configuration assumed; before the Ga ion exposure and after.

Since the width parameter W in the Gaussian depth profile (Eq.(47)) is set, the task is reduced to the determination of the maximum eigenstrain value $\varepsilon_{\mathrm{max}}$. The solution of the problem, including the value of the beam curvature b/h, depends linearly on $\varepsilon_{\mathrm{max}}$. The detailed calculation is shown in the Appendix.

A further validation of the eigenstrain model was conducted using FEM. A reduced three-dimensional model of the beam, taking into account its symmetry, was built and solved after imposing the eigenstrain profile found from the beam bending analysis. The contour plots of the three relevant strain components are shown in Figure 27.

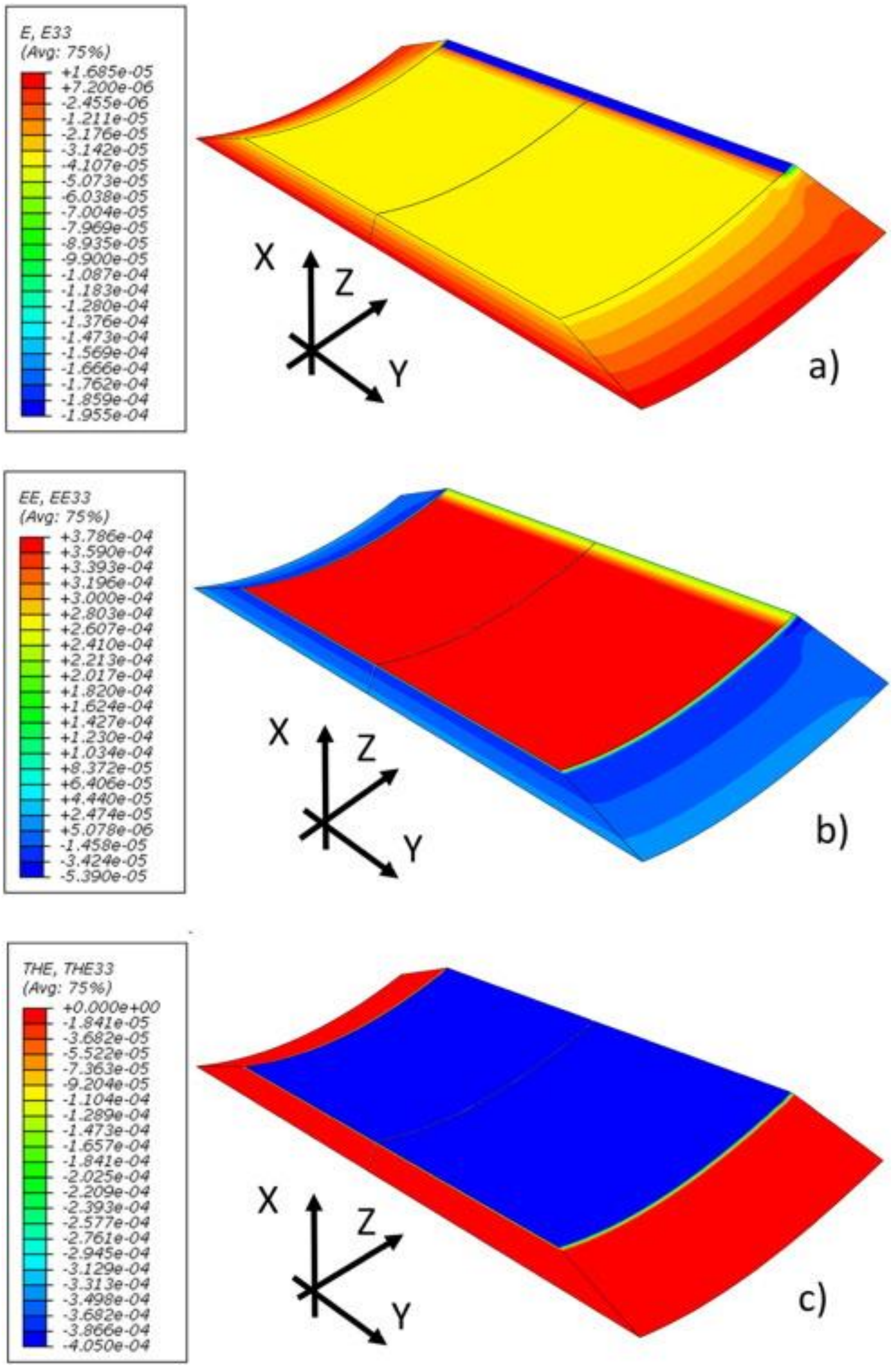

Figure 27 Contour plots of strain within the beam cross-section: a) total strain, b) elastic strain, and c) eigenstrain.

The strain profiles are plotted as a function of depth into the beam cross-section are shown in Figure 28. As it is possible to observe, the steep gradient of eigenstrain in the shallow region of the beam is reflected in the distribution of elastic strain. Whilst, the total strain distribution follows a linear profile, as expected according with the beam theory.

Good match is seen between the analytical solution and the results of the FE model both in terms of cross-sectional strain distributions and the induced beam curvature.

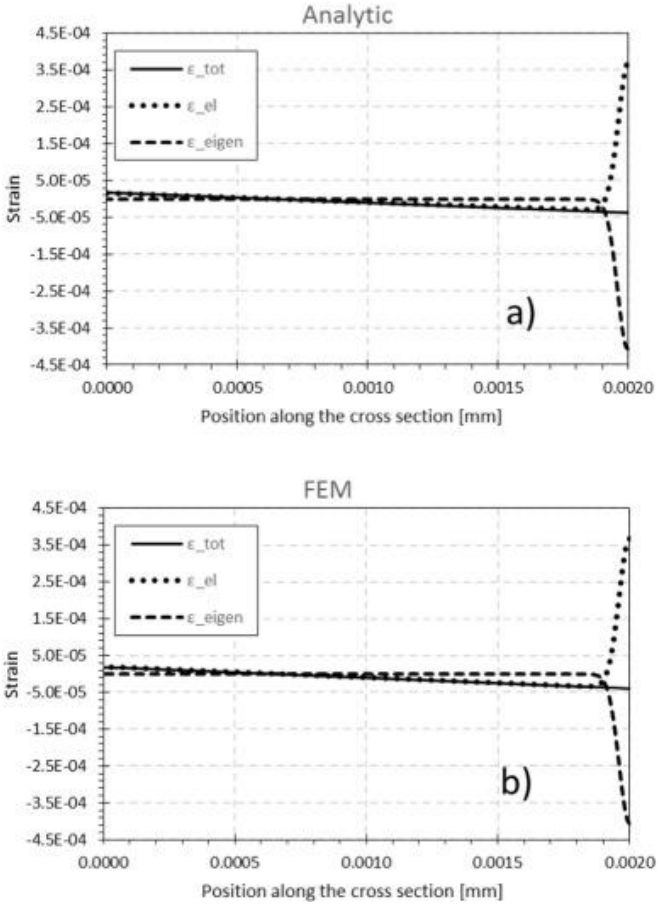

Figure 28 Total strain, elastic strain and eigenstrain within the beam cross-section obtained from a) the analytical solution, and b) the FEM simulation.

As reported in the Appendix, the maximum magnitude of eigenstrain was determined to be $\varepsilon_{max}=-(4.1\pm1.4)\times10^{-4}$. The uncertainty was determined from the parabolic fit to the shape difference between the initial and final cantilever profile.

Silicon material, after ion exposure, usually experiences dilatation which can be represented as an introduction of positive eigenstrain [186]. Nevertheless, the experiment presented in this section highlighted a negative eigenstrain value. The shrinkage occurred at the material can be explained by the temperature at which the ion implantation occurs. In fact, previous works reported such phenomena as function of material temperature [186] and [187]. Other explanation may be sought into the effect of nano-cavities shrinkage in Silicon materials as reported in [188]. Therefore, the intense presence such features may affect the overall material response of the irradiated layer.

The ε_{max} value defines the scale of the entire profile of eigenstrain induced in the target material (Si) under the selected process parameters. Since eigenstrain is an intrinsic parameter of the process (Ga exposure), the knowledge of the ε_{max} parameter can be applied to other situations and geometries when Si ion beam milling is involved. This result is applied to the consideration of FIB-DIC pillars below, but may be used for other types of micro-structured mechanical components (e.g. MEMS).

3.2.4. Eigenstrain abstraction form MD simulation

This section deals with the adaptation of the output from atomistic scale modelling and experimentation to the description of the consequences of Ga+ ion beam milling accompanied by ion implantation and damage.

In the context of nanoscale analysis of strains and stresses, linking atomistic data to equivalent continuum descriptors presents a considerable challenge, since in this context the very classical concepts of strain and stress come into question. Whilst strains are conventionally defined in terms of dimensional and shape changes with respect to a reference configuration, frequently at nanoscale the reference state is not specified, nor possible to define it due to the indistinguishability between identical atoms. A particular challenge arises when the original configuration is not a perfect crystal, but rather an amorphous or highly defected structure.

Extraction of stress values from molecular dynamics (MD) result is based on the Virial Theorem [189]. The state-of-the-art is described in a recent review [190].

In the present study the effect of Ga+ ion beam milling on the damage and residual stress state in single crystal silicon substrate was evaluated using LAMMPS molecular dynamics code [191].

The model setup illustrated in Figure 29 involved a material volume containing up to ~500,000 silicon atoms with the dimensions of $22\times8\times22\text{nm}^3$ and $20\times7\times69\text{nm}^3$ for the ion energies of 5keV and 30keV, respectively. (001) and (111) surfaces were irradiated by up to 400 Ga+ ions at the grazing angle of 10° from the surface plane. In-plane periodic boundary conditions were imposed. Si-Si interactions were described by the modified semi-empirical Stillinger-Weber potential [192] merged with the Ziegler-Biersack-Littmark (ZBL) potential [164] for short interatomic distances. Ga-Si interactions were described by the ZBL potential. Collision cascade simulations were performed within the NVE thermodynamic ensemble using a variable time step for a maximum of 15ps. A thermostat wall at 300K was used to dissipate the incident ion kinetic energy [193]. Atoms leaving the simulation box were removed from the system (considered sputtered). Atomic stress tensor was obtained by averaging of Virial stress over 10ps, with Voronoi volume evaluated for each atom (see [191] for further detail). Residual stress depth profiles illustrated in Figure 30(a) and (b) for 10° grazing angle incident Ga+ ion beams of energy of 5keV and 30keV, respectively, show variation from superficial tension to sub-surface compression. Incident ion beam energy affects both the depth of modification and the magnitude of induced residual stress.

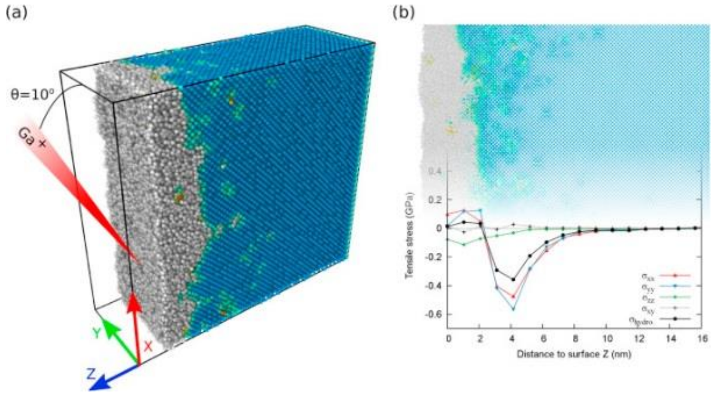

Figure 29 The illustration of (a) MD model setup, simulation geometry and (b) output.

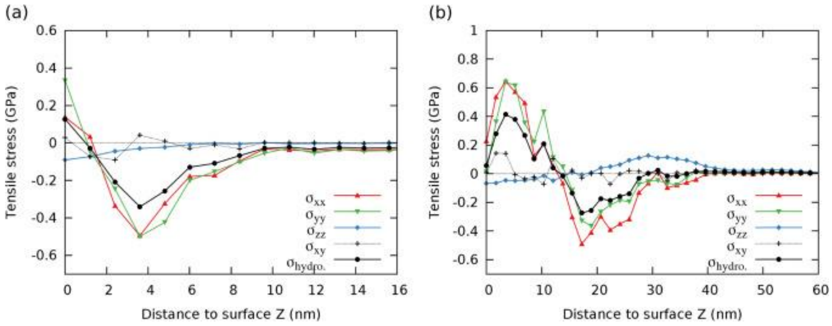

Figure 30 Residual stress profiles as a function of depth below the surface for the ion energy for (a) 5keV and (b) 30keV, respectively [191].

It is noteworthy that the residual stress shape and resembles the density variation profile evaluated by XRR. Furthermore, the thickness of the affected layer is comparable with that seen in the XRR experiment.

Eigenstrain as a means of bridging the scales relies on abstracting inelastic permanent strain from finer scale and applying it as a perturbation at the coarser scale. The task of determining the underlying eigenstrain from residual stress information (e.g. from MD) represents an inverse problem [70]. The material volume dimensions and boundary conditions were replicated in a Finite Element model. The variation of elastic properties from pristine crystalline Si to those of the amorphised layer were described by a smooth function, with Young's moduli values taken from the literature [194] and [160] to be $E_{cryst,111}$=188GPa and $E_{amorph.}$=80GPa, respectively.

Since the study aims to validate several conceptual connections, notably between MD results and the abstraction of eigenstrain profile, and between the eigenstrain-based FE simulation of the deformation of a particular flexible member (AFM cantilever) and the observation of its curvature after ion beam milling in FIB-SEM. Consequently, the previously described geometry of a thin flexible silicon cantilever free from pre-existing residual stress subjected to 30keV Ga+ ion milling at normal incidence was adopted. Since experimental FIB milling on the Si cantilever was conducted at normal incidence, MD simulations we also performed for this beam-sample interaction geometry, with other conditions similar to those described above. The results of the eigenstrain-based FE simulation illustrated in Figure 31(b) illustrate that the elastic strain profile calculated from the FEM compares satisfactorily with the outcome of MD simulation, as shown in Figure 31(a).

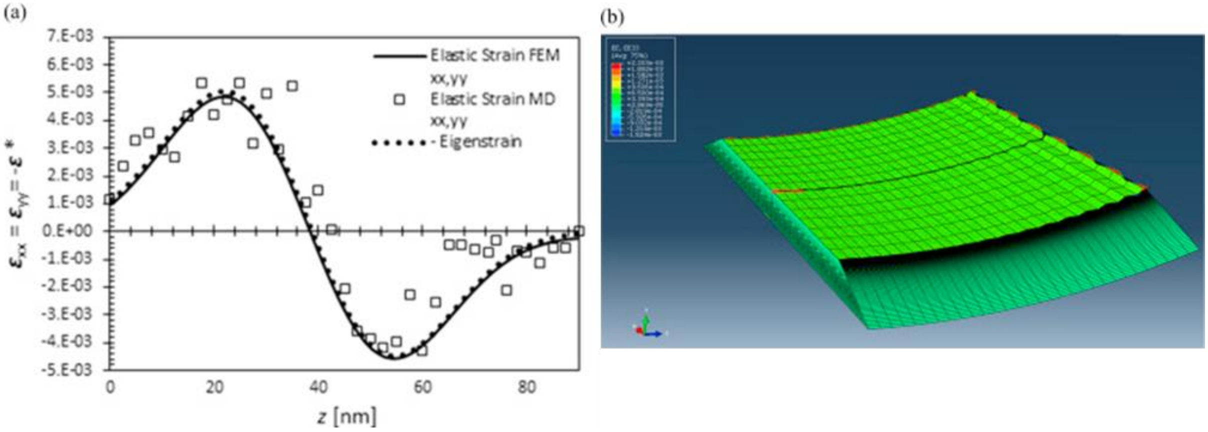

Figure 31 (a) Abstraction of strain and eigenstrain from the residual stress results of MD simulation. (b) The result of the incorporation of eigenstrain in the continuum FEM simulation.

The radius of curvature of the cantilever predicted by the FE simulation using the eigenstrain profile abstracted from MD simulation is 36.8mm. In comparison, the experimentally observed curvature radius was 40.8mm. The difference of ~10% between these results is likely to be associated with the fine details of ion flux on the sample, but the disagreement may be reduced further by careful calibration.

The approach described in the present study provides a basis for further parametric evaluation of focused ion beam damage eigenstrain effect as a function of fluence, incidence angle, and energy.

3.2.5. Correlation between density change and eigenstrain

In order to shed some light onto the correlation between eigenstrain and density change within the affected layer, we abstracted the eigenstrain distribution from the residual elastic strain distribution provided by MD simulations seen in the previous section (3.2.4). As shown in this section, FEM modelling framework allows prescribing an eigenstrain profile based on the residual elastic strain obtained by MD simulation data, and matching the residual stress predictions. The curves for the residual elastic strain from MD, eigenstrain, and eigenstrain-based residual elastic strain prediction are shown in Figure 32(a). In Figure 32(b), the two trends (density change and eigenstrain) are compared with the purpose of establish a correlation.

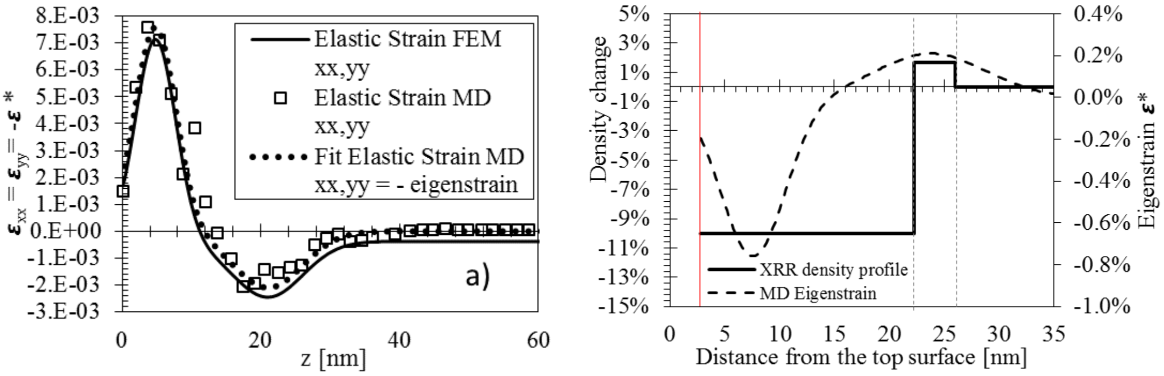

Figure 32. (a) Simulated and fitted residual elastic strain compared with the obtained inverse eigenstrain profile. Note that xx and yy are the in-plane components of the target surface

It is evident that the trend in the evaluated XRR density profile is correlated with the eigenstrain distribution provided by the MD simulation. This observation suggests that a relationship may be established between eigenstrain and the density change, as follows:

$$\sum_{i=1}^{3} \varepsilon_i^* \propto \Delta\rho \tag{50}$$

However, it is important to note that this correlation cannot be simply one-to-one, as some aspects of material damage and deformation may be accommodated through other mechanisms that are not correlated with eigenstrain, e.g. (nano)voiding, fissuring, decohesion, etc. The swelling (density decrease) or densification (density increase) caused by FIB-induced damage is likely to be anisotropic, causing differential deformation in the in-plane and out-of-plane directions. Furthermore, volumetric change is not translated into stress-inducing eigenstrain in its entirety: some elements of inelastic deformation are known as ‘impotent’, in the sense that they do not lead to residual stress generation (consider the fact that eigenstrain distribution that is uniform or linear everywhere within a body does not produce any residual stress). Also, the conversion of structural modification induced by radiation into eigenstrain is related to the changes in the material modulus.

3.2.6. Ring-core modelling and effect on the apparent surface strain

Finite element simulations

The linear elastic ring-core milling simulation was performed for a continuum solid material. The material was considered to be homogeneous and isotropic. It worth noting that miniaturised components such micro-pillars may present lack of homogeneity due the presence of small voids or defects. Nevertheless, at this stage we do not consider the affection of in-homogeneities in our model.

The elastic properties of the sample were taken to correspond to those of silicon. However, it is clear from the details of the analysis below that the elastic properties cancel out during the strain-based calculation, and are not involved in the results. Thus, systematic use of strain quantities forms a great advantage of the present procedure, since it obviates the need to consult the material constitutive law which is necessary when stress quantities need to be computed. The material was considered to be stress-free prior to FIB milling, and the effect of the surface eigenstrain induced by ion damage was determined in terms of the surface strain change.

FIB milling causes Ga ion amorphisation in the near-surface regions of the central micro-pillar. In this study we consider ion damage that leads to shrinking strain produced within the host material, it is assumed that FIB milling generates a compressive surface layer of eigenstrain that varies with the depth from the surface. For the purposes of current analysis, both the hoop and longitudinal (pillar extension direction) components of eigenstrain were applied within the model. In order of formulate the problem analytically, the permanent inelastic strain induced by FIB milling (eigenstrain) is assumed to follow the same half-Gaussian peak profile, obtained from the experiment seen above, as a function of the radial position (Eq.(51)). This profile is chosen to reflect the concentration profile following ion damage in materials that is characterised by a finite mean stopping length of the implanted ions that is associated with the width of the Gaussian peak profile.

The eigenstrain function applied in the model has the form:

$$\varepsilon^*_{\vartheta\vartheta}(r) = \varepsilon^*_{zz}(r) = \varepsilon^*_{max}\, e^{-\frac{(R-r)^2}{2W^2}} \tag{51}$$

Here $\varepsilon_{\max}$ denotes the magnitude of the maximum compressive eigenstrain introduced at the surface, and W represents the width of the Gaussian curve. These two parameters are depending upon the milled material properties and the FIB process parameters and are obtainable using the experimental procedure presented in the present section.

The diameter and radius of the pillar (D=2R) and the radial coordinate r are shown in Figure 33(a). A schematic representation of the FIB milling process and the position of application of the eigenstrain profile are depicted in Figure 33(b).

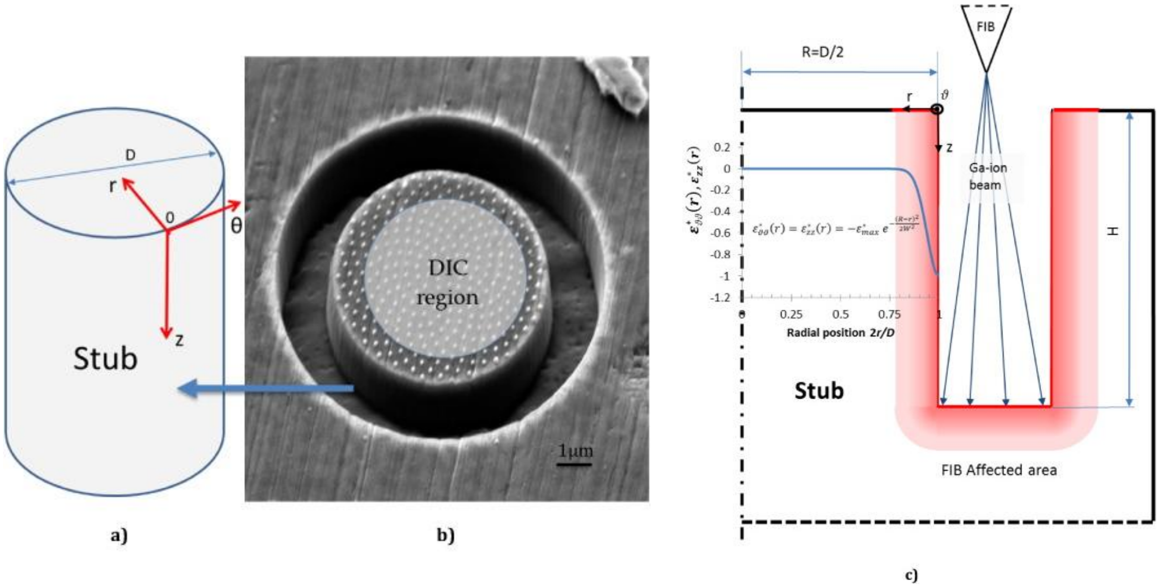

Figure 33 FIB affected area representation and modelling. a) Coordinate system representation. b) SEM image taken during FIB milling. c) FIB milling process schematization: Highlighted in red the regions where the ion implantation appears. The half Gaussian profile represents the eigenstrain imposed at the geometry

Axisymmetric modelling of the ring-core milling process was accomplished using the FEM suite ABAQUS© v.12. The model was subdivided into regions, allowing the material removal by FIB milling to be modelled by modifying the properties of selected material domains by setting their properties to that of "air". The mesh was refined in the regions where high stress gradients were expected,

Parametric analysis

The parametric analysis was conducted by varying the width of the Gaussian curve with respect to the other principal length scale of the problem, the pillar radius. The dimensionless parameter that describes this ratio is $w=W/R$. Parametric characterisation was achieved by running multiple simulations for milling depths h/D between zero and unity, and considering the apparent strain change at the pillar surface as input for residual stress interpretation using the FIB-DIC procedure. The dimensionless parameter that was introduced in order to reflect the strain change induced by FIB damage was the strain calculated at the pillar top surface. Due to the linearity of the eigenstrain FEM problem, the elastic strain at pillar surface scales proportionally to the maximum eigenstrain value imposed, ε_{max}. It is important to note that during milling the residual elastic strain that arises at the pillar surface varies as a function of radial position, and also depends on the geometric relationships between pillar radius R, the milling depth h, and the eigenstrain distribution width parameter, W. However, for the purposes of numerical presentation of the results it is convenient to select a single dimensionless parameter to represent the milling-induced straining of the pillar surface.

One suitable dimensionless expression has the form $|err(0)/\varepsilon_{max}|$, where $err(0)$ denotes the residual elastic strain arising at the centre of the pillar surface, and ε_{max} has been defined earlier in Eq.(47).

Once the effect of FIB milling is calibrated, by means of the numerical model described below, the error introduced into the FIB-DIC residual stress evaluation can be quantified. Then, this defines the threshold in terms of the minimum pillar dimensions for which sample residual stress effects still dominate over the FIB-induced strain effects, sufficiently to obtain reliable residual stress measurement.

In FIB-DIC measurement, the DIC measurement is performed on the top stub surface calculating an average strain value over a certain area that is smaller than the entire one (Figure 33(b)). For this reason we propose also an alternative dimensionless expression to represent the consequence of the Ga damage. From the numerical results, the average value along the radial direction can be evaluated and hence we obtain a value which can be compared with the one from DIC analysis. In this case we considered the mean value of $err(r)$ evaluated between r=0 and r=0.9R; we called it <err>. This means that the average was done over a reduced surface of the stub like DIC analysis as shown in Figure 33(b). Once again the mean value was turned into a dimensionless quantity dividing by the maximum eigenstrain value imposed, $\varepsilon_{\max}$. The quantity then assumed the form of <err>/$\varepsilon_{\max}$.

This secondary representation allows the direct quantification of the amount of strain that affects the FIB-DIC measure. Once a threshold of acceptability of this effect is set, in terms of <err>, the minimum pillar dimension can be deduced.

To a good approximation, the parametric outcomes can be summarised using polynomial or power fitting functions, as reported in the figures.

Results

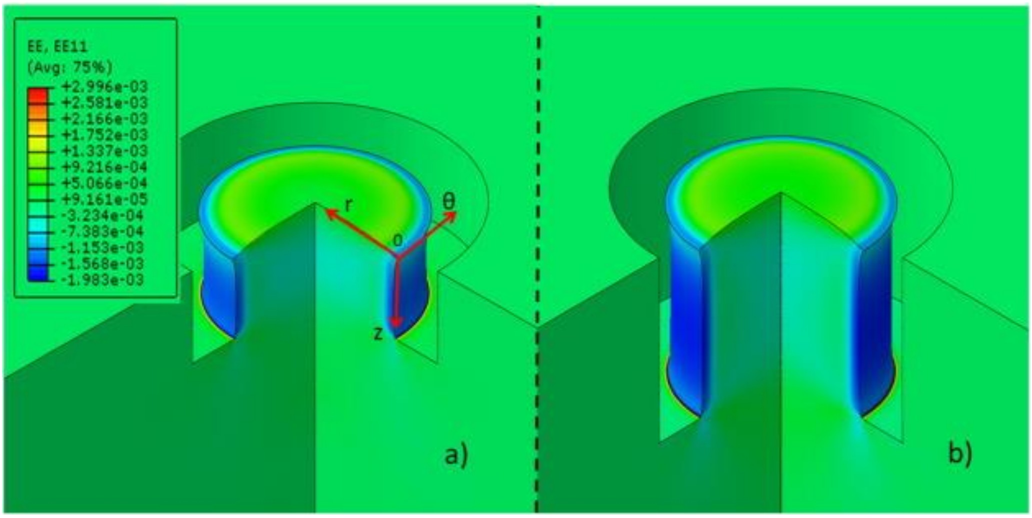

Figure 34 Example of radial residual elastic strain due to FIB ring-core milling imposing an eigenstrain profile withW/R=0.1 as extension, depth ratio a) h/D=0.5 and b)h/D=1

The plot of the radial strain as a function of the radial position is shown in Figure 35 for the top surface, providing the visualisation of strain change in the affected area. In this analysis we do not take into account the perceived strain changing during the whole milling process. Thus, the elastic strain field we consider is referred to the last milling step, then at the depth h/D=1. This strain change function has been normalised, both in ordinate and abscissa, with the maximum value assumed. Seven different W/R

ratios were analysed and plot; starting for a very narrow Gaussian shape $W/R=2.5\times10^{-3}$ to the wider one $W/R=0.1$.

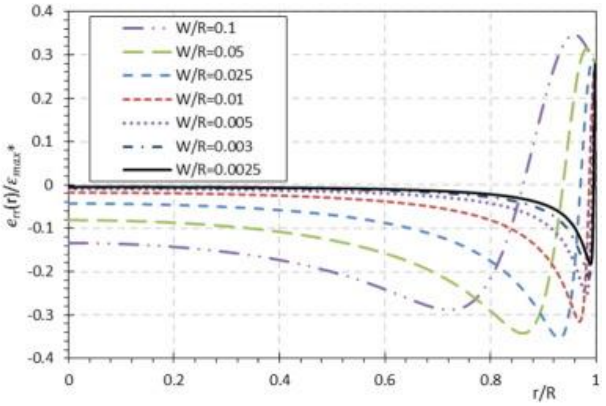

Figure 35 Normalised elastic strain along the radial direction for various W/R ratios at depth of milling h/D=1.

Using the results of FEM analysis it was possible to evaluate the elastic strain at the centre of the micro-pillar, and the average value across the reduced area spanning 90% of the entire radius of the pillar. On this basis, a function was obtained that shows the ion damage effects on the FIB-DIC ring-core measurement (Figure 36(a) and (b)). In order to identify the minimum pillar radius, an example determination of the threshold pillar radius *R** is shown.

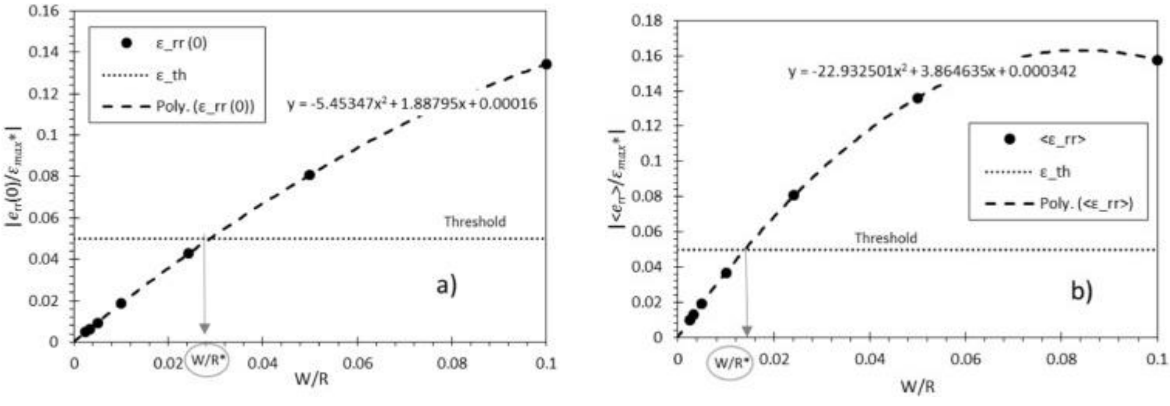

Figure 36 FIB induced effect on the stub top surface. Examples of minimum pillar diameter determination. a) Considering the value of the elastic hoop strain at the centre of the stub surface as most relevant quantity. b) Considering the average over the 90% of the reduced radius as most relevant quantity.

To perform reliable residual stress measurement using the FIB-DIC micro-ring-core technique, the error due to Ga ion damage during FIB milling must be controlled. This information provides a guide to the experimentalist during setup of the experiment. For example, from the point of view of the FIB-DIC procedure, the probe current and voltage are process parameters that influence the outcomes in terms of the induced ion damage. Although it is clear that reducing ion beam voltage and current lead to the reduction of ion damage effects, this also leads to slower material removal rates, making the experimental measurements more time consuming. Therefore, in practice an optimal compromise between these objectives needs to be found. The present results provide a firm quantitative basis for optimising the experimental conditions.

The half Gaussian function shape, imposed by means of eigenstrain, is reflected in both the hoop and radial stress components that assume similar general trends (Figure 35). As expected, the predominant FIB damage induced effect is present in the vicinity of the surface exposed to Ga Ions. If the FIB damage is localised primarily within the micro-pillar skin, a negligible effect is perceivable at the centre zone of the top surface of the micro-pillar. For values of W/R higher than ~0.005, the consequence of the induced effect becomes relevant, and then the entire micro-pillar is subjected to additional elastic residual strain.

The function shown in Figure 36(a) and (b) confirms the expected trend, in that smaller pillar diameters correspond to high values of the perceived strain at the top surface of the pillar. In order to make this effect negligible on the global FIB-DIC measure, it is necessary define a threshold of acceptability. This threshold defines the conditions when the micro ring-core method can be applied for the determination of residual stress ignoring the influence of FIB ion damage.

Figure 36(b) displays the variation of the average strain determined by DIC in the region of interest defined by the 90% radial extent of the micro-pillar surface. This perceived strain value is related directly to the experimental implementation of the FIB-DIC micro-ring-core procedure, and thus provides the most relevant and direct basis for setting the threshold for the FIB-induced straining effect. Once the FIB milling parameters are defined, then so are the parameters W and ε_{max}. This determines the intersection of the strain-induced curve with the chosen threshold, and thus provides the basis for determining the minimum acceptable pillar radius, R^* (Figure 36).

It is worth noting that the imposition of the same magnitude of threshold, for the two different approaches, leads to different pillar dimension evaluation. In fact, in Figure 36 it is possible to observe the greater value of the ratio W/R^* in the case when the induced radial strain at the pillar centre is considered (Figure 36(a)) compared to use of the strain averaged over the reduced area (Figure 36(b)). This means that the latter defines a greater minimum pillar size, and hence is more conservative.

Application to silicon material

Once the eigenstrain induced by Focused Ion Beam was quantified through the experimental procedure presented in this section, parametric analysis can be used to assess the impact on the residual strain measurement using FIC-DIC. This analysis is fully valid only if identical FIB process parameters were used both in the eigenstrain determination experiment, and in the FIB-DIC measurement.

The parameter that defines the maximum magnitude of eigenstrain was evaluated to be $\varepsilon_{max}=-4.1\cdot10^{-4}$. Hence, the analysis of the apparent strain on the stub surface is reported now as a function of the pillar radius alone (Figure 37).

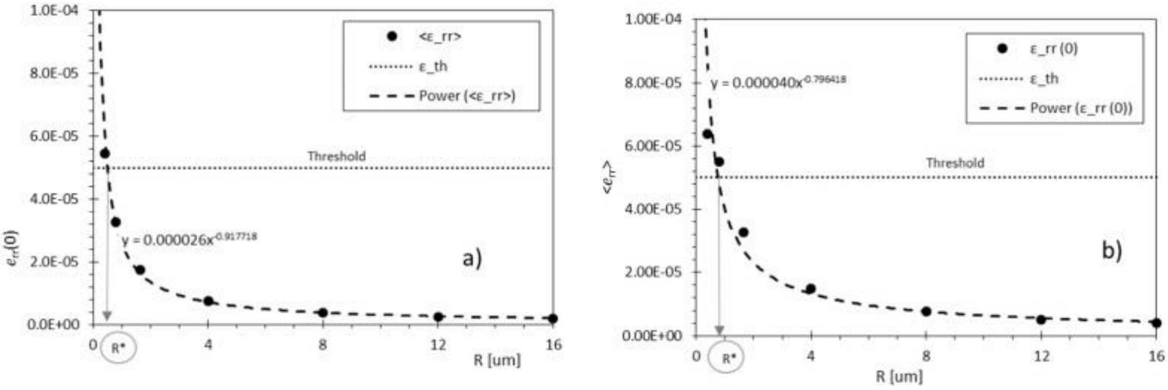

Figure 37 Minimum micro-pillar radius determination. a) Based on the apparent strain at the centre. b) Based on the average strain within the area of 90% radial extension upon at the micro-pillar top surface.

The choice of an appropriate threshold is crucial in this analysis. The fundamental idea is that the effect of ion damage must be negligible in terms of the magnitude of the apparent residual strain that is causes. Since this last one cannot be known a priori, we decided to compare this effect with the error due to DIC analysis. The in-house Digital Image Correlation software built for the purpose of residual strain evaluation can deliver the accuracy of strain relief determination the order 10^{-4} or better. Accordingly, we choose a threshold equal to half of the DIC accuracy, namely, 0.5×10^{-4}.

Assuming the depth of material affected by ion beam induced amorphisation to be known, the choice of admissible value of induced strain (threshold) and the knowledge of the maximum amplitude of induced eigenstrain allowed the determination of the lower limit for the micro-pillar radius. As shows in Figure 37, this evaluation led to the conclusion that the FIB damage effect becomes significant when micro-pillar radii become less than 1μm. Particularly, if only the centre of the top micro-pillar surface is considered to be representative of the entire strain field, the lower bound for the admissible micro-pillar radius turns out to be even smaller, namely ~0.5μm.

3.2.7. Conclusion

Precise evaluation of the consequence of FIB milling is important in the context of the ongoing quest for feature miniaturisation. The success of nanoscale sample preparation by ion beam machining is determined not only by the ability to create the desired geometric features, but also by the degree to which the material properties are preserved within the small volumes of interest. When the sought properties and structure are modified either partially or completely, the results obtained can be subject to aberration, or may become completely misleading, as for example as a consequence of ion beam-induced amorphisation of single crystals.

Residual stress is an important property of material state that is often difficult to determine at the micron scale, e.g. due to significant amount of plastic deformation [195] and [196]. One of the challenges to progressive miniaturisation of FIB-DIC ring-core measurement is the FIB-induced Ga ion damage that affects the strain measured at the surface.

Following, we carried out novel experiments in which the effect of ion beam damage was quantified (in terms of the maximum eigenstrain induced). Once the maximum magnitude of eigenstrain was found, and its depth extent and the residual stress evaluation error threshold were set, parametric analysis presented here was used as a tool for FIB-DIC experiment design: lower bounds on the micro-pillar diameters were set. One important aspect of the present model is its flexibility that allows it to be re-run for arbitrary depth of Ga ion damage depending on the substrate material, ion energy and flux, angle of incidence, etc., leading to different dependence of eigenstrain on the depth from the surface. The reported experimental procedure for the quantification of eigenstrain is an efficient way of characterising the residual stress field arising from the interaction between the ion beam and the target material.

The characterisation of the amorphous layer arising after Ga-ion exposure at low grazing angle was performed using XRR technique. The experimental evidence collected and interpreted in this work are of considerable relevance to the task of advancing the understanding of the characteristics of the damaged layer produced by Ga-ion irradiation. The superficial layer of modified density in Si subjected to normal incidence Ga-ion beam milling was studied using XRR and found to be ~23nm in thickness, in good agreement with previous measurements and observations reported in the literature. The layer of modified properties could be further sub-divided into two layers, separated by diffuse interfaces, with different densities. An evident proportional correlation between the density change and the eigenstrain distribution (simulated through MD) was found. This results indicates that the arising of eigenstrain cannot be imputed mainly to the volume transformation occurring in the amorphous layer. Rather, other material processes are of more relevant importance (e.g. nano voiding, defect population and elastic properties modifications).

Moreover, MD simulations at normal incident angle of the Ga-ion beam allowed the validation of these by comparison with the experimental evidence produced by Silicon cantilever bending. Satisfactory agreement was found in terms of curvature radius.

The present work also contains specific results for the lower bound pillar sizes in the case where the target material is silicon. To ensure aberration-free residual stress evaluation, the pillar radius should not be smaller than 1μm. A less conservative way of determining this value, considering only the value of strain induced at the centre of the pillar, leads to a minimum radius of ~0.5μm.

Although the experimental characterisation of the eigenstrain magnitude cannot be performed to a wider class of materials, given the limitations in obtaining stress-free cantilevers, the proposed assessment procedure may still be applied to other crystalline materials. In fact, the validated MD model may be employed for the simulation of eigenstrain in different materials and therefore allowing the evaluation of eigenstrain distribution and magnitude necessary for the simulation of the minimum pillar radius.

4. Residual Stress and Plasticity-Induced Crack Closure Contributions in Fatigue Crack Growth Rate Modification at the Occurrence of an Overload/Underload

4.1. Study of Overload Effect on Fatigue Crack Propagation Using EBSD, FIB-DIC and FEM Methods

4.1.1. Introduction

The first part of this section dedicated to the study of Overload/Underload focuses on the specific case of an aluminium alloy. A Compact Tension Specimen that was the subject of the present study was first cycled at a constant load amplitude and load ratio R=0.1 to induce crack nucleation and propagation. OL was then applied at a certain crack length. After this, the original constant amplitude cyclic loading was continued until the fatigue FCGR prior to the OL was recovered. The evolution of the crack at the surface of the specimen was monitored by microscopic imaging using in-situ loading in a SEM. The crack surfaces were also examined afterwards using the same SEM. The crack path, morphology, microstructure and residual stress around a crack propagated beyond an OL was examined. EBSD was used to map the region of interest around the crack to help in understanding the microstructural mechanisms involved in the crack retardation induced by the OL. By analysing the intragranular misorientation it was possible to obtain an indication of the plastic strain distribution in the vicinity of the crack flanks and near the tip. Experimental quantification of residual stress was performed at chosen salient locations using the FIB-DIC ring-core method. Experimental residual stress results were assessed and interpreted by means of comparison with FEM of near crack-tip plastic strain at the OL location and at the final crack tip. This comparison allowed the understanding of which characteristics of crack propagation can be captured using a fundamental model. Especially at this small scale where microstructural features may play their relevant role and therefore a more complex model would be required.

4.1.2. Material Description and Fatigue Test

The sample used to carry out this experiment was made from aluminium alloy AA6082 (BS specification HE30). A 35mm miniature Compact Tension (CT) sample was machined from a 3mm thick rolled plate. Figure 38(a) depicts the geometric shape, the characteristic dimensions and the direction of the applied load. In this experiment, a relatively sharp fillet radius was created at the notch tip (R<0.1mm) to facilitate pre-cracking. Fatigue testing was conducted using a servo-hydraulic machine, for the crack nucleation and first propagation segment, and in a compact *in situ* tensile testing stage was used in an SEM for the overload application and further propagation. The loading history is schematically described in Figure 38(b).

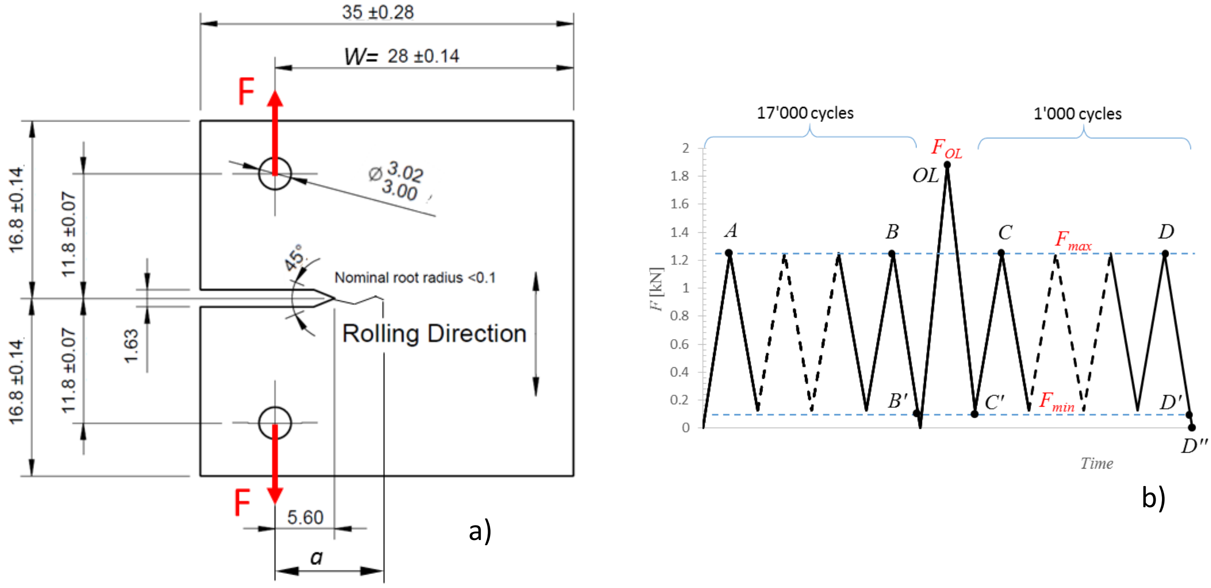

Figure 38 a) Sample geometry (all dimensions are given in mm). b) The loading history.

For the first step, from the point A to B’ (Figure 38(b)) the applied force range was $\Delta F=1.125kN$, the maximum cyclic load $F_{max}=1.25kN$ and the minimum $F_{min}=0.125kN$. After 17000 cycles the crack had propagated to a total length, a, of 7mm. Cyclic loading was then interrupted and several SEM images were taken along the entire crack extension. At this stage (Point OL in Figure 38(b)), the specimen was subjected to a single 50% overload of magnitude $F_{OL}=1.875kN$ $(1.5 \cdot F_{max})$. The same constant amplitude test used previously was then conducted for a further 1000 cycles. At the end of the fatigue test the crack had grown a further 0.4mm in length (point D’ in Figure 38(b)). The crack was imaged at various locations, with particular attention to the extent of crack associated with its growth past the point of overload application. This procedure allowed comparison to be made with the previous crack morphology prior to overload application.

The Stress Intensity Factor (SIF) can be evaluated for any crack length using the formula [197]:

$$K_I = \frac{F}{b}\sqrt{\frac{\pi}{W}}\left[16.7\left(\frac{a}{W}\right)^{\frac{1}{2}} - 104.7\left(\frac{a}{W}\right)^{\frac{3}{2}} + 369.9\left(\frac{a}{W}\right)^{\frac{5}{2}} - 573.8\left(\frac{a}{W}\right)^{\frac{7}{2}} + 360.5\left(\frac{a}{W}\right)^{\frac{9}{2}}\right] \tag{52}$$

Here a is the crack length from the point of load application, W is the total ligament width, and b denotes the specimen thickness. These dimensions are illustrated in Figure 38.At the first application of cyclic loading before crack propagation, the SIF range applied to the sample was $\Delta K_A=11.87\ MPa\ \sqrt{m}$. As the crack extended, the SIF increased and reached the value of $\Delta K_B=19.45\ MPa\ \sqrt{m}$ at point B. The overload applied at that crack depth corresponded to the magnitude of SIF equal to $K_{OL}=32.42\ MPa\ \sqrt{m}$. According to Irwin’s formulation [198] for the plastic zone determination, such plastic zone turned out to be of 0.94mm. The test was continued and ultimately arrested at point D where the final SIF range was $\Delta K_D=20.23\ MPa\ \sqrt{m}$.

Crack growth behaviour

The fatigue crack growth rate (FCGR) is summarised in the Paris diagram shown in Figure 39.

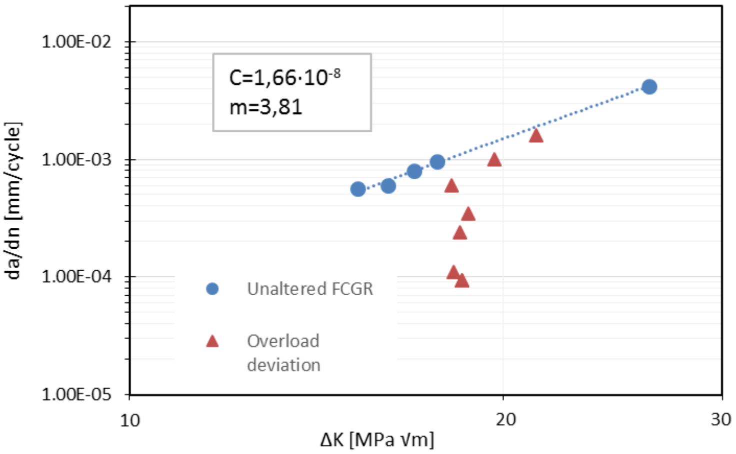

Figure 39 Fatigue Crack Growth curve

As expected, right after the overload application the crack propagation was retarded; da/dn drops immediately by an order of magnitude, and only gradually returns to the steady state behaviour. Assuming that at the last point of measurement of crack length, the crack had reached the unaltered material zone, the FCGR curve can be described analytically according to Paris’ Law (18) with the coefficients C and m reported in Figure 39.

4.1.3. SEM and EBSD analysis

SEM imaging analysis

The application of an overload causes retardation of crack propagation that constitutes a considerable improvement in fatigue resistance of the mechanical component examined. In the present study we are focusing exclusively on the study of the mechanisms that operate during and following the OL, without considering the effective retardation of the crack propagation in terms of the number of cycles.

SEM imaging of the crack flanks prior (B in Figure 38(b)) and after the application of the overload (D' in Figure 38(b)) has allowed the visualization of the crack shape and its evolution. The crack propagated through the material in the direction perpendicular to the predominant cyclic tensile stress. The crack image taken at point B in the propagation history is shown in Figure 40(a). To collect this image, the sample was loaded to $F_{max}=1.25kN$ and the surface imaged in the unpolished state. At this stage the crack flanks appear rough. Significant out-of-plane plastic deformation at crack flanks is not apparent. In contrast, the image of the crack taken at point D' in its propagation history (Figure 40(b)) shows the crack flanks being in contact over the entire length of crack between points B and D'. In the region of contact, some evidence of local out-of-plane plastic deformation can be found. Such deformation is the consequence of intense local compression that induced material flow and extrusion in the direction of least constraint (out-of-plane). These considerations suggest that crack propagation beyond the OL was accompanied by crack closure.

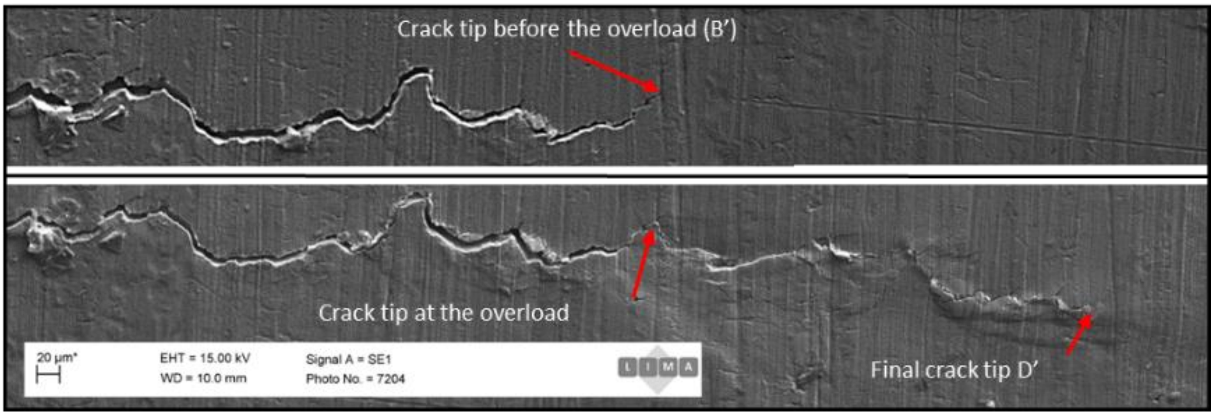

Figure 40 SEM images of the crack obtained from an unpolished surface a) before the overload application, at $F_{max}=1.25kN$ (B), and b) after the application of the overload, at $F_{min}=0.125kN$ (D').

Focusing now on the crack tip at the time of overload application, the following observations and comments can be made. In Figure 41 the crack tip is shown at several points during the overload cycle (before OL at maximum force, and after OL at minimum force). The crack tip at B' is illustrated in Figure 41(a). The OL ultimately led to additional crack extension of around 10µm, as seen from the comparison with Figure 41(b). Following the OL, the crack propagation in this direction was halted, and fracture continued to grow in a direction different from the previous growth direction at the tip. Moreover, crack growth in Mode I appears to have been arrested. There is also evidence of significant crack tip blunting. The crack remained stationary until a new nucleation direction was established (Figure 41(d)). It is worth noting that this new propagation direction lies at approximately 90° to the original crack growth direction, and possesses significant Mode II character. The same crack deviation right after OL was experienced by several authors [199-201]. The crack therefore prefers to propagate around the plastic zone instead of advancing along its original path direction.

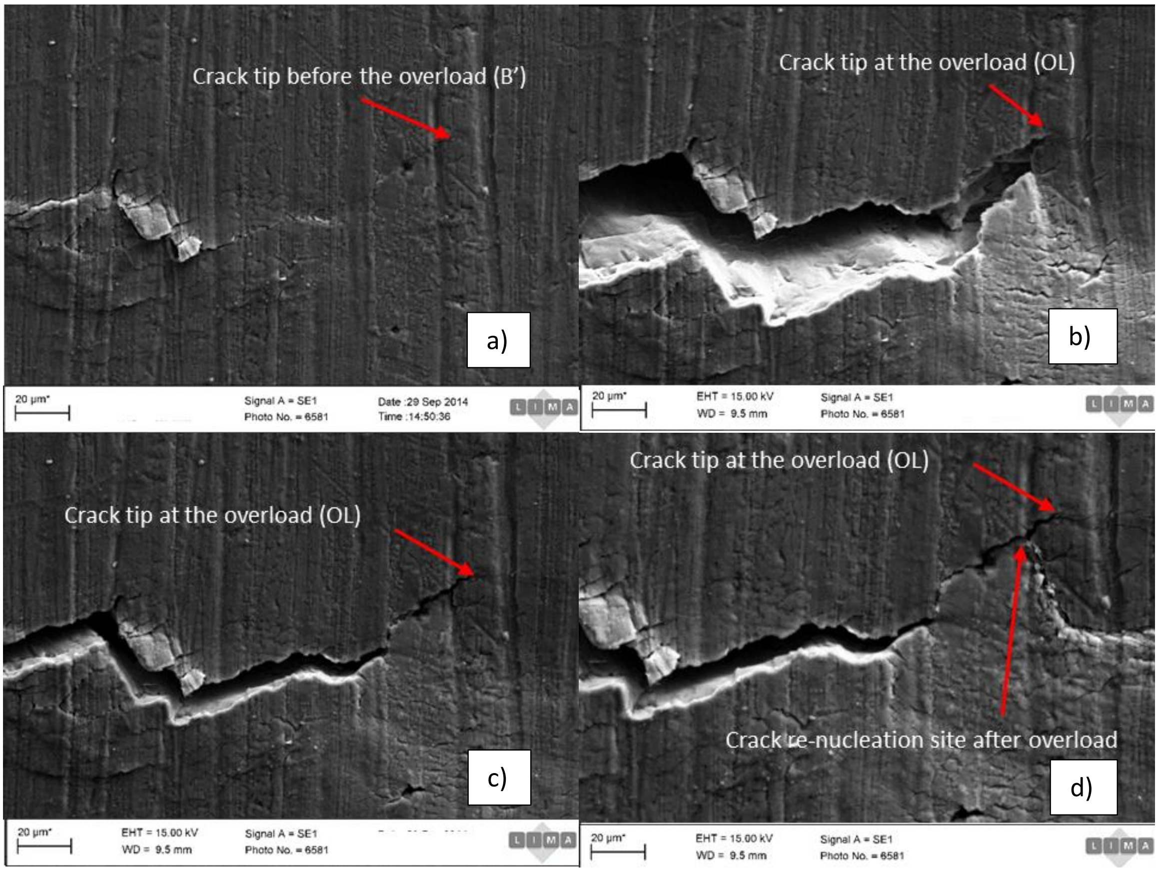

Figure 41 SEM images of the crack tip obtained from the unpolished surface at various instants in the crack growth history: a) before OL at F_{min}=0.125kN (B'), b) at OL, at F_{OL}=1.875kN (OL), c) after OL, at F_{min}=0.125kN (C'), and d) after OL at F_{min}=0.125kN (D').

EBSD analysis

EBSD technique was adopted for the purpose of mapping the grain morphology and orientation around the crack. Crystal lattice orientation varies both between and within grains (intragranular misorientation). The latter in particular is closely associated with plastic deformation and strain gradients induced by dislocation glide. Note that whilst statistically stored dislocations (SSD) accommodate uniform plastic strain causing significant lattice distortion by little rotation, geometrically necessary dislocations (GND) that accommodate steep changes in plastic strain (such as observed at crack tips) lead to large lattice rotation and hence misorientation [63, 202]. Therefore, capturing misorientation variation is of interest for the purpose of characterising intragranular deformation gradients, e.g. from features such as slip bands or dislocation pile-ups in the vicinity of grain boundaries. EBSD analysis requires a well-polished sample surface. To obtain extremely smooth, good quality surface the sample was reduced in size to contain only the region of interest and ground with abrasive cloths up to 1200 grade. Then, smooth cloth polishing with 3µm and 1µm diamond suspension was adopted. The final polishing step used 0.1 µm colloidal silica, with subsequent addition of hydrogen peroxide to reduce potential deposits.

The sample was mapped using an electron beam at 25kV energy and 18.5nA current. Two main acquisition steps were performed. The first was an overview of the crack that comprises the location that the crack passed before the application of the overload; the pixel size in this last case was 3.2µm. The second mapping stage focused on imaging the region of overload application and subsequent propagation with the pixel size of 0.76µm.The grain shape and boundaries can be visualized in detail by means of EBSD analysis. Since considerable amount of material was removed during surface preparation, the crack morphology appears slightly different in Figure 42 and Figure 44 from that previously seen in Figure 40 and Figure 41.

The EBSD map in Figure 42 shows that morphologically the grains have a somewhat elongated shape in the rolling direction, and the grain size varies between 20-250µm. In Figure 43 the pole figure is reported for the three main phases used for Kikuchi pattern indexing, accounting for over 95% of the indexed points. These three phases were: Al (51.4%), $Al_{0.3}$ $Cu_{7.01}$ $Fe_{1.7}$ $Mg_{0.2}$ (15.9%) and Al Mn_3 (27.7%). The pole figures reveal the preferred orientation of the crystals that is close to the <001>

direction being aligned with the rolling direction defined in Figure 38. This orientation preference was confirmed for all three phases. The analysis of the crack propagation manner within the microstructure has highlighted a predominant transgranular mode (i.e. cutting grains). Quantitatively, transgranular propagation occurs for ~60% of the grain involved in the crack propagation and, in the remaining ~40%, the propagation is intergranular mode.

Except for few grains on left side of Figure 42 where the propagation manner is unclear, the crack propagated mainly in a transgranular mode.

The coarse mapping of the cracked surface, overlaid on the band contrast map, (Figure 42) shows the crystal orientation of the grains surrounding the crack. As expected, orientation indexation presented a challenge at the crack line and in other regions where large plastic deformation occurred. The position of the large deformation caused by the overload is represented by the yellow circle shown in the Figure 42. At this position it was not possible to obtain grain orientation form Kikuchi pattern analysis, due to the large plastic strain causing severe distortion of the crystal lattice leading to the degradation in the pattern quality.

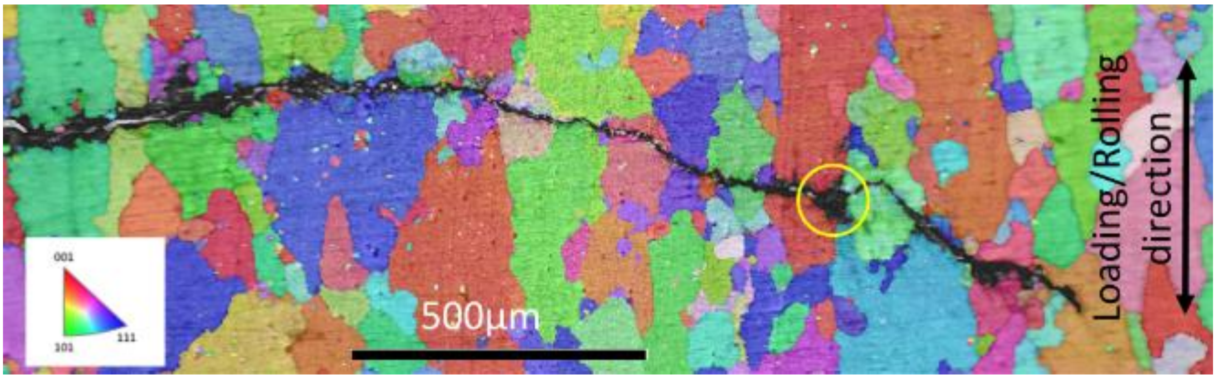

Figure 42 A superposition map of grain orientation (colour derived from the inverse pole figure for the Rolling Direction shown in the inset) on the grey scale Kikuchi band contrast map for the crack over the length of 1.75mm on the polished surface of sample cross-section. The location of OL application is indicated by the yellow circle.

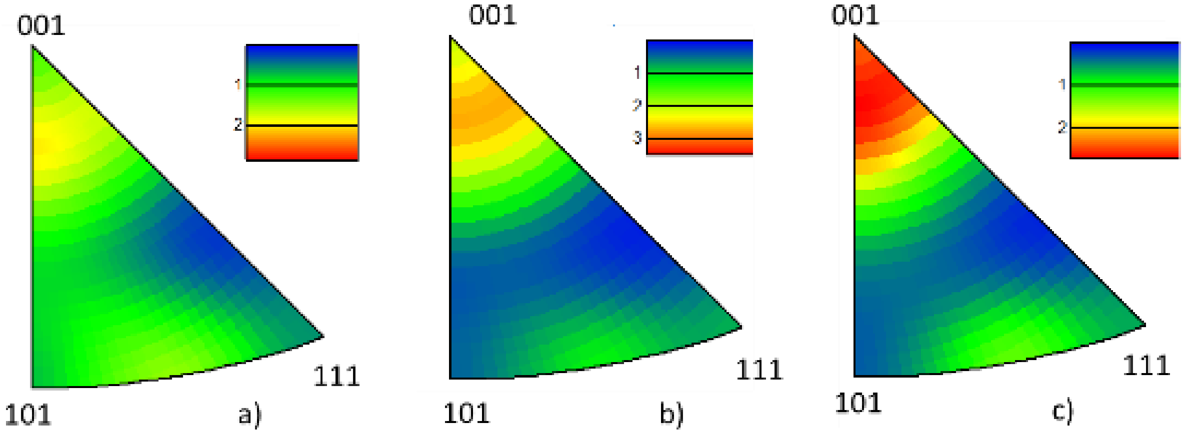

Figure 43 Inverse Pole Figures (with respect to the rolling direction) obtained for the three principal phases within the material. The colour bar is given in terms of the multiple of uniform density (m.u.d.) a) Al. b) Al Mn_3 C. c) $Al_{0.3}Cu_{7.01}Fe_{1.7}Mg_{0.2}$

A more detailed analysis of the grain orientation is shown in Figure 44(a). The purpose of this map is the collection of the EBSD information focusing more closely on the region of crack propagation after the overload. The high-resolution mapping mode (pixel size 0.76 μm) allowed the visualization not only of the grain orientation, but also the relative changes in orientation within a single grain, i.e. intragranular lattice misorientation [203]. Regarding the crack closure effect after the overload, the EBSD map provides the following insight. At the crack flanks the local orientation is highly affected by their contact. These changes in the local orientation are due to the plastic deformation in the direction perpendicular to the crack surface. This provides additional supporting evidence of the crack closure effect present during the propagation phase derived from EBSD analysis.

The misorientation observed within grains provides indirect information about the strain distribution within the material. The interpretation of misorientation using the grain-based approach [204] allowed the graphic representation of the regions affected by high strain. The result is shown in Figure 44(b) that shows the map acquired at zero load and is related to residual plastic strain. The map is qualitative, so that no colour bar is provided, but the conventional "reduced rainbow" colour scheme is used, with blue corresponding to low and red to high values. The regions of high residual plastic strain are located in the vicinity of the crack line, as expected. The residual strain that arises along the crack flank is associated with the process zone at the crack tip during propagation. Another potential cause may be the plastic deformation due to crack surface contact as described previously. The region associated with the OL is indicated by the letter "A" in Figure 44. No evident alteration was experienced in this area. Especially at the very vicinity of the crack flank, where the lattice distortion is particularly high and, as a consequence, indexation of the backscattered pattern was not possible, and the orientation map could not be acquired for the totality of the scanned pixels. However, the lack of indexing is itself an indication of the plastic deformation occurred. For this reason, we can consider the region near the OL location one of the most stressed regions.

In any case, according to the plastic region extension evaluated through Irwin's formulation (0.94mm), the entire region mapped by EBSD lies in the plastic zone. This may justify the graphical absence of the expected high plastic deformation surrounding the OL site. Furthermore, since such technique is mainly able to capture plastic deformation change within grains [205], we cannot rely on the comparison between the plastically deformed regions at different grains.

The presence of the region of high residual plastic strain expected at the crack tip is confirmed (indicated by the letter "B" in Figure 44).

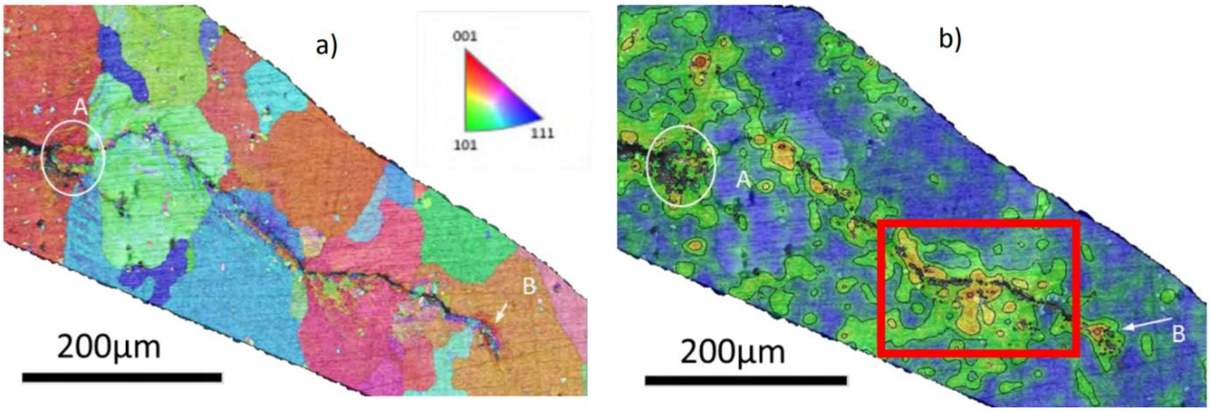

Figure 44 a) Orientation map obtained from the polished surface of sample cross-section around the crack grown beyond the overload application. The overload site is indicated by the letters OL, and the final crack tip by the letter D''. b) Contour map of deformation intensity, as derived from EBSD misorientation evaluation.

4.1.4. Residual stress measurement and numerical interpretation

FIB-DIC ring-core measurements

Analysis conducted using EBSD mapping highlights the regions where significant plastic deformation occurred. For instance, at the OL site, the lack of indexation of the Kikuchi patterns indicated that localised large plastic deformation occurred. Nevertheless, since the entire map lies on the OL plastic zone, no evident differences in plastic deformation can be observed along the crack path except some very localised areas. In order to provide quantitative information about residual stresses, FIB-DIC ring-core measurements were conducted at carefully selected locations. It is worth noting that all measurements conducted corresponded to the last stage of crack propagation, i.e. point D'' indicated in Figure 38(b). The locations of interest (sites) where we focused our effort are reported below and graphically represented in Figure 45

I) Several locations along the crack path at 15-30 μm from either the crack flank (dotted in Figure 45)

II) A line of measurements aligned perpendicular to the crack line 20 μm behind the OL site

III) A line of measurements aligned perpendicular to the crack line at the OL site

IV) A line of measurements perpendicular to the crack at the final crack tip

V) A line of measurements along the crack continuation ahead of the crack tip

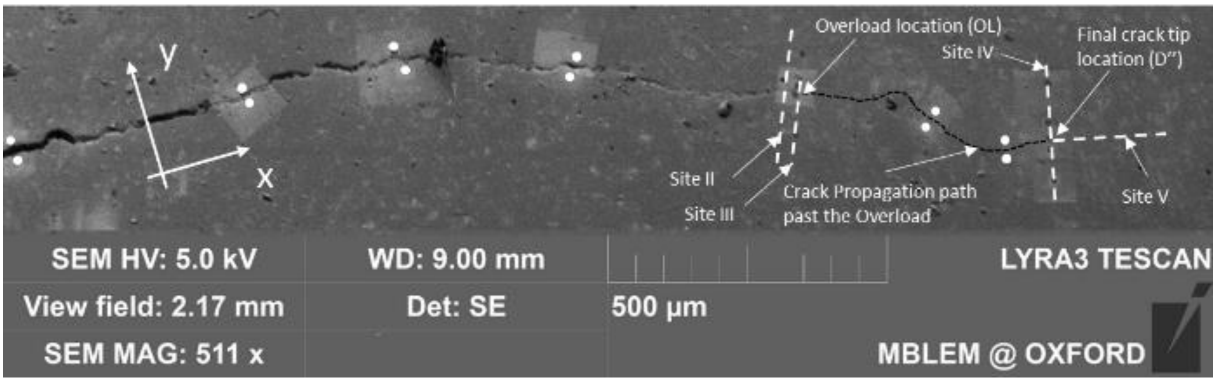

Figure 45 FIB-DIC milling positions across the crack path. The dashed white lines indicate the spatially resolved line measurements while the white dots denote the single point measurements.

Since the FIB-DIC method relies on the DIC analysis for the quantification of strain relief, the pillar top surface needs to show reasonable contrast so that the displacements can be evaluated accurately.

Since the polished surface does not possess such inherent contrast, the sample surface was coated with an extremely thin (~5nm) soft layer of sputtered Au-Pd. Such coating layer provided a randomly distributed texture onto the surface ideal for DIC analysis, and at the same time does not introduce any additional stress to modify the pre-existing conditions.

At each measuring point, the incremental procedure of material removal was followed that produced a sequence of n=50 images. An illustration of the milling process as the material is being removed and the images acquired is depicted in the Figure 46:

These images were analysed using DIC software [30] and a data refinement procedure was adopted for the detection and rejection of outliers. As a result, strain relief curves were obtained for two orthogonal directions associated with the crack growth direction that were labelled x and y as defined in Figure 46.

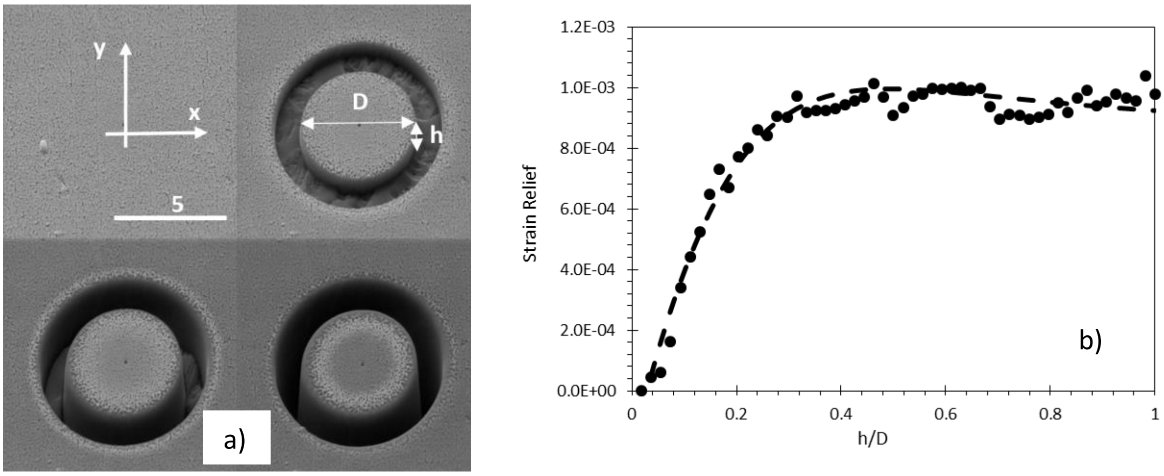

Figure 46 a) Illustration of the progress of the milling procedure (measurements in μm) b) Strain relief curve fitting example. D is the pillar diameter and h is the trench depth.

The experimentally determined strain evolution can be described by the parametric function developed on the basis of Finite Element Analysis (FEA). At the end of the fitting procedure, the residual strain and its standard deviation were evaluated at 95% confidence.

As the last step, the residual stress was evaluated using Hooke's law under the assumption of plane stress state:

$$\sigma_{xx} = \frac{E}{(1-\nu^2)}\left[\varepsilon_{xx} + \nu\,\varepsilon_{yy}\right] \tag{53}$$

$$\sigma_{yy} = \frac{E}{(1 - \nu^2)}\left[\varepsilon_{yy} + \nu\,\varepsilon_{xx}\right] \tag{54}$$

The evaluation of residual stress at this small scale introduces a further source of error due the material elastic anisotropy within the single grain. Since the examined material shows large structured grains, there is a high probability that the milling point lies within a single grain and therefore, the elastic anisotropy may affect the evaluated value of stress. As reported in the previous chapter (Chapter 3.1), a statistical approach to quantifying this if the local grain orientation is unknown. Accordingly, the error at 95% of confidence for aluminium alloy amounts to 8%. This was taken into account alongside other sources of error (i.e. DIC peak tracking and relief strain fitting procedure), and the overall uncertainty reported as error bands in the resulting plots.

Residual stress modelling

Since the purpose of the simulation was to make comparison with experimental measurements using FIB-DIC ring-core milling at sample surface, a two-dimensional plane stress modelling was employed. The software used for FEM simulation was Abaqus©. In the simulation described below the material was assumed to follow the isotropic hardening rule having hardening exponent n=0.05 and strength coefficient K=540MPa. Taking advantage of the specimen symmetry, half model was generated and meshed as shown in Figure 47. Mesh refinement was introduced at the locations corresponding to the locations of FIB-DIC line measurements. In order to achieve accurate simulation results, a convergence analysis was performed; the optimal mesh element size at the region of interest turned out to be of 2μm. The displacement boundary condition due to symmetry was applied at the nodes where no material separation was present. Crack advance was simulated by progressive removal of boundary conditions requiring the nodes to remain bonded. Crack flank interpenetration at locations where plasticity crack closure took place during the unloading phase was avoided using a fictitious contact surface opposing the crack flank. The inequality describing the contact condition was unilateral so that the crack was free to open. As described in a previous publication [206], this technique has been shown to be successful at simulating residual stress evolution at the crack tip. The model was progressively run at three different stages of crack propagation in order to attempt capturing the stress field evolution. The first stage considered a crack length of 35 μm shorter than the one at the OL, the second at the OL and the third at the last at the stage indicated as D’’ in Figure 38(b).

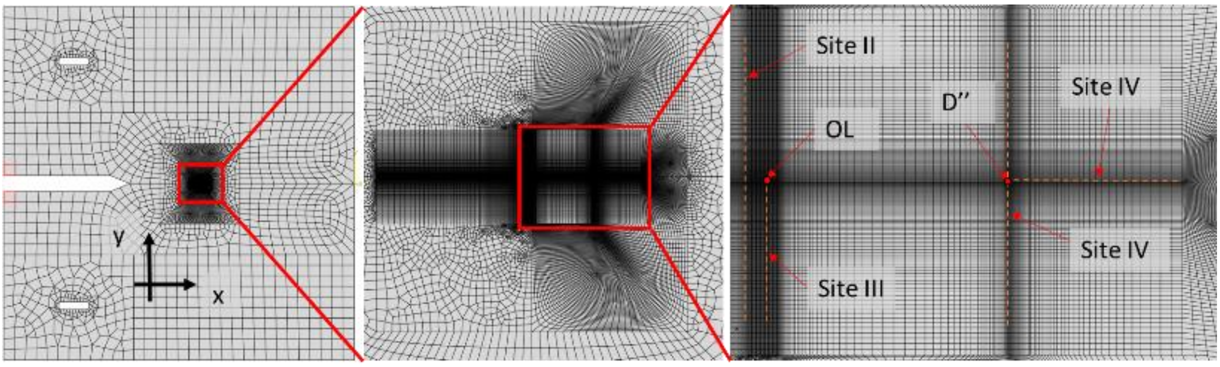

Figure 47 Discretised 2D model, mesh refinement details at regions of interest

Results and discussion

In this section, residual stress predictions provided by FE modelling are compared with the evaluation by means of FIB-DIC ring-core milling. Within the model, residual stress quantification was performed for the situation when the crack has propagated past the locations on the crack flanks depicted by the dots in Figure 46. We begin the discussion with the analysis of experimental results for stresses along the crack that are shown in Figure 48. It shows the variation of the measured residual stress values along the crack line (markers and error bars). Continuous curves through the markers are given as a guide to the eye. The overload location corresponds to $x = 0$. It is apparent from the plot that behind the overload ($x < 0$), a slight compressive residual stress layer is present. Both stress components manifest a similar magnitude that lies in the range between -150MPa and -50MPa.

Leaving aside the overload location that will be examined in detail later, we note another region of moderate compressive residual stress found along the crack flanks at locations corresponding to crack growth past the overload. Particularly, at 0.48mm forward from the overload site, a more compressive value of residual stress was measured in the crack opening direction (*yy* component). It is worth noting that this location corresponds to the region of high plastic deformation highlighted by EBSD mapping and indicated by the square in Figure 44(b).

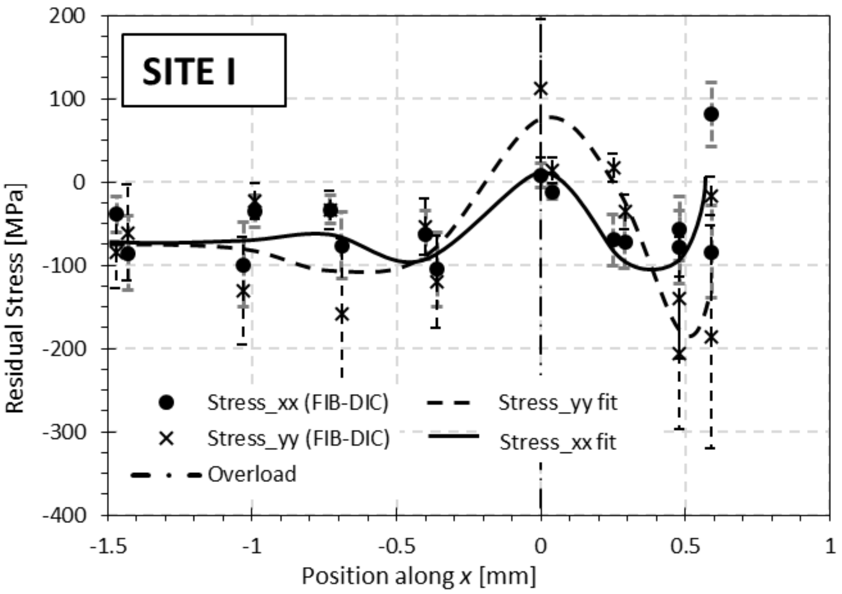

Figure 48 Residual stress obtained by FIB-DIC along the crack flanks extension (Site I).

The sites II, III, IV and V were numerically modelled; some contour images are reported below in *Figure 49*.

We report direct comparison between numerical and experimental results for selected lines indicated in Figure 47. Line plots of stress components *xx* and *yy* are given in Figure 50.

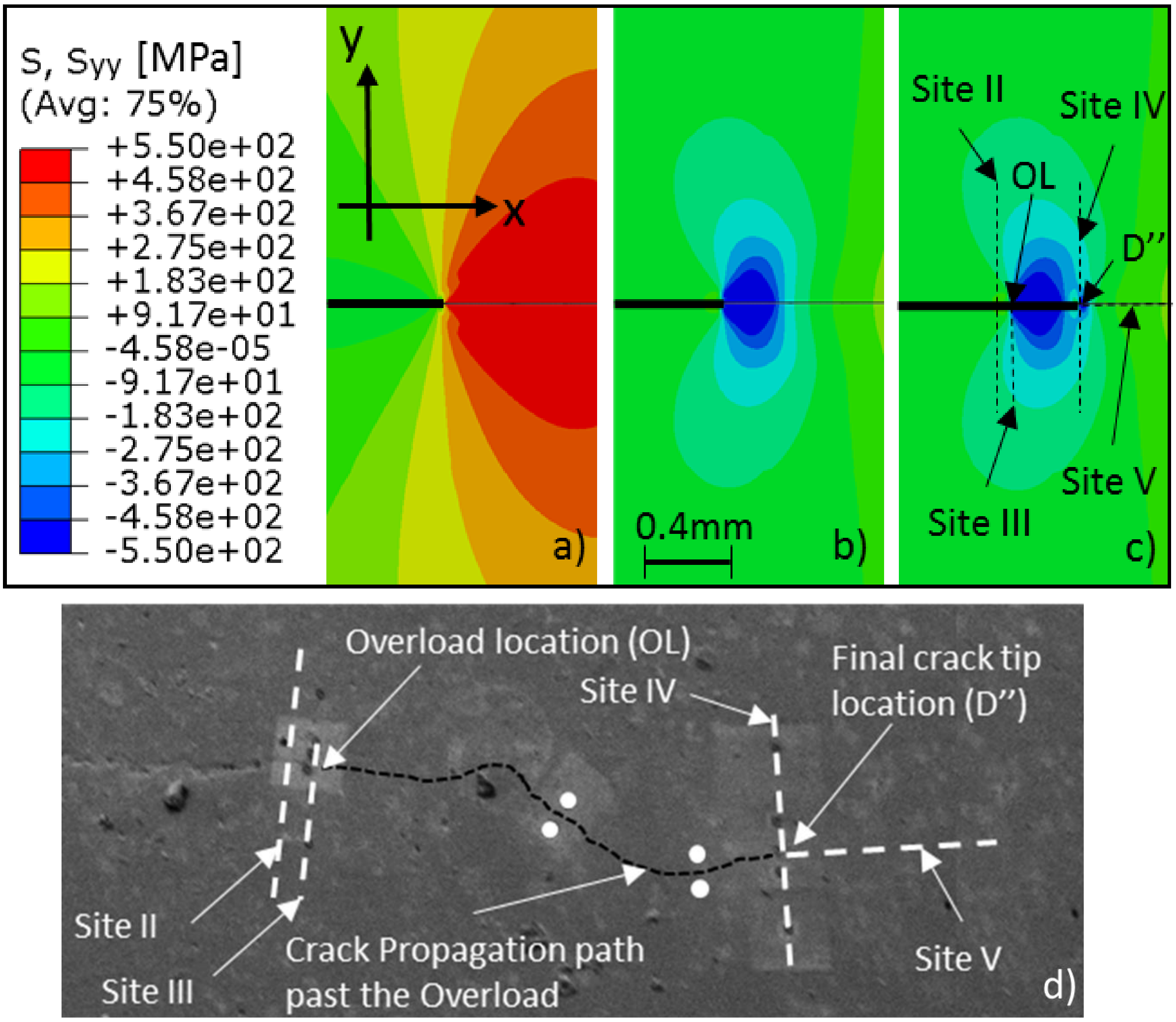

Figure 49. Stress yy component contour plots. a) At the overload (OL). b) At B'' and c) At D''. The solid line indicates the formed crack. d) Magnified region of interest from Figure 45.

Focusing our attention on the region close to the overload location (Figure 50(a),(b),(c),(d)), the compressive residual stress field induced by this single anomalous load application is evident. Compressive stress values that reach -450MPa were measured. At Site II (Figure 50(a-b)) the *xx* stress component is well matched in magnitude. The trend of the *yy* stress component shows good agreement. However, the same quality of agreement was not found for the model predictions and measurements near the overload location (Site III). Although the trend is correct, not all measurement points are matched well.

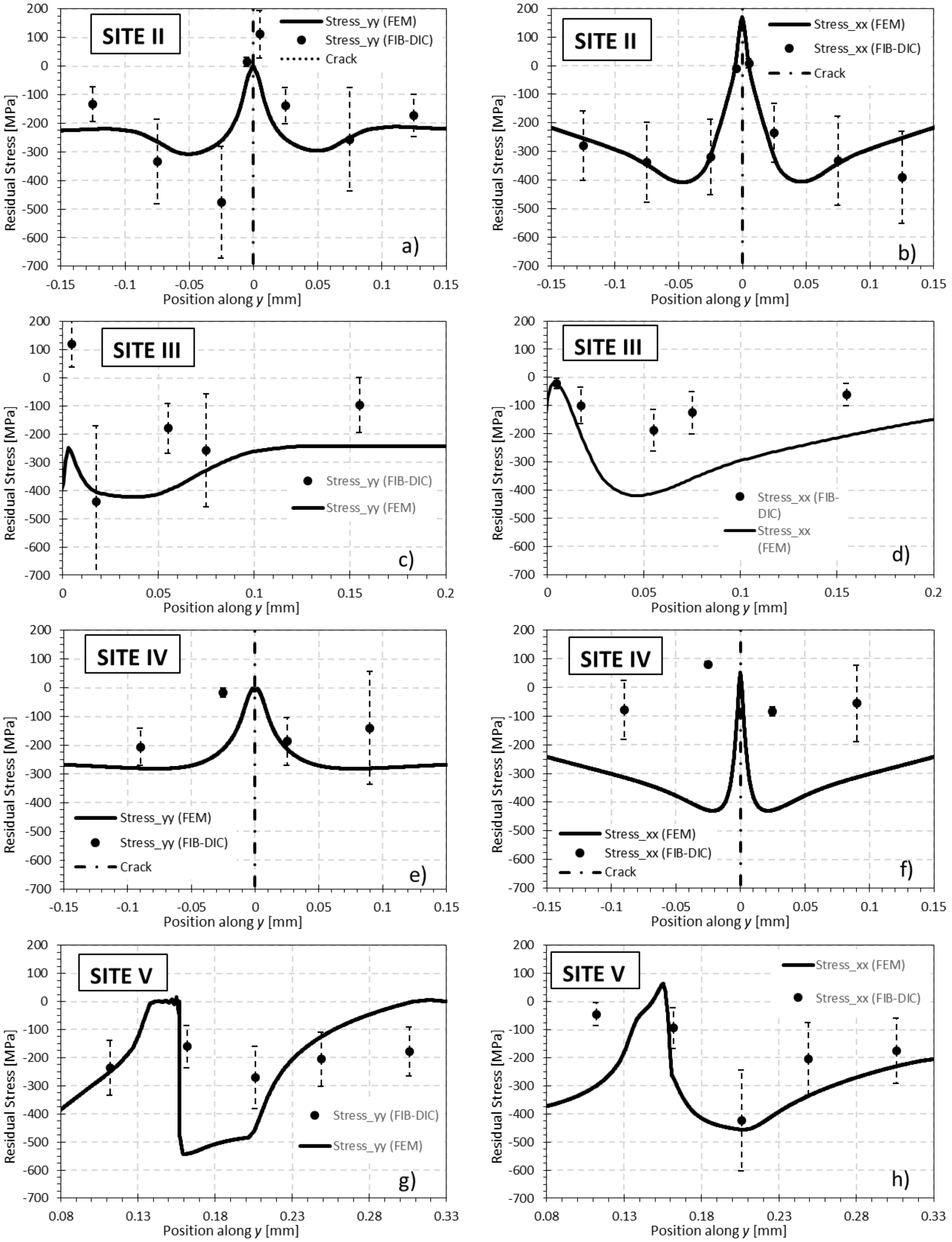

Figure 50 Residual stress comparison. FIB-DIC vs. FE simulation at the propagation stage D''. a) σ_{xx} Site II, b) σ_{xx} Site II, c) σ_{yy} Site III, d) σ_{xx} Site III, e) σ_{yy} Site IV, f) σ_{xx} Site IV, g) σ_{yy} Site V, h) σ_{xx} Site

Further measurements were performed at the final crack tip Sites IV and V. In Figure 50(e-f), correct trend is seen between model values and FIB-DIC ring-core measurement points, but the magnitude varies. Finally, for the line extended beyond the crack tip reported in Figure 50(g-h), good match was observed for both *xx* and *yy* components of stress, in that similar trends and satisfactory magnitude agreement were achieved. Particularly, the residual stress shown in Figure 50(h) can be compared to the outcomes of [207]. In fact, in this work the authors attempted the measurement of residual stress at the crack tip, by means of indentation technique. At the near crack tip, the residual stress trend turned out to be very close to that reported in the present section. Likewise the FIB-DIC method, indentation provides information about the residual stress state at the free surface. Since also the gauge volume is in the same order of magnitude, qualitatively, the two results can be compared. Other techniques have been successfully adopted for stress measurement at the crack tip [128-130, 208], but in those cases, an average value was evaluated along the entire sample thickness using Synchrotron-based Powder Diffraction (SPD). Even though the gauge volume was considerably different from the one used in the present section, the compressive residual stress region that we experienced was also found by measurement using SPD.

At this point it is worth noting that a range of various simplifications were adopted in the numerical model. For example, the discretisation of crack propagation steps may need refining in order to accurately reproduce the amount of residual stress left at the crack wake as the crack itself propagates. Also, although elastic anisotropy of single crystal aluminium is relatively low and can be considered negligible, plastic anisotropy induced by crystal slip may cause large variation in the effective yield stress according to the Schmid factor for slip. Furthermore, whilst in the overload region deformation is dominated by the single load application and unloading, elsewhere along the crack flanks the material experiences cyclic deformation that corresponds to a different hardening behaviour. Accurate description of the Bauschinger effect is likely to improve the accuracy of modelling. These considerations provide a means of understanding the discrepancy, and also give justification for further, more detailed analysis using crystal plasticity modelling.

Furthermore, the model used in the present analysis does not take into account the real crack path meandering that is significant at the fine scale. Small crack path deviation from the idealised straight line changes local stress conditions and in turn changes the resultant residual stress field. For instance, the map depicted in Figure 44(b) shows a localised area (indicated by the square in red) where intense plastic deformation is present. This corresponds to a steep change in the crack propagation direction.

It is important to note that experimental residual stress measurements were performed at the micron scale. As a consequence, intragranular stress values were obtained in most cases. In contrast, FEM simulation did not take into account the microstructure and stress variation within and between grains. Also, an additional simplification is made assuming that the problem is two-dimensional while in reality the three-dimensionality effect might have its contribution. Finally, it is also well known that the difference in deformation response between phases and their interaction has profound effect on the local residual stress evolution [208-210].

It is important to consider that all present outcomes are based on experiments performed using a single sample. Therefore, a variability of the results may be observed if exactly the same experiments are reproduced using a similar sample. This is due the quasi-random distribution of the material grain size, shape and orientation which may have a remarkable impact on local crack path shape and crack propagation rate.

4.1.5. Conclusion

The mechanisms involved in crack growth retardation after overload have been the subject of intense study for many decades. The principal aspects of the problem usually brought into consideration are plastic deformation, residual stress, and material property modification (hardening and damage). Identifying and separating the influence of each effect on the overall propagation rate is important for constructing reliable predictive models for the resulting deviation from steady state crack growth rate prescribed by the Paris law. In this study we focused our attention on two aspects of the problem, namely, plastic deformation (and in particular its consequence in terms of lattice distortion, that can be assessed using Electron BackScatter Diffraction), and residual stress that can be evaluated at the appropriate length scale using Focused Ion Beam and Digital Image Correlation (FIB-DIC) analysis. Plastic strain evaluation by EBSD revealed that areas of high deformation (lattice distortion) were found both along the crack flanks and at the overload site. Residual stress state around the crack is complex and arises due to the combination of the steady state plastically deformed layer developed along at the crack flank during fatigue crack propagation over many cycles, and also due to the much larger single overload plastic zone and the associated change in the crack flank profile that leads to crack closure. High misorientation and plastic deformation (and hence residual stress) were in evidence in the area of overload (OL).

Of particular interest is the clear evidence that the overload caused complete arrest of the major crack and led to the nucleation of a new, deflected crack. By all appearances, this important phenomenon occurred immediately during and following the overload. If this scenario is to be accepted, then the apparent crack retardation occurs due to the combined influence of the crack driving force reduction due to deflection, and the effect of residual compressive stress caused by the formation of the large plastic zone ahead of the crack tip.

In order to substantiate further the arguments given above, FIB-DIC micro-ring-core method was employed to quantify the magnitude of micron-scale residual stresses found at locations of interest around the crack. The results were critically compared with the predictions of FE simulations for a homogenous, isotropic, simple hardening material model. The purpose of this comparison was to identify which aspects of the complex crack growth process could be captured correctly based on this fundamental model, and which require more refined simulation. The results open the avenues towards better understanding of the stress field generated by the overload and crack propagation. It can be noted that in general the expected trends were seen in almost the entire set of measurements, although for some locations the agreement was not found in terms of stress magnitudes. This mismatch may be imputed to several aspects not captured correctly in the numerical model, such as the influence of local cyclic hardening on the stress-strain curve, crack profile change due to local crack kinking, and local material anisotropy and inhomogeneity that were not included in the simulation. A more detailed model ought to be constructed that would take into account these aspects to describe faithfully the residual stress field.

4.2. Residual Stress and Crack Closure in Fatigue Crack Growth Retardation Due to Overload

4.2.1. Introduction

Crack closure and residual stress can be considered as the primary causes of FCGR retardation phenomenon. The purpose of the present section is to seek to separate the influence of these two mechanisms. This is first done experimentally, by creating test conditions when the former mechanism (crack closure) is switched off, and only the latter (residual stress) is operative at the crack tip. Secondly, based on the test results and theoretical consideration, the analysis of FCGR around the overload phenomenon is carried out in order to elaborate a quantitative description for the contribution made by each mechanism to the retardation effect.

In order to isolate the contribution of residual stress in crack retardation, a comparative study was carried out of fatigue crack growth rate change following an overload between a high loading ratio (R=0.7) and the commonly used low loading ratio (R=0.1) regimes. Therefore these two loading configuration were used in the present experiments.

The experimental tests were conducted using Compact Tension (CT) specimens of AZ31b magnesium alloy that had been subjected to severe plastic deformation by Constrained Groove Pressing (CGP) to obtain fine-grained microstructure with the typical grain size of the order of 1-2µm. The crack length and the appearance of possible secondary crack branches were monitored via optical imaging using a long-range telescope and digital camera, with the effective pixel size of the order ~0.5µm.

In the high loading ratio fatigue crack growth experiment the effect of plasticity-induced crack closure is inhibited [211], or may be entirely nullified. To confirm that this is the case, *in situ* digital image correlation (DIC) evaluation of crack opening was performed, and direct evidence of the lack of crack closure was obtained. Further corroborating evidence was sought by analysing the fracture surface using Scanning Electron Microscopy (SEM) as well as regarding the loading case (R=0.1). On the other hand, the crack retardation effect observed at R=0.1 is due to the combination of residual stress and crack closure and here again this is confirmed by DIC and fractography.

Furthermore, the quantification of the strain distribution ahead of the crack tip during the overload application was conducted by means of Synchrotron X-ray Powder Diffraction (SXRPD) for the loading ratio of R=0.7. Experimental measurements were then used to validate further an elasto-plastic 3D FEM model used also for the study of the crack acceleration induced by an Underload (Chapter 4.4). The numerical model was used to perform the evaluation of the strain state arising as a consequence of OL for the case of R=0.1. Using this model, the juxtaposition between the two considered load ratios was then assessed.

Comparing the FCGR obtained in the two loading ratio cases (R=0.7 and R=0.1), it was possible to carry out careful analysis of the difference in the crack retardation effect as the crack extends. Firstly, a modification of Walker's model [212] allowed the attribution of the unique equivalent SIF range to describe FCGR behaviour for any positive loading ratio. This approach opened the way to presenting the experimental outcomes in a form that is independent of the loading ratio. The deviation from the steady state value of the equivalent SIF range after the overload application is considered as a measure of the magnitude and extent of the crack growth retardation effect. Using the effective SIF range reduction ratio β, the sole influence of residual stress is considered at R=0.1, and the effect of closure could also be isolated by considering the difference between the R=0.1 and R=0.7 results.

4.2.2. Material Description and Fatigue Test

The material sought for conducting the various experiments reported in this chapter required to have specific combination of properties. Above all, good ductility was sought to give a large plastic region at the crack tip and in which residual stress is accommodated. Secondly, since SXRPD technique was to be used for residual stress evaluation, fine-grained material was required to give good compromise between high spatial resolution and good grain averaging and sampling statistics. For the reasons listed we chose to focus our attention on the magnesium alloy AZ31b treated using a severe plastic deformation processing route that lead to grain refinement and strengthening in combination with good ductility. The resulting grain size varied in the range from 1μm to 5μm, yield stress of the order σ_y=262MPa and maximum elongation of 10%.

Fatigue tests were performed on CT specimens machined from a 2mm-thick plate with the in-plane dimensions depicted in Figure 51(a).

Cyclic load was applied to the sample by means of a servo-hydraulic testing machine at frequencies of 7÷10hz. Static loading for *in situ* strain mapping using SXRPD was applied using a 5kN Deben®

machine. Crack tip opening displacement measurement was used as a means of cross-validation between the two loading arrangements, to ensure that the loading conditions ahead of the crack tip were consistent between the two experimental configurations.

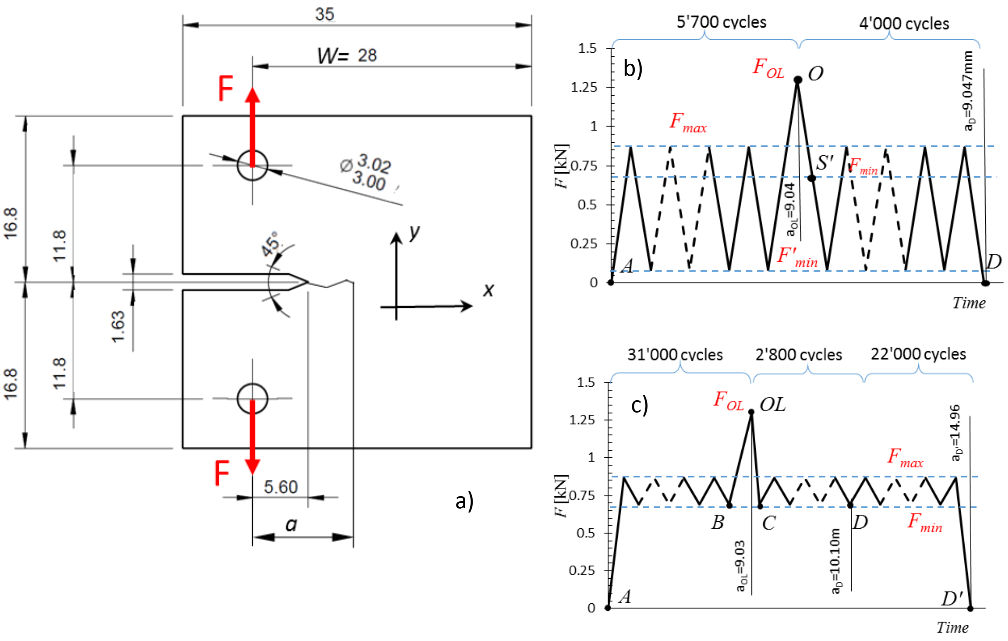

Figure 51 (a) Sample geometry (dimensions in mm), and loading history for (b) sample with R=0.1, and (c) R=0.7.

Two fatigue experiments at constant loading ratios of R=0.1 and R=0.7 were conducted, and a single peak overload (OL) was applied in both. The loading histories for both experiments are reported in Figure 51(b) and 1c. Both experiments show the same magnitude of maximum force (F_{max}=866.7N) and the overload force (F_{OL}=1300N) that was 50% in excess of the maximum cyclic load, meaning that the overload ratio was R_{OL}=1.5. To achieve the required loading ratios, the lower cyclic load imposed was F_{min}=606.7N for R=0.7, and was F^{I}_{min}=86.7N for R=0.1. The single anomalous overload peak was applied at the crack length of a=9.05mm for the R=0.1 sample, and at a=9.03mm for the R=0.7 sample, respectively. Further fatigue crack growth experiment was conducted beyond the overload until the prevailing trend in the FCGR was re-established.

4.2.3. Crack propagation result

Experimental Result

Crack growth rate retardation was observed in both samples. The diagram of crack length versus the number of cycles is plotted in Figure 52. The change in the trend towards slower growth rates is apparent in the propagation past the OL. The fitting lines in Figure 52 indicate the local discontinuities in the FCGR and the apparent shift in the steady-state growth trend.

It worth noting that the experiment at R=0.7 manifests a complete arrest of crack propagation, unlike the R=0.1 case. Re-nucleation occurred after 2500 further cycles past the OL. This behaviour is evident in Figure 52(b): right after the OL the crack length plot becomes horizontal, and only departs once the crack re-nucleates, eventually approaching the steady state crack growth trend.

Stress Intensity Factor (SIF) values for FCGR curve construction were evaluated using the equation for a compact tension specimen provided by Murakami (52):

Figure 53 presents crack propagation data in the form of crack growth rate as a function of crack length (Figure 53). The OL-induced retardation is apparent from the drop of the growth rate d*a*/d*n* at OL, followed by the gradual return to the steady-state rate. Assuming that the crack growth rate gets fully restored once the crack reaches the unaltered material zone, the FCGR curve can be described analytically in accordance with Paris' Law:

$$\frac{da}{dn} = C\ \Delta K^m \tag{55}$$

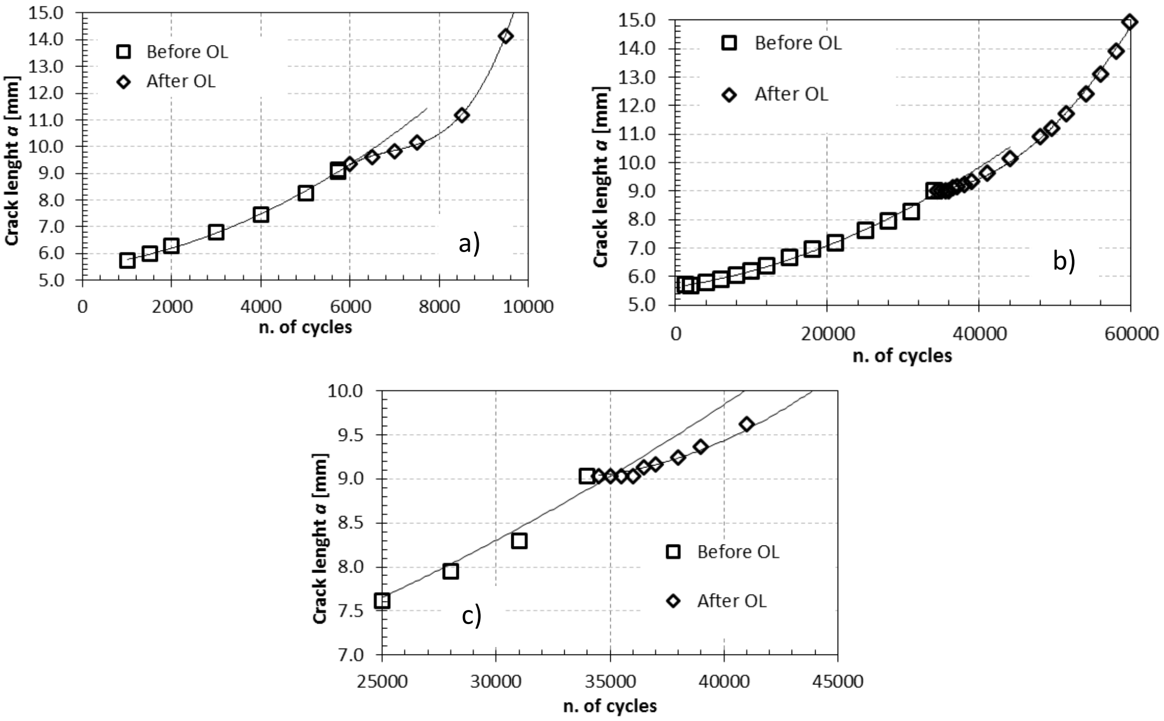

Figure 52 Crack propagation during fatigue tests at a) R=0.1, b) R=0.7 and c) R=0.7 crack arrest detail.

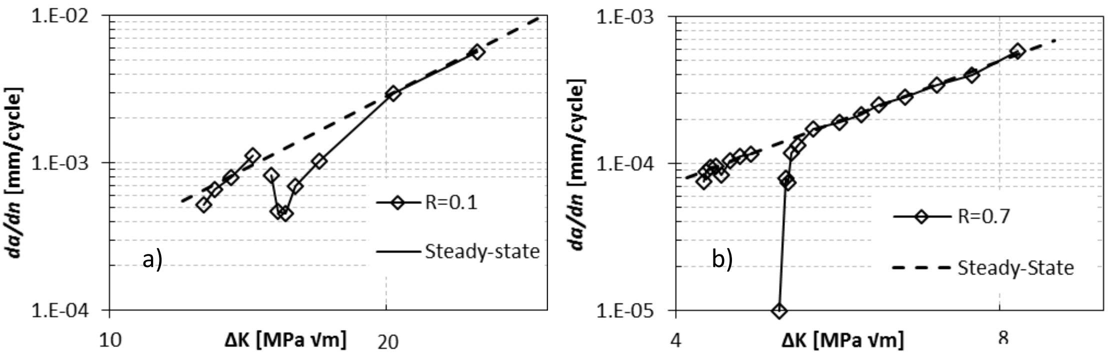

Figure 53 Fatigue Crack Growth Rate diagrams. a) R=0.1 b) R=0.7

The coefficients C and m are listed in Table 4.

Loading Ratio *R*	*C [m/(cycle MPa √m)]*	*m*
0.1	1.91×10^{-10}	3.21
0.7	1.76×10^{-9}	2.71

Table 4 Paris' law parameters

Walker's model

The idea of mean stress effect correction that was introduced by Walker [212], after previously been widely adopted in the context of stress-life curves [213-215], has been successfully applied in the context of fracture mechanics [216, 217].

Walker introduced an equivalent parameter ΔK_{eq} to describe the FCGR for any combination of maximum SIF K_{max} and minimum SIF K_{min} that can be expressed in terms of the load ratio $R\geq0$. The equivalent SIF range ΔK_{eq} is defined as follows:

$$\Delta K_{eq} = K_{max}(1-R)^{\gamma} \tag{56}$$

Here γ is a measure of material-specific FCGR sensitivity to the mean stress that ranges between 0 and 1. Noting that $\Delta K = K_{max}/(1-R)$, we adopt a way more convenient for the present purpose to express equation (56) directly in terms of the SIF range:

$$\Delta K_{eq} = \Delta K(1-R)^{\gamma-1} \tag{57}$$

Considering the expression for fatigue crack growth rate given by the Paris law as the particular case of R=0, we write:

$$\left(\frac{da}{dN}\right)_{R=0} = C_0\,\Delta K^{m_w} \tag{58}$$

Where C_0 and m_w are the material constants, and subscript w refers to the use of the Walker parameter. Based on the above, expression for the general case is obtained by substituting equation (58) into (62), replacing ΔK with ΔK_{eq}:

$$\frac{da}{dN} = C_0\,[\Delta K(1-R)^{\gamma-1}]^{m_w} \tag{59}$$

This formulation provides a description of the FCGR at *any* positive load ratio $R \geq 0$ in terms of three constants: γ, C_0,m_w. Those constants can be obtained by means of a linear regression using the logarithmic form of (60), as follows:

$$\log\left(\frac{\mathrm{d}a}{\mathrm{d}N}\right) = \log(C_0) + m_w \log(\Delta K) + m_w(\gamma - 1)\log(1-R) \tag{60}$$

The fitting procedure was applied to the set of experimental data presented here in the crack propagation regime unaffected by the OL, as represented by the dashed line in Figure 53 The material parameters were found to be: $\gamma = 0.649,\ C_0 = 3.34 \times 10^{-10} \frac{m}{cycle\,MPa\sqrt{m}},\ m_w = 2.95$.

4.2.4. Crack closure evaluation

DIC analysis

The presence of plasticity-induced crack closure during the fatigue test was verified using DIC. This method has been successfully adopted in the past [128, 218] and shown to be an efficient way to evaluate the relative displacement of crack flanks during cyclic loading. The tracking points can be positioned along the crack wake so that the closure effect is evaluated as function of position from the crack tip. The necessary requirements for the correct elaboration of peak tracking using DIC is the adequate image resolution and the presence of small features that ensure brightness variation within the image and allow peak tracking. The image acquisition system consisted of a Questar long range telescope attached to a camera having with 640x240 pixel resolution, and an effective pixel size of 1µm for the actual setup used.

The presence of crack closure was verified before and after the application of the OL. For both the loading conditions (R=0.1 and R=0.7), a sequence of images was acquired once the crack had propagated past the overload position for further 0.55mm. The tracking points were positioned at several locations behind the crack tip toward the notch position namely, 25µm, 100µm, 200µm and 400µm.

The acquisition was run at the reduced loading frequency of 0.2 Hz and the frame rate of 4 frames per second, to avoid image blurring. Thus, each cycle was described by ~20 images. The software used for DIC measurement was that developed by Eberl et al. [219].

The evaluated relative displacements plots, considering zero as the closed crack condition, as function of the applied external load are reported in Figure 54 below.

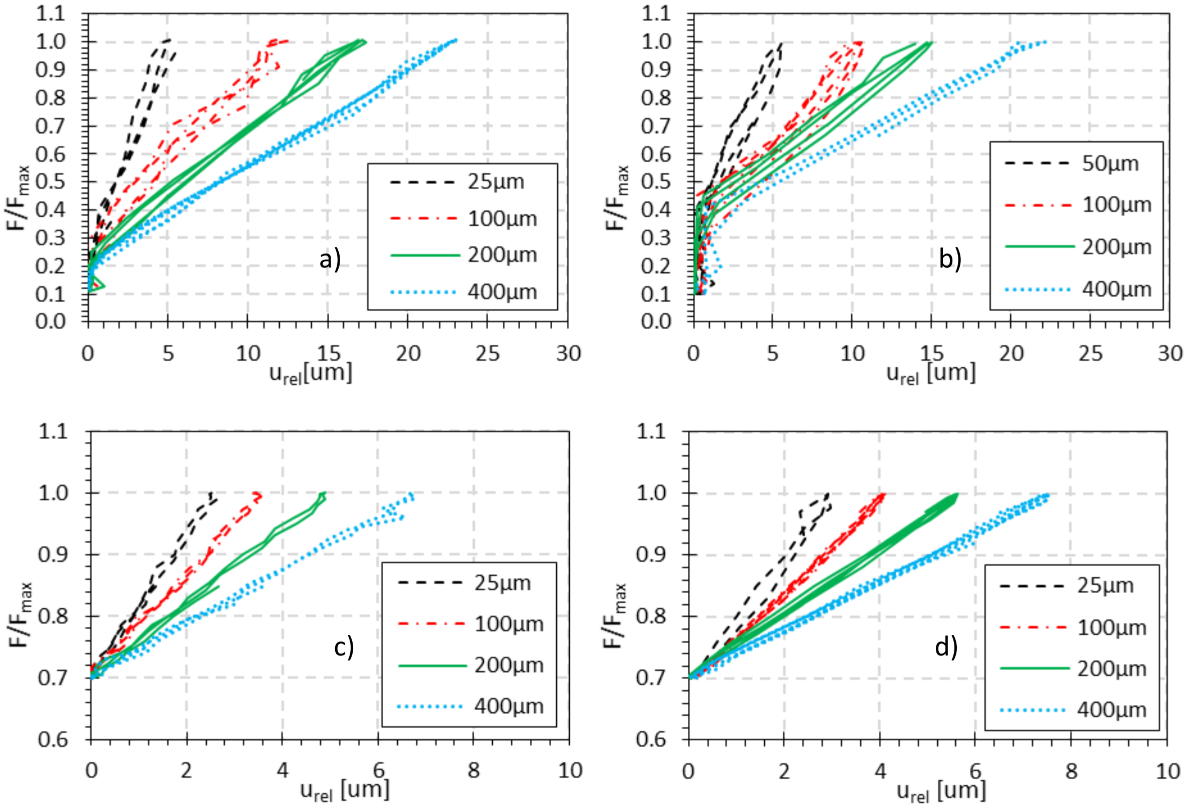

Figure 54 Crack flank relative displacement as function of the applied external load. The n.5 plots of each graph represent the trend at different distances from the crack tip towards the sample notch. Before (a) and after (b) the OL at R=0.1. Before (c) and after (d) the OL at R=0.7.

The DIC analysis allows unequivocal identification of the conditions for crack closure to be present during crack growth past an OL.

Figure 54(a) shows how, despite the absence of anomalous loads, the crack closure is present. In fact, all the measurements display a reaching of the crack flanks contact just slightly before the external load reaches its minimum value. It is worth noting that, as expected, this effect becomes milder at further distances from the crack tip. Let us now consider the instant after the introduction of the OL, the first more evident observation can be drawn by looking at the load at which the crack closes. Indeed, the application of the OL reduced the range of load variation where the crack remains open compared to the sample without OL. Again, at further positions from the crack tip, the closure effect shows an almost imperceptible reduction of its effectiveness.

The observed closure phenomenon represents a significant reduction of the total SIF range experienced by the crack tip by up to one fourth of the total range of its variation. Similarly, subsequent loading from the minimum load does not immediately manifest itself in the crack opening, but rather only appears when the load reaches about the same load level.

Regarding the sample loaded at R=0.7, no evidence of crack closure is detected. Figure 54© and Figure 54(d) show that both before and after the OL, the displacements follow a nearly straight curve without any anomalies associated with the crack closure. Absence of crack closure was experienced even in the very vicinity of the crack tip (~25um).

In summary, DIC analysis reveals the presence of crack closure induced by the OL only under the loading ratio condition of R=0.1. In contrast, adopting R=0.7, i.e. high value of F_{min} inhibits possible crack flank contact.

Let us analyse the effect that crack closure had on the reduction in effective stress intensity factor range for the experiment at R=0.1. Considering the displacement plots shown in Figure 54, the reduction in the SIF acting at the crack tip once the crack closure is active can be evaluated. Assuming a linear relation between load and the crack tip SIF, the following assessment can be made:

$$\alpha = \frac{F_{op}}{F_{max}} = \frac{K_{op}}{K_{max}} \tag{61}$$

Here α is the ratio between the maximum load and the load required for opening the crack (subscript op).

The effective SIF range acting at the crack tip can therefore be evaluated as follows:

$$\Delta K_{eff} = \Delta K\ (1 - \alpha) \tag{62}$$

The effective stress intensity factor taking into account the crack closure effect is defined as:

$$\Delta K_{eff} = K_{max} - K_{op} \tag{63}$$

The record of the loading history during the images acquisition allowed the determination of the loading level at which the crack starts opening. Averaged values of opening load were assessed over the crack lengths measured (i.e. up to 0.4mm). The solution of the (61) provided $\alpha_{after}=0.35$ and α_{prior}=0.18 respectively prior and after the OL introduction. The physical meaning of α is the reduction of the stress intensity factor range when the crack closure was operating. Eventually, using the equation (62) it is possible to evaluate the value of the effective range of stress intensity factor at the crack length analysed by DIC. This value can be computed for both, prior and after the OL application. These turned out to be respectively$\Delta K_{eff,bef}$=12.5 MPa √m and $\Delta K_{eff,aft}$=9.9 MPa √m.

Fractography

Further insights into the crack propagation mechanism can be obtained through fracture surface analysis using SEM imaging at variable magnification to allow the exploration of the morphology of asperities left by material rupture at several length scales.

The two samples considered in this study were examined with particular attention focused at the overload site. Figure 55(a) and Figure 55(b) provide overview images of the crack surface at the zone of interest. The dashed lines in figures indicate the crack front at the instant of overload application. The crack front profile clearly does not follow a straight line due to the difference in constraint between the bulk and the free surface. Although no analytical solution is available for describing this phenomenon quantitatively, it is well known to be highly dependent on the Poisson's ratio [218]. This three-dimensional effect induces a variation of SIF at the crack front as a function of position across the sample's thickness.

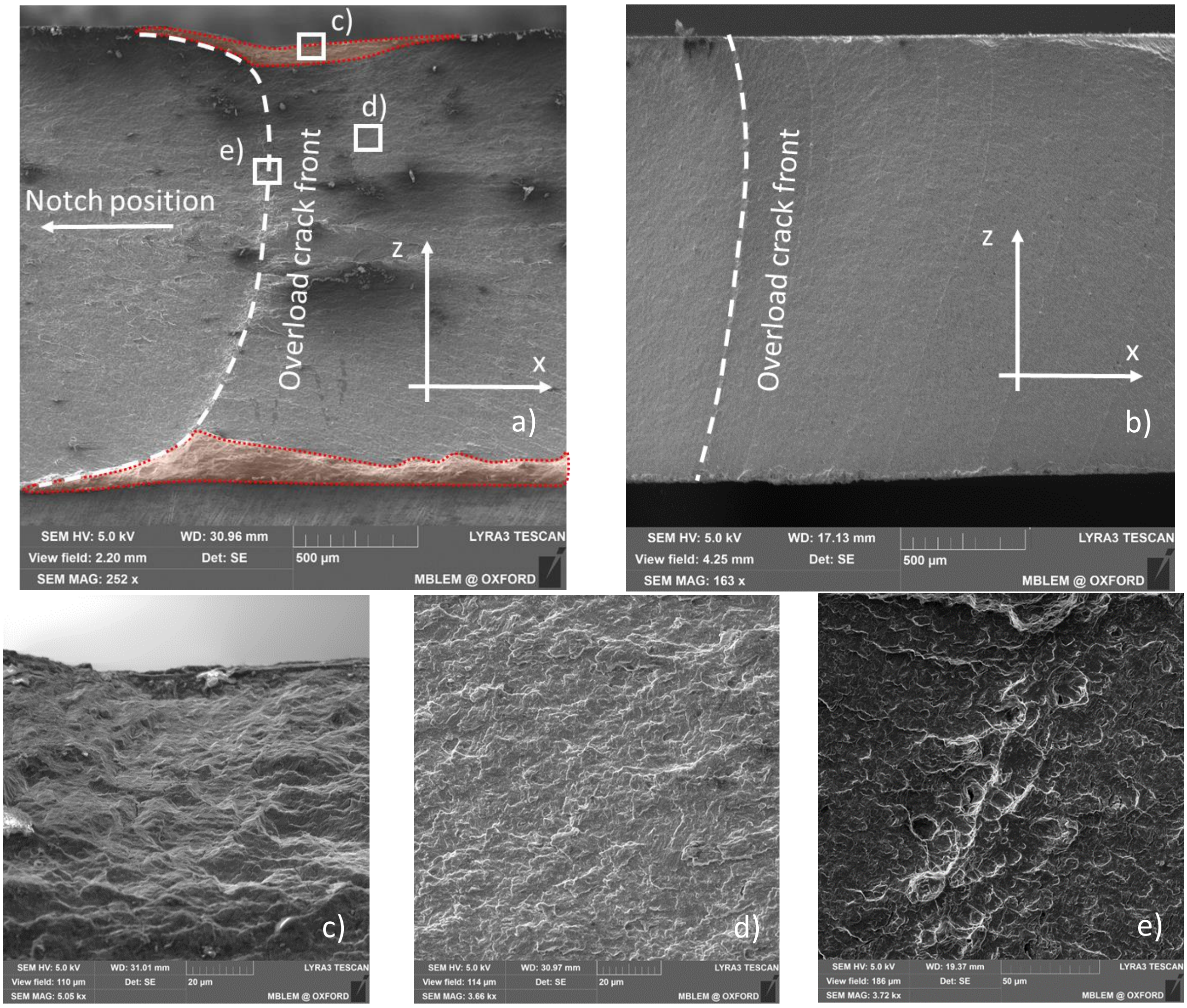

Figure 55 Crack surface SEM fractography. a) Overview image of the overload site (R=0.1). b) Overview at the OL site (R=0.7). c) Crack Closure detail (R=0.1). d) Surface detail (R=0.1). e) Overload site detail (R=0.1)

Comparing the two images, an observation can be made that the enhanced plastic deformation is present in the sample (R=0.1) at the vicinity of the free surfaces along the through thickness z direction (highlighted in red). This is associated with the change in the stress state (principal stresses in particular), as studied numerically and reported in the literature [220]. In contrast, the same observation cannot be made readily for the sample fatigued at R=0.7, since no evident plastic deformation “lip” is evident. Furthermore, higher magnification imaging at these deformed areas (site c) reveals another interesting aspect shown in Figure 55(c). The surface roughness at site “c” is visibly different compared to site d. A possible explanation for this observation is that crack closure was operative within the highlighted near-surface region during crack propagation past the overload. This is in agreement with previously reported studies [220] that suggest high values of crack opening stress intensity factors to be found for locations lying nearby the free surface. The hypothesis that we put forward (and that allows additional corroboration) is that crack closure modifies the apparent roughness of the fracture as consequence of repeated contact between crack flanks during cycling. It has been argued in the literature that the region of material that undergoes contact due to crack closure should not depend upon sample thickness [221], unless the thickness is comparable with the closure zone size. Note that the fact that no apparent crack closure occurred during the loading ratio R=0.7 test is corroborated by Figure 55(b) that does not show any altered zone at all.

Finally, the change of crack surface morphology due to the overload proper is shown in Figure 55(e). The higher topology of the central “ridge” in the image corresponds to the large plastic deformation that causes closure and leads to the consequent change in the FCGR observed in the experiment.

4.2.5. Residual stress measurement using SXRPD

Experimental measurements using SXRPD

Synchrotron X-ray Powder Diffraction (SXRPD) is a powerful tool for spatially resolved strain studies in polycrystalline materials. Since high energy, high flux X-ray beams are required for mapping the lattice parameter variation in the bulk of load-bearing components, synchrotron-based instruments are often used. During the past decade successful use of this technique has been reported for crack tip stress/strain evaluation [128-130, 211, 222, 223].

The experiment reported here was aimed at spatially resolved residual strain evaluation along the crack extension line within the sample, at four different stages of crack propagation, with respect to the load application history. In terms of the crack retardation due to overload, in the sample tested at R=0.7 (analysed by SXRPD) this effect is expected to be caused uniquely by the compressive residual stress, whereas in the R=0.1 sample, a combination of crack closure and residual stress retardation is present. The purpose of the synchrotron-based experiment was therefore to measure the evolution of the near-tip strain (stress) state using SXRPD technique.

Experiment was conducted on the I15 beamline at Diamond Light Source (DLS, Harwell, UK). X-ray energy was set to 76.6keV, with the beam size defined by collimating slits as 45x45μm. In situ sample loading was provided by a 5kN Deben© portable stage that was mounted on a diffractometer able to accomplish movements along the x’,y’ and z’ axes, as indicated in Figure 56. The test was performed in transmission mode, and it was assumed that out-of-plane stresses are negligible (plane stress approximation). A series of complete Debye-Sherrer rings was acquired using a PerkinElmer flat panel 1621-EN detector (2048x2048 pixels, pixel size 0.2x0.2mm^2) placed on the axis of the incoming beam, as shown in Figure 56. The sample-detector distance was adjusted to obtain an optimum combination of coverage and positional precision for the rings of interest.

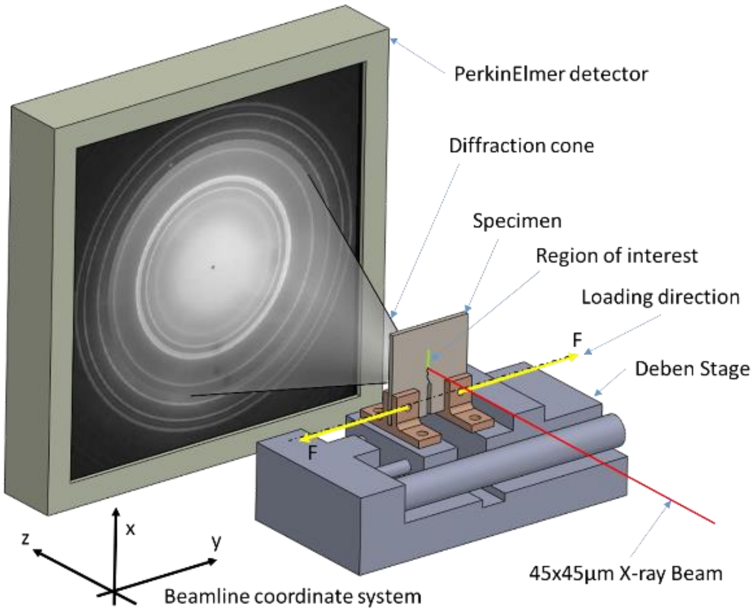

Figure 56 X-ray Synchrotron Powder Diffraction setup in transmission mode

Referring to Figure 51(c) which shows the loading history, spatially resolved strain line profiling was performed at the instants denoted as B, OL, C and D. The line scan step adopted was equal to the X-ray beam spot size (45µm), and each line scan covered approximately 2mm in length ahead of the crack tip.

For the purposes of strain analysis, the (101) Debye-Scherrer ring was subjected to radial binning performed to extract the equivalent 1D X-ray diffraction profile for scattering in the direction parallel to the load application. The lattice spacing variation Δd was then evaluated throughout the scan, for use in the differential form of Bragg’s law to determine strain, as follows:

$$\varepsilon_{yy} = \frac{\Delta d}{d_0} \tag{64}$$

As it is well known, determination of strain using the above formula requires the knowledge of strain-free lattice parameter d_0. Defining this parameter often presents a practical challenge, since finding an appropriate unstrained location within or outside the sample is not always possible. An approximate assessment, considering a stress-free region of the sample, was made. Afterwards, further refinement was performed by comparison and subsequent matching with the solution given by elastoplastic FEM analysis.

The procedure for precise determination of d_0 was carried out using the set of measurements acquired at step B (Figure 51(c)), and once d_0 was found by matching with the FEM solution, the remaining line scans were interpreted accordingly. In reference to the coordinate system shown in Figure 51(a), *yy* strain component profiles, from the experimental measurements, at the various stages of crack growth are reported in Figure 57 using markers and dashed curves, together with the FEM solutions shown as continuous lines.

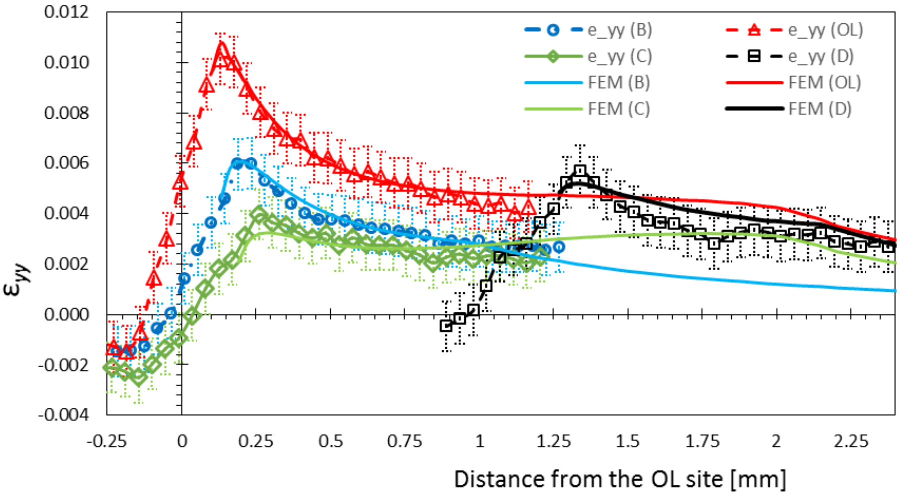

Figure 57 Strain profiles (yy component) along the crack bisector at various crack propagation stages.

Satisfactory agreement is found between the FEM solution given using nominal load, and SXRPD measurements.

These results confirmed the magnification of compressive residual strain due to the Ol application. In fact, the strain profile referring to the propagation stage “C” in Figure 57 shown a lower magnitude of strain compared to the propagation stage “B” that identifies the instant prior the OL.Plastic deformation occurring at the crack tip when the OL is operative is far greater than that induced by the cyclic loading, when the latter reaches its maximum magnitude. Therefore, as a consequence, the release of the OL implies higher magnitude of compressive residual strain. The effect that compressive residual strain has on the cyclic strain at the crack tip is a shift of towards lower magnitudes as experienced by our measurements.

The strain measurement at the propagation stage “D” is at the same magnitude levels of the strain found prior the OL. This proves that, when the crack past the OL site of 1mm, the compressive strain state returns back to the unaffected conditions, as the OL never occurred.

We note that negative strain values found in the crack wake are consistent with the strain profiles reported by Croft [223] who also used a similar experimental technique.

FEM strain state evaluation after the overload

After further validation of the elastoplastic model proposed in (Chapter 4.4), the strain field ahead of the crack tip arising after the application of an OL could be simulated to high accuracy and with good confidence. With the purpose of understanding whether the baseline fatigue crack propagation affected the resulting strain state, we simulated both cases that we studied experimentally up to the stage when the crack reaches the propagation stage that corresponds to the cyclic load application right after the OL occurrence. To compare the strain fields between the two cases, the reference load was imposed in the model that corresponded to the minimum load reached in the R=0.7 test (i.e. F_{min}=606.7N). Strain profiles were extracted at the same crack length and load conditions corresponding to the instants shown in the Figure 51(b-c) labeled ad C and S’, for R=0.7 and R=0.1, respectively.

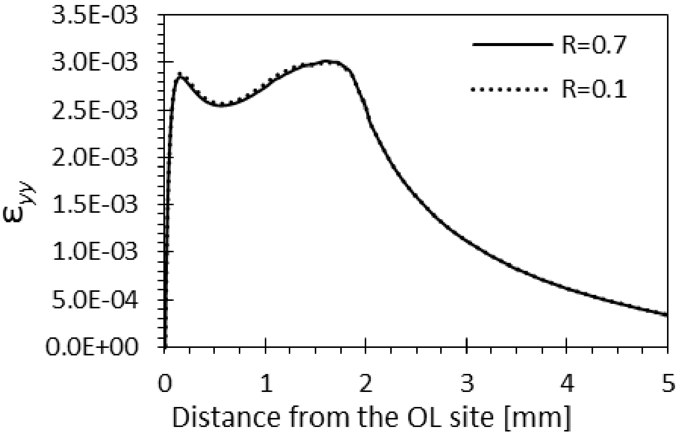

Figure 58 Strain field plot along the crack propagation direction at the propagation stage and load indicated as S and S’ in Figure 51(b) and Figure 51(c).

It is evident that the introduction of an OL ‘overwrites’ the effect of previous cyclic material deformation: at the same load level the two strain profiles are practically indistinguishable. In view of this result, it is clear that the change in strain states that arise for the two baseline cyclic conditions immediately after the OL are indentical. This leads to an important conclusion that in both loading conditions the residual strain and stress and their influence on crack retardation are practically identical.

4.2.6. Residual stress and crack closure contribution

The studies of the overload effect under constant ΔK fatigue at several loading ratios $R_K=K_{min}/K_{max}$ have been previously carried out by Ishihara [224] and Borrego [225]. Whilst the former reported an enhancement of fatigue life at higher R_K, the latter observed the opposite trend. We believe that the controversy partly stems from the lack of understanding of the roles of plasticity-induced crack closure and residual stress effects, respectively.

It is reported in the literature [226] that crack closure plays an important role in affecting the growth rate if controlled loading ratio R is lower than 0.7. Our experiment confirms this, since no traces of crack closure were detected in the sample cyclically loaded at R=0.7 either by DIC or SEM fractography. The same study [226] also reported that the FCGR variation with R could be captured by the effective stress intensity factor range that is strictly related to the crack opening and closure levels. It is also worth noting that the FCGR slope in the Paris’ regime does not appear to change for different loading ratios. Our test results (Table 4) agree with this observation. In the near-threshold regime of crack propagation, a more prominent effect is observed, as reported in [227], as the loading ratio varies.

Given that the crack propagation under varying loading ratio R is mainly influenced by the change in closure level, we focused our attention on the behaviour of FCGR at the occurrence of overload for different R.

Effective equivalent stress intensity factor range

Despite several minor modifications proposed in the decades since its introduction, the concept of effective stress intensity factor introduced by Elber [127] remains the most widely and generally accepted means of quantification for the principal crack driving force [228-230].

In the Paris regime of propagation, the fatigue crack growth rate dependence on the effective stress intensity factor range follows a power law relationship (55). Under the assumption that the steady-state

FCGR described by (55) and shown in Figure 53 is representative of the behaviour unaffected by the overload, we can calculate the SIF range that would give the same fatigue crack propagation rate *da/dn* that was observed experimentally. This can be accomplished by using the equivalent SIF range ΔK_{eq} according to Walker's formulation, which in this specific case also becomes the equivalent effective SIF, $\Delta K_{eq,eff}$. By rewriting equation (59) as

$$\frac{da}{dN} = C_0\, \Delta K_{eq,eff}{}^{m_w} \tag{65}$$

the totality of the experimental results can be directly superimposed onto the Paris master curve in a form independent of the load ratio R, for the purposes of comparison. Next, $\Delta K_{eq,eff}$ can be readily calculated by inversion of (65), i.e.:

$$\Delta K_{eq,eff} = \sqrt[m_w]{\frac{1}{C_0}\frac{da}{dn}} \tag{66}$$

Once the new parameter $\Delta K_{eq,eff}$ is computed using (66) for each instant of crack propagation, all the experimental points fall onto the prediction of Walker

The normalised SIF range reduction ratio ("knock-down" multiplier) due to the overload and its consequences can be evaluated through the normalised ratio β expressed in terms of the effective $\Delta K_{eq,eff}$ computed above, and the equivalent SIF range ΔK_{eq} corresponding to each experimental point evaluated by means of (57).

$$\beta = \frac{\Delta K_{eq} - \Delta K_{eq,eff}}{\Delta K_{eq,eff}} \tag{67}$$

This ratio represents the reduction in the equivalent stress intensity factor range from the unaltered one following the overload occurrence. With the purpose of comparing the outcomes from the tests at R=0.1 and R=0.7, the variation of reduction ratio β was considered, and found to be fitted well with a log-normal function given by:

$$\beta = \frac{\emptyset}{\sigma\, a' \sqrt{2\,\pi}} \exp\left(-\frac{(\log a' - \mu)^2}{2\,\sigma^2}\right) \tag{68}$$

Here a' is the local crack extension length defined from the OL site, and $\emptyset, \mu$ and σ are the fitting parameters which define respectively its amplitude, skewness and width. Fitting was performed for the two data sets to obtain the parameter values for $\beta_{R=0.1}$ and $\beta_{R=0.7}$.

Since the goal of the present work is the attempt to distinguish the contribution of residual stress and crack closure in crack growth retardation, parameter β can be used as a measure of the durability of contribution to OL retardation from each mechanism. For the case of R=0.7, the only active mechanism is residual stress, while at R=0.1 a combination of residual stress with crack closure is present. It is worth mentioning that crack arrest was observed in the case of R=0.7. At this stage, before the crack started propagating again, the value of $\beta_{R=0.7}$ became infinite, and therefore is no longer comparable with the$\beta_{R=0.1}$.

FE simulation of the strain state generated by the application of the OL revealed that is was not significantly affected by the conditions of cyclic propagation that occurred earlier. Based on this important observation we assume from this point onwards that the residual stress influence on the crack growth retardation is the same for the two load ratio conditions examined.

In order to deconvolve the contribution of crack closure mechanism from its combination with residual stress at R=0.1, the curve for $\beta_{R=0.7}$ was subtracted from that for $\beta_{R=0.1}$ according to equation (69). In adopting this additive description of the two effect we are aware of the fact that the interaction between crack closure and residual stress may be complex, and may require more intricate approach to capture it correctly. However, it appears to offer the most suitable first approximation.

The additive decomposition that was applied only within the range of states when both cracks at R=0.1 and R=0.7 were propagating, i.e. da/dn $\neq$0, led to the expression:

$$\beta_{closure} = \beta_{R=0.1} - \beta_{R=0.7} \tag{69}$$

Figure 59 below presents the experimental data points, curve fits and the closure contribution evaluated using equation (69).

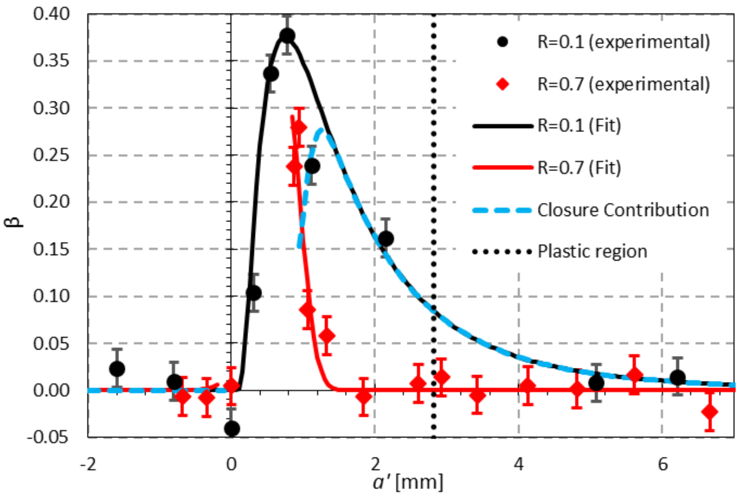

Figure 59 SIF reduction ratio β for a) R=0.1 ($\beta_{R=0.1}$) and b) R=0.7 ($\beta_{R=0.7}$)

The dashed vertical line denotes the plastic zone boundary according to the following relation from linear elastic fracture mechanics:

$$r_p = \gamma\left(\frac{K_{max}}{\sigma_y}\right)^2 \tag{70}$$

where coefficient γ is a parameter dependent on the sample thickness and on the stress-strain response of the material. Under the assumption of elastic-perfectly plastic material behaviour, this coefficient can be readily computed using the equation given below [231]. It has been noted [232] that the adoption of this formulation finds satisfactory agreement with three-dimensional numerical simulation, which leads to:

$$\gamma = 0.35 - \frac{0.29}{1 + \left[1.08\,\frac{K_{max}^2}{t\,\sigma_y^2}\right]^{2.15}} \tag{71}$$

Using the value of α according to (71) in equation (70), the plastic zone radius was found to be ~2.8mm.

4.2.7. Discussion

The introduction of the stress intensity factor reduction ratio β has allowed the quantification of the retardation effect in terms of the effective equivalent SIF range variation past the OL. For comparison, the evaluation of this parameter was conducted for both load ratio conditions (R=0.1, R=0.7). The experimental data was then fitted with the log-normal function, with the purpose of subsequently subtracting the results from each other and attempting the discrimination of the two contributions. As a consequence of this analysis, the contribution from crack closure could be assessed, as shown by the dashed curve in Figure 59. The maximum contribution to retardation from the crack closure mechanism is found to occur at the distance of half the plastic zone size (i.e. $a' \cong r_p/2$). It is also worth noting that although the magnitude of the crack closure effect is comparable in magnitude with the residual stress one, the crack closure effect persists to greater crack lengths compared to the shorter acting residual stress effect that fades in magnitude within approximately half the size of the plastic zone, when the crack closure effect reaches its maximum.

Some conclusions can be drawn regarding the persistence length of each of the two crack retardation mechanisms. The sample tested at R=0.1 showed a persistent retardation effect even at crack extensions well in excess of the plastic zone size. This is likely to be related to the size of the plastic zone created by the overload that exceeds significantly the reversed plastic zone size [122]. In contrast, the sample cyclically loaded at R=0.7 manifested FCGR retardation limited only to a fraction of the plastic zone size. As confirmed by DIC analysis and fractography, plasticity-induced crack closure was not operative for this sample, and thus the crack retardation effect only caused by residual stress has a much shorter persistence length compared to the clack closure mechanisms.

For the load ratio R=0.1, following the OL, the crack tip experienced an effective equivalent SIF range reduction by up to 37% followed by its gradual restoration to the steady state condition. For the sample tested at R=0.7, after crack re-nucleation, an immediate drop of around 27% in the effective SIF range was seen, which subsequently quickly returned to the steady state value at distances less than 1.3mm from the OL location, corresponding to about half of the OL plastic zone extent.

It is also worth noting that right after the application of the OL (instant “C” in Figure 51), experimental strain measurement indicated a drop in magnitude compared to the unaltered condition “B”. This decay of strain magnitude is imputed to the effect of compressive residual stress induced by the high plastic deformation occurred at the crack tip which, in turns, changed the mean strain level during the cycling load toward lower values. This confirms the hypothesis that residual stress in this test case (R=0.7) is indeed the main reason for the effective SIF reduction. The change in strain magnitude was then compared with the one experienced at load ratio R=0.1 by means of elasto-plastic FEM simulations. It turned out that the cyclic load occurring prior the OL does not have a significant effect on the strain field alteration ahead the crack tip. Therefore, the residual strain field involved in the crack retardation can be considered equivalent for both the load cases.

DIC analysis of crack opening displacements revealed the level of crack closure before and after the occurrence of the OL. It was experienced that the crack closure was already operative prior the OL application but at lower level compared to the one seen after the OL. It is important to highlight that before the OL application, the crack closure level was gradually reducing at higher distances from the crack tip. Indeed, at 0.4mm the closure was barely detectable. It is worth mentioning that the plastic radius at this instant (prior OL) was of around 1mm. Quantification of these values could be made by looking at the effective SIF range that was subject to a drop of around 35%, at 0.55mm from the OL site in the case of R=0.1. This value overshoots the influence of the sole crack closure effect, $\beta_{closure}$. This still reasonable divergence was expected and can be explained by the fact that the DIC analysis solely is able to assess the closure at the sample free surface. This implies that the closure level assessed with DIC may commit errors since it neglects the gradient of closure level that occurs as the position ranging from the plane-stress to the plane-strain states.

In other words, the retardation contributions due to crack closure and residual stress for two different load cases were each independently verified using alternative independent techniques (XRD/FEM and DIC), showing satisfactory agreement.

Considerations reported above lead to the conclusion that the residual stress ahead the crack tip is operating solely within a region confined to about half the size of the plastic zone generated by the overload. In contrast, crack closure is an effect that persists longer following OL. For low load ratios, plasticity-induced crack closure affects FCGR immediately once the crack moves past the overload site.

4.2.8. Conclusion

The role of plasticity-induced crack closure and residual stress/strain on crack retardation after occurrence of overload has been studied. Several techniques adopted for the investigation of this phenomena turned out to be complementary in helping understand the two mechanisms operating.

In order to separate the two contributions, fatigue samples were loaded at high load ratio (R=0.7) at which crack closure was inhibited. This allowed the investigation of residual stress as the main cause of crack retardation. The comparison with the sample tested at R=0.1 permitted the analysis of fatigue crack growth rate effect in combination with crack closure.

Crack closure was additionally characterised for both samples using DIC and fractography tools. Both techniques confirmed that crack closure operated solely in the sample at R=0.1. Also, fractography analysis highlighted the regions where crack flank contact occurred.

The residual strain induced by overload in the sample loaded at R=0.7 was studied using synchrotron X-ray powder diffraction SXRPD. The conclusion was drawn from the strain maps that immediately following the overload, the crack tip experienced a reduction of the strain value magnitude, due to induced compressive residual strain. Further measurement at 1mm past the overload showed that the mean stress intensity factor was completely restored.

A new parameter β, the SIF reduction ratio, was introduced. It describes the relative reduction of the equivalent SIF range, and allows appreciating the effect of residual strain only, and also in combination with crack closure. It was found that residual stress alone slows down the crack growth within a distance from OL site equal to approximately half of the plastic zone size due to the overload. This reduction of the SIF range is in good agreement with the results of SXRPD. On the other hand, the addition of the crack closure effect in the R=0.1 sample meant that the persistence length of the OL was similar to the plastic zone size.

The separation of the two effects was sought by means of fitting functions, and allowed clear identification of the crack closure persistence length. It is now possible to conclude that, despite inaccuracies that may arise from data scatter and fitting, it is possible to conclude that the crack closure contribution becomes active immediately upon the crack advances past the OL location, and reaches its maximum effectiveness at the same time as the residual stress effect vanishing, around half the plastic zone size. The SIF range reduction ratios evaluated by DIC and SXRPD techniques were in good agreement with the values assessed using the normalised effective SIF (β).

The present study considered an Mg alloy as an example of this reduction factor assessment but, obviously, it can be applied to other ductile material. A variation in extension and magnitude of the two contribution is expected for other material depending primarily upon the intrinsic ductility characteristics; that governs the plastic deformation and therefore the plasticity induced crack closure and residual stress.

The separation of contributions from closure and residual stress are of great significance in the context of crack growth prediction in variable amplitude fatigue. Existing models [232] are unable to capture this effect, since they simply assume that the modified plastic zone induced by OL corresponds to the extent of crack retardation. However, as demonstrated in the present study, crack closure effect may have the prevailing role in longer term crack retardation. Furthermore, it has been shown that its occurrence is directly linked with the load ratio of prior fatigue crack growth, rather than with the OL plastic zone size. Further studies ought to address the challenge of introducing a mathematical description of these contributions into analytical and numerical models of OL crack retardation.

4.3. Modelling of Fatigue Crack Growth Rate Retardation

4.3.1. Introduction

The subject of this work is the attempt of modelling the retardation occurring at the application of an Overload (OL) based on techniques from literature, at two different loading ratios (R=0.1 and R=0.7). In addition, constant amplitude crack propagation tests were performed at the two loading rations in order to assess the material mean stress sensitivity.

In the first instance, the constant amplitude loading results were modelled using a Walker model [212]. In this way, the FCGR for both the loading ratios could be represented as function of a unique equivalent Stress Intensity Factor (eSIF) which accounts the material sensitivity to the mean stress. Wheeler model [233], was then introduced for the modelling of the FCGR response at the OL occurrence. Recently, some modified versions of the Wheeler model were proposed in order to capture also the gradual reduction in FCGR after the OL until it reaches its minimum (delay part) [232], and [234]. The modified Wheeler model proposed by Yuen was implemented for the two loading ratios; this could be done incorporating the eSIF calculated through Walker.

4.3.2. Material Description and Fatigue Tests

The material and samples geometry are the same used previously in Chapter 4.2. A sample denoted as DA1 was cyclically loaded at constant amplitude (without OL). The load range was between the maximum load of F_{min}=0.87kN and minimum load of F_{max}=0.087kN, i.e. the load ratio R=0.1. Additional experiments were conducted on two samples designated DA2 and DA3 with a different load ratio R=0.7, but maintaining the maximum load unchanged, with the maximum and minimum loads of 0.87kN and 0.69kN, respectively.

For both load ratios of R=0.1 and R=0.7, a single anomalous OL was applied when the crack had reached the length of 9mm. The magnitude of the OL was such that the ratio between the OL and the maximum cyclic load was R_{OL}=1.5, therefore F_{OL}=1.3kN. For R=0.1 and R=0.7 the samples subjected to OL were designated respectively DA OL1 and DA OL2.

An additional sample (Parent material) was tested under the same loading conditions as sample DA1 with the purpose of obtaining the baseline fatigue crack propagation rate data for the same material before CGP processing.

4.3.3. Fatigue Test results

The analysis of the experimental data (i.e. number of cycles and crack length) allowed the construction of FCGR curves vs. driving force for crack growth. The calculation of the SIF for the micro-CT sample was conducted by using the convenient formulation proposed by Murakami [197]. Figure 60 shows all experimental points obtained in this fatigue testing campaign.

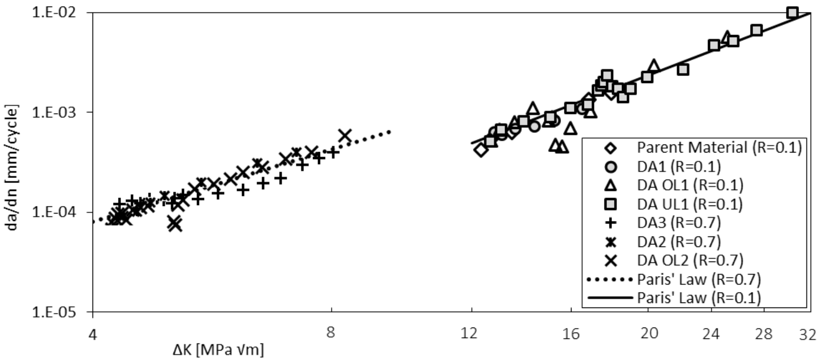

Figure 60 FCGR results for the two loading conditions (R=0.1 and R=0.7)

The first observation that can be drawn from these experimental outcomes is in regards to the fatigue performance of the processed material compared to the un-processed material at R=0.1. The plastically deformed material showed the same fatigue resistance as the parent material: the experimental points overlap, and no noticeable systematic differences are apparent. This observation provides the evidence that severe plastic deformation treatment applied to Mg alloy sheet material did not alter its fracture toughness and fatigue strength. This is a very important observation, since the most commonly noted result of SPD treatments is the improvement of tensile strength that often is accompanied by a reduction in the fatigue and fracture properties.

The fitting of the experimental data with the Paris equation (18) within the Paris law regime of propagation provides further information regarding the propagation behavior. The fitted coefficients are reported in Table 5.

Loading Ratio R	C [m/(cycle MPa √m)]	m
0.1	2.34×10^{-10}	3.07
0.7	2.85×10^{-9}	2.41

Table 5. Paris coefficients for the two load ratios.

4.3.4. The Walker model and its integration with the Wheeler model

Walker model calculation

Considering solely the set of experimental data presented here in the crack propagation regime unaffected by the OL, linear regression can be applied, leading to the graphical representation of the outcomes in Figure 61.

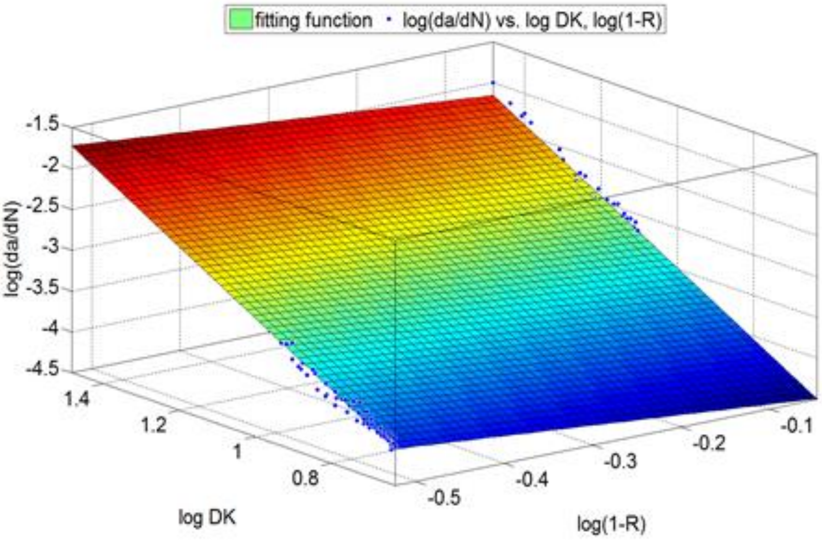

Figure 61. Three-dimensional representation of the fitting function to the experimental data

It is clear from Figure 61 that the fitting plane captures the trends for both sets of data. This is also confirmed by the low value of residuals. The outcomes of the outlined fitting procedure are hence the Walker parameters: $\gamma = 0.666,\ C_0 = 5.25 \times 10^{-10} m/(cycle\, MPa\, \sqrt{m}),\ m_w = 2.75$.

The value of γ denotes the relatively high sensitivity that the material has to the mean stress.

The modified Wheeler model

With some simplifications adopted, the fatigue crack growth retardation due to an overload can be predicted using the Wheeler model. Wheeler assumes that the retardation occurs immediately after the anomalous load application and the extension in which the retardation persist coincides with the plastic zone generated by the overload.

Such retardation is predicted thanks to the introduction of the retardation coefficient $\emptyset_R$ in the Paris' law formulation as follows:

$$\frac{da}{dN} = \emptyset_R \left(\frac{da}{dN}\right)_{CAL} \tag{72}$$

$$\text{where: } \emptyset_R = \begin{cases} \left[\dfrac{r_{p,i}}{a_{OL} + r_{p,OL} - a_i}\right]^{m_{wh}} & \text{if :} \quad a_i + r_{p,i} < a_{OL} + r_{p,OL} \\ 1 & \text{if :} \quad a_i + r_{p,i} > a_{OL} + r_{p,OL} \end{cases} \tag{73}$$

The retardation coefficient $\emptyset_R$ is a function of the overload effective plastic radius $r_{p,OL}$, the current cyclic plastic radius $r_{p,i}$ (i.e. generated at each cycle by the baseline load after OL), the current crack length a_i and the crack length at which the OL is applied a_{OL}. The magnitude of retardation is controlled by the shaping exponent m_{wh} and is obtained by matching to the experimental data.

Nevertheless, Walker model is not able to predict the retardation delay, i.e. the potential presence of initial short crack acceleration and overloads interaction. As mentioned earlier, some studies have attempted to include these effects in a Wheeler-based model. Concerning the purpose of the present work, we decided to introduce the delay correction to the original Wheeler model. In this way, the gradual FCGR deceleration occurring past the OL could be modelled. This task could be accomplished introducing the delay parameter $\emptyset_D$ as described by Yuen [232]. Therefore, the formulation of the FCGR becomes:

$$\frac{da}{dN} = \emptyset_R \emptyset_D \left(\frac{da}{dN}\right)_{CAL} \tag{74}$$

Similarly to the retardation coefficient, the delay coefficient can be expressed as:

$$where\text{: } \emptyset_D = \begin{cases} \left[\dfrac{a_{OL} + r_{d,OL} - a_i}{r_{d,i}}\right]^{m_{mod}} & \text{if :} \quad a_i + r_{d,i} < a_{OL} + r_{d,OL} \\ 1 & \text{if :} \quad a_{OL} + r_{d,OL} > a_i + r_{d,i} \end{cases} \tag{75}$$

Here $r_{d,OL}$ is the size of the OL effective delay, $r_{d,i}$ is the size of the current effective delay zone and m_{mod} is the shaping exponent for the modified model.

Several equations have been proposed in the past aimed at estimating the plastic radius that should be coincident with the effective plastic radius. The extension of the plastic zone is known to be function of the Stress Intensity factor K and the yield strength of the material σ_y and is usually defined as:

$$r_p = \alpha \left(\frac{K_{max}}{\sigma_y}\right)^2 \tag{76}$$

Here α is the plastic zone coefficient that is mainly dependent on the sample thickness, maximum SIF and mechanical properties. From one of the most popular and simple formulation proposed by Irwin

[198]to the more recent expressions based on Finite Element modelling [231], many attempts have been made in order to evaluate this coefficient. Nevertheless, in practical use it is observed that the extent of the plastic zone does not correspond to the real retardation length (effective plastic zone). Therefore the best fitting with the experimental data provides the most reliable value [232]. In this work, we followed the fitting procedure firstly introduced by Yuen where the plastic zone coefficient is calculated by:

$$a_r = r_{p,OL} - r_{p,r} = \alpha_r \left[\left(\frac{K_{OL}}{\sigma_y} \right)^2 - \left(\frac{K_r}{\sigma_y} \right)^2 \right] \tag{77}$$

Thus, the total retardation crack length a_r is thought of as the difference between the effective plastic zone induced by the OL and the plastic zone induced by the last cycle immediately before the crack outgrows the affected region.

Similarly to the plastic zone which corresponds to the retardation extension, Yuen [232] proposed the definition of the delay zone r_d. This coefficient in turn can be evaluated in the same way as shown in (78):

$$a_d = r_{d,OL} - r_{d,d} = \alpha_d \left[\left(\frac{K_{OL}}{\sigma_y} \right)^2 - \left(\frac{K_d}{\sigma_y} \right)^2 \right] \tag{78}$$

Here $r_{d,d}$ and K_d are respectively the delay radius and the stress intensity factor when the crack propagates to the length of $a_{OL} + a_d$.

<u>*The Walker-Wheeler models integration*</u>

So far, the model we described is able to predict fatigue crack retardation at low loading ratio R. Since we want to extend this model further to high values of R, we propose to assemble the two models described above. This can be readily implemented considering the Wheeler model that uses the eSIF evaluated according to Walker. In this way any combination of load ratio and overload retardation can be modelled by replacing the FCGR evaluated by Walker (59) into the Wheeler retardation model (74). The final formulation becomes:

$$\frac{da}{dN} = \emptyset_R \emptyset_D \left[C_0 \left[\Delta K_{eq} \right]^{m_w} \right] = \emptyset_R \emptyset_D \left[C_0 \left[\Delta K (1 - R)^{\gamma - 1} \right]^{m_w} \right] \tag{79}$$

4.3.5. Discussion and Conclusions

The proposed calculation framework for the modelling of the overload effect on the FCGR retardation was applied to the experimental data.

It is noted that regarding for the load ratio R=0.7, the crack arrested its propagation right after the OL, and no delay part was detected. Therefore, since the proposed model is not able to account for the arrest effect, for this specific case we did not attempt the modelling of the delay part of propagation after OL. On the other hand, in the case of R=0.1, the delay was observed and the full modelling procedure was implemented.

The matching process aimed at the evaluation of the model's coefficients produced the values showed in Table 6.

R	m_{wh}	m_{mod}	α_r	α_d
0.1	1.25	1.95	0.742	0.199
0.7	0.40	-	0.218	-

Table 6. Wheeler model coefficients.

The results of the Walker-Wheeler model application are graphically represented on the Paris diagram of equivalent SIF evaluated using Walker ΔK_{eq} against the FCGR $\frac{da}{dN}$, as shown in Figure 62. Modelled and experimental FCGR (a) Loading Ratio R=0.1 (b) Loading Ratio R=0.7. Overall, the application of the model provided satisfactory matching with the experimental data. Figure 62 illustrates that good agreement is achieved with a very low level of scatter and deviation.

We note that the values of the shaping exponent and the plastic zone coefficients differ in the two loading conditions. It is important to make this observation because the Wheeler model is built on the correlation between the plastic radius and the extent of the OL effect. This means that theoretically the two loading cases should show the same values, since the OL load level is the same. However, at the high loading ratio R the effective plastic radius produced by the OL ($r_{p,OL}$) resulted to be less than one third smaller of the one at R=0.1. This leads us to think that different crack propagation and retardation mechanisms were operating in the two experiments. The two predominant causes of crack retardation are thought to be the plasticity induced crack closure and the presence of compressive residual stress ahead of the crack tip. In the particular case of very high loading ratio it has been remarked that the crack closure effect may not be present [225]. In has been experienced that at R=0.7 the crack closure is completely absent, as shown in the previous Chapter 4. The absence of crack closure after OL at R=0.7 provides an explanation of the difference between the two sets of results. Indeed, the model does not account for the two mechanisms separately, and the reduction of retardation due to high R cannot be considered in the model.

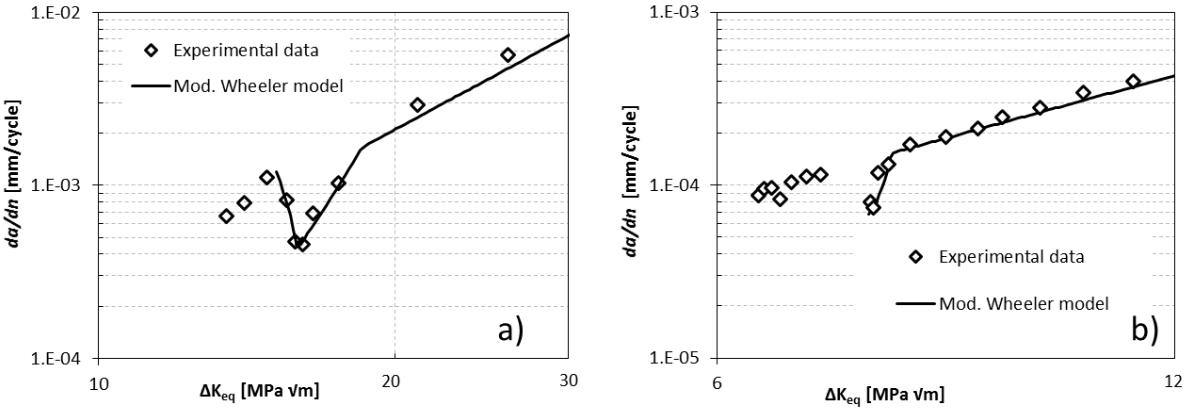

Figure 62. Modelled and experimental FCGR (a) Loading Ratio R=0.1 (b) Loading Ratio R=0.7

Once the Walker-Wheeler model coefficients have been calibrated, the newly formulated model can be used for the prediction of the OL effect on crack retardation at different load ratios and different OL levels. It is important to note that the coefficients evaluate for the Wheeler model need to be interpolated for obtaining a more reliable prediction at load ratios R that differ from the two analysed in this chapter (i.e. R=0.1 and R=0.7). Obviously, further experimental points may help improve the statistical coverage and thus the reliability of the model, especially at loading conditions largely different from the two treated here.

4.3.6. Conclusions

The fatigue crack growth response of Magnesium alloy AZ31b subjected to CGP severe plastic deformation was analysed in the present work. The FCGR comparison between the parent material and the CGP-processed material, both tested at the load ratio R=0.1 revealed no substantial differences. This indicates that no significant alteration occurred in the fatigue resistance with the application of the thermo-mechanical treatment. The fitting of experimental data with the Paris coefficients showed nearly the same FCGR curve slope for the two loading ratios.

Fatigue tests conducted with the introduction of an OL revealed the retardation behaviour of the material. In both fatigue baseline situations crack propagation showed retardation, and in the case of R=0.7 the crack was even arrested for 2000 cycles.

The fatigue crack growth behaviour was modelled using the combination of the Walker model that accounts for material sensitivity to mean stress, and a modified Wheeler model for the crack retardation prediction of crack delay after the occurrence of OL. This model can be used for the prediction of FCGR at different load and overload ratios upon the interpolation of the fitted coefficients.

Physical meaning and the values of the model parameters can be sought into the roles of crack closure and residual stress state ahead of the crack tip induced by the loading history. It is for this reason that the effort put in the Chapter 4 needs to be reflected into an improved model that strengthen the accuracy and robustness. Future studies may be addressed into this direction, along with the capability of predicting crack arrest.

4.4. Mechanism of Fatigue Crack Acceleration Following the Occurrence of an Underload

4.4.1. Introduction

In order to obtain a better understanding of the causes of crack acceleration due to UL and to assess their contribution, in this study we use the combination of modern mechanical microscopy techniques, namely, Synchrotron X-ray Powder Diffraction (SXRPD) for residual and 'live' strain mapping, Digital Image Correlation (DIC) for 'live' deformation monitoring and three-dimensional Finite Element Method (FEM) for numerical modelling strain evolution during relevant instants of the crack propagation.

Our proposed strategy consists of the analysis of the strain field evolution in the course of an UL application. We also wish to address and resolve the disagreement that exists between published reports regarding the dependence of the FCGR acceleration as a function of the amplitude of the baseline fatigue load. To this end, we analyse the strain field variation following the application of UL using non–linear FEM analysis. Furthermore, the crack closure effect was visualised directly by means of DIC analysis of the relative displacement of crack faces, allowing explicit evidence to be extracted and presented [235, 236]. DIC was used to record the crack flanks relative displacement using a sequence of images of the crack tip and its near wake acquired during fatigue test. The correlation between these images and the instantaneous applied load provides a means of direct evaluation of the crack opening load, and the calculation of the reduction in the effective Stress Intensity Factor.

Fatigue tests were carried out using mini-Compact Tension (CT) samples extracted from a rolled plate of Mg alloy AZ31b A samples was first subjected to cyclic constant amplitude loading at the load ratio R=0.1. After crack was nucleated and propagated, a single UL was applied to the sample. Two additional samples were tested at constant amplitude until failure occurred in order to provide a baseline for comparing the behaviour of the UL sample behaviour. In the case of strain field assessment around the crack tip, a sample was firstly fatigued at constant load amplitude and before the UL application, a single OL was applied to the sample. The strain mappings were performed using synchrotron diffraction (SXRPD) prior, during and after the UL application. SXRPD has been used in previous studies for the characterization of the stress field [83, 237-239], in particular around the crack tip during crack propagation and at the occurrence of an overload [128, 129, 222, 223, 239]. This method allows high spatial resolution observation of the elastic strain state surrounding the crack tip, the identification of the plastic zone, and monitoring its evolution during subsequent crack propagation. The high energy and flux provided by synchrotron X-ray beam ensure that the experimental data collection was carried out in transmission mode. Therefore, the subsequent strain analysis is performed on the bulk of the sample, allowing fast data collection and the construction of two-dimensional strain maps of the area of interest at the crack tip. We focus our attention particularly on the visualisation of the strain component parallel to the loading direction.

The purpose of carrying out FEM analysis in the first instance was to comparing numerical predictions with experimental observation and then validate the simulation approach. The validated model was firstly used to perform parametric analysis varying the baseline fatigue load in terms of loading ratio keeping constant the loading range. Secondly, the effect of the underload magnitude was also explored through an additional parametrical analysis. As output of these simulations, the computed J-integral was considered to be representative of the material propensity to crack propagation. Therefore, in the loading cycle following the underload, the J-integral range and its mean value were computed; these values formed the basis for discussion and observation of the results.

4.4.2. Material description fatigue test and results

The material of choice for the experiment outlined in the previous section must fulfil a number of requirements in order for meaningful results to be obtained. Firstly, sufficient amount of ductility is required, since it enhances the effect of retardation/acceleration due to OL/UL through the creation of large plastic zone. This must be balanced against stiffness to ensure sufficiently high magnitude of yield strain which in turns, produces high values of elastic strain at the crack tip that are more easily measurable keeping errors low. Secondly, high resolution SXRPD requires the material to be suitably fine-grained to ensure good polycrystal averaging over multiple grains of many possible orientations within the gauge volume to give rise to smooth powder diffraction patterns that lend themselves naturally to interpretation. Magnesium alloy AZ31b subjected to severe plastic deformation by Constrained Groove Pressing (CGP), under controlled temperature conditions in order to promote re-crystallisation, possesses a refined grain size in the micron range, and displays an increase in tensile strength with respect to the base heat treatment, without compromising toughness [240, 241]. The resulting favorable combination of properties is characterised by the yield stress is of $\sigma_y \approx 260$MPa, 10% of total elongation and the grain size distributed in the range from <1µm to 5µm maximum. Previous work has been carried out and reported concerning fatigue crack growth behaviour of this alloy under variable loading history, the overload (OL) effect in particular [242], confirming the feasibility of the experiment proposed presently.

A 2mm-thick miniature Compact Tension (CT) specimen (35mm) was used for fatigue testing. The same sample geometry was successfully adopted in the previous Chapter 4.1. Cyclic loading was applied using a servo-hydraulic fatigue rig capable of applying cyclic loading up to 20kN. The baseline constant amplitude fatigue loading was performed at the frequency of 7Hz. Simultaneously, the crack progression length was monitored and recorded using an optical microscope system providing images having pixel size of around 1µm, allowing precise determination of the crack length and evaluation of fatigue crack growth rate (FCGR), and video recording of the crack opening and closure for subsequent DIC interpretation. The fatigue test setup is depicted in Figure 63(a).

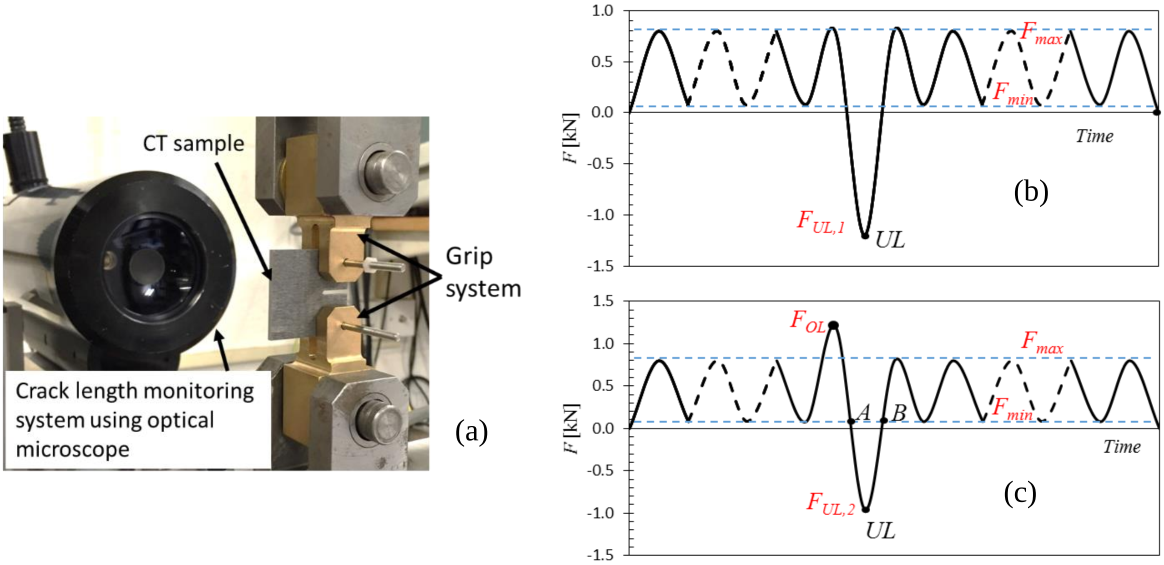

Figure 63 (a) Test setup arrangement, (c) fatigue loading history sample s.3 (c) and fatigue loading history sample s.4.

Four samples were employed in the experiment. Two samples denoted *s.1* and *s.2* were cyclically loaded at constant amplitude until complete sample fracture occurred. The cyclic loading ranged from the minimum load of F_{min}=80N to the maximum load F_{max}=800N, with the load ratio R equal to 0.1. The sample (*s.3*) was cyclically loaded until it had reached the crack length of 4.5mm when an UL was applied having magnitude of $F_{UL,1}$=-1200N. Further constant amplitude fatigue loading allowed the assessment of crack propagation rate as the crack advanced. During the whole fatigue test, images of the crack flanks were taken with the purpose of performing DIC analysis. The load history is summarised in Figure 63(b). A fourth sample (*s.4*) was tested at the same fatigue baseline as the two baseline samples, but subjected to a single overload (OL) of F_{OL}=1200N followed by an Underload (UL) $F_{UL,2}$=-960Nwhen the crack length reached 4.5mm, as illustrated in Figure 63(c). Such particular loading history was chosen in order to validate the numerical model in an extreme situation where both anomalities (OL/UL) are present. The OL/UL application was in situ during the SXRPD experiment, a miniature tensile loading stage provided by Deben© was used. The strain field around the crack tip was mapped at various loading levels. A single UL of magnitude was applied. The UL ratio defined as the FUL divided by the maximum value of the baseline cyclic loading Fmax was equal to R_{UL}=-1.2.

Crack propagation results

The monitoring of the crack length as a function of the number of cycles during the fatigue test allowed the evaluation of crack growth rate variation with the applied stress intensity factor range. As seen in Figure 64(a), in the case of the sample subjected to UL, a brief acceleration of the crack propagation rate was observed. The UL induced an instantaneous increase in the propagation rate. Using the SIF formulation found in [197], the fatigue crack growth rate (FCGR) and related Paris' curve were constructed (Figure 64(b)). The plots in Figure 64 incorporate the data from the totality of the tested samples. Fatigue crack growth rate (FCGR) acceleration is apparent. The FCGR plot in Figure 64(b) provides the basis for quantitative evaluation of the duration of acceleration effect, as it becomes apparent when the effect of UL vanishes and the steady-state condition is re-established. Quantitative analysis reveals that the FCGR alteration persists over 0.57mm crack advance following the UL application. A close-up plot of the FCGR is shown in Figure 64(c) where the sample subjected to UL and OL/UL were plot exclusively; this helps visualising the difference between the two.

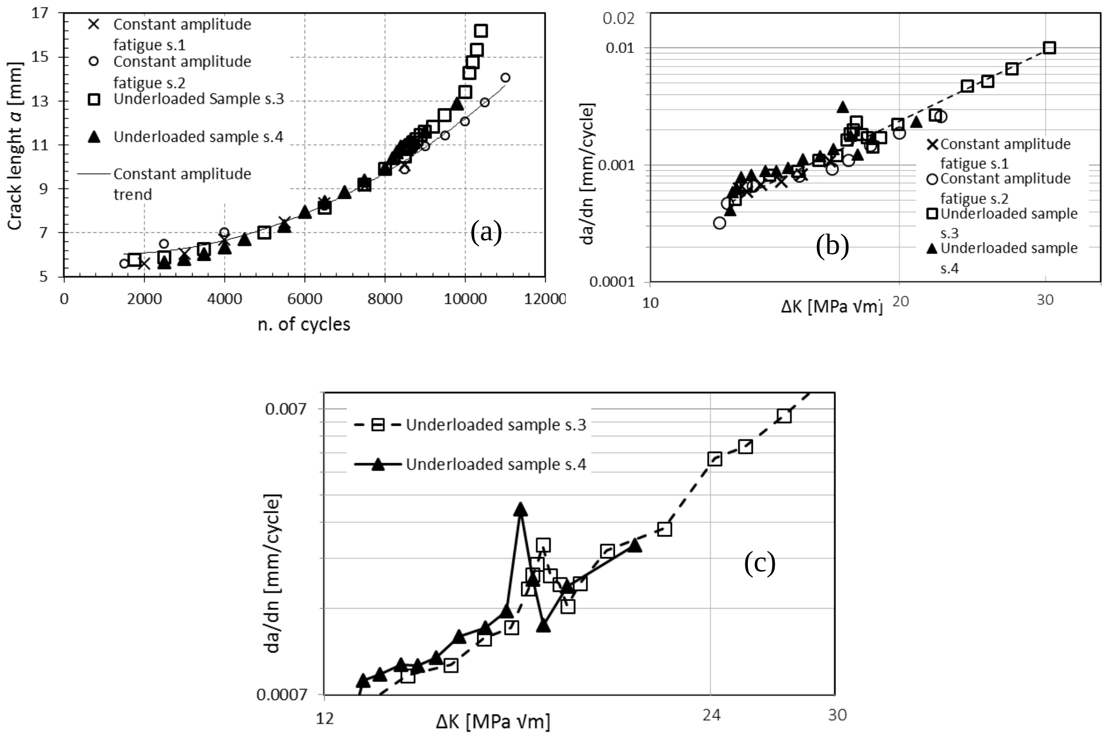

Figure 64 Fatigue crack propagation results. (a) Crack length vs. n of cycles (b) Fatigue Crack Growth Rate (FCGR) vs. SIF range and (c) enlargement of the FCGR vs. SIF range at the occurrence of the Underloads for samples s.3 and s.4.

The two samples tested under steady-state constant cyclic amplitude conditions (*s.1* and *s.2*) were used to extract the power law fit to the FCGR vs ΔK dependence, leading to the Paris' law expression (18) for this material:

In which the coefficients C and m were found to be equal to 2×10^{-7} [mm/(cycle MPa √m)] and 3.21, respectively. The line corresponding to the above equation is shown dashed in Figure 64(b).

4.4.3. Strain field evaluation

<u>*SXRPD experimental setup*</u>

In order to map the distribution of strain at the crack tip, three sets of measurements were performed at various loading conditions. Sample *s.3* used in the SXRPD experiment was mounted upright in the Deben® miniature tension-compression stage capable of applying load up to ±5kN. A small segment of the loading history reported in Figure 63(b) around the UL application were reproduced *in situ*, with the three conditions of measurement identified as *A* (before underload), *UL* (during underload), and *B* (one cycle following the underload).

The strain maps at the crack tip were constructed using SXRPD strain analysis. The experiment was performed at Test Beamline B16 at the UK synchrotron facility, Diamond Light Source (DLS) located at Harwell Oxford (UK). Given the sample thickness of 2mm, the high flux, high energy beam provided by Synchrotron X-ray was used to perform the test in transmission mode. In this modality of mechanical microscopy, the diffraction patterns obtained provided averaged information about the lattice parameter variation through the entire sample thickness. The X-ray energy used was 20keV and the beam size 45µm×45µm.

The sample arrangement is shown in Figure 65. The sample was placed in the upright configuration with respect to the tensile stage, so that contemporaneous load application and beam mapping was possible. The tensile stage was placed on a beamline translation stage in order to allow the movement required for the scanning along the *x* and *y* laboratory coordinate axes defined according to Figure 65, (*z* axis associated with the incident X-ray beam, *x* axis horizontal and *y* axis vertical in the plane perpendicular to the incident beam). 2D diffraction patterns consisting of sharp and smooth Debye-Scherrer rings were acquired by means of a Photonic Science X-ray Image Star 9000 detector.

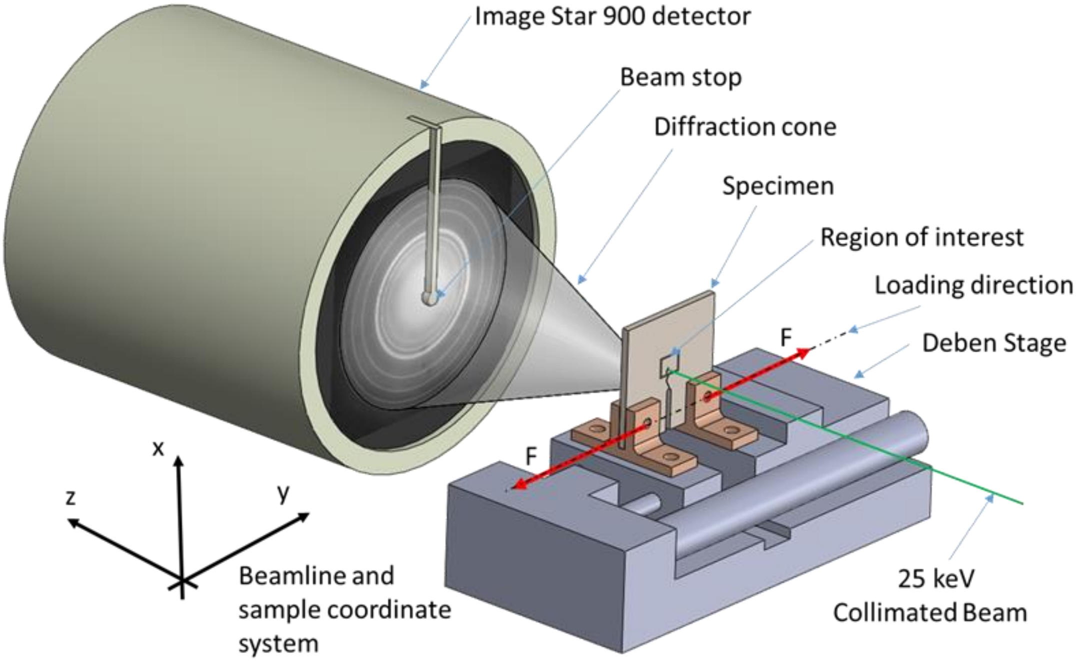

Figure 65 Experimental setup indicating the coordinate system, principal experimental devices adopted and sample orientation.

SXRPD strain mapping

In order to determine the strain field map around the crack tip from the acquired diffraction patterns, azimuthal integration (binning) of Debye-Scherrer rings was performed for the grain family corresponding to the reflection with the Miller index (20.0) of the hcp structure of magnesium alloy AZ31b. The strain component aligned with the loading direction was sought by integrating the sector of the ring within the range ±30°. The adoption of such sector of integration leads to a maximum relative error of ~8.5% in strain determination in terms of the maximum difference between principal strains. In the present case, the analysed strain component is considered be one of the in-plane principal strains. Following binning to obtain the equivalent 1D X-ray diffraction profile as function of the diffraction angle 2Θ, the variation of lattice spacing Δd was evaluated throughout the scan, and used as input in the differential form of Bragg's law that allows the strain to be determined (64).

As is well known, the determination of strain using the above formula requires the knowledge of the strain-free lattice parameter d_0 that denotes the distance between crystal planes in the unstrained condition. Such parameter is not always easy to be determined, since *a priori* knowledge of the location where the value of strain approaches zero or a known value is problematic, the use of powdered sample is fraught with difficulties of preserving identical scattering conditions and sample-to-detector distance, and solute chemistry variations due to heat treatment history may cause the variation of lattice parameter compared to the literature values for the material studied. The strategy adopted in order to overcome this issue was to rely on the use of FEM as a modelling in order to obtain most reliable matching of simulation to observation, whilst considering d_0 as a fitting parameter to minimise the disagreement. More specifically, the predicted strain field was considered in a region lying sufficiently far away from the crack tip not to be affected by local plasticity, yet sustaining measurable elastic strain. Further matching with the numerical model allowed the refining of d_0 that turned to be 0.244nm. Therefore, this value was used to determine the magnitude of experimentally measured strain field at any point on the maps.

A Matlab routine was used for the analysis of 1D diffraction patterns. For each experimental position the (20.0) reflection was fitted with a Gaussian peak curve, and the relative change in the lattice spacing corresponding to the peak centre was calculated. Strain maps were constructed in Matlab. The

d_0 was then varied seeking the best match of these results with the numerical prediction along the crack bisector.

FEM analysis

Since the experimental strain field mapping is the average value along the sample thickness, the modelling of crack growth cannot be performed under the simplification of plane-stress or plane-strain. To better reproduce the real case, a three-dimensional FEM analysis was performed with the purpose of capturing the strain field variation through the thickness of the sample. Given the importance of accurately represent the material hardening behaviour within the FEM software, a combined hardening rule was implemented. Such rule provides the description of the kinematic hardening rule by means of the Chaboche model [243] and the cyclic softening/hardening behaviour by superposition of an isotropic hardening rule as described in [244]. This model decomposes the backstress into several components where each of the components, individually evolved according to an Armstrong and Frederick hardening law [245]. The idea of decomposing the backstress has become a main interest since. Furthermore, in order to improve the uniaxial and multiaxial ratcheting simulation, modifications have been made to the Chaboche afterwards.

This model required an accurate calibration that was accomplished using a supplementary model where cyclic behaviour was simulated and, by matching the result with the experiment, the model's coefficients were found. The kinematic part was calibrated using two backstresses. Values of the combined kinematic/isotropic model found are summarised in the Table 7.

$\boldsymbol{C_1}$ [MPa]	$\boldsymbol{\gamma_1}$	$\boldsymbol{C_2}$ [MPa]	$\boldsymbol{\gamma_2}$	$\boldsymbol{Q_\infty}$ [MPa]	$\boldsymbol{b}$
90000	9000	600	3	50	2

Table 7 Combined hardening rule coefficients

Regarding the kinematic part, the coefficients C indicate the slope of the hardening rule and γ is the rate at which the kinematic component approaches its asymptote. As far as the isotropic rule is concerned, the parameter Q_∞ is the asymptotic value of strain hardeinig/softening and b is the rate at which the isotropic component approaches its asymptote.

A quarter of the CT sample was modelled taking advantage of the symmetries in order to minimise the computational effort. The 8-node linear brick elements were used for the discretisation of the model.

The mesh convergence allowed the finding of a good compromise between the computational speed and result quality. The half thickness of the sample was subdivided in n.6 elements, the elements present at the vicinity of the crack wake were made 0.1mm x 0.02mm and, at the OL/UL application site, the mesh elements were 0.02mmx0.02mm as depicted in Figure 66. In total, the model was constituted of 27‘000 elements.

The strain evolution, as the crack propagated through the sample, was simulated by considering several propagation steps from the nucleation until the final stage. The crack propagation was subdivided in n.12 steps. The first 10 steps after crack nucleation were equispaced of 0.4mm and the last two steps were respectively 0.3 and 0.2mm. Although the real propagation da/dN was considerably smaller than the numerically modelled propagation step, such discretisation was thought to be sufficiently small to capture the plastic deformation induced by the whole propagation process; this was confirmed by a convergence of result analysis. At each propagation step, the cyclic load was applied to simulate the material cyclic response. In order to capture the crack flanks contact and thus the induced plasticity crack closure, an hard contact was modelled at the surface where the contact could happen as shown in Figure 66. The modelled contact was of the type ``*Hard*`` with the method ``*Augmented Lagrange*``.

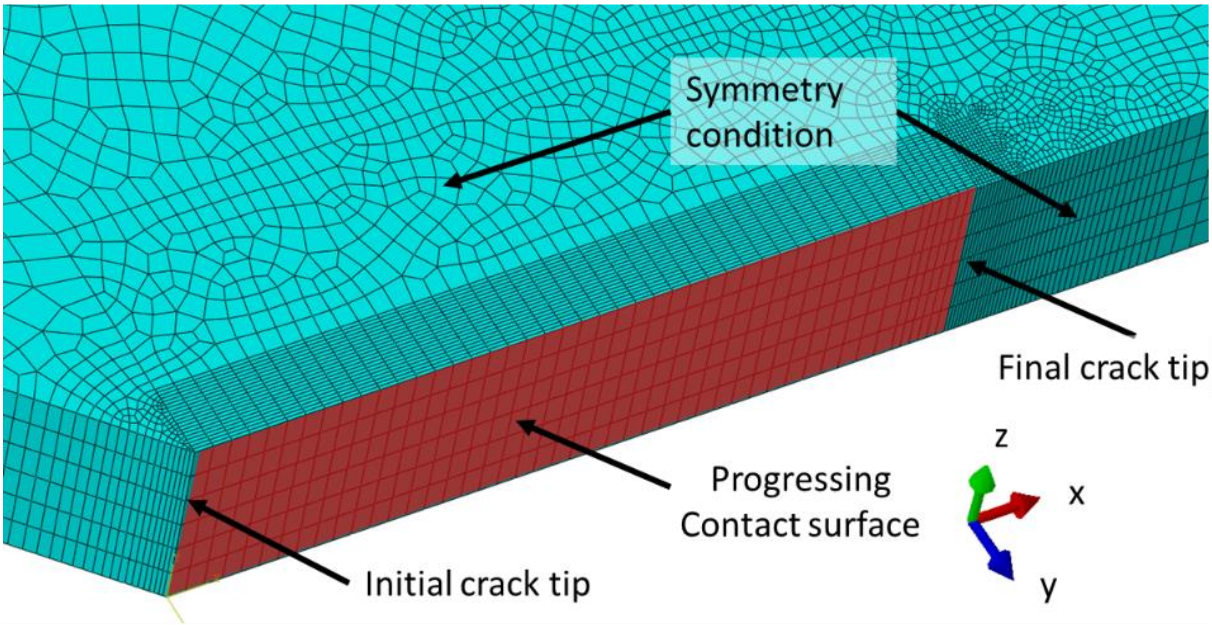

Figure 66 Model discretisation. Detail of the mesh refinement along the crack propagation path

SXRPD results and FEM model validation

After matching the numerical outcomes with the experimental ones by refining of the material d_0, the obtained maps can be plotted. Figure 67 shows contour plots for the three instants of loading (A, UL, B) considered. Note that the crack tip is not always located at the centre of the Figure as a consequence of the choice of experimental setup. The crack tip location is indicated by the wedge-shaped black lines on the left of each map and, after rough estimation, it was precisely localised by matching with numerical model

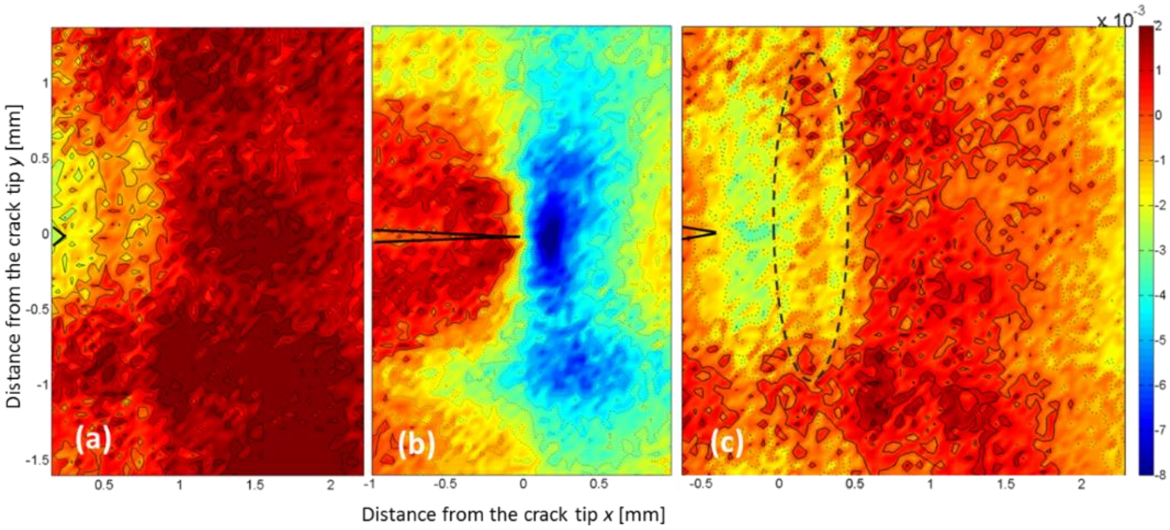

Figure 67 Strain contour map ε_{yy} obtained by SXRD. a) before (instant A) b) during (instant UL), and c) after (instant B) UL application.

In the first map shown in Figure 67(a), the region of interest in the strain field surrounding the crack tip has been captured. The strain field at the application of the UL is revealed in fine detail in Figure 67(b).

Compressive strain ahead the tip was detected in all the loading steps. As expected, at the occurrence of the UL, high magnitude of compressive strain was generated, and a steep gradient of strain ahead of the crack tip was observed.

It is worth noting that ahead of the crack tip in the cases before and after the UL in Figure 67(a) and Figure 67(c), a small jump can be observed along the crack bisector, producing a sort of banding effect in the maps (Circled by dashed line in Figure 66(c)). This suggests that a pre-existent background residual strain may persist in the material arising from the previous severe plastic deformation during material forming.

The comparison of the strain fields obtained is reported in *Figure 68* as line plots along the crack bisector. The experimental results are shown along with the error bands at 95% of confidence arising from the error of peak position obtained from the Gaussian fitting of the diffraction peaks, propagated to calculate the strain uncertainty.

The comparison between the experimental and numerical results shows satisfactory overall match in terms of the trend in strain variation. Even in terms of strain magnitudes, the numerical predictions appear to match the experimental profiles. Unfortunately, the strain field ahead the crack tip for the loading condition A(Figure 63(b)) shown in Figure 68(a), cannot be verified since lack of experimental points.

On the basis of the results presented in this section we draw the conclusion that satisfactory validation has been obtained of the numerical approach selected, and that it can be adopted for further analysis of UL effects on FCGR.

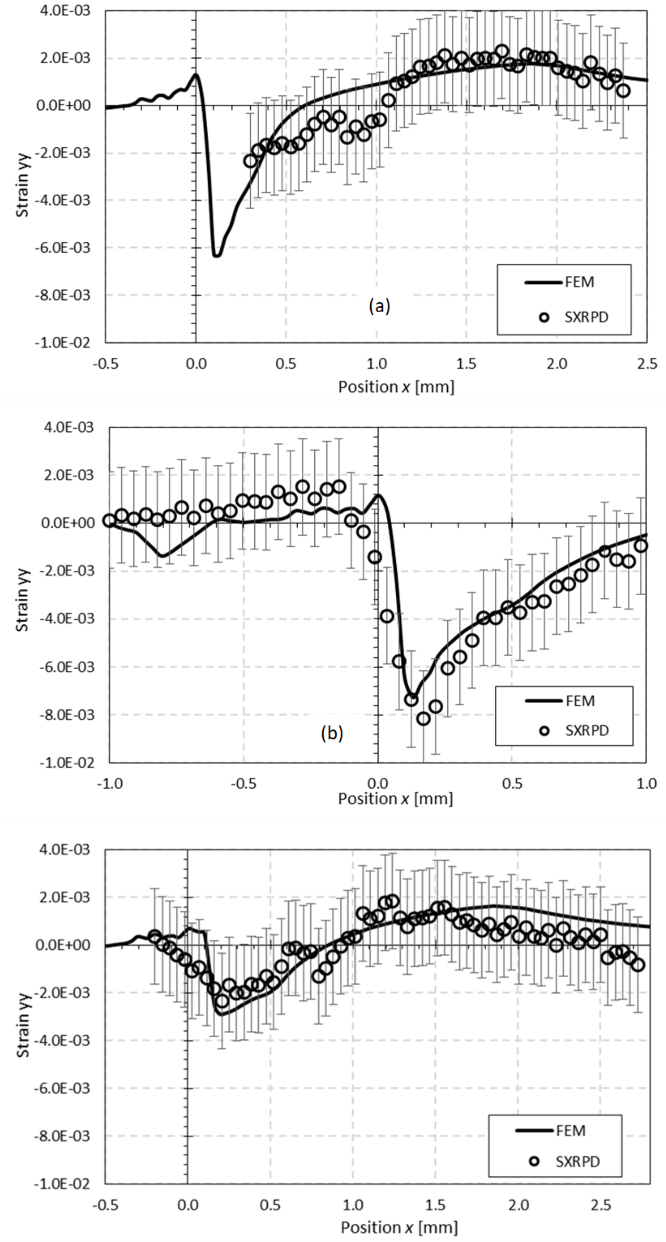

Figure 68 Experimental vs. FEM results of the elastic strain in the direction of the external load ε_{yy}. The origin of the x axis indicates the crack tip position. Comparison along the crack bisector (a) before UL (instant A) (b) during UL (instant UL), and (c) after UL (instant B).

<u>*FEM parametric analysis*</u>

To advance the understanding of how the crack growth is affected by the cyclic loading and the magnitude of the UL, several parametric analyses were performed. In the elastoplastic regime, one of the effective parameter that can be used as representative of the crack driving force is the J-integral [246-248]. This parameter is known to be efficient in accounting also the effect of crack closure [249], therefore we used such J-integral, in particular its range within each cycle, for the assessment of the crack driving force change as the UL magnitude and baseline loading vary. The range of J-integral was then evaluated at the cycle that follows the UL application in each simulation. The computation of the J-integral value was performed at the distance of 0.5 mm from the free surface of the sample in order to obtain a good compromise between the plane-stress condition (free surface) and the quasi-plane-strain condition (mid-thickness). The path of integration was chosen wide enough with the purpose of avoiding artefacts that may arise from the crack tip plastic zone.

The first parametric analysis was focussed on the evaluation of the UL magnitude effect on the variation in J integral range ΔJ. The cyclic fatigue loading was kept constant and it was the same as shown in Figure 63(b). Along with the range, the mean value was also monitored since it may play an important role on fatigue damage. Therefore, the mean value of J–integral in the cyclic loading and the ratio defined as the minimum value divided by the maximum value ($R_J=J_{min}/J_{max}$) were assessed. With this end, n.7 analysis were performed. The Figure 69 shows the variation of both the mean value J_{mean} and the range ΔJ.

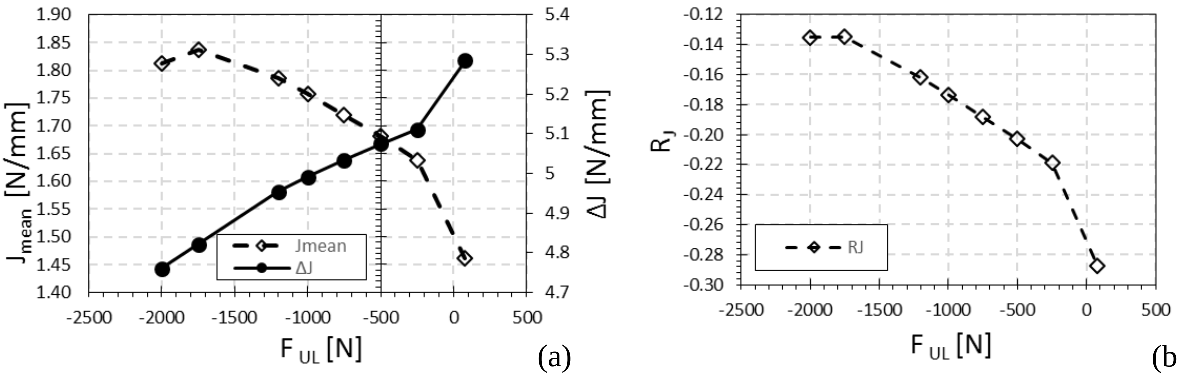

(a) (b)

Figure 69 Parametric analysis results for the variation of the magnitude of UL. Plots show the variation of (a) the mean value J_{mean} *and the range* ΔJ *of the J-integral, and (b) of the J-integral ratio* R_J.

Regarding the effect of the baseline fatigue loading, we studied several cases where the loading range applied to the sample was kept constant equal to the above shown analysis ΔF=720N and the variable was set to be the external loading ratio R. The results are shown below in Figure 70.

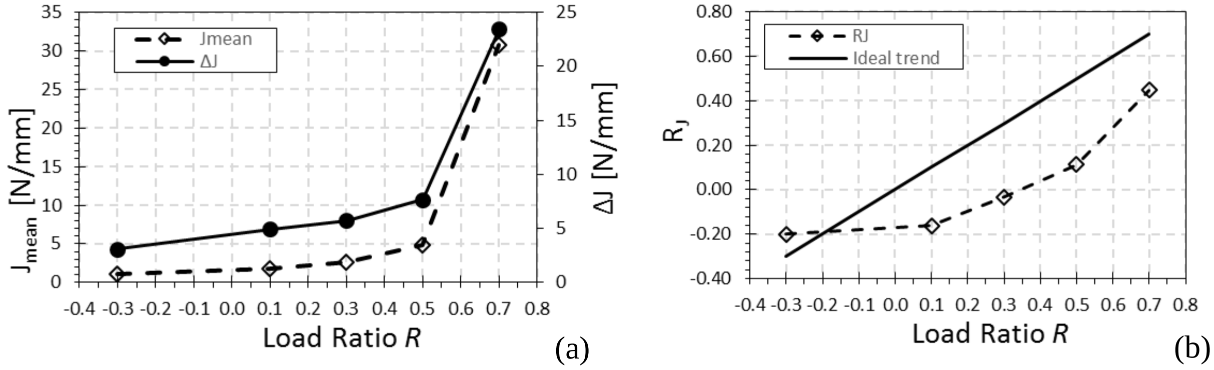

(a) (b)

Figure 70 Parametric analysis results varying the baseline loading ratio. (a) Mean value J_{mean} *and range* ΔJ *of the J-integral plot and (b) J-integral ratio* R_J *plot.*

Crack closure analysis

As previously discussed in reference to previous publications, crack acceleration may occur mainly due to the combination of tensile residual stress with the change in the crack closure level. Here we analyse how the crack closure mechanism deviates from the steady-state trend after an UL occurs.

The fatigue test setup used in the present study allowed capturing a sequence of detailed images of the crack tip and wake during cyclic test at low frequency (0.1Hz). As successfully previously conducted by other researcher [218, 221, 250-252] a DIC analysis is able to capture the crack flanks relative displacements. Using a Matlab-based DIC software [253], this relative crack flank displacement, also known as the Crack Opening Displacement (COD), was monitored at the distance of 0.25mm behind the crack tip towards its wake. Such analysis was performed once the crack had reached different lengths: 7.73mm, 8.18mm, 8.56mm, 9.09mm, 9.65mm, 10.35mm (before UL), 10.35mm (at UL), and 10.52mm, 10.84mm, 11.01mm (after UL).

An example the COD behaviour in the presence of crack closure is reported in Figure 71(a), where the COD is plotted together with the applied load, so that the direct comparison is possible. The COD follows the sinusoidal profile of the applied load very well whilst the magnitude of applied load remains high. However, in the course of unloading, the COD reduces to its minimum value of zero before the load reaches the cyclic minimum, as the flanks come into contact that does not allow any further relative movement. The most important bit of information that can be extracted from this type of graph is the crack opening load denoted F_{op} below, i.e. the value of load at which the crack flanks first come into contact during unloading part of the cycle, or separate under increasing load. For example, for the case shown in Figure 71(a) crack closure occurs at around 200N of applied external force. In the majority of the cases, the opening load is correspondent to the closure load (an example is given in Figure 71(a)).

The opening load can be used for the calculation of the opening stress intensity factor, and hence the effective stress intensity factor. For the purpose of exploring the variation in crack closure level as the crack moves past the UL region, we report the normalised opening load as a function of the crack length in Figure 71(b).

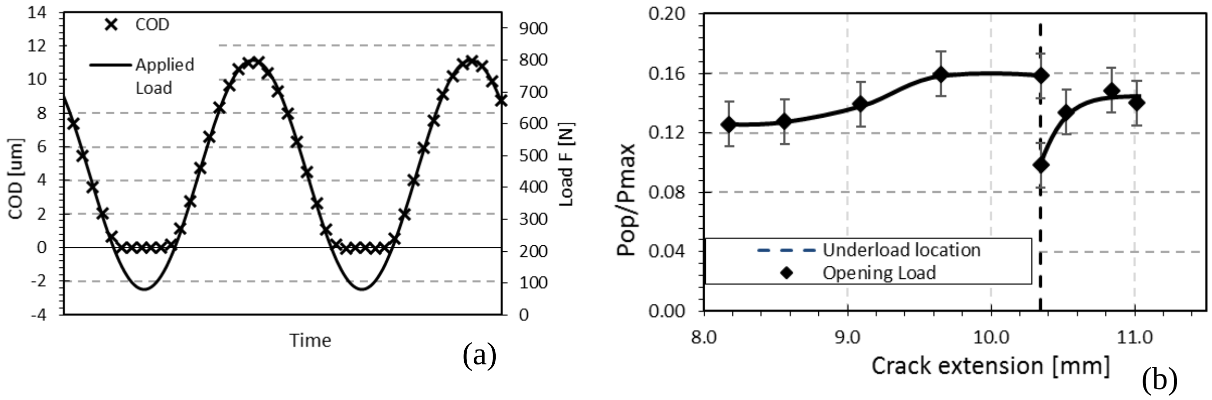

Figure 71 Crack closure analysis. (a) Example of simultaneous crack opening displacement and applied load plots example at crack length a=2.577mm. (b) and normalised opening load plot during crack propagation.

The opening load was normalised with respect to the maximum load (800N). The error arising from the calculation of the opening load was estimated, and is reported using error bands at 95% confidence. As Figure 71(b) shows, at small crack lengths the crack closure ratio was around 0.13. As the crack propagates this value increases gradually until it reaches the value of 0.16 immediately prior to the UL application. After UL occurs, a clear drop in the crack closure ratio is observed, down to the value of 0.10, or 37.5% lower. The prompt return of the FCGR to the steady-state condition is here confirmed by the fact that after ~0.5mm of further crack propagation the crack closure ratio returns to the value ~0.15.

The opening load could be used directly for the calculation of the actual FCGR, by computing the effective SIF at the crack tip as:

$$\Delta K_{eff} = K_{max} - K_{op} \tag{80}$$

Here K_{op} is the SIF at the opening load F_{op}, and K_{max} is the SIF when the load reaches its maximum value during cycling. The effective SIF ΔK_{eff}, according to the DIC closure analysis, was reconstructed and plotted against the FCGR (*Figure 72*).

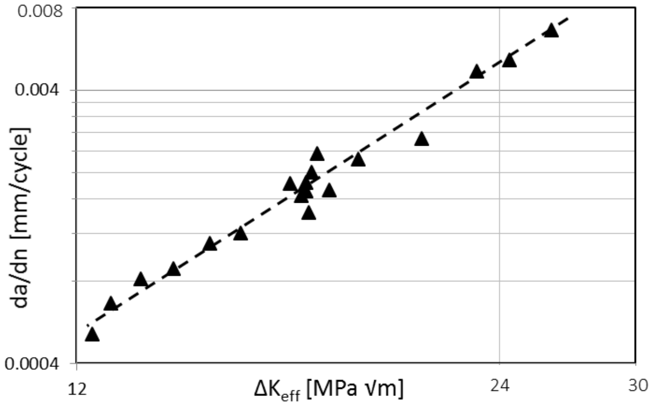

Figure 72 Effective Stress Intensity factor plot relative to the analysed sample s.3.

The reduction of K_{op} leads to an enhancement of the effective SIF and subsequent crack acceleration. In fact, in Figure 72 it is possible to note that the alteration given by the UL (acceleration) that was clearly visible in the plot in Figure 64(c) it is now attenuated by correcting the closure effect. Further implications of these findings are discussed in the following section.

4.4.4. Discussion

Fatigue test involving the application of a single peak compressive underload (UL) were used to explore the crack acceleration effect that persists over a certain range of subsequent crack extension (sample s.3). Alongside this test, a more complex loading history was applied to an additional CT sample for the in-situ measurement of the strain evolution (sample s.4).

In both the experimental tests, where OL and/or UL were involved, crack acceleration was experienced. The results summarised in Figure 64, specifically in the close-up in Figure 64(c), have highlighted two slightly type of accelerations. In the case of sample s.3 (no OL), even though the UL magnitude was greater that the case of sample s.4, the effect of retardation in terms of FCGR was of smaller magnitude. On the other hand, if we consider the extension of such retardation, then we can certainly say that for the sample s.3 it persist for longer crack propagation length. This effect may be due to the interaction of OL/UL that produced a great acceleration at the first stages of propagation and a quick restoration to the steady-state regime. In fact, in some cases the sole occurrence of an OL may create a short acceleration preceding a more persisting retardation region.

Supporting experimental measurements of the strain fields were mainly aimed at the validation of a three-dimensional FE model. Such FE model allowed the identification of the role of strain field change ahead of the crack tip and the modification of the crack closure effect that were identified as the crucial determining mechanisms that caused the observed phenomena.

Crack acceleration is believed to be associated with the tensile residual elastic strain (and stress) present immediately ahead of the crack tip, or with the reduction in the level of residual compression induced by the prior steady-state crack propagation stage. We attempted to capture this tensile strain region experimentally using SXRPD. No direct evidence of local tensile strain could be detected ahead the crack tip after the occurrence of UL but, a prominent change in the strain level was observed. Indeed, by comparing the Figure 68(a) and Figure 68(c), it is evident that the compressive strain peak ahead the crack tip was attenuated with the introduction of the UL.

However, the experimental result obtained was also used as the basis for developing and validating a numerical simulation based on FEM calculation that allowed parametric analysis to be conducted.

Two different parametric FE analyses were performed with the goal of evaluate the effect of the baseline cyclic loading, in terms of loading ratio R, and the magnitude of UL applied.

The analysis at constant baseline fatigue loading was performed at R=0.1 at the same amplitude as shown in Figure 63(b). As it is possible to see in Figure 69(a), as the absolute magnitude of the UL increases, the range of J integral ΔJ decreases. For an UL, that varies from 80 to -2500N, the ΔJ varies of around 10%. Exactly the opposite trend can be observed for the mean value of J integral J_{mean}; in fact, as the UL absolute magnitude increase, the J_{mean} increases too. In the case of J_{mean}, the variation in the same range of UL change is of 24%. Another way of visualising this is by plotting the local J integral ratio defined as $R_J = \frac{J_{min}}{J_{max}}$ as shown in Figure 69(b). This led us to believe that, in the case of R=0.1, the crack acceleration is due to the drop of the mean value of J integral which is predominant to the increase of ΔJ.

The second parametric analysis was conducted keeping constant both the magnitude of the UL (F_{UL}=-1200N) and the load range ΔF=720N, varying the load ratio R. In this instance both the J_{mean} and the ΔJ increase monotonically as the load ratio R grows, as shown in Figure 70(a). Particularly, at high loading ratios (e.g. >0.5) the ΔJ is amplified of around one order of magnitude. Of course, this analysis does not attempt to capture how the ΔJ evolves during the further propagation but, surely right after the UL application for the first cycles the material is stressed more than the unaltered condition and thus more prone to promote crack propagation. The plot of the R_J against the external loading ratio for this analysis, shown in Figure 70(b) reveals also another important aspect. As we can see, the local R_J is reduced with respect of R when this last one is positive. This would let us to think that, at R>0 the crack should be less prone to propagate when the UL is involved but, it is important to bear in mind that at the same time the range of J integral grows much faster as the R increases. Therefore, the conclusion is that the chance in loading ratio is reflected in greater part in the change of J integral range. Furthermore, high load ratios of the fatigue baseline enhance the effect of UL.

A graphical representation of the effect of the loading ratio R is shown in the Figure 73. These FEM contour images superimposed to the 6x deformation amplification, provide some insights about the causes of such magnification of the ΔJ when high loading ratio of the baseline is involved. In the Figure 73(a) and (b), we can see the crack status at the minimum load applied, before the UL, for two loading radio cases (i.e. R=0.7 and R=0.1). The following two Figure 73(c) and (d) show the strain and deformation status during the application of the UL (same magnitude) respectively for R=0.7 and R=0. It is clear that, whereas the loading ratio is high, the UL produces much larger deformation at the crack tip compared with the one at R=0.1. In fact, for R=0.1 the majority of the deformation occurs at the notch root. This effect is due to the level of crack closure and blunting induced by the baseline. Indeed, the high F_{max} during cycling produced great level of blunting and closure that then allows this ``pincer`` effect at the crack tip when UL occurs. For low loading ratios, when the crack closes under the effect of the UL, the stresses are distributed along the crack flanks and not concentrated at the tip.

In is worth mentioning that, if the crack faces go in contact, the compressive forces that arise may flatten the asperities present and, as consequence, the magnitude of the roughness-induced crack closure is reduced.

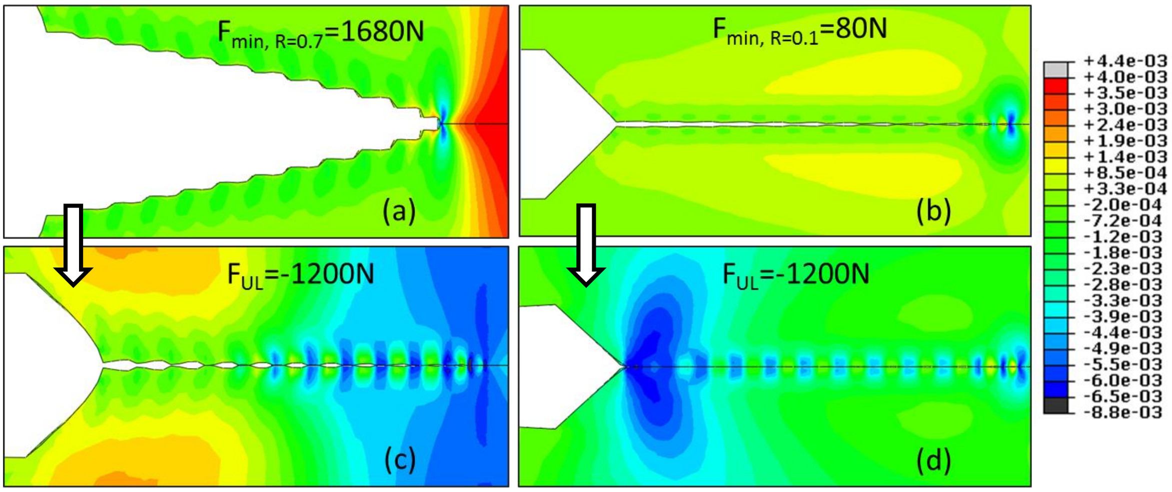

Figure 73 Contour plots of the elastic strain component parallel to the load applied ε_{yy} at the relevant load conditions, plotted over the deformed geometry after the application of magnification factor (6x). (a) Before the application of the UL at the minimum load F_{min} in the case of load ratio R=0.7. (b) Before the application of the UL at the minimum load F_{min} in the case of load ratio R=0.1. (c) During the application of the UL right after the cyclic loading at R=0.7. (d) During the application of the UL right after the cyclic loading at R=0.7

In summary, the enhancement of the tensile strain with the increasing baseline load leads to the conclusion that crack acceleration after UL is crucially dependent not on the UL magnitude, as might be surmised, but rather on the magnitude of the predominant cyclic maximum load prior to the UL application. Thus, our conclusion is in agreement with [254], but is based on the advanced and detailed insight into the processes occurring at the micro-mechanical level at the tip of a growing fatigue crack.

Along with the strain field change at the crack tip, the plasticity induced crack closure is another mechanism thought to be involved in crack acceleration. To examine this hypothesis, the investigation of crack closure was conducted by means of DIC analysis. In this way, the crack closure/opening load ratio was evaluated at several crack propagation stages before and after the UL. It turned out that right after the UL occurrence the crack closure/opening load was reduced, Figure 71(b). The correction of the SIF range by means of the effective SIF range ΔK_{eff}it is demonstrated that crack closure plays a crucial role in crack acceleration following UL application. Also, the extent of the deviation in crack closure/opening load corresponds correctly to the length of crack propagation over which acceleration is observed.

4.4.5. Conclusion

The work presented in this chapter provides experimental and numerical evidence of the mechanisms involved in the propagation of a fatigue crack propagation past an occurrence of compressive underload (UL). The strain field at the crack tip was mapped by synchrotron X-ray diffraction, which was used for validating a numerical model of deformation. Experimental measurement did reveal a limited reduction of the compressive strain experienced in the plastic region ahead the crack tip. FEM parametric analysis revealed that lower values of the baseline fatigue loading ratio reduced the strain field alteration after UL and, if they were low enough, made the effect of UL negligible. The underlying mechanism behind this effect was explained considering the crack tip blunting and crack closure induced by the fatigue baseline. Keeping the load range constant, it is possible to observe and enhancement of the crack closure and blunting effects when the loading ratio increases, which in turns, has a massive impact on the effectiveness of the UL. It is worth highlighting that at low loading ratios, the UL produces great deformation along the entire crack faces and therefore the asperities are smoothed with a consequent reduction of the roughness induced crack closure effect. Regarding the repercussion of the UL magnitude on the driving force, this is surely less prominent that the baseline loading ratio. In fact, great variation in UL magnitude produces small change in the mean value of the cyclic J integral that is thought to be the predominant parameter in this case.

Crack closure was monitored throughout crack propagation. The opening load displayed a sudden drop of 37.5% after UL application, and a gradual return to the steady-state value. The restoration of the unaltered crack closure state occurs at around 0.5mm from the UL position, which is in agreement with the crack propagation length over which acceleration is observed. The drop in the opening load can be seen as an enhancement of the effective SIF range, and therefore provides a clear explanation for the acceleration effect observed.

In conclusion, the mechanisms that contribute to crack acceleration are mainly: crack tip blunting, crack closure and change in residual stress state at the crack tip. The increase of strain magnitude was not as obvious as the reduction in the opening load due to crack closure. This leads us to believe that the contribution given by crack closure is greater than the one given by the crack tip plastic strain effect.

5. Residual Stress evaluation and modelling in polycrystalline materials

5.1. Residual Stress in shot peened notched samples

5.1.1. Introduction

In the present section, the FIB-DIC ring-core method was adopted for the evaluation of residual stress induced by SP in samples made from aluminium alloy Al-7075-T651 and having three different V-notch root radii. The measurements for each specimen were performed along the notch bisector and along a line perpendicular to it running at a certain distance from the notch root. Taking full advantage of the DIC analysis it was possible to evaluate the residual strain in two orthogonal directions. The measurements are interpreted, and the results discussed in comparison with a small and efficient mathematical model based on the eigenstrain approach.

5.1.2. Sample description and FIB-DIC measurements

Sample Description and Measurement Locations

The samples used in the study were machined from a 4mm-thick rolled aluminium alloy plate (Al7075-T651). They had different notches of varying severity machined in them in order to obtain three notched samples. All notches were V-shaped and differed from each other only in the fillet radius at the notch tip. The geometry and the main dimensions of the samples are depicted in Figure 74. Table 8 shows the geometric characteristics related to Figure 74(a), and the corresponding values of the Stress Concentration Factor K_t.

Sample n.	**Fillet radius ρ [mm]**	K_t
1	2	1.52
2	0.5	2.37
3	0.15	3.76

Table 8. Samples' geometrical specifications

The central part of both lateral and frontal surfaces of the specimens were shot-peened to an Almen intensity of 4.5 N using a 90 impingement angle with ceramic (ZrO2 and SiO2) beads of 60–120 lm diameter that provided complete coverage of the notch roots and the top surface (Figure 74(a)); details about the shot peening process are given in [92].

The top surface examined by FIB-SEM microscopy were first ground using abrasive cloths up to 1200 grit, followed by smooth cloth polishing with 1µm diamond particle suspension in aqueous solution and then, as the final step, using colloidal silica solution. The grinding and polishing procedure has resulted in the removal of the material layer at the top surface that was affected by the shot peening treatment.

The milling micro-pillar markers (measurement sites) were placed as shown in Figure 74(b). In the very vicinity of the notch tip, a very high gradient of stress may be found. Consequently, the two closest milling points were spaced 12.5µm apart from each other, with the first marker the same distance from the surface. The remaining measurement points were spaced 50µm apart. Due to the requirement of final alignment between FIB and SEM beams prior to milling, the arrangement described above may not always have been respected. However, the actual distances were used and the data points corrected accordingly. The transversal line of markers ran perpendicular to the notch bisector (Figure 74(b)) at an actual distance of 75µm from the notch root in all samples in the set.

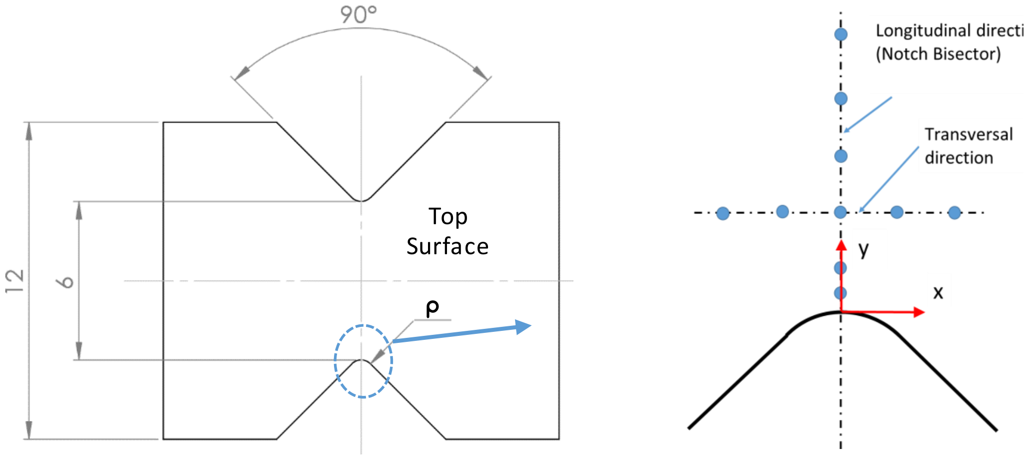

a)

b)

Figure 74. Schematic representation of the milling locations. a) Sample overview (circled the milling location). b) Milling positions at the notch tip.

FIB Milling Procedure

In order to perform DIC analysis, the surface must show good contrast derived from the features already present, e.g. roughness, precipitates etc., or be “decorated” to create such contrast to enable time-depending tracking of surface displacement. Since the surface of polished samples used in the present study did not present these characteristics, in-chamber electron beam deposition of a Pt pattern was used. The Gas Injection System (GIS) was used to deliver a local flow of a Pt-containing volatile organic compound, and electron beam was used to precipitate Pt onto the surface to create a so-called “sunflower” pattern of dots (Figure 75(b)).

Micro-pillars of ring-core geometry of nominal diameters of D_1=7.5µm and D=5µm (Figure 75(d)) were milled at each measurement point (Figure 75(a)). The milling procedure was subdivided into n=50 steps, and SEM images of the micro-pillar top surface were acquired at each step. A micrograph of the monitored region of sample surface carrying the sunflower pattern is shown in Figure 75(c). Once the procedure was complete, the relative distances between the centres of the milling positions were measured by means of SEM at lower magnification.

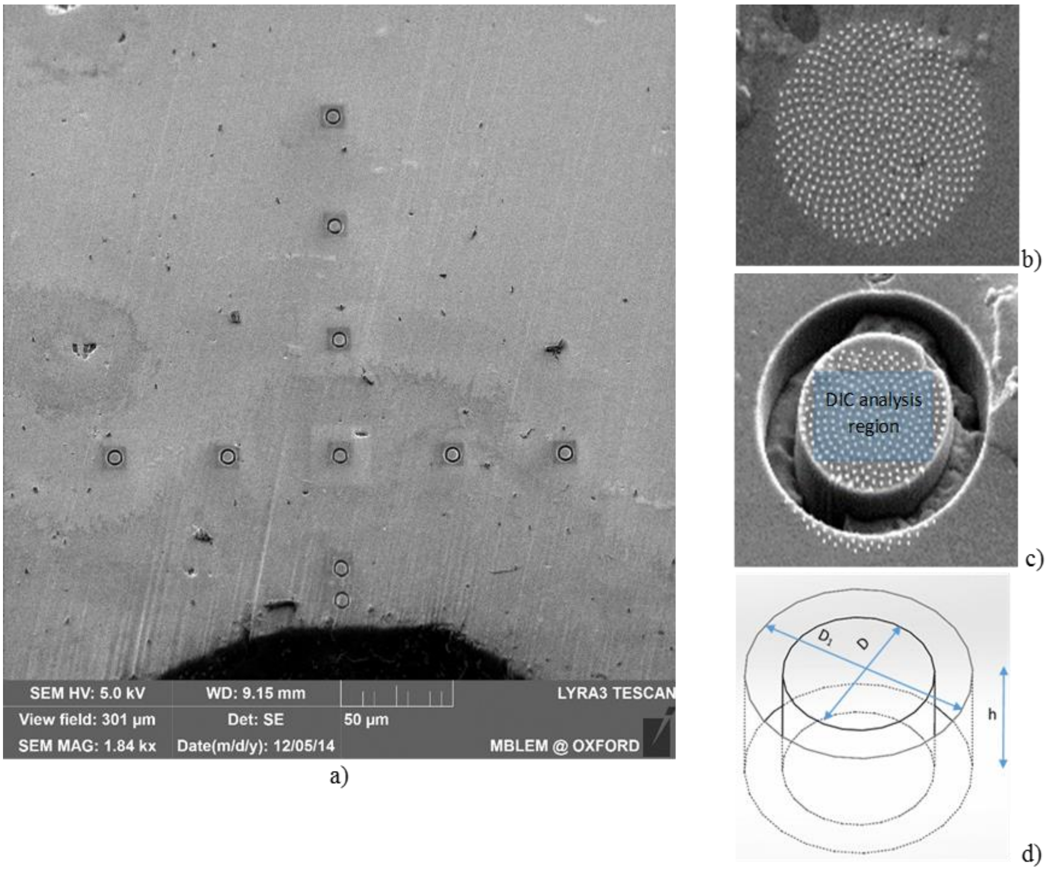

Figure 75. Milling positions and ring core characteristics. a) SEM image overview in correspondence of the notch ($\boldsymbol{\rho}$ *=0.15mm) after FIB-DIC measurements. b) Sunflower pattern created with Pt deposition. c) Surface analysed with DIC during milling process. d) Ring core geometry dimensions.*

DIC Analysis and Fitting Procedure

The images collected at each milling step were analysed by means of Digital Image Correlation (DIC). For the purpose of tracking the displacement occurring during the milling procedure, a reference grid was created on the sunflower pattern. Large scale rigid body displacements due to the SEM image drift were corrected for. The raw DIC tracking data were post-processed to remove outliers and to filter out the noise. The procedure was produced the curve for the strain relief as a function of the milling step for two orthogonal directions *x* and *y* previously defined at the sample surface (Figure 74(b)). Figure 76 shows the experimental result, in terms of the strain relief at each milling step, for a given direction (*x* or *y*) obtained as the average across the entire tracking grid. This strain evolution culminates in the achievement of complete relief to zero strain, with the overall increment providing the information necessary for the evaluation of the residual strain present in the material prior to milling.

The experimentally determined strain evolution can be described by a parametric function (81) developed on the basis of Finite Element Analysis (FEA) which contains two fitting parameters: the complete elastic strain relief $\Delta\varepsilon^{\infty}$, and the normalized milling depth z.

In the present study we propose a new definition of the normalized milling depth (82). Comparing this new definition with the previously established approach [20], we point out the difference in terms of additional free fitting parameters δ and κ being introduced in the evaluation of the normalised milling depth z:

$$\varepsilon^{*} = 1.12\,\Delta\varepsilon^{\infty}\left(\frac{z}{1+z}\right)\left[1+\frac{2}{(1+z^{2})}\right] \tag{81}$$

$$z = \frac{\left(\frac{h}{D}+\delta\right)}{k} \tag{82}$$

The physical meaning of parameter δ is the offset adjustment of the reference surface depth from which fitting begins. This helps accommodate the effect of surface roughness on the strain relief vs. depth curve. The parameter κ accounts for the possible imprecision in the calculation of milling depth that can be adjusted to obtain the best agreement with the theoretically predicted curve.

The fitting procedure was implemented in Matlab©. The algorithm adopted was based on the minimisation of the absolute residuals (LAR - Least Absolute Residuals). At the end, the standard deviation of the residual strain was evaluated at 95% of confidence. An example result of fitting the new function (81) to the experimental data is shown in Figure 76, together with small cartoons indicating the stage of the milling process.

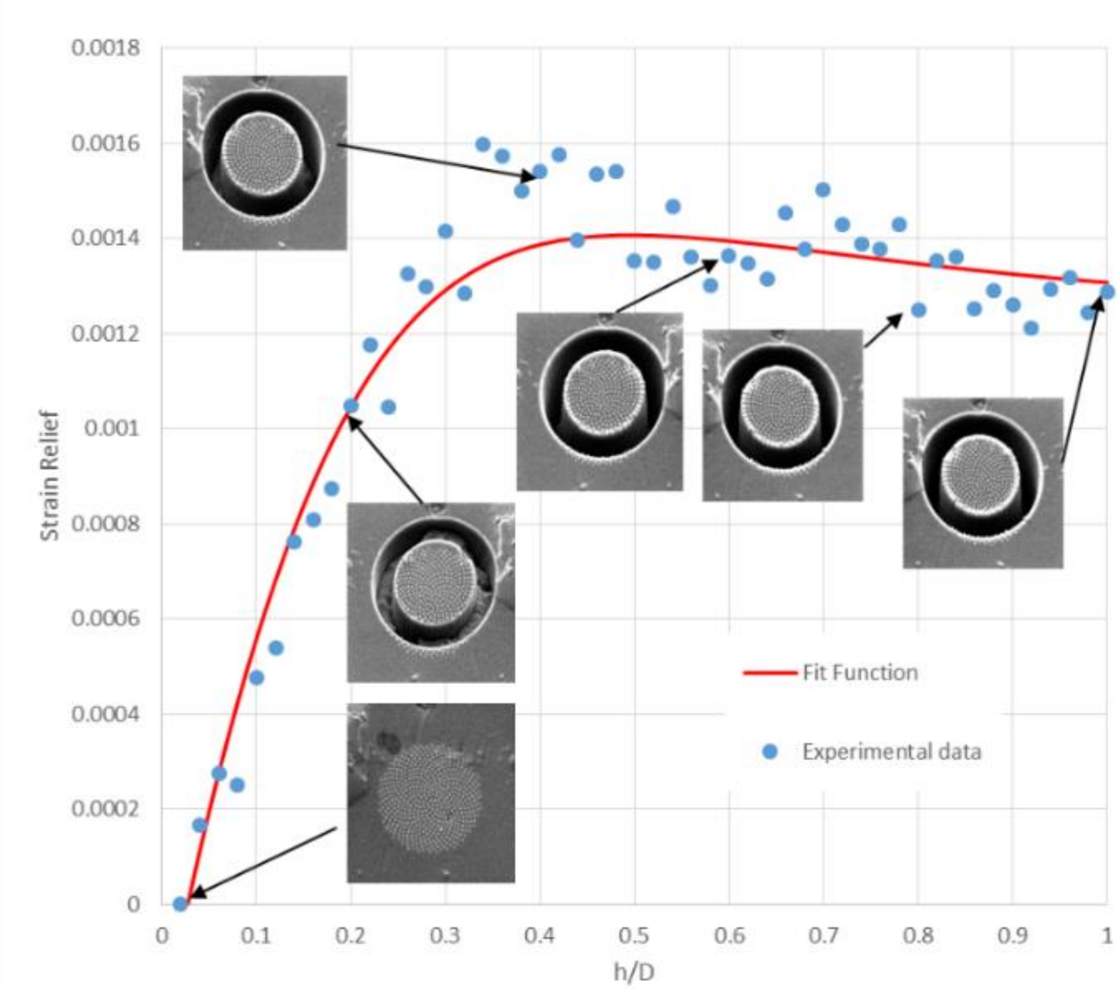

Figure 76. Strain Relief profile, fitting curve and cartoons of the images utilised for the DIC analysis. The figure shows the curve for strain component ε_{xx} at the position 0.0375mm from the notch tip (Sample $\boldsymbol{\rho}$ =0.5mm)

5.1.3. Eigenstrain modelling

For the purpose of this work we proposed a simple numerical model of the residual stress generation within the sample due to a distribution of eigenstrain induced by the plastic deformation during shot peening. Using the plane stress approximation, we modelled an annular domain in which the inner radius was set to be equal to that of the notch root of the samples examined. Accordingly, three different geometries were analysed. The imposed eigenstrain profile was chosen to be a function given by a product of an exponentially decaying function and a linear function of the form:

$$\varepsilon^{*}(y) = A(B - y)\, e^{-C\, y} \tag{83}$$

where y denotes the distance from the surface. The profile given by this function is illustrated in Figure 77 and is seen to correspond to the eigenstrain profile, as function of the depth normalized by the relative fillet radius, typically encountered after shot peening [144]. The normalised depth is the abscissa of the plot shown in Figure 74.

For the purpose of the present brief discussion, only the hoop residual stress is compared with the experimental data. The magnitude and the shape of the eigenstrain profile was chosen to obtain broad general agreement with the set of measurements for three samples. Then statistical analysis was conducted to evaluate the confidence interval in the context of experimental observation. The results are presented in the following section.

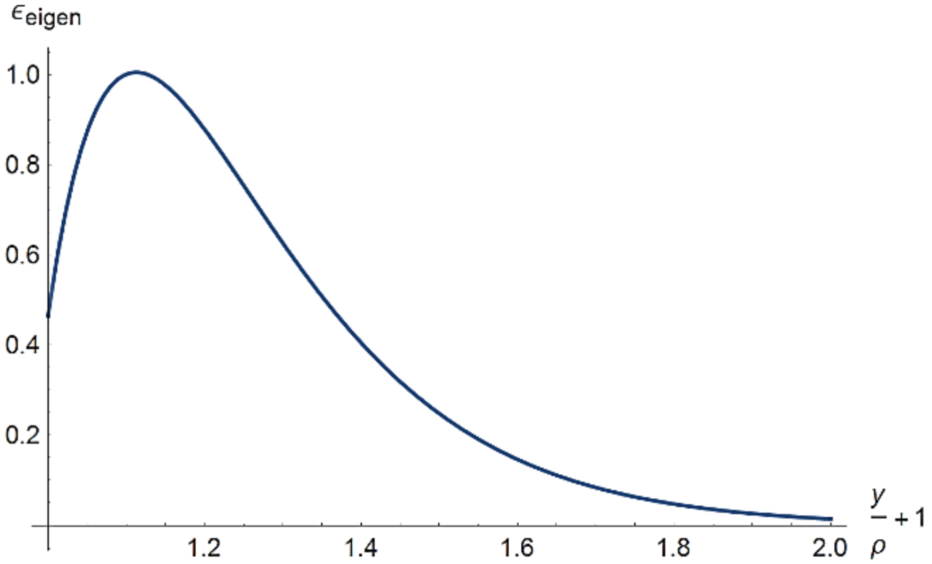

Figure 77. Eigenstrain profile applied in the model.

5.1.4. Results and Discussion

The fitting procedure returns the value $\Delta\varepsilon^{\infty}$, the experimentally evaluated residual strain. Since the interrogated volumes of material lie very close to the sample surface, the residual stress profiles were calculated under the assumption of plane stress. For the material analysed in this study Young's Modulus of E = 73 GPa and Poisson's Ratio of ν = 0.33 were used.

The results obtained from the FIB-DIC analysis are shown in Figure 78. The graphs reported include error bars that indicate the standard deviation derived from the fitting procedure. The error contribution from DIC analysis would result in error bars associated with each of the points in Figure

74. However, these were not taken into account in this study, as their contribution was judged unlikely to cause a significant difference for the results.

The presence of the expected localised compressive residual stress σ_{xx} in the vicinity the notch tip is confirmed by the experimental results (Figure 78(a)). The near-surface compressive layer was present in all of the samples examined in the present study. The residual stress trend typical for shot peened components that is well known for flat samples is confirmed: a high gradient of compressive stress from the surface extends over ~100μm into the sample bulk. Typically in shot peened components the compressive residual stress reaches a maximum at a certain distance from the notch tip [255-257]. In the present study this peak was not observed directly due to the spatial resolution chosen.

Samples with the larger notch root radius show higher compressive residual stress magnitude. The difference between the **ρ** = 2mm sample and the **ρ** = 0.5mm sample was limited in terms of stress profiles. The **ρ** = 0.15mm one shows a somewhat lower compressive stress magnitude compared to the other samples, suggesting a reduced efficiency of shot peening treatment.

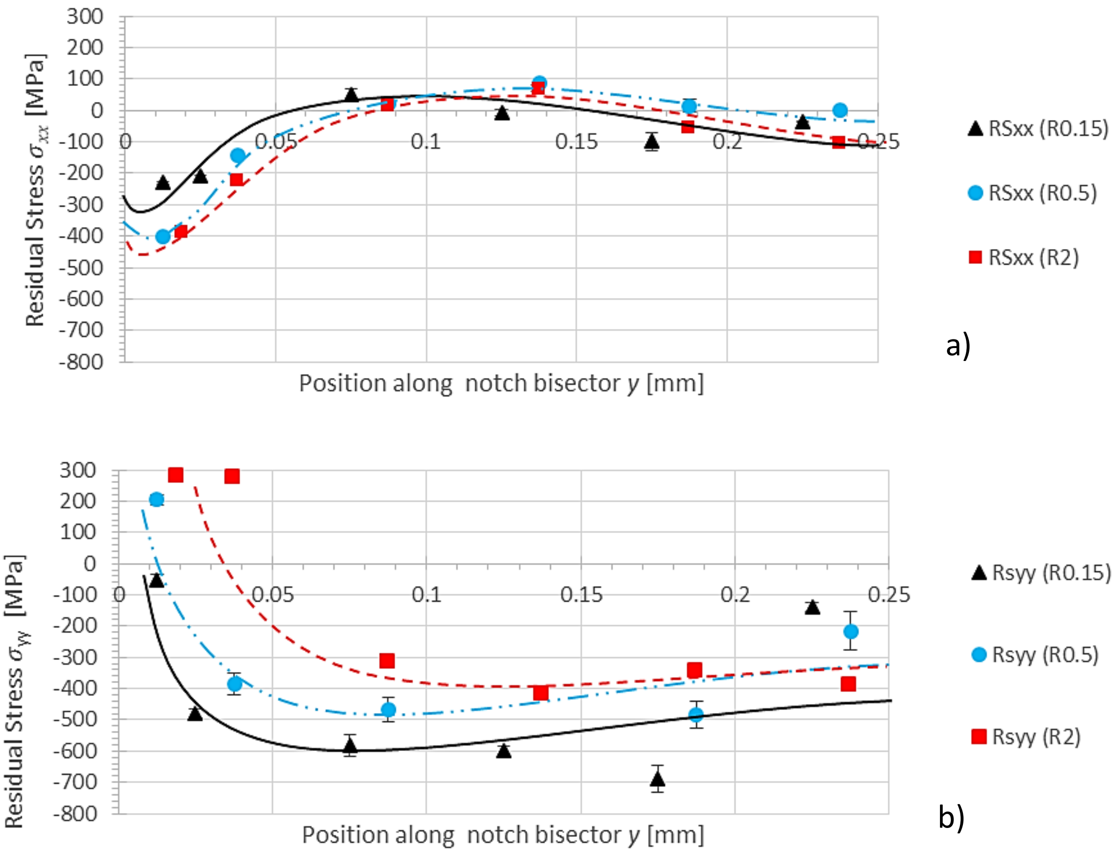

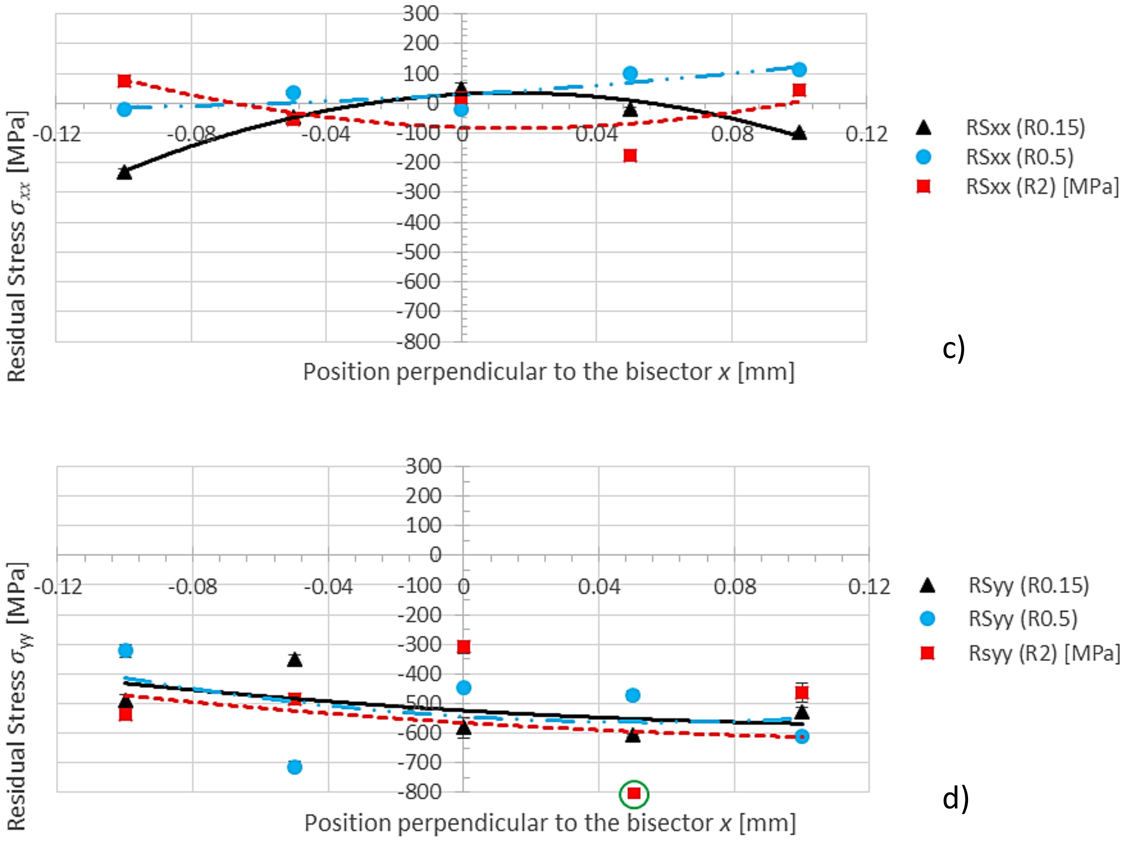

Figure 78. Residual Stress profiles. a) σ_{xx} along the notch bisector. b) σ_{yy} along the notch bisector. c) σ_{xx} along the path transversal to the notch bisector at 0.75mm from the notch tip. d) σ_{yy} along the path transversal to the notch bisector at 0.75mm from the notch tip.

Figure 78(b) shows the results for the orthogonal component of stress σ_{yy}. In this case the near-surface region has low residual stress values, and the maximum compression is reached at depths of around 0.10÷0.15mm. The residual stress σ_{yy} is seen to have undergone relief at the vicinity of the free surface (notch root) as expected due to the traction-free boundary condition. A persistent largely uniform compressive stress σ_{yy} is found at distances larger than ~0.15mm from the notch root. This background stress is likely to be associated with a compressive residual stress state present prior to shot peening due to some manufacturing process (e.g. rolling, or quenching prescribed by the T651 thermo-mechanical treatment of the alloy).

Regarding the stress variation along the path transversal to the notch bisector, the σ_{xx} component (Figure 78(c)) shows more fluctuations in the samples with smaller fillet radius, although overall the variation is small, and no evident peaks can be identified. The same behaviour is observed for the other component of stress (σ_{yy}) along the same transversal path, except for a single outlier point (circled in Figure 78(d)) that suggests an anomalously high value of stress. Conventional approach to the analysis of experimental data is to dismiss this point, associating the anomalous value with the errors in the experimental procedure and interpretation, e.g. reduced SEM image quality in y direction (slow scan) compared to the x direction (fast scan), and the possibility of presence of a microstructural feature such as a grain boundary.

The comparison of the eigenstrain modelling results with experimental observations shows adequate agreement for the general trend of the residual stress profile and magnitude (Figure 79). The data are represented as function of the longitudinal direction normalised by the fillet radius of the relevant sample. The statistical analysis of the data dispersion based on the model used allowed the assessment of the confidence interval indicated by the shaded band. This confidence band for each sample defines the limits in which the experimental data are likely to lie with the probability of 95%. The presence of compressive residual stress at the notch root is confirmed (σ_{xx}), as is its gradual decay with depth, followed by low level tensile stress in the bulk. Figure 79 reveals that the model agrees with the experimental data particularly well for sample 2, for which the confidence band is narrower than for other samples.

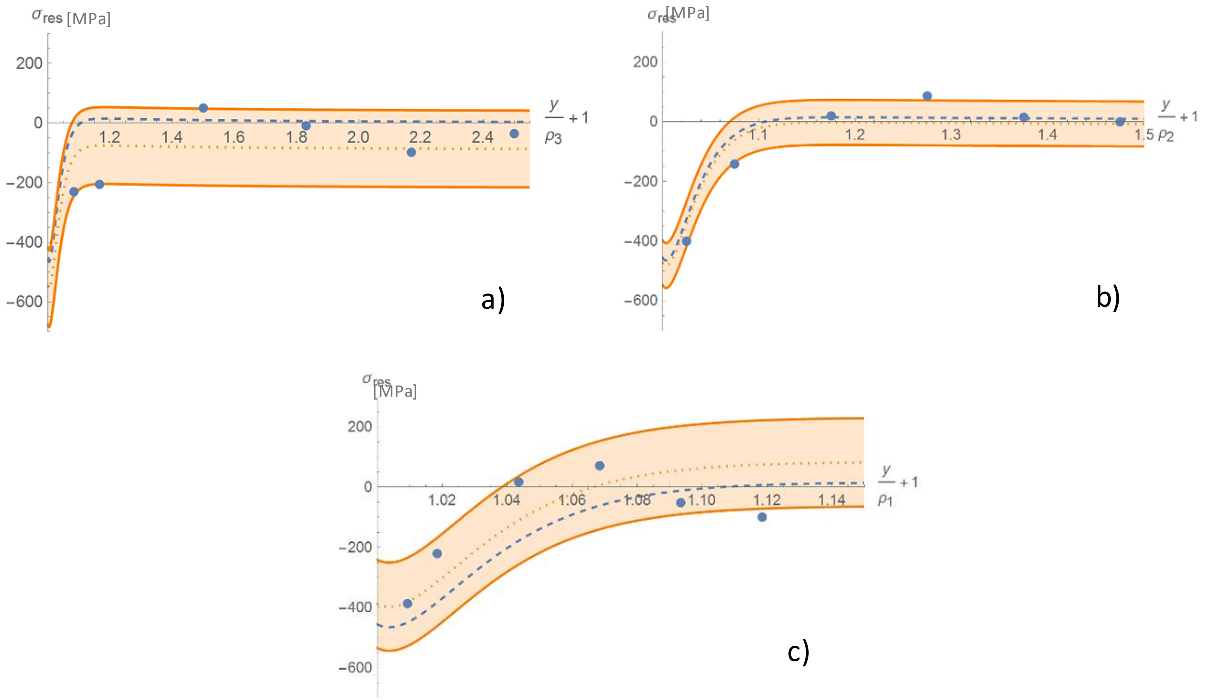

Figure 79. Residual Stress (σ_{xx}) result along the notch bisector and comparison with eigenstrain modelling result. The band in orange colour represent the confidence band at 97% of probability based on the mathematical model. The blue dotted line represents the model's prediction. a) Sample n.1 ($\boldsymbol{\rho_1}$=2mm). b) Sample n.2 ($\boldsymbol{\rho_2}$=0.5mm). c) Sample n.3 ($\boldsymbol{\rho_3}$=0.15mm).

5.1.5. Conclusions

The experimental evaluation of residual stresses carried out in the present study allowed the analysis of the residual stress profile along the bisector line for three shot-peened samples with different notch root radii. Stress evaluation was also conducted along an additional line extended perpendicularly to the bisector and running at 0.75mm from the notch root. The polishing of the front surface, with consequent material removal, has eliminated the layer of material previously treated with shot peening. This conclusion emerges from the observation that no significant compressive residual stress σ_{xx} are present at distances greater than ~0.06mm from the notch tip. The highest value of compressive residual stress σ_{xx} near the notch was found in the sample with the biggest notch radius (**ρ** =2mm), whilst the lowest value was obtained for the smaller notch root radius sample. Regarding the other stress component σ_{yy}, the compressive state extends along the entire bisector extension. The effect of the shot peening is unlikely to extend up to such depths and we consider that it may be associated to a pre-existent compressive residual stress state prior the shot peening treatment due to some manufacturing process.

Given the fact that identical eigenstrain profiles were used in all cases, this effect is likely to be associated purely with the sample geometry, and the geometry-dependent mechanism of residual stress generation due to eigenstrain imposition.

The high spatial resolution given by the use of the FIB-DIC micro-ring core method allowed the residual stress evaluation in very narrowly defined regions of interest. The stress profiles evaluated by this method show good consistency between measurement points and lead to relatively narrow scatter band.

The comparison between the results presented in this work and the eigenstrain interpretation revealed general good agreement in terms of trend and magnitude. Particularly in the case of the sample having smallest notch root radius **ρ** =0.15mm, the model agreed with the experimental observations with 95% confidence.

Further more detailed analysis of residual stress generation can be carried out using either FEM or analytical modelling. This would provide a firm basis for reliable fatigue durability prediction of engineering components treated with this type of shot peening process. Further measurements, using different techniques, are required for the cross-validation of the results presented.

5.2. Intragranular Residual Stresses

5.2.1. Introduction

The present work is aimed at evaluating and quantifying the scatter of intra- and inter-granular RS (Type II and III) within a polycrystalline material, in the specific case where the macroscopic RS (Type I) is well known. In order to perform the study, a miniature bent beam with a well-known macroscopic RS distribution was prepared. The sample was machined from an aluminium alloy plate and plastically deformed through the application of bending in the four-point configuration. In this way, the middle section of the beam was subjected to uniform bending moment associated with the same magnitude of plastic deformation (eigenstrain), that upon unloading generated Type I macroscopic residual stress that was uniform along the beam length, and varied only as a function of one coordinate transverse to the beam extent. Based on the macroscopic stress-strain curve evaluation, a numerical FE model was set up to assess the RS field arising after deformation. In order to establish the connection with micro-scale RS in the simulation, the deformation field obtained from macro-scale analysis served then as input (boundary conditions) for a Crystal Plasticity FEM model (CP-FEM). The combination of models at different length scales enabled the simulation of stress across the scales, from the continuum large scale down to the crystal level. As the outcome of this multi-scale modelling, the RS simulation predictions across the scales (Type I, II & III) can be compared with experimental results.

To this end, EBSD and the FIB-DIC micro-ring-core method were employed for the evaluation of local crystal orientation/grain discrimination and RS evaluation, respectively. The knowledge of grain orientation allowed extracting information regarding the Schmid factor of each probed grain with respect to the principal loading direction (along the beam extent), with the view to elucidating the correlation of this parameter with the local RS magnitude.

Several series of RS measurements were performed. In a region where constant magnitude of Type I residual stress was expected, the deviation of the measured values from the mean are directly representative of the Type II + Type III residual stress sum. In addition, multiple measurements within a single grain provided an assessment of Type III residual stress alone.

The profile of residual stress variation across the beam represented the sum of all three types of residual stress. In this case, the Type II + Type III sum could also be extracted by comparison with the macro-scale profile provided by the simulation that was validated by matching the mean profile to the observation. The comparison between the simulated and experimental Type II+III RS fields was conducted using a statistical approach.

In the following sections, after presenting the details of this investigation and its results, we evaluate the dispersion of experimental data using 95% confidence interval and discuss the implications of the findings for structural integrity assessment.

5.2.2. Sample and Test Setup Description

Four-point bending experiment was performed on a miniature beam carefully machined from a plate of Aluminium alloy AA6082. The choice of material was made on the basis of grain size consideration (10-150µm) to enable multiple RS measurements within a grain.

The load applied during bending was precisely monitored to allow accurate calculation of the bending moment and the assessment of the attendant plastic deformation (eigenstrain) that generates the residual stress upon load release. In addition, the beam curvature was also monitored as an additional measure of consistency between FE numerical model and the sample macro-scale deformation response.

A schematic representation of the test is reported in Figure 80a along with the principal beam dimensions.

Microtest deformation stage by Deben Research (UK) is capable to applying forces up to 5kN. The test was performed under displacement control, and applied force and crosshead displacement were monitored (Figure 80(b)). Minor instabilities of deformation were observed at higher loads during the test (Figure 80(b)) that were associated with rearrangements within the contact regions between loading pins and sample. These occurred away from at the centre of the beam, and did not affect the deformation within the region of interest.

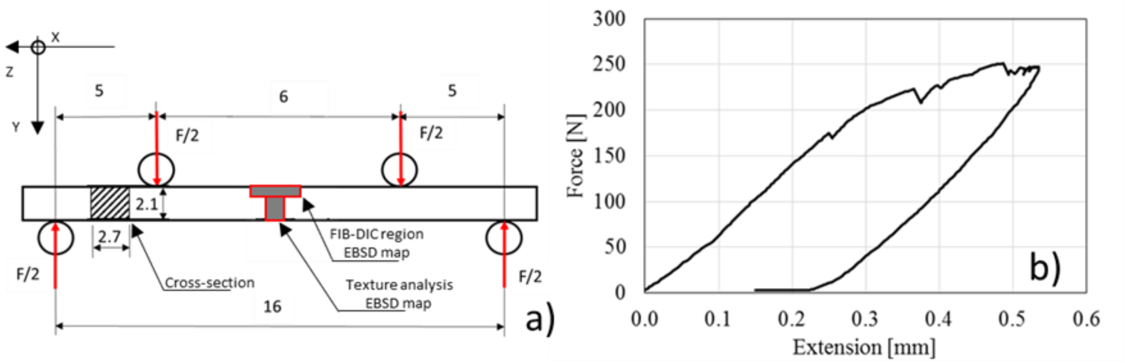

Figure 80. Bending test. a) Four-point bending experiment schematic illustration. Dimensions in millimetres. b) Force-extension curve recorded during four-point bending load application and removal.

5.2.3. FEM simulation

Large scale simulation

The RS field arising due to inelastic bending was numerically evaluated using a three-dimensional non-linear deformation model. The simulation was subdivided into two steps (loading and unloading) in order to capture the residual stress. A refined mesh was used in the region of interest (central part of the beam) to ensure accuracy and reliability of the results. Computational time was optimised by using problem symmetry. Isotropic hardening was used, with the parameters calibrated by matching the macroscopic stress-strain curve.

The match between the beam curvature predicted by the simulation and the actual sample was verified by the graphical superposition of the real scale result onto the beam optical image at the maximum load (Figure 81). The beam curvature upon load release was also matched correctly. The deformed shape and contour plot are shown in the inset below the loaded sample image in Figure 81.

.

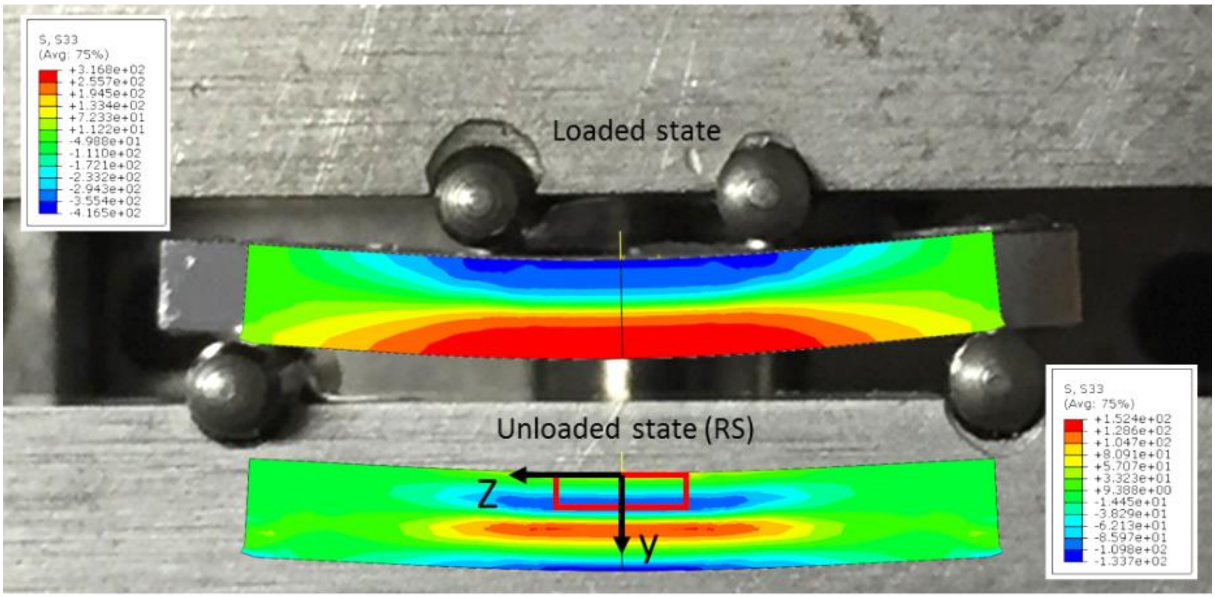

Figure 81. Beam curvature and superposition with FEM simulation at the maximum load applied. The contour plots show the σ_{zz} RS component. The contour plot at the bottom is superimposed on the the unloaded beam contour. The red rectangle indicates the region for EBSD mapping.

Crystal Plasticity simulation

The modelling of crystallographic plastic deformation was performed on the basis of the FE numerical simulation code that has been reported previously [258, 259]. A Representative Volume Element (RVE) in the form of a unit volume cube was discretised into a 3D (8x8x8) mapped mesh composed of C3D20 elements [260]. In the first instance, a Voronoi tessellation was performed to create a population of 600 grains with random crystal orientations.

The second simulation was performed with the aim of incorporating a more realistic material crystal orientation into the analysis. To this end, texture data obtained using EBSD was fed into the CP-FEM code. Correct implementation of the characteristic crystal orientation enhances the model fidelity considerably, and improves the accuracy of residual stress simulation. The RVE was populated with grains of different sizes to capture the large grain size variability found by EBSD analysis. Local crystal orientations were assigned in accordance with the ODF obtained experimentally, ensuring that the overall crystal texture of the sample is reproduced in the RVE.

In the present approach, grain boundaries were not modelled explicitly, in order to keep the computational effort practical. This approach was preferred over the simulation of the actual local morphology of the grains because the present study aims at the statistical description of the origins of residual stresses, and at validating the model that can be potentially used for prediction of residual stress where the underlying crystal morphology is unknown. In passing, it is worth noting that a number of studies are found in literature, where the actual grain morphology and orientation is accounted for in some detail [261, 262].

Alongside aleatoric uncertainty introduced by neglecting the factors described above, another class of error source may play its relevant role, the epistemic uncertainty due to numerical errors [263]. Epistemic uncertainty cannot be described by a probability distribution and it originates from the presence of inaccuracy in the model itself, e.g. internal parameters in the model, round-off errors, and uncertainty in errors due to numerical algorithms.

Slip system hardening was described as follows:

$$h_\alpha = [q + (1 - q)\delta_\alpha]h \tag{84}$$

Where α identifies the active slip system, h is the self-hardening rate and q describes a latent hardening parameter, with values in the range $1 < q < 1.4$.

The elastic and plastic parameters of the material studied were taken from literature: anisotropic stiffness coefficients $C_{11} = 108GPa$, $C_{12} = 61GPa$ and $C_{22} = 29GPa$ [157], and the Critical Resolved Shear Stress (CRSS) $\tau_c = 142.9MPa$ [264]. The hardening parameters were calibrated in the course of simulation to obtain agreement with macro-scale model behaviour.

Periodic and symmetry conditions were imposed to the RVE as boundary conditions. In order to emulate the material loading history, a macro-scale FEM model was employed. At the appropriate relevant instant in the loading history, the strain imposed by the macro-scale model were transferred to the micro-scale model by imposing the equivalent displacements to the RVE. Iterative refinement of the hardening parameters was performed to match the average RVE stress value to the local stress value from macro-scale FEM simulation. In what follows, and for the purpose of comparison with the experiments, the RVE was chosen to lie in the outer-most region of the beam that undergoes compression during bend loading, as indicated in Figure 82 which shows the stress distribution at two stages of loading for both macro- and micro-scale models.

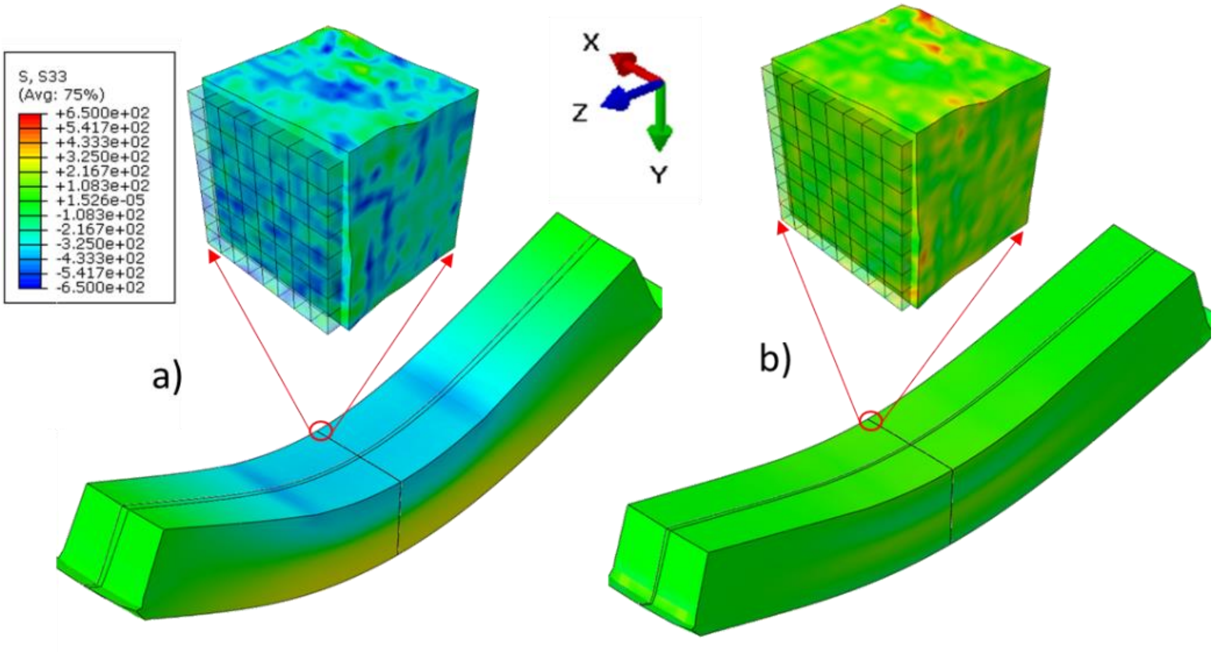

Figure 82. Illustration of stress contours from multi-scale FEM coupled simulation. a) Loaded configuration at the maximum load. b) Unloaded configuration.

The comparison of the statistical distributions of stress values within the RVE with that obtained from experimental measurements is reported in Chapter 5.2.5.

5.2.4. EBSD and FIB-DIC micro-ring-core analyses

Sample surface preparation was conducted using 400, 800 and 1200 grit grinding paper, followed by fine polishing in a water-based solution containing a suspension of 9µm, 3µm and 1µm diamond particles, followed by 0.1µm colloidal silica finishing as the last step. The underlying sample microstructure was analysed in terms of grain shape and orientation using EBSD.

In order to obtain representative statistical distribution of the underlying crystal orientation, texture analysis was conducted by collecting a large 2D EBSD map across the entire sample width of 0.5mm, as shown in Figure 81(a). This area was considered sufficiently large to obtain a statistically representative and robust description of crystallographic texture. EBSD results and pole figures are illustrated in Figure 83. A useful representation of material texture in the context of theoretical and numerical analysis (CP-FEM) is the use of the Orientation Distribution Function (ODF), depicted in Figure 83(c).

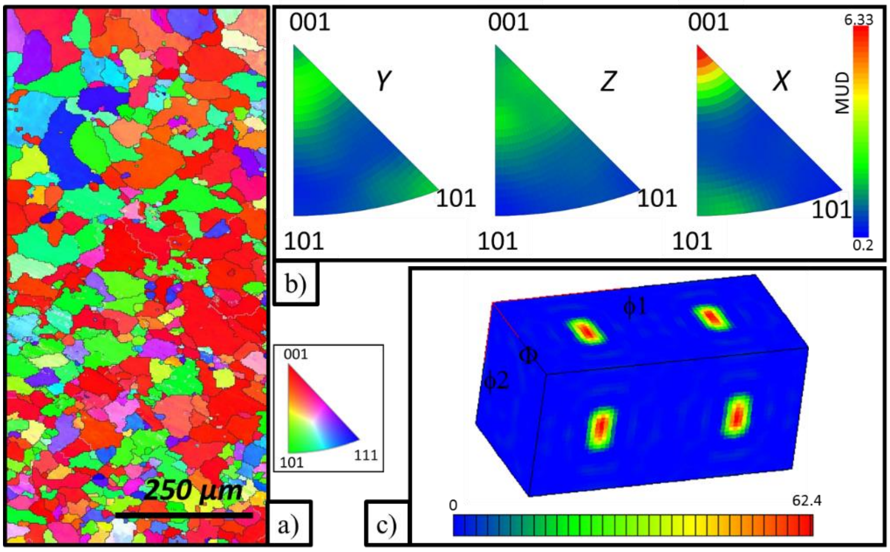

Figure 83. EBSD texture analysis. a) Orientation map IPF-X. b) Inverse Pole Figures. The colour bar is given in terms of the multiple of uniform density (m.u.d.). c) Orientation Distribution Function (ODF) contour plot.

A second region selected for EBSD mapping, indicated in Figure 81(a) by the horizontally elongated red rectangle, was selected for the purpose of FIB-DIC micro-ring-core measurements.

FIB-DIC micro-ring-core measurement procedure consists of using Focused Ion Beam (FIB) for progressive milling of an annular trench-like feature. As milling advances, sequential images of the material surface are acquired with the purpose of tracking the evolution of the elastic displacements taking place using DIC. Post processing of the obtained in-plane displacements field allows the evaluation of the relief strain profile that is fitted with a master-function derived by numerical simulation of the process. The outcome of fitting is the determination of the residual elastic strain that was present in the material prior the milling-induced relaxation. An additional calculation enables the assessment of residuals stress by linear combination of the in-plane residual elastic stress components through Hooke’s law.

In order to facilitate DIC displacement tracking, a thin layer of Pt was deposited on the sample surface, exhibiting random features on the order of tens of nanometres in size after brief exposure to the focused ion beam for ‘etching’. FIB energy was set to 30keV for milling. The ring-core milling process was conducted in 40 steps, with n=10 SEM images collected at each milling with low dwell time. This procedure is known to minimise the effect of SEM imaging artefacts on strain assessment. The inner diameter of the ring-core was chosen to be 5μm, meaning that the measurement approach adopted provided average values of RS within a gauge volume having this lateral extent and the depth up to approximatively one third of the inner ring-core diameter [154].

The first series of RS measurement was performed at different locations at a distance of ~ 40μm from the beam side surface along the *y* axis. Due to the uniformity of bending moment within the central region of the beam, continuum analysis predicts that Type I RS field is uniform within this area. For each measurement not only of the RS magnitude was evaluated, but also the associated error bar corresponding to 95% confidence range that was found using error propagation through the multiple steps of the analysis process (DIC tracking, strain fitting, and allowance being made for material elastic anisotropy [21, 265]).

The plot in Figure 84 presented the results of RS evaluation within specific grains that are indicated on the corresponding EBSD map that reveals the grain morphology and orientation (by colour), and also shows the FIB-DIC marker locations.

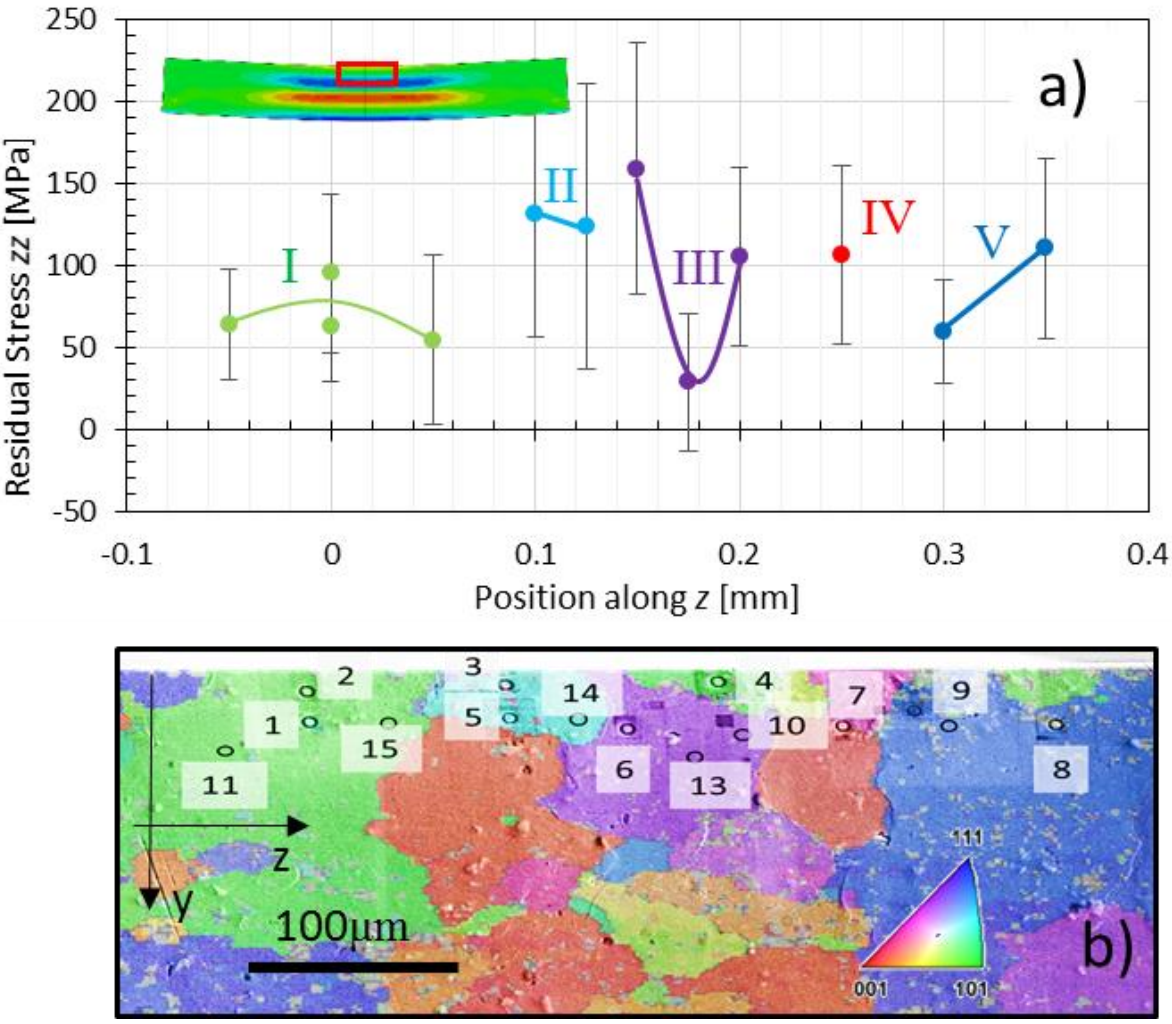

Figure 84. Results of experimental of RS component σ_{zz} in the first region of interest. (a) Plot of the longitudinal RS component σ_{zz} for the grains identified in (b) EBSD grain orientation map. Note that the two graphs refer to the same z-coordinate system origin and scale. Also, the colours of the points in plot (a) match with those of the belonging grains in (b).

The positions of individual measurement identified by the black circles are numbered in the map in Figure 84(b). To help the identification of the grain to which each measurement belongs, the plot in Figure 84(a) reports the RS values using markers of the same colour as the associated grain in the EBSD map.

Figure 84 reveals that RS variation can be observed within individual grains (Type III, intragranular) and from grain to grain (Type II, intergranular) against the backdrop of the uniform Type I macrostress. The adjacent grains numbered I and II show significant difference in the mean RS magnitude, with the mean RS magnitude in grain II around 50MPa greater than that in grain I. The mean

RS in grain III appears to lie between the values in grains I and II, but the spread for the three point measurements within grain III is much greater than for the four point measurements within grain I. This is clearly related to the greater magnitude of Type III intragranular RS in grain III. Finally, it is observed that the cluster of points for the measured RS values at this location is centred around the Type I macroscopic RS value predicted by the continuum simulation, as illustrate in Figure 85 for the values close to zero of the *y*-axis.

To investigate the RS variation further, the second series of FIB-DIC measurements were carried out at different positions along the *y*-axis across the beam cross-section, in accordance with the coordinate system shown in Figure 82. Figure 85 allows two observations to be made:

(a) The overall shape of RS profile across a plastically bent beam is captured correctly. In particular, it can be noted that the sign of RS (tensile vs compressive) has been captured correctly. It is also interesting to note that the quality of agreement is particularly high within the elastic core of the beam, whilst in the near-surface regions that experienced large plastic bending strain the deviation observed is larger.

(b) Deviation from the macroscopic RS value is observed that is statistically meaningful, in that the predicted value lies outside the error bar that indicates 95% confidence interval.

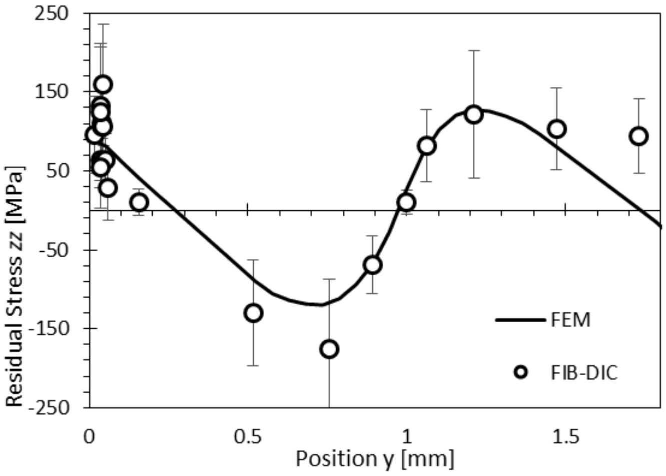

Figure 85. Experimentally determined RS variation across the beam (markers with error bars) plotted together with continuum FE prediction for macroscopic RS profile (solid curve).

When RS measurement data is considered, it may be tempting to associate to the observed scatter with errors associated with deficiencies of experimental setup or interpretation. The present results show that this may be a dangerous simplification: the deviation of measured values from expectation is likely to be caused by fine scale inhomogeneities of deformation (eigenstrain) giving rise to Type II and III residual stresses. The details of grain morphology such as size, shape, the nature of grain boundary, the relative (mis)orientation between neighbours and the attendant elastic-plastic anisotropy are well known to have an impact of deformation mechanisms that is manifested not only at the microstructural level, but also at larger scale [266, 267].

The ease of plastic flow varies depending on the crystal lattice orientation with respect to the loading direction, giving rise to intergranular eigenstrain and the associated Type II RS as a consequence. Schmid factor is a well-known measure of the propensity of a single crystal of given orientation to undergo plastic slip under uniaxial loading. However, since the relevance of Schmid factor for polycrystals remains the subject of controversy, we present a brief discussion of this matter in the following sections.

Similarly, the development and evolution of inelastic deformation features such as slip bands within individual grains that are known to be affected by the grain shape lead to intragranular eigenstrains that give rise to Type III residual stresses.

Finally, it is important to note that Type II and III micro-scale residual stresses are no less physical than Type I macroscopic RS. Hence, procedures need to be developed to take correct account of these stresses in design against structural failure. To help answer these questions, in the following sections we present statistical analysis of RS distributions, and examine the correlation between Schmid factor and RS at the grain level.

5.2.5. Statistical analysis of Residual Stress

In accordance with eq. (85) we perform a point-wise calculation of Type II+III RS as follows:

$$\sigma_i^{RS,II+III} = \sigma_i - \sigma_i^{RS,I} \tag{85}$$

Here $\sigma_i^{RS,II+III}$ denote the deviation of RS from the macroscopic average value that corresponds to Type II and III combination, and is calculated as the difference between σ_i, the total RS measured at point i, and $\sigma_i^{RS,I}$ that denotes the macroscopic Type I RS extracted from the simulation result for the same position where σ_i measurement was performed.

The data for Type II+III RS was processed and represented in the form of a histogram shown in Figure 86. It was found that, to the first approximation justified by the quality and amount of the data available, the distribution of $\sigma^{RS,II+III}$ RS values conforms well to a Gaussian distribution that is shown in Figure 86 by the dash-dot curve. Further accumulation of detailed data may reveal intricacies of statistical distributions.

At this stage it is worth mentioning that our finding is consistent with reports for 'live' stress by other authors [268, 269] who drew their conclusions from HR-EBSD analysis of micro-scale stress within a specimen subjected to external uniaxial load.

For the purposes of Uncertainty Quantification (UQ) incorporation in design on the basis of continuum simulation it may be required to incorporate the presence of Type II+III RS in the overall assessment of statistical deviation from the macroscopic RS prediction. Previously, UQ has been reported for experimental RS evaluation using FIB-DIC procedures [21, 265]. This procedural error can be amalgamated with the uncertainty that arises from the deviation between the actual RS values and macroscopic description, i.e. $\sigma_i^{RS,II+III}$.

The standard deviation of experimental data for the totality of measurement points is found as:

$$S''_{\sigma^{RS,II+III}} = \sqrt{\frac{1}{n_1 - 1}\sum_{i=1}^{n_1}\left(S_{\sigma_i}\right)^2} \tag{86}$$

where S_{σ_i} is the standard deviation for each experimental FIB-DIC point, and n_1 is the number of experimental points.

The dispersion of the actual residual stress values from macroscopic predictions can be assessed by calculating the standard deviation as follows:

$$S'_{\sigma^{RS,II+III}} = \sqrt{\frac{1}{n_1 - 1}\sum_{i=1}^{n_1}\left(\sigma_i^{RS,II+III}\right)^2} \tag{87}$$

where n_1 is the number of measurements.

The overall standard deviation can be evaluated by combining the above as follows:

$$S_{\sigma^{RS,II+III}} = S''_{\sigma^{RS,II+III}} + S'_{\sigma^{RS,II+III}} \tag{88}$$

Thus obtained, S_σ was used to define the confidence band that describes the variability of RS values around the continuum macroscopic predictions. At each position i across the beam, the confidence limits were defined as follows:

$$[\sigma_i^{RS,I} - z^* S_{\sigma^{RS,II+III}};\ \sigma_i^{RS,I} + z^* S_{\sigma^{RS,II+III}}] \tag{89}$$

where z^* is the critical value related to the required confidence level. To attain the confidence level of 95% the value of z^* needs to be set to 1.96.

On the basis of the above calculations, S_σ value of 53 MPa was found. The statistical distribution of the RS II+III stresses can be visualised graphically for both the numerical simulation results (CP-FEM) and experimental evaluation (FIB-DIC), as illustrated in Figure 86(a) and (b), respectively. RS II+III stress values from CP-FEM simulation were obtained by collecting the stress values at integration points and subtracting the mean RVE value, according to eq. (85).

The information regarding Type III RS was extracted solely from the CP-FEM simulation, as follows: RS Type II+III values at the integration point j belonging to grain k were calculated using (85), and the mean value for the specific grain (Type II) was subtracted:

$$\sigma_{jk,CP-FEM}^{RS,III} = \sigma_{jk,CP-FEM}^{RS,II+III} - \frac{1}{N}\sum_{j}^{N} \sigma_{jk,CP-FEM}^{RS,II+III} \tag{90}$$

where N is the number of integration points within grain k.

Type III RS standard deviation *for the entire RVE* could be evaluated as:

$$S_{\sigma_{CP-FEM}^{RS,III}} = \sqrt{\frac{1}{n_1 - 1}\sum_{i=1}^{n_1}\left(\sigma_{jk,CP-FEM}^{RS,III}\right)^2} \tag{91}$$

This calculation allowed the quantification of Type III RS standard deviation that turned out to be 66MPa and 56MPa, respectively for the untextured and textured polycrystalline materials.

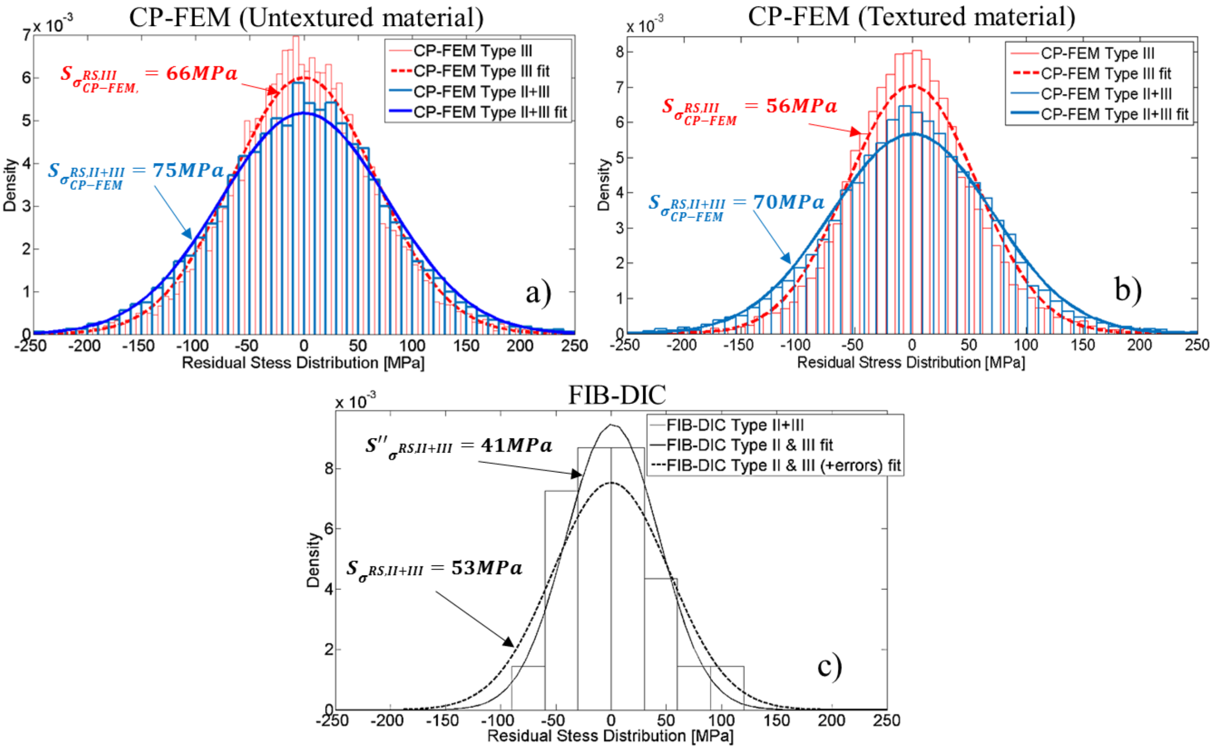

Figure 86. Probability density functions derived for the distributions of residual stress values obtained from a) CP-FEM simulation for an untextured polycrystalline material, b) CP-FEM simulation for the textured rolled Al plate and c) FIB-DIC experimental evaluation.

For the purpose of comparison, the values of standard deviations are in the bar chart in Figure 87.

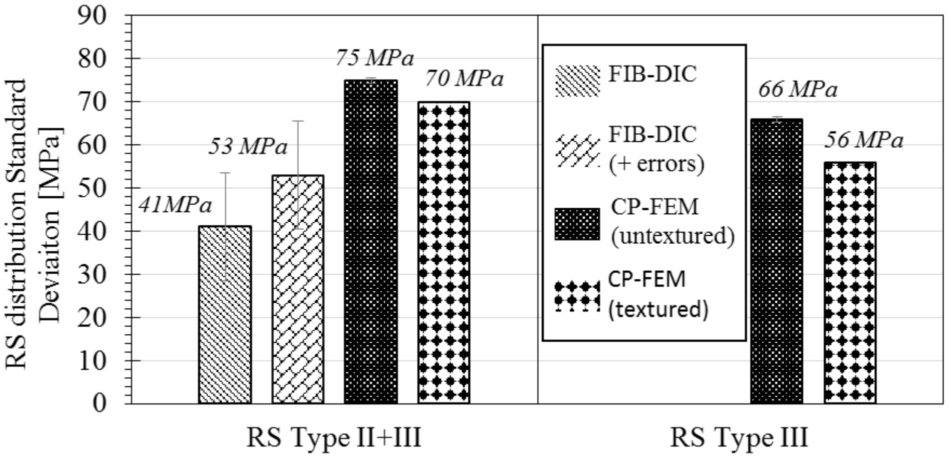

Figure 87. Residual Stress Standard Deviations comparison

RS Type [MPa] / **Technique**	**II+III**	**III**
FIB-DIC	41	-
FIB-DIC (incl. measurement error)	53	-
CP-FEM (untextured material)	75	66
CP-FEM (textured material)	70	56

Table 9. Type II+III and Type III Standard Deviation values

It is apparent from the plots presented in Figure 87 that a wider distribution (by ~40%) was obtained by the CP-FEM simulation compared to the experimental measurements (RS Type II+III), concerning the untextured polycrystalline material. When the measurement error propagation is accounted, the difference in the Gaussian widths reduces to ~29%, but persists. On the other hand, if the actual texture of the polycrystalline material is considered, RS Type II+III shows a smaller difference compared to the experimental result (~24%). A reduction of the RS standard deviation was experienced also regarding the sole Type III RS; considering the material texture, the gaussian width reduced of ~15%.

The discrepancy between CP-FEM model prediction and experiment measurements highlights the fact that matching the macro-scale (Type I) RS is insufficient for obtaining a statistically representative Type II+III description to underlie subsequent in-service modelling. However, the experimental findings show a relatively large uncertainty due to the nature of the experimental technique itself. It is therefore worth noting that the confidence interval is very close to the values attained through the numerical simulation, therefore acceptable matching was found overall. This hints that in order to obtain a better representation of RS Type II+III distributions, the accounting of grain boundaries and defects, etc might play their role. Furthermore, since rolling was employed to produce the alloy plate studied here, we surmise that the material inherited not only the grain structure, but also the pre-existing RS state from prior processing history.

It suggests that in order to obtain statistically representative RS Type II+III distributions, it is important to account for the effects of crystallographic and morphological texture, the presence of grain boundaries and defects, etc. Since rolling was employed to produce the alloy plate studied here, we surmise that the material inherited not only the grain structure, but also the pre-existing RS state from prior processing history.

Type III RS evaluated through the numerical simulation highlighted a narrower distribution compared to the sum Type II+III as expected. Nonetheless, this distribution width was larger than obtained in the experiments.

Using the confidence band defined according to (89), the plot in Figure 88 was constructed that reports the macroscopic RS prediction (solid curve) and the correspondent confidence band indicated by the two dashed curves. Furthermore, all experimental points are also included with their respective error bars. The Gaussian distribution function shown by the inset illustrates how Type II+III RS cause a spread around the mean Type I RS value at any position across the beam.

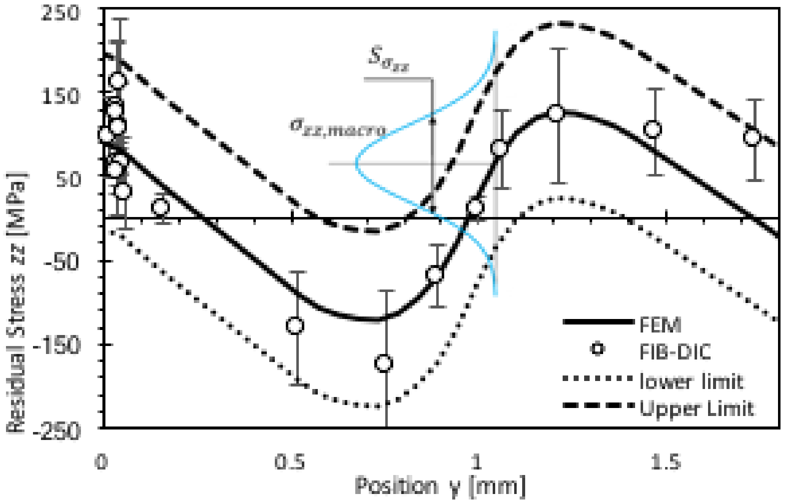

Figure 88. Experimental RS measurement and Finite Element Analysis prediction. The Upper and Lower limits define the band at 95% of confidence. An example of normal distribution is shown by the blue continuous line.

It is evident that all experimental points lie within the band that corresponds to 95% confidence level, supporting the validity of the proposed approach. It is worth noting the relative magnitudes of Type II+III residual stresses, on the one hand, and of Type I stresses, on the other. The half width of the band magnitude (54MPa) is comparable with Type I RS magnitudes, so that the presence of the finer scale RS may mean that the actual stress at any given location may differ in sign from the prediction.

This representation of RS point values by statistical distributions is potentially great significance for structural integrity and reliability design of mechanical systems, in that it can underpin design based on the appropriate confidence level selected for specific applications. Considering for instance a hypothetical problem of design against crack nucleation, whereas high structural integrity reliability is sought, the employed RS should be that that consider a worse-case scenario (i.e. upper limit with a certain confidence). In the same way, whereas high performance is required, a less conservative approach can be chosen being, again, aware of the probabilistic occurrence of an adverse event.

5.2.6. Influence of the Crystal Orientation on Residual Stress Development

It is well known that the crystal plasticity activity is highly dependent on the local orientation of the material, besides the external load applied. In fact, in all the crystalline structures there is always a specific slipping plane that is more prone to resolve shear stress. Such slip plane can be described upon knowledge of the so-called Schmid factor with regards to the loading direction. According to the Schmid's law, the amount of shear stress that can be resolved is:

$$\tau = \sigma \cdot m \tag{8}$$

where σ identifies the external load and m is the Schmid factor. The latter is defined as:

$$m = \cos(\phi) \cos(\lambda) \tag{9}$$

where ϕ is the angle between the loading direction and the slip plane normal, and λ is the angle between the slip plane normal and the slip direction. For crystals with fcc lattice there are 12 equivalent slip systems of the $(111) < 1\bar{1}0 >$ type available. Since the onset of slip occurs on the system with the highest resolved shear stress, calculation of m must be performed for each system, and the greatest value selected.

Since full crystal orientation is available for each grain from the EBSD map acquired, Schmid factor with respect to the loading direction can be calculated for each measurement point. The details of sample orientation are reported in the Appendix.

The purpose of abstracting the Schmid factors was the understanding of the nature of measured RS deviation from the macroscopic stress. According to the Schmid's law, grains exhibiting high values of Schmid factor are more prone to undergo to plastic deformation and, in turns, will generate higher values of residual stress. The plot in Figure 89 shows the direct comparison of the $\Delta\sigma_i$ quantities with the corresponding Schmid factor values. The dotted lines are polynomial fits that serve as guide to facilitate the visualisation of the trends behaviour.

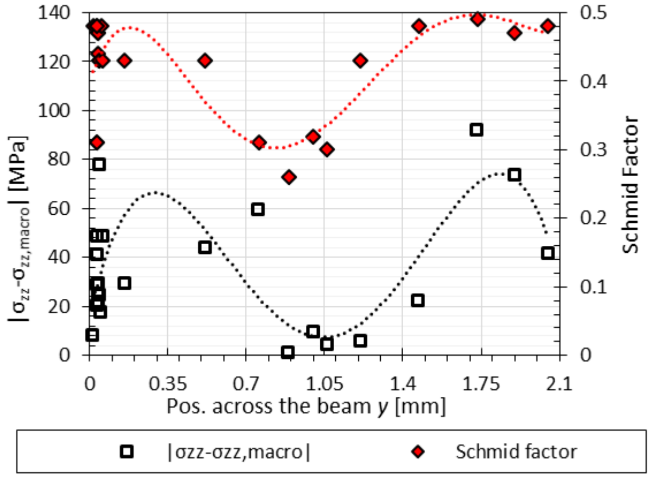

Figure 89. Measured RS deviation from the macroscopic prediction (lower curve and square markers) and the corresponding Schmid factor values (upper curve and diamond markers).

The comparison of the two curves in Figure 89 suggests the existence of a correlation between the two quantities, the orientation dependent Schmid factor of a given grain, on the one hand, and Type II+III RS, $\Delta\sigma$, on the other. Indeed, the lower values of Schmid factor in the middle region appear to match well the lower values of the absolute magnitude $|\sigma_i^{RS,II+III}|$ of Type II+III RS. This compares favourably with reported unsuccessful attempts to find correlation between Schmid factor and total RS value, $\sigma^{RS} = \sigma^{RS,I} + \sigma^{RS,II} + \sigma^{RS,III}$. Rational analysis of the correlation suggests that best correlation is likely to be found when only Type II RS component is used, $\sigma^{RS,II}$. Nevertheless, it is worth noting that the deformation response of grain is strongly affected by the neighbouring grain, setting a limit to the validity of Schmid factor as a universal correlating parameter. Nevertheless, it is worth noting that the deformation response of grain is strongly affected by the neighbouring grains, setting a limit to the validity of Schmid factor as a universal correlating parameter. In turns, locally the stress state is no longer uniaxial but rather multiaxial, leading to an inaccurate quantification of slip activity using this approach. This is also repeatedly highlighted in [55] where a “true” Schmid factor is evaluated in order to account the actual stress state acting in the considered grain.

5.2.7. Conclusion

Type I, II and III RS measurements conducted by FIB-DIC at the grain-level show a significant degree of scatter. Consideration of the results revealed that to a great extent this scatter can be interpreted as a statistical distribution of Type II and III residual stresses. Statistical description of Type II+III RS dispersion around the macroscopic Type I value was proposed.

The principal outcomes of the present study of intra- and inter-granular Type II+III RS were:

1. Overall, the mean values of the measured residual stresses follow closely the macroscopic continuum Type I RS variation predicted by the numerical model calibrated against the macroscopic stress-strain curve of the material and incorporating appropriate description of hardening.
2. A series of measurements was conducted at a location where the nominal macroscopic Type I residual stress was constant. The results revealed significant scatter in both inter-granular Type II RS, and intra-granular Type III RS. It was confirmed that the range of spread of Type II+III RS values can be as large as the Type I residual stress value itself.
3. The Type II+III RS statistical distribution of the measured stress from the nominal macroscopic value by the continuum model was found to conform well to Gaussian statistics. Based on the data collected, the breadth of this distribution was found to be of the order of ~41MPa.
4. Error propagation that incorporates FIB-DIC measurement inaccuracies was used to assess the 95% confidence interval that corresponds to Gaussian statistics with the breadth of ~53MPa. This is consistent with the result reported above, and incorporates the contribution from the measurement error. As highlighted in [270], the overall stress state might significantly depend on the 3D morphology of the grains below the free surface, over a thickness of at least twice the average grain size. This can be considered as a supplementary error source. Moreover, a further cause of error may be of epistemic type. As highlighted in section **Error! Reference source not found.**, epistemic uncertainty are not due to physical causes but rather to numerical inaccuracy [263]. All the listed causes concur in the generation of the mismatch experienced between numerical and experimental results.

5. The statistical distributions of RS obtained by experiment and numerical modelling found 29% of disagreement if a randomly distributed crystal structure is simulated, whilst whereas a realistic crystal texture of the material is accounted this disagreement drops to 24%. The mismatch is thought mainly due to the pre-existing RS state from prior processing history, beside minor simplifications adopted in the CP-FEM model (e.g. no grain boundary)
6. Type III RS evaluated by CP-FEM simulation showed a standard deviation of the distribution of 66 MPa and 56 MPa, respectively for the untextured and textured CP-FEM simulations.
7. Analysis of the local Schmid factor showed a limited correlation with the Type II+III RS scatter. The origin of Type II+III RS deviation from Type I macroscopic prediction is thought to be due to the multiaxial stress state induced by the microstructure and nearest neighbour grain interaction.
8. The results obtained have significant implications for design, in that they reveal the magnitude of grain level RS variation and provide an improved basis for rational design that incorporates statistical information and allows reliable uncertainty quantification.

5.3. Depth-resolved analysis of the composition, grain orientation and residual stress due to wire EDM primary and finishing cut

5.3.1. Introduction

Electrical Discharge Machining (EDM) is a wide-spread manufacturing technique able to produce high quality finish cut surfaces. Provided the workpiece is made from a conductive material, material removal is effected using erosion caused by electric sparks. These recurrent sparks are generated by the discharge occurring between two electrodes, one being the workpiece and the other the tool, that are separated by a dielectric liquid. In the specific case of wire-EDM, the tool is a wire that is continuously wound through as the machining advances, to avoid its failure and to supply fresh material to sustain a repeatable process.

From the thermal point of view, electrical discharge acts as a source of heat flux into a limited volume that undergoes to melting and/or evaporation. The material that re-solidifies within the machined region is referred to as the White Layer (WL) for its bright appearance under the optical microscope. Beneath this re-cast layer, the portion of material next to the WL does not undergo melting, but experiences solely rapid heating and subsequent quick cooling (i.e. quenching) [271]. By analogy with welding, this is called the Heat Affected Zone (HAZ). The re-cast layer has been the subject of numerous studies due to its potential detrimental effect on structural integrity. Indeed, it is common knowledge that the presence of the WL reduces the mechanical component life when it is subject to cyclic loading [272], accelerating fatigue failure. This type of component breakdown is facilitated where concentration of stress is present alongside with the presence of weakening features, such as cracks, pre-existing tensile stress state and loss of ductility within the WL. It has been widely verified that the WL possesses higher hardness and lower ductility compared to the parent material [273]. Such enhancement in material brittleness is thought to be associated with the phase change taking place during material re-solidification [274].

Review of the literature reveals that a number of mechanisms associated with the WL were identified as responsible for promoting early fatigue failure [275, 276]. The presence of cracks or features that may help the crack initiation and propagation ought to be considered in combination with the high magnitude thermal stresses induced in the material by the electrical discharge [277]. In the case where thermally induced stress exceeds the material ultimate tensile strength, so-called thermal cracks are produced [278]. In the course of material solidification within the very shallow layer in the presence of high temperature gradient, the generation of residual stress is inevitable [279]. As mentioned earlier, in the great majority of cases reported in the literature, the residual stress within the altered material is of tensile nature for several types of metallic materials [279-282]. Numerous models have been proposed with the purpose of understanding and predicting the thermal history evolution during discharging [283, 284] and, in some studies, thermal analysis was used in combination with structural modelling to predict the stress distribution [283-286]. Although the spatial and temporal scale of recent Molecular Dynamics (MD) simulations is insufficient to capture the complete process history, the results indicate that the fundamental mechanism of stress generation within the affected material [287] can explain the potential generation of thermal cracks. It is noteworthy that material phase change also produces inelastic deformation and thus is likely to act as another source of residual stress.

Nevertheless, due to the unavailability of techniques for residual stress measurement within the WL, experimental results for residual stress distributions have been reported at the spatial resolution that exceeds the thickness of the WL itself. Furthermore, the different phase and roughness of the WL impeded the adoption for the interrogation of this thin layer using advanced techniques such as synchrotron X-ray diffraction. The advent of the microscopic version of the ring-core method, the so-called micro ring-core FIB-DIC [78, 84], made it possible to probe micromechanical systems at the (sub) micron-scale, independently from the material crystalline/amorphous structure, phase, and deformation state.

The present study focuses on the characterisation of the WL generated by single and double pass EDM cutting of two samples of Al alloy AA5052. The first sample denoted “A” was subjected only to a regular cut (also known as Main Cut, MC). The second sample denoted “B” was subjected to MC, followed by the second pass at a different, lower power setting (Trim Cut, TC). TC is known to reduce the surface roughness and WL thickness, and may also reduce the WL porosity [288]. It is therefore of considerable interest to characterise the WLs both structurally, and in terms of the residual stress. Initial studies of the morphology and chemical composition were conducted by means of SEM and Energy Dispersive Spectroscopy (EDS) techniques, respectively. In order to reveal the white layer structure using EDS and Electron BackScattered Diffraction (EBSD), a FIB cross-section was prepared. Orientation maps obtained by EBSD provided important information concerning the crystal orientation and phases in proximity of the WL. Finally, FIB-DIC was employed for the residual stress evaluation within the WL for both the single pass (*A*) and double pass (*B*) samples.

The results are discussed in the context of seeking better understanding of the interaction between the residual stresses generated by thermal effects, and those arising from material phase change.

5.3.2. Sample description and FIB sectioning preparation

An aluminium alloy AA5052 was the material used for this experimental investigation. Two samples were machined from a 4mm thick plate as illustrated schematically in Figure 90. Sample *A* was produced by performing a single cut pass using MC, while Sample B after the first MC pass was subjected to the second pass under TC conditions. Brass wire used for performing the EDM cut had the diameter was 0.25mm and its continuous replacement was ensured by the constant feed and spool rotation that resulted in the wire speed of 135mm/s. Process parameters of both MC and TC conditions are reported in Table 10.

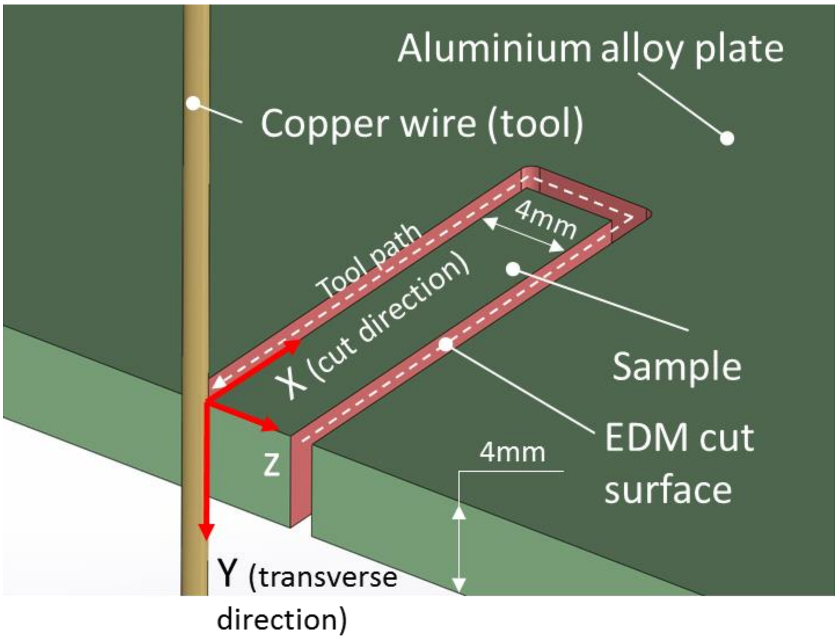

Figure 90 Sample cut schematisation

In Al alloys SEM microprobe analysis, high quality and high resolution of EBSD mapping can only be achieved by accurate surface preparation. Conventional sample surface preparation techniques such as grinding are not always sufficient for this kind of material due to the possibility of surface deformation and chemical modification. To overcome this issue, fine surface polishing was performed using FIB with the ion beam energy of 30keV and beam current of 0.17nA at the edge of sample A, as illustrated schematically scheme in Figure 91(a). This resulted in the creation of a 50x50µm polished region shown in Figure 91(b), It is evident that rough material surface) was entirely removed, presenting a cross-sectional view of the material affected by EDM cut at the top of the image.

Pass	Voltage [V]	Current [A]	Dielectric flush pressure [bar]
Main Cut (MC)	*24*	*17*	*4*
Trim Cut (TC)	*63*	*4*	*0.1*

Table 10 EDM process parameters used for main cut (MC) and trim cut (TC).

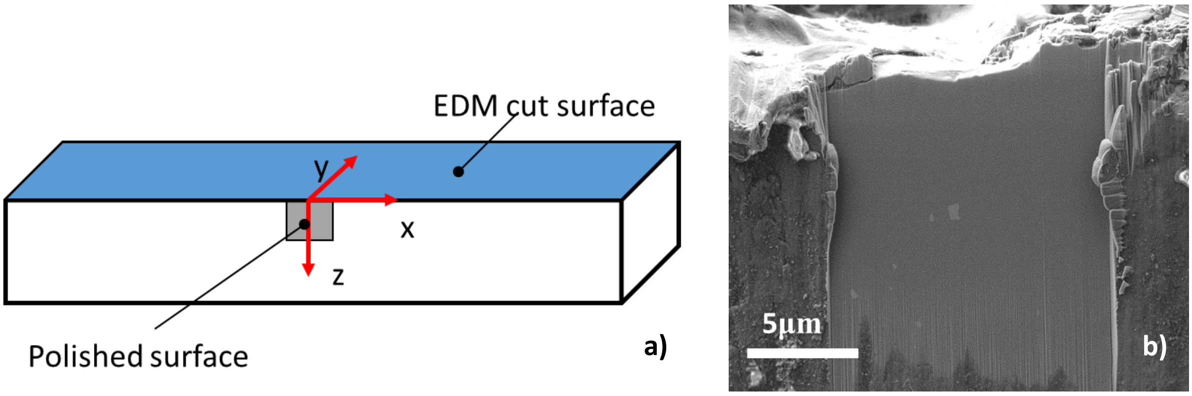

Figure 91 FIB cross-section polishing: a) Schematic illustration of the location of region of interest, and b) SEM image of the ion-polished surface.

5.3.3. Surface morphology

Thanks to the high depth of field provided by the SEM, surface finish of the studied samples could be investigated. As shown in Figure 92, EDM cutting (MC) resulted in the characteristic surface morphology consisting of molten and solidified regions with smooth surface, interspersed with the regions of rougher appearance that is suggestive of atomisation and tearing. It is also apparent that the EDM machined surface undergoes a noticeable change after trim cut (TC) is conducted. The surface of Sample A following sole MC treatment displays larger scale features than those arising after TC. The overall surface roughness appears to be considerably reduced after TC, and Sample B is seen to show a smaller spacing between asperities.

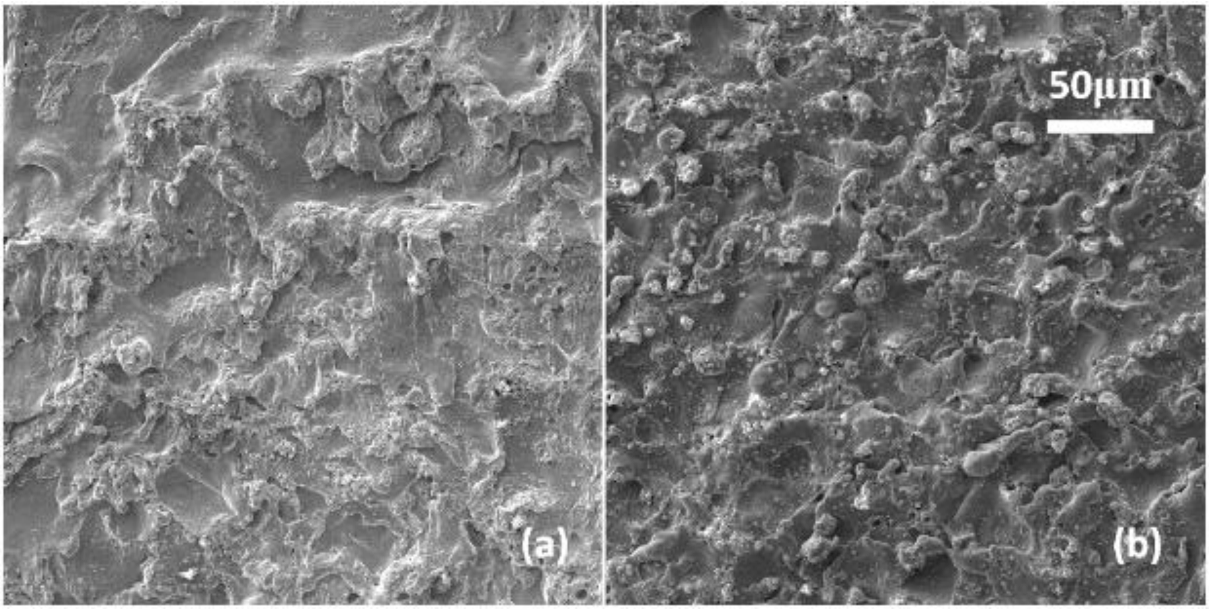

Figure 92. SEM images of the EDM section surfaces: a) Sample A: MC. b) Sample B: MC and TC

Close-up images of Sample A show further interesting characteristics that are worth highlighting. From Figure 93 it is apparent that the surface is characterised by the presence of porosity, with features of maximum diameter of ~2-3μm, and down to a ~100nm and smaller. Further imaging at different magnifications reveals that these features can either have a rounded shape of near-spherical pores, as indicated by the circle in Figure 93(a), or of elongated voids with sharp edges, as indicated by the ellipse in Figure 93(b).

It is well-known that the presence of superficial flaws, defects and discontinuities is likely to exert strong influence on the structural integrity of components and assemblies. Sharp notch-like features serve as the locations of stress concentration and may give rise to crack nucleation under external monotonic and/or cyclic loading. An interesting generic question that arises in this context concerns the possibility of existence of a critical flaw size below which the presence of a defect does not exert any considerable influence on structural integrity. It is also worth noting that no evidence of thermally induced cracking (thermal tearing) has been found.

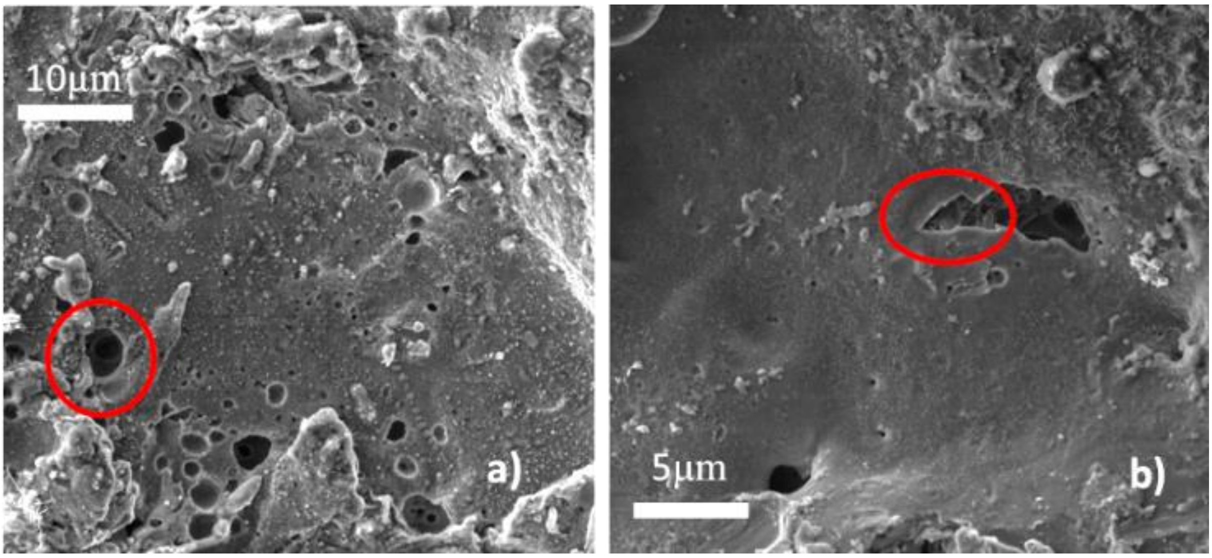

Figure 93 SEM magnified images of EDM cut surface of Sample A: a) Rounded pore features, and b) sharp-edged voids

The FIB polished cross-section reveals the presence of a non-uniform and discontinuous white layer (WL). Figure 94(a) obtained using backscattered electron (BSE) detector shows clearly the presence of WL detached from sample surface. Such WL shape may be linked to a change in composition at the interface between the two solidified layers that arises during the solidification process itself. This interfacial layer can be seen as a darker band that separates the particle from the substrate, and possesses a different elemental and phase composition compared to WL and base material that becomes apparent due to BSE imaging possessing subsurface contrast. On the other hand, when WL is embedded in the base material, as shown in Figure 94(b), it becomes difficult to distinguish due to the contrast change. As guide to the eye, a dashed line is superimposed on the image, showing that WL extends to around 2.5µm beneath the top surface.

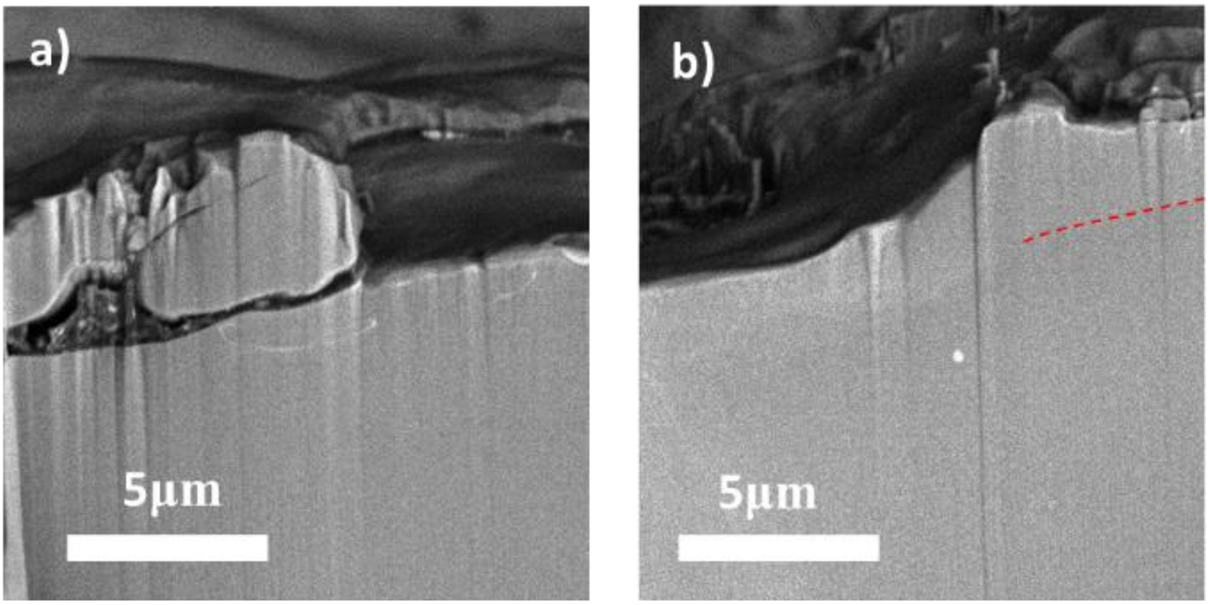

Figure 94 Close-up BSE images of the cross-section prepared by FIB milling: a) detached WL, and b) Embedded WL shown in more detail.

5.3.4. EDS analysis

Material melting and re-solidification at the processed surface occurs over a very limited period of time due to the high thermal conductivity of the parent metal and convective cooling by the flow of dielectric (deionised water) over the sample surface that assist heat dissipation. Similarly, material melting, dispersion and re-deposition occurs also at the surface of brass wire, leading to a degree of Cu and Zn re-deposition on the Al alloy sample surface. EDS mapping of the EDM machined surface shown in Figure 95(a) detect the presence of 'foreign' particles that had been detached from the wire and re-deposited on the EDM cut surface of the sample. Small Cu particles with the size of a few microns are clearly visible, as well as the slightly larger parts of Zn. Whilst these particles were deposited when the re-solidification of the sample surface had already been concluded, it is also possible to discern another fraction of brass contaminants that became mixed with the Al alloy when both were in the liquid state. The consequences of this effect can be seen in the EDS map shown in Figure 95(b), in which high concentration of Cu and Zn is visible that is associated with the WL. This suggests that Al parent material became enriched with Cu and Zn, raising the possibility of phase transformation occurring within the WL. Phase transformation arising as a consequence of EDM cutting has been reported in the past for martensitic [289].

It is also worth showing EDS concentration maps for Carbon (Figure 95(c)) which clearly show the enrichment of in C within WL. Carbon enrichment may a cause of material embrittlement typically reported for WL alongside Hydrogen embrittlement [290].

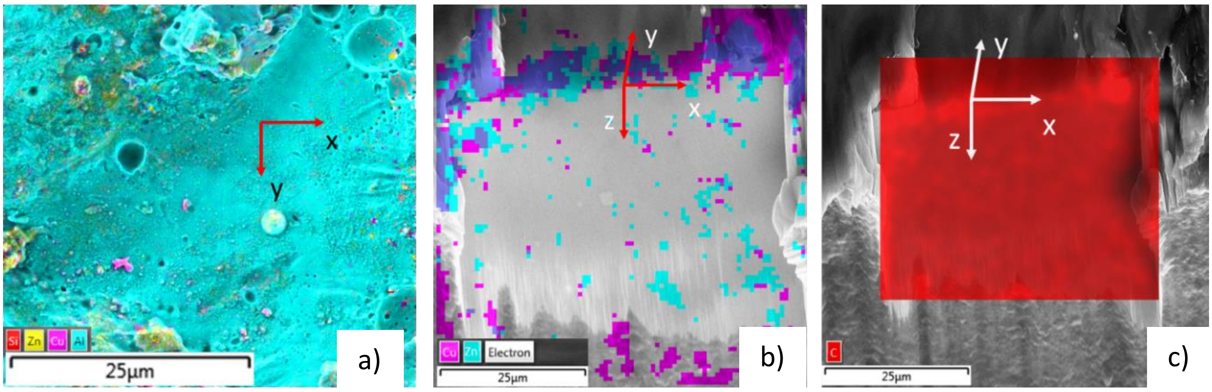

Figure 95 EDS maps of single pass EDM machining (MC): a) Top surface. b) Cu and Zn concentration within the cross-section. c) Carbon concentration at the cross-section

5.3.5. EBSD crystal orientation analysis

EDSB is usually employed when the material microstructure orientation is sought. An early EBSD study of crystal orientation within the EDM affected layer was conducted by Fu et al. [291] for Nitol shape memory alloy. This study showed material recrystallization occurring within the white layer, and revealed its non-uniform structure. The same authors in a later publication [292] show that the application of a trim cut reduces considerably the non-uniformity of the newly generated grain structure.

In the present section we report the interrogation of the underlying crystal structure that was performed within the FIB-polished section. Electron beam energy used for mapping was 25keV, and the spot size of 0.2µm was used. The map shown in Figure 96(a) collected from the polished cross-section is displayed using the colour legend shown by the basic crystallographic triangle with respect to direction Y. EBSD map reveals the relatively large grain size (in excess of 20µm) within the substrate. The presence of grain misorientation is barely visible in the vicinity of the EDM-machined surface, particularly at the grain boundary. EBSD fails to capture the underlying crystal structure in the majority of the WL area due to Kikuchi patterns having poor quality or not being visible. The absence of Kikuchi patterns is often taken as an indication of lack of or low material crystallinity, i.e. a heavily deformed / defected, or predominantly amorphous structure. Previous studies affirmed the presence of regions within the WL where the material loses crystallinity [293]. Another possible explanation of the poor indexation due to low quality of diffraction pattern can be excessive plastic deformation having occurred within WL.

To make further progress, it was decided to map a small portion of the entire FIB-machined section at high resolution and using measures to remove background and improve pattern quality by image averaging. To shed some light on the WL phase composition, high precision ESBD analysis was focused on phase discrimination rather than local grain orientation. The resulting map is shown in Figure 96(b), in which phases containing high concentration of Cu and Zn are shown in green, whilst the remaining parent metal fcc structure is shown in red. In the vicinity of the EDM-machined surface a thin layer contains Cu and/or Zn-rich phases, confirming that phase transformation occurred within the WL.

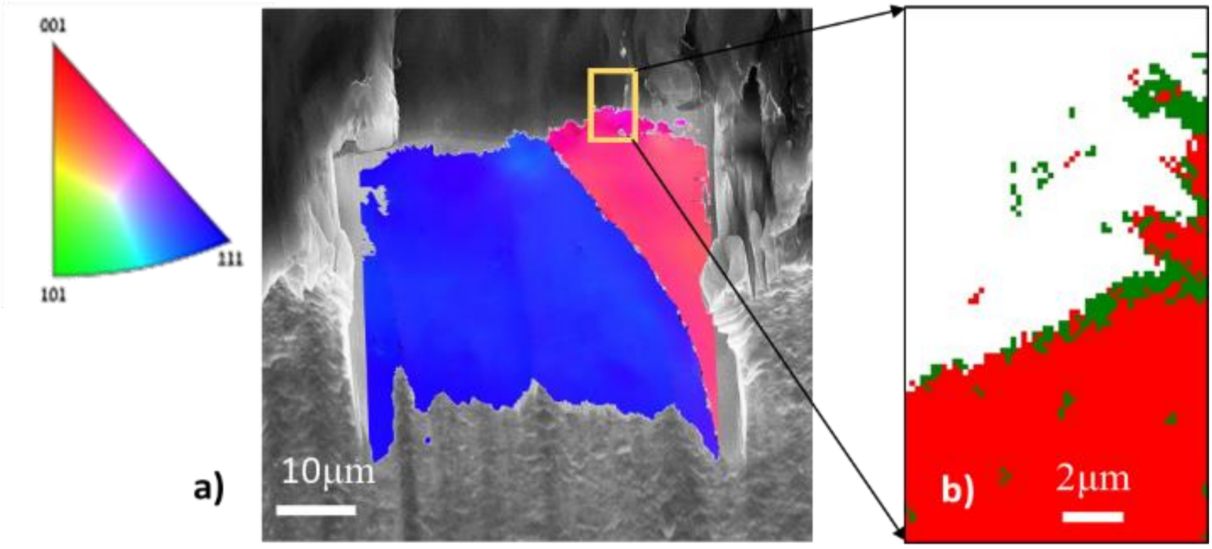

Figure 96 EBSD analysis results: a) EBSD map at the FIB-machined cross-section shown using the colour legend defined by the basic crystallographic triangle with respect to direction Y shown on the left, and b) Phase map close-up within the white layer, with regions coloured in green corresponding to phases rich in Cu and/or Zn

5.3.6. White layer residual stress profiling

In the current study FIB-DIC micro-ring-core method was employed for residual stress profiling within the WL and the underlying heat-affected zone (HAZ). The method is sensitive to the residual stress in the shallow layer of material close to the surface of the sample. The depth sensitivity of FIB-

DIC ring-core method has been extensively discussed previously. It has been shown that the thickness of such layer is linearly dependent on the ring-core diameter *D*, and that the highest influence on the overall strain relief perceived at the surface of the central micro-pillar is exerted by the material layer lying at the depth ~0.3*D*. It is has also been shown that the resolution of residual stress in the layers lying within the depth range between the material surface (0D) and ~0.05*D* is strongly affected by the trench width, surface roughness, ion damage, and thus cannot be reconstructed with confidence. Furthermore, it turned out that the depth range that provides most useful information about the residual stress underneath the material surface lies at the depths ~0.1D-0.3D. In other words, the absolute depth at which residual stress can be reconstructed well depends on the ring-core diameter. This means that smaller ring-core diameters provide more accurate residual stress measurements for the shallower depths (with the limitations already noted previously), while the use of larger ring-cores is more effective in probing the residual stress at larger depths. A combination of multiple ring-core diameters allows the reconstruction of the depth profile ranging from shallow to large depths with high fidelity, allowing the error to be reduced considerably compared to a single ring-core measurement.

In this work, **three** different ring-core diameters were used, namely, 5μm, 10μm and 15μm. An example of the ring-core milling performed at the EDM-machined surface of Sample A in shown in Figure 97(a) along with the characteristic dimensions. The adoption of these three diameters allows resolving the residual stress profile to depths up to 5μm. The aim of the present study was to obtain information about residual stresses at very shallow depths (up to ~3μm) within WL, and at medium (~3-10μm) depths within the HAZ zone. However, instead of repeating the previously reported approach that involves milling ring-cores of greater dimensions that can be rather time consuming, a different strategy was adopted. The approach consisted of pre-machining of a 25×25μm trench with the depth of 5μm using higher beam current in order to establish a new 'surface', thus allowing the data acquisition process to be speeded up. Subsequently, a 15μm diameter ring-core was milled in this trench so that an additional 5μm thick layer could be probed starting from this depth. Concerning this specific ring-core configuration, the residual stress depth profile reconstruction was performed using the same influence functions that were used for the previous measurements. This calculation could be performed by assuming that the material removal during the trench milling did not alter the residual stress present in the material right beneath the bottom of the trench.

The 15µm ring-core feature within the trench is shown in the SEM image in Figure 97(b). The new surface of material created by the FIB milling of the trench was appreciably smooth and did not show sufficient contrast for reliable DIC analysis. This issue was overcome by using Gas Injection System (GIS) to perform EB-CVD deposition of a Pt “sunflower” pattern visible as white dots in Figure 97(b).

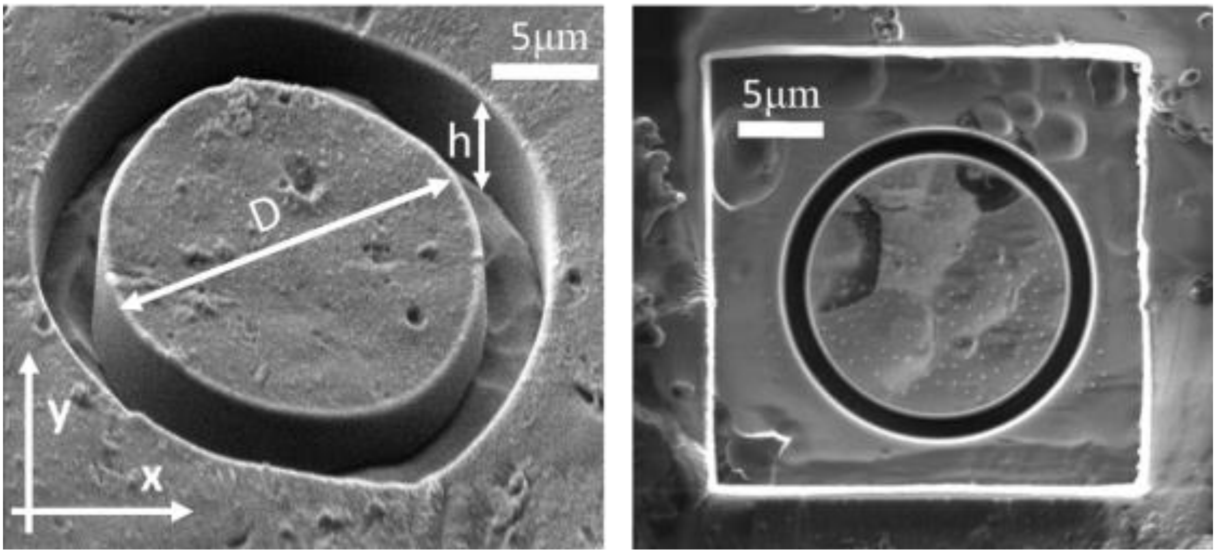

Figure 97 FIB-DIC ring core procedures: a) FEM image of D=15µm ring core in Sample A, and b) FIB image of D=15µm ring core in Sample B following trenching.

As the FIB-DIC milling process advanced, images of the material surface within the ring-core (pillar top surface) were acquired sequentially by SEM. The evolution of the average strain within the central region extending over 80% of the core diameter (strain relief) was assessed by means of Matlab-based DIC software [219] for directions *x* and *y* indicated in Figure 97(a). Examples of the evaluated relief strain as the function of normalised milling depth *h/D* are shown in Figure 98. Specifically, the strain components in the *x*-direction (SEM fast scan) for both samples are reported in the plot in Figure 98(a), and along *y*-direction (SEM slow scan) in Figure 98(b).

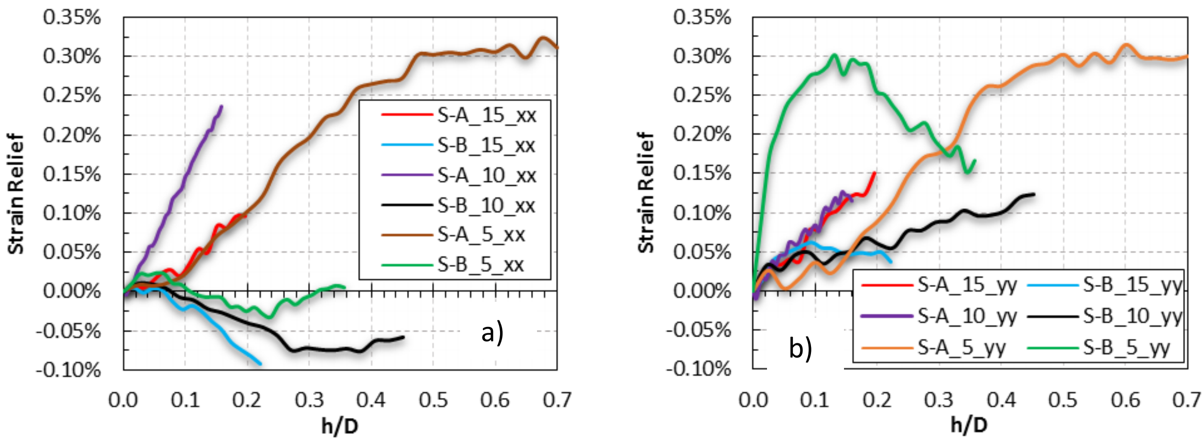

Figure 98 FIB-DIC relief curves: a) xx component of strain, and b) yy component of strain.

Relief strains were interpreted individually in order to abstract the information about the residual strain present in the material. Once the residual strains profiles were known for both samples and both orthogonal components (*xx* and *yy*), the residual stress profiles were assessed using Hooke's law formulation for plane stress:

$$\sigma_{xx} = \frac{E}{(1-\nu^2)}(\varepsilon_{xx} + \nu\varepsilon_{yy}) \tag{92}$$

$$\sigma_{yy} = \frac{E}{(1-\nu^2)}(\varepsilon_{yy} + \nu\varepsilon_{xx}) \tag{93}$$

Young's Modulus E and Poisson's ratio ν used for this material were 71 GPa and 0.3, respectively. Furthermore, DIC error propagation was preformed [21] and the error due to uncertainty of the local elastic orientation was accounted for.

In Figure 99, residual stress profiles are reported accompanied by the error bars that correspond to 95% confidence level. In addition, we report also the hydrostatic residual stress profile σ_H. The residual stress variation for the range depth between ~0.5mm and 5µm is obtained from the data for the three ring-core diameters milled directly into the EDM-machined surface. At deeper positions, the residual stress information is obtained solely from the 15µm diameter ring-core milled within the 25×25 trench obtained by FIB milling (Figure 97(a)). The lack of information relative to the residual stress at depth ranging between 5-6µm for the sample A is due to the trench for the 15µm ring-core having been milled to excessive depth during preparation.

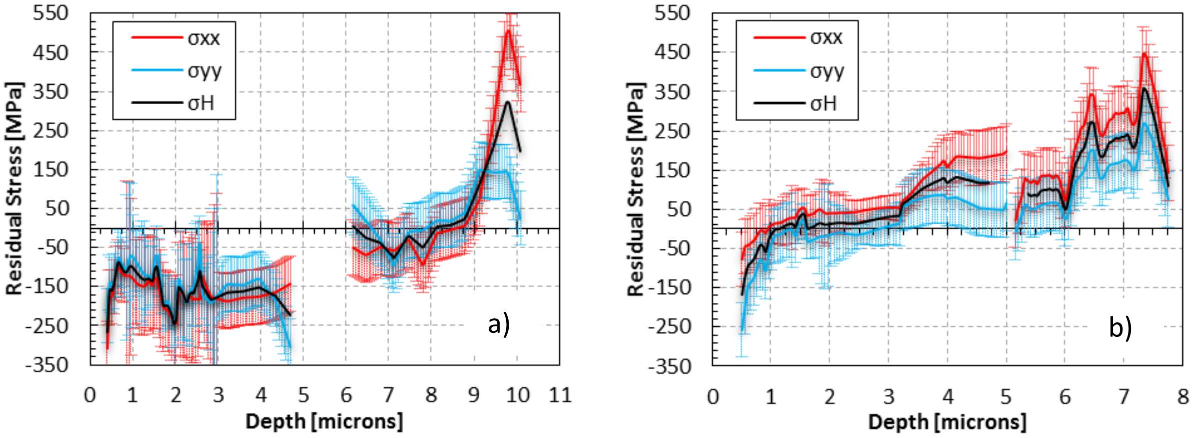

Figure 99 Residual Stress depth profiles for: a) Single pass (MC) and b) Double pass (MC+TC) EDM-machined surfaces

5.3.7. Discussion and Conclusions

The near surface structure and residual stress produced by EDM machining of Al alloy surfaces using the main cut (MC) and trim cut (TC) setting were investigated. The surface white layer (WL) and the underlying heat-affected zone (HAZ) were examined using modern techniques capable of exploring material characteristics down to the sub-micron scale. SEM imaging of the modified surface allowed the observation of the characteristic features created by EDM machining, such as the elemental composition variation and that (sub)micron sized pores that are of great importance from the viewpoint of structural integrity and component reliability. Thermal cracks are often reported to be present at EDM surfaces according to the literature [278], thought to be the consequence of the combination of material shrinkage and tensile residual stress arising during re-solidification. However, no trace of thermal tearing cracks was detected in the present study for either cutting setting (MC or TC). The absence of this type of cracks provides an indication of the nature of intrinsic residual stress: the absence of tearing crack formation in the material softened by the local elevated temperature suggests that only compressive or moderate tensile residual stress were be present in the WL. FIB sectioning was used for the observation of WL cross section. The combination of different modes of SEM imaging and micro-analysis revealed that WL thickness following main cut (MC) processing was in the range of ~2-5 μm.

As far as the analysis of the chemical composition is concerned, additional conclusions can be drawn by considering the phase transformation in the near-surface layer. The presence of Cu and Zn-enriched layers was found within the WL. The contaminant species were released by the EDM wire during the discharge machining and deposited onto the target material surface. It is well-known that phase transformation may be associated with material volume changes, giving rise to eigenstrain, the source of inelastic deformation and residual stress [57, 146, 294]. Such inelastic deformation (eigenstrain) must be made compatible by the elastic strains, which in turn give rise to residual stresses that must obey equilibrium conditions. It may be expected that one part of residual stress in the WL and HAZ arises from the phase transformation.

Further clues about the phase transformation taking place within the WL were extracted from EBSD analysis. For the majority of the WL cross-section areas no EBSD diffraction pattern was found, suggesting that the re-cast layer formed during EDM machining had low crystallinity or was amorphous. Nevertheless, for some locations EBSD patterns were interpretable and revealed the presence of phases rich in Zn and Cu. The lack of crystallinity was also noted by other authors via TEM lamella analysis that revealed the presence of amorphous regions in EDM-machined tool steel [293].

While XRD analysis techniques cannot overcome the issue of low crystallinity and phase transformation for the quantification of residual stress depth profile, FIB-DIC provides reliable assessment independently on the material structure. The use of multiple ring core diameters, in addition to trench milling for probing the material at higher depths below the surface, allowed the reconstruction of the residual stress profile through the WL and partially into the HAZ. The two samples manufactured be single main cut (MC) and by both main and trim cut (TC) were studied. A compressive residual stress state layer was found at the shallowest regions of both the samples. The compressive residual stress, in the case of sample A, persists for depth up to 5μm and its magnitude ranges between 100-250MPa for both the stress components (longitudinal and transverse with respect to the EDM wire). Similar compressive residual stress was detected in the TC sample. However, in the sample subjected to trim cut (TC), the compressive residual stress vanishes rapidly as the depth approaches to 1μm. The layer containing compressive residual stress for both samples is consistent with the thickness of the WL. It is therefore clear that for the examined material, and under these cutting conditions, it is the WL that gives rise to compressive residual stress. It is of fundamental importance to note that the residual stress measurements performed in the past by other authors relied on the use of XRD technique. This technique evaluates the residual stress by measuring the lattice spacing variation of a certain family of crystal planes, so that the formation of a new phase in the WL prevents proper comparison of lattice strain variation with the parent material. Therefore, XRD is not able to assess accurately the residual stress profile variation from WL to HAZ. We conclude that the results for residual stress profiles reported in the literature are in most cases relevant solely to the HAZ. On the other hand, the FIB-DIC ring-core method is independently of the crystal structure, and provides a reliable measurement, provided the change in the overall material elastic properties due to phase transformation can be ignored. The cause of compressive residual stress is thought to be associated with the phase transformation in the WL. Phase transformation is often associated with material volumetric strain. The containment and compatibilisation of this misfit strain through elasto-plastic deformation of the surrounding material gives rise to compressive residual elastic strain (r.e.s.) that gives rise to self-equilibrated residual stresses. However, we stop short of concluding that WL always experiences compressive residual stress, since the volumetric strain effects of the phase transformation must be material-specific. This is in line with some reports in the literature of WL containing thermal cracks that are likely associated with tensile residual stress present in it.

As far as the deeper material layers were concerned, tensile residual stresses were found in the heat underlying affected zone (HAZ). This finding is in agreement with the evidence from the majority of the literature reports. The residual stress within the HAZ region was only probed within the few microns below the WL-HAZ interface. Nevertheless, high values of tensile stress were observed, with magnitudes that were slightly higher in absolute magnitude than those found in the WL.

5.3.8. Conclusions

White layer (WL) and the underlying heat affected zone (HAZ) created by EDM machining of an Al alloy using main and trim cuts (MC and TC) were studied. Advanced tools were employed for the analysis of the WL structure characterisation and the quantification of the intrinsic stress. SEM images highlighted the presence of pores of irregular shape that may show either sharp or rounded edges, particularly at the WL surface of the sample subjected to solely to the main cut (MC).

EDS analysis showed the presence of high concentration of Cu and Zn within the WL which is thought to arise as a consequence of the elemental diffusion and sputtering of the Cu-Zn-containing tool wire. This elemental enrichment gave rise to the formation of new phases within the WL as confirmed by the EBSD analysis. Also, loss of crystallinity was observed in some regions of the WL, where it is likely that material amorphisation took place.

The residual stress analysis clearly showed the presence of a compressive stress state lying within shallowest layer of the EDM-machined surface. The presence of compressive residual stress was consistent with the thickness of the WL for both samples. It is worth noting that in the case of trim cut sample (TC), the compressive layer was considerably thinner than that of the sample subjected to sole main cut. This type of residual stress is thought to be mainly the consequence of expansive volumetric strain occurring when phase transformation takes place. Upon transition into the HAZ, the residual stress state becomes tensile, as is well documented by other authors. It is therefore evident that the origin of residual stress needs to be sought in two different mechanisms manifest during EDM cutting, namely, phase transformation (in the WL) and material quenching and plastic deformation (in the HAZ). The balance between these two processes is specific to the particular material and cutting process conditions.

Future studies will be addressed firstly at the analytical modelling of the thermo-mechanical processes involved during the machining process. Compressive residual stress state is beneficial in resisting fatigue failure. On the other hand, the presence of notch-like features along with material embrittlement are widely seen in literature as unfavourable. Therefore, process optimisation may proceed by studying EDM-machined surfaces and cross-sections through them in the way illustrated in the present report in order to optimise implications for structural integrity.

5.4. Eigenstrain Reconstruction of Residual Stress in an Additively Manufactured and Shot Peened Nickel Superalloy Compressor blade

5.4.1. Introduction

In the past, eigenstrain modelling has been successfully used for the reconstruction of arbitrary residual stress fields in both two- or three-dimensional numerical models [58, 295]. The eigenstrain distribution that induces a typical residual stress profile found after shot peening can be described by a continuous function that depends on the argument given by the distance from component surface that has been subjected to the treatment [296]. This assumption is based on the view that shot peening under given treatment conditions leads to the introduction of a well-defined eigenstrain distribution that, in the absence of particularly sharp tips, corners or notches, does not depend on the sample geometry [297]. When complex component geometries need to be analysed, the boundary shape description may not be possible by global analytical function(s). In such cases, the introduction of eigenstrain into the numerical model must be accomplished by combining the local functional description with the global numerical assignment of values to elements. The present study is devoted to the implementation of this approach for a particular case of aerofoil cross-sectional shape of compressor blade. The required prescription of in-plane eigenstrain tensor as a function of distance from the free surface was performed using a pre-processing routine written in Matlab for the evaluation of distances from boundary outline contour (shortest radius) at each Integration Point (IP) of the FE model. In addition, the angles formed by the shortest radius with global Cartesian axes are used to ensure the correct prescription of the local eigenstrain components, namely, compressive inelastic strain in the direction of surface normal, and expansion eigenstrains of opposite sign and 50% magnitude in the perpendicular plane.

In the present chapter we report the evaluation of residual strains within the cross-section of an additively manufactured compressor blade that was subsequently treated by shot peening (SP). Residual strain measurement was conducted by means of two experimental techniques, namely, FIB-DIC micro-ring-core [20, 76, 84] and synchrotron X-ray powder diffraction (SXRPD) [298-301] in transmission mode. These techniques perform residual strain evaluation based on two different principles and in different gauge volumes. As well as other variants of the FIB-based milling technique [91, 92, 302-305], the FIB-DIC micro-ring-core technique relies on the principle of the strain relief after the introduction of a cut that creates new traction-free surfaces, whereas as far as SXRPD is concerned, strain is evaluated by monitoring the lattice parameter change for crystalline material. FIB-DIC micro-ring-core method is able to measure local residual strain at or near free surface of material regardless of whether it has crystalline or amorphous structure. In contrast, SXRPD technique is applicable to polycrystalline materials and, due to high penetrating ability of hard X-rays, produces a gauge volume that spans the entire sample depth, while micron scale lateral resolution can be readily achieved. These distinctions between the two techniques are carefully traced through the discussion, and are used in combination for the purpose of cross-validation.

For the purposes of analysis, the Leading Edge (LE), Trailing Edge (TE) and Middle position (M) on the blade were analysed using the techniques described above along several lines. Once the reconstruction of eigenstrain distribution was achieved, it was employed to visualise residual stress and strain fields everywhere within the blade and in specific regions of interest.

5.4.2. An approach to eigenstrain analysis for arbitrary 2D geometry

The distribution of residual stress/strain generated by a surface treatment process can be reproduced by the eigenstrain approach. The introduction of an eigenstrain distribution within the model by means of a continuous function can capture the intrinsic strain distribution generated by the underlying process operation by applying eigenstrain to simulate the inelastic deformation arising as a consequence of a treatment such as surface processing.

Generally, a two-dimensional (2D) solid mechanics problem can be considered in the plane-stress or plane-strain approximation. The choice of the most appropriate approximation is determined by the constraint experienced by the material in the out-of-plane direction. Depending on the nature of the problem, the eigenstrain distribution in a 2D domain can be specified. In particular it is interesting to consider a situation when eigenstrain components are also confined to the plane of consideration, so that the problem arising can be referred to as the plane eigenstrain problem.

Schematic diagram in the Figure 100 shows how at each arbitrary point P lying within the model, the x- axis orientation of a Local Cartesian coordinate System (LCS) can be identified as the direction of vector that connects to the nearest contour point C, $\overline{PC}$. Consequently, the angle α denotes the rotation angle of the LCS with respect to the Global Cartesian coordinate System (GCS). According to this schematisation, the components of eigenstrain in the LCS ($\varepsilon^*_{x^I}$ and $\varepsilon^*_{y^I}$) can be prescribed by using ε^*_x and ε^*_y in the GCS upon the knowledge of the rotation angle α.

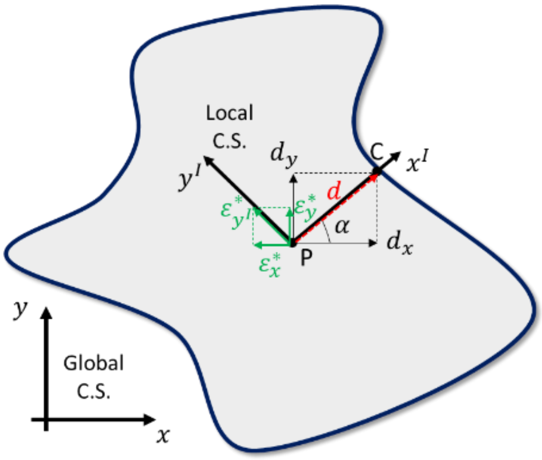

Figure 100 . Schematic diagram illustrating the relationship between contour geometry and the LCS at the point P defined in terms of the distance d to the nearest contour point C, and angle α made by the vector $\overline{PC}$ with the global coordinate direction x

Prescribing eigenstrain distribution using a continuous function requires the computation of the minimum distance for arbitrary point P from the nearest point on the sample contour, C. In order to impose correct eigenstrain components along the directions normal and parallel to the boundary contour, the angle α must be found that is formed by the surface normal at point C and the abscissa axis of the GCS.

The practical implementation of such algorithm within the Abaqus environment represents a challenge, given the difficulty of defining the boundary contour from element node data. An alternative approach is to evaluate the required value of distance and angle prior to the FE computation using a Matlab-based routine. The procedure involves the use of a binary mask representing the sample geometry, with the values set to 1 within the sample, and 0 outside. For each pixel within the mask that has the value of unity, the distance to the nearest null value pixel can be evaluated readily. The output from this pre-processing step is incorporated into the Abaqus model by extracting integration point (IP) coordinates and computing the distances and angles by interpolation of the values from Matlab image analysis. Abaqus subroutines are then used to set the distance and angle data for each IP as internal variables, and to compute the correct eigenstrain components accordingly.

The detailed list of the steps needed for the implementation of the above procedure, along with comprehensive description, is reported in the Appendix. With the aim of checking the correctness of the imposed eigenstrain, in particular the right component discrimination, the principal directions can be visualised during the post-processing. Figure 101(b) below illustrates a quiver plot of principal directions. In this specific case, two principal components of eigenstrain imposed were perpendicular and parallel to the model edges (blue line). The vectors indicate the principal directions are seen to be consistent with the contour orientation, particularly as the boundary is approached. It is possible to observe in Figure 101(b) that the red arrows (directions of maximum principal stress/strain) are actually locally perpendicular to the contour, whilst the other direction (indicated by the black arrows) is locally tangent to the contour.

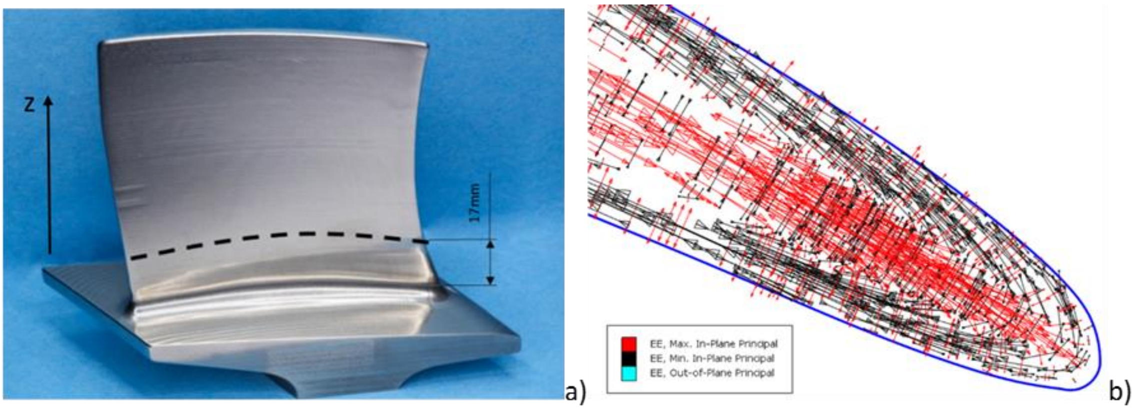

Figure 101 (a). Compressor blade image and cross section location. (b) Example of principal direction assignment within the cross-section represented by a quiver plot.

5.4.3. Residual stress reconstruction in ALM shot peened blade

Additive Layer Manufacturing

Additive Layer Manufacturing (ALM) is an emerging technique for the production of complex three-dimensional mechanical components. If the material involved is metal or alloy, the fundamental idea of this technique is the melting of a stationary bed or a jet of compound powder, usually by means of rastering a high energy focused laser beam or, in some cases, using conventional weld arc. Therefore, the final product is built up by adding one cross-sectional layer of material at a time [306]. This process is usually interfaced with 3D CAD models, so that near-net-shaped components can be formed by reproducing the sequence of cross section contours that compose the model. The introduction of this technique has allowed the designers to optimise their objects, particularly to improve the performance and reduce weight. The application of ALM is not limited only to the macroscopic scale, but also applied to micro-scale and nano-structures [307]. The technique delivers outstanding performance in the welding of dissimilar materials, reducing various unwanted side effects that arise with the use of other methods [308].

In recent years ALM has begun to be increasingly utilised in aerospace applications, particularly when high temperature performance is sought [309]. Compressor blades are a prominent example of a mechanically loaded component that is simultaneously subjected to high temperature. Gas turbine engines contain numerous blades that are exposed to cyclic loading and whose failure leads to the loss of efficiency or even destruction of the entire system. Thus, periodic monitoring and replacement of turbine blades is necessary. In some cases the repair of damaged parts using ALM (instead of replacement) is a feasible solution that is also significantly less costly [310, 311].

Despite its supreme versatility, ALM may give rise to some undesired effects in the component manufacturing. The most obvious is porosity: since the technique does not involve the application confining pressure during solidification from melt, gradients in material density may arise. The combination of this effect with the high gradients in temperature may lead to the generation of defects [312]. Furthermore, the rapid changes in the local temperature and thus steep temperature gradients within the component may give rise to thermal stresses. If this stresses exceed the material strength, voiding or cracking may appear [313]. Finally, during cooling from the processing temperature, uneven material shrinkage may give rise to residual stress and distortion [314].

Methods for experimental residual strain measurement

Residual stress measurement can be accomplished using several techniques, but only a few of them are able to provide resolution down to the finest scale of e.g. microns. In the present study two experimental techniques were employed for residual stress evaluation, FIB-DIC micro-ring-core milling and synchrotron XRD.

Compressor blade description and sample preparation

Additive manufacturing techniques were used to create an IN718 compressor aerofoil as shown in Figure 101(a). Particularly, the technique adopted was the Laser Metal Deposition (LMD) using a laser and blown powder. Shot peening was applied along the entire contour of the component in order to induce compressive stresses close to the surface regions. Based on the results of prior vibrational testing, a cross section of the aerofoil was selected as the region of interest for this study. This fatigue test enabled to pinpoint the critical region of this component (i.e. crack nucleation location). This was at 17mm from the blade root, as indicated in Figure 101(a).

In order to implement the semi-destructive FIB-DIC micro ring-core and SXRPD analysis techniques for the residual strain measurement, free surfaces at the region of interest and a near-constant stress distribution along the blade extension were sought. For this reason, sectioning of the aerofoil was performed in the circumferential direction parallel to the outer edge of the aerofoil using a diamond cutting wheel. As result, a 2mm thick cross-section across the entire blade was extracted.

Surface material removal of the layers of material affected by cutting was performed using Grade 320 grinding paper. Following this, increasingly fine grit sizes (up to Grade 4000) were used to improve the surface finish. Polishing of the surfaces was then performed using 0.1 µm diamond suspension. In order to minimise induced surface stress and increase the surface contrast of the sample, etching was then performed on the surface using a weak acetic acid solution. In fact, controlled chemical etching enabled the removal of the shallowest layer impaired by sample preparation.

Three milling regions on the cross section were selected for FIB-DIC and SXRPD residual strain analysis. A montage cross section showing regions of stress analysis and approximate mapping positions is reported in Figure 102.

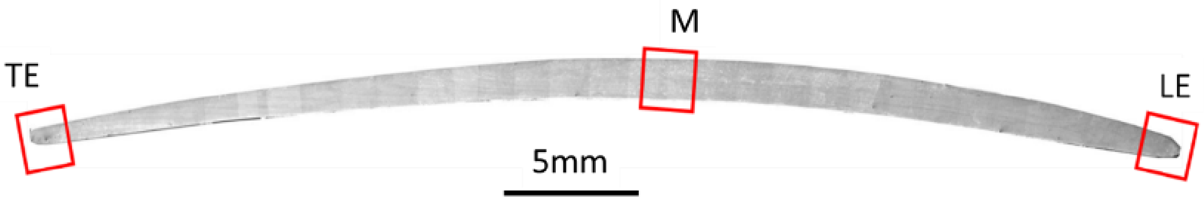

Figure 102 Blade cross-section and measurement locations

FIB-DIC measurement

Residual stress distributions were obtained by repeatedly performing the strain analysis procedure with set increments ranging from 100 to 50 microns between between each FIB-DIC measurement. Following this testing procedure, the final FIB milling parameters were chosen to be 30keV and 0.17nA.

The optimal SEM parameters were found to be 5keV and 260nA. The incremental FIB milling of the surface was performed in synergy with the SEM image acquisition. A SEM image was collected, at the resolution of 2001x2001 pixels, after each milling process and 50 images were recorded for each measurement. Figure 103 shows an example of images taken at different stages as the ring core milling advanced.

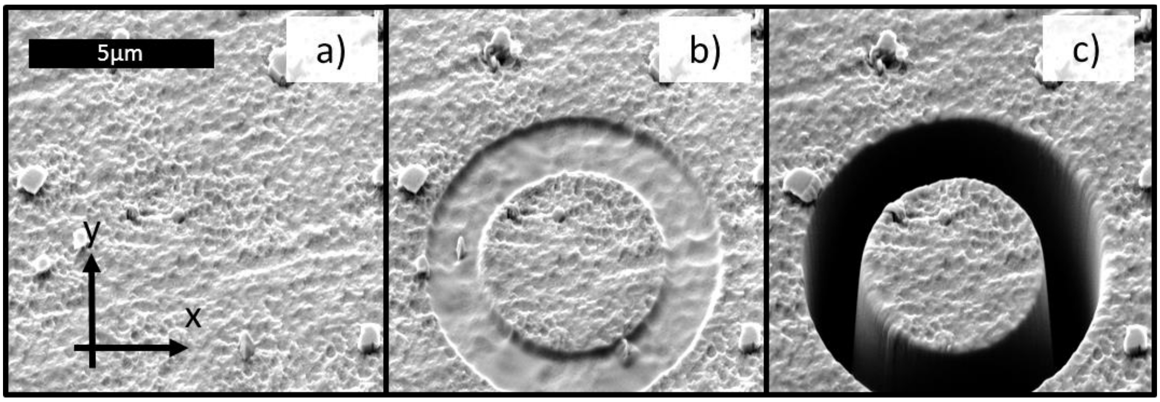

Figure 103 Micrographs showing typical ring core milling process. a) Images of preliminary surface showing the contrast required for DIC arising from the etching process. b) Intermediate milling stage showing the ring-core milling shape. c) Marker appearance as the final milling depth (note the presence of instrumental tilt correction)

The introduction of DIC at this stage allowed the reconstruction of the strain relief at the stub top surface. For the sake of convenience the average strains were measured in the two perpendicular directions (x and y in Figure 103). These directions were accurately chosen to match the sample contour directions that were thought to be coincident with the principal strain/stress direction. At each milling point therefore, a pair of relief curves were obtained. The interpretation process of the relief curves leading to the abstraction of residual strains present within the material prior to milling was conducted by master curve fitting. The uncertainties arising from this process were assessed and reported with the final residual strain values as error bars, as will be shown in the subsequent sections.

SXRPD measurements

SXRPD analysis was performed at beamline I15 at Diamond Light Source, Harwell. A monochromatic beam with the photon energy of 76 keV was focused down to less than $70 \times 70\ \mu m^2$ in size by two 1.2m long Kirkpatrick-Baez mirrors, and then cleaned up by a collimator of 70 µm diameter positioned close to the sample. The sample was placed into a specially manufactured mount and an optical system was used to align the beam with the FIB-DIC marker locations at micron-scale precision. A raster scan was then used to collect diffraction patterns in steps of 50 µm from the edge of the sample. A PerkinElmer flat panel 1621-EN detector (2048x2048 pixels, pixel size 0.2x0.2mm^2) was used to record the resulting diffraction patterns.

A general observation can be made regarding the diffraction patterns collected. As seen from Figure 104, the relatively large grain size present within the sample induced pattern "graininess". In particular, the larger grain sizes at the two extremes of the blade (TE and LE) produced poor powder diffraction pattern quality compared to the pattern obtained at the middle position (M). Due to these limitations it was only possible to obtain SXRPD patterns that lend themselves to reliable interpretation only from the middle position of the blade, and also for the *yy* component of strain at the blade Trailing Edge (TE).

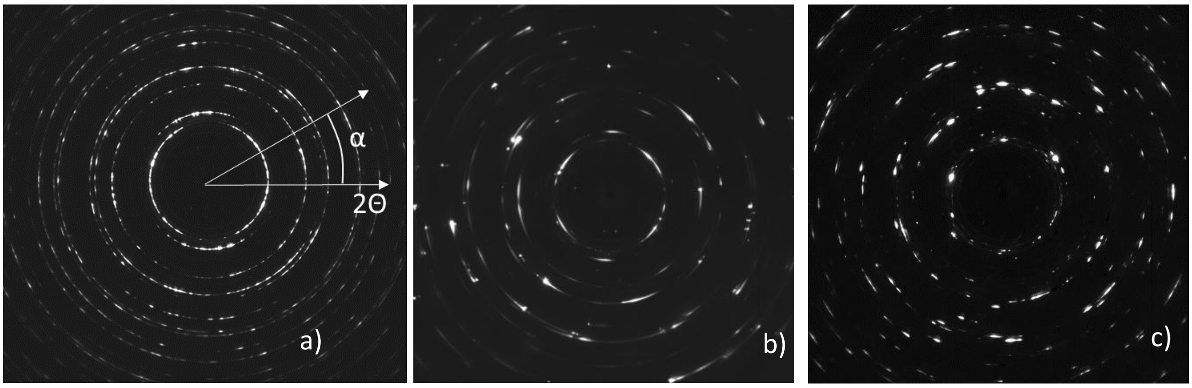

Figure 104 Debye-Scherrer rings at various cross section locations: a) Middle position in the blade "MP". b) Trailing Edge blade "TE". c) Leading Edge blade "LE".

For the reasons given above, 60° azimuthal integration was used to improve the grain sampling statistics of the resulting 1D spectra. A critical examination of the Debye–Scherrer rings revealed that sample graininess had least impact on the ϒ phase <200> peak. Lattice parameter quantification was performed using this peak for the scattering vectors parallel and perpendicular to the sample contour. Furthermore, in order to improve the sampling statistics, integration of the patterns for the relevant strain direction was performed for both diametrically opposing segments spanning 60° angular range. Final interpretation was performed using least squares minimisation to reduce noise further and minimise the error due to small error in the ring centre determination.

For a given Miller index hkl, the conversion between the XRPD lattice parameter variation (d_{hkl}) and the estimate of lattice strain (ε_{hkl}) is given by (3):

In this study, the direct comparison between the absolute residual strain values obtained by FIB-DIC, at the middle position of the blade (MP), and relative values obtained by XRPD was used. Small changes in d_{hkl}^{0} correspond to the change in the vertical offset in the stress profiles. This simple relationship allows us to use FIB-DIC data to support the refinement of the unstrained lattice parameter of face-centred cubic γ phase of IN718, which was determined to be a_{γ}^{0}=3.59756 Å.

Residual strain reconstruction and comparison with experiments

Due to the nature of the studied sample, the residual stress problem can be treated in the plane stress approximation, with the out-of-plane components (longitudinal direction of the blade indicated by the z axis in Figure 101(b)) of stress being assumed null. This is also true for the case of FIB-DIC measurements. Preliminary numerical simulations showed that the imposition of non-null eigenstrain distribution of any shape along the direction perpendicular to the local contour line did not give rise to noticeable residual elastic strain and residual stress. This can be understood by considering the fact that material expansion along these directions is not constrained, so that the material deforms freely and no permanent misfit arises due to the eigenstrain introduction.

Consequently, the present problem was reduced to the sole analysis of the eigenstrain component in the tangent direction to the model contour.

Eigenstrain distribution was imposed in a point-wise fashion at each IP of the FE mesh. For the purposes of algorithmic implementation, eigenstrain was defined by means of a continuous function of the shortest distance of each IP from the component contour.

Additive Layer Manufacturing process intrinsically introduces a residual stress field within the mechanical part, on which the additional eigenstrain generated by Shot Peening (SP) is superimposed. The outcome of SP can be described by a tensile tangential eigenstrain profile which has non-zero value at the surface, increases in magnitude with depth, and vanishes at the depth up to a few hundred microns. The residual stress profiles generated by SP can be described using a shifted cosine function superimposed on a linear background, as introduced in the paper by Watanabe et al. [315]. A further extended analysis of the residual state in a shot-peened plate was presented in the paper by Korsunsky

[41], which demonstrates that the residual stress profile arises from the superposition of linear bending on the inverted eigenstrain profile. In other words, in the Watanabe et al. formulation the shifted cosine term (truncated at the depth where it reaches zero value) that corresponds to the eigenstrain introduced by shot peening.

It is clear that this choice of eigenstrain representation is made on the basis of matching experimental observation, and is not unique. As an alternative, in the present study we consider the eigenstrain profile to be represented by a shifted Gaussian function. In practice, the difference in the profile representation between shifted Gaussian and shifted cosine is minimal, as illustrated in Figure 105(a). However, the choice of Gaussian function obviates the need for truncation, and also paves the way for the representation of more complex distributions by linear combination of multiple Gaussian peaks, as illustrated below.

The effect of severe plastic deformation that occurs in the region affected by SP tends to dominate over any pre-existing residual stress state inherited from prior processing. In fact, the SP effect overcomes and removes the residual elastic strain caused by the ALM process. Therefore, in the vicinity of the component contour it is correct to impose solely the SP residual elastic strain (eigenstrain) profile. On the other hand, within the bulk of the component away from the contour the consequences of the ALM process are expected to be present, and needs to be captured by the introduction of an appropriate eigenstrain profile. Generally, residual stresses in AM-built components are thought to be highly dependent on the manufacturing path and therefore on the specific geometry of the mechanical component, as well as other parameters (beam spot size, power density, scan speed, etc.) This is a topic of strong interest in the scientific community since no fundamental understanding in this mechanism is yet available.

In our experiments the residual elastic strain was evaluated with greatest accuracy at the Middle position of the blade, compared to the other positions. Therefore, this region was chosen for calibrating the eigenstrain distribution. Given the predominance of SP eigenstrain in the near contour region, we first use error minimisation to calibrate the parameters of the Gaussian profile that describes the eigenstrain in the form:

$$\varepsilon_{SP}^{*} = A_{SP}\, e^{-\frac{(d-b_{SP})^2}{2c_{SP}^2}} \tag{94}$$

In the expression in Eq.94, A_{SP} is the Gaussian amplitude, b_{SP} is the coordinate shift, and c_{SP} is the Gaussian width. Argument d is the distance of the IP from the model contour. FEM calibration were performed by varying the three parameters and minimising the deviation from the experimental data. Once satisfactory agreement was found, the background eigenstrain that represents the ALM process in the inner region of the blade was sought in the same way. Again, a Gaussian function was adopted (95) for the FEM optimisation process. Subscript BG indicates the reference to the background profile:

$$\varepsilon_{BG}^{*} = A_{BG}\, e^{-\frac{(d-b_{BG})^2}{2c_{BG}^2}} \tag{95}$$

Table 11 summarises the coefficients found by performing FEM calibration that were adopted for residual elastic strain prediction.

Contribution	*A*	*b*	*c*
Shot Peening (SP)	0.0065	0.80	0.24
ALM background (BG)	0.0075	0.12	0.25

Table 11 Eigenstrain distribution parameters

The complete eigenstrain profile was constructed by summing the two contributions:

$$\varepsilon^{*} = \varepsilon_{SP}^{*} + \varepsilon_{BG}^{*} \tag{96}$$

The plot in Figure 105(b) illustrates the two contributions (SP and background), shown in solid and dashed lines. In addition, the total eigenstrain imposed to the model is shown by the thick black line.

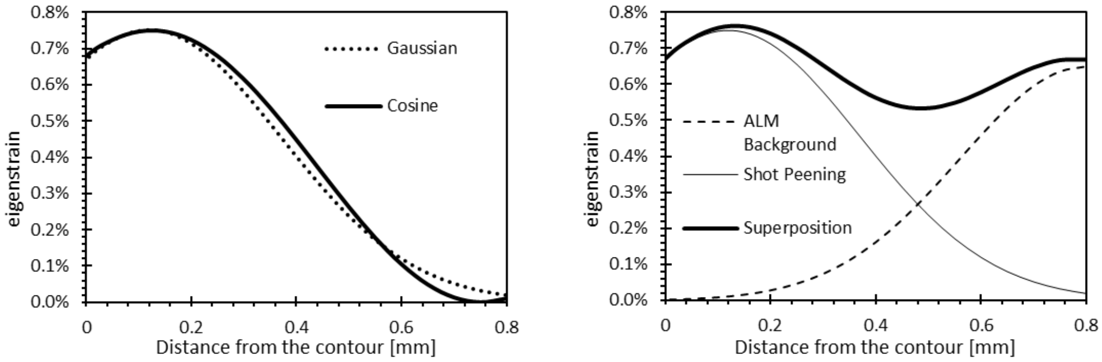

Figure 105 Eigenstrain distribution. (a) Shape function comparison. (b) Contributions and superimposition

The blade geometry was modelled by contouring the SEM blade image acquired within a 2D modelling software. Following the steps described in the Appendix, the eigenstrain distribution was implemented in the FEM model, and the solution obtained for the three regions analysed. Consistent eigenstrain profile of Figure 105(b) was imposed in the subsequent analysis of other regions of the blade, in order to obtain validation of the correctness of the calibration approach adopted in the present study.

The results provided by FEM post-processing can be visualised using coloured contour maps and by plotting 2D strain profiles of each component along selected paths. The residual elastic strain variation was compared with experimental measurement lines.

The experimental results at middle position of the blade (MP) were collected across the entire blade thickness using SXRPD and across a reduced length close to one edge using FIB-DIC. These and possessed good accuracy in both cases. Figure 106 shows experimentally measured residual strain components along with the residual elastic strain reconstructed by eigenstrain. Contour maps in the following Figures show the maximum principal residual elastic strain.

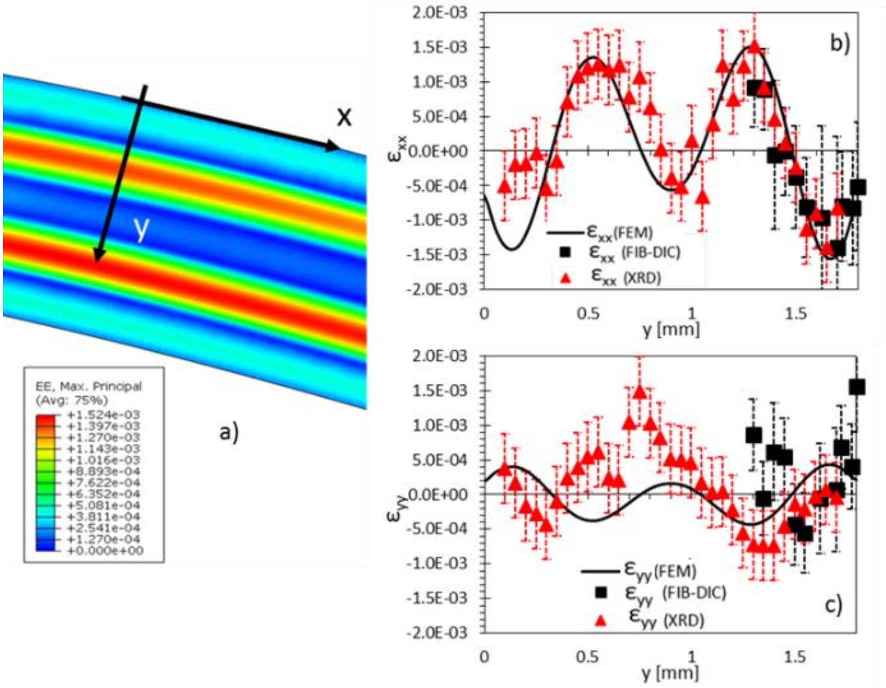

*Figure 106 Residual strain distribution across the blade cross section (position **MP**) and comparison with eigenstrain reconstruction. (a) Max principal elastic strain contour plot. (b)* ε_{xx} *(c)*ε_{yy}

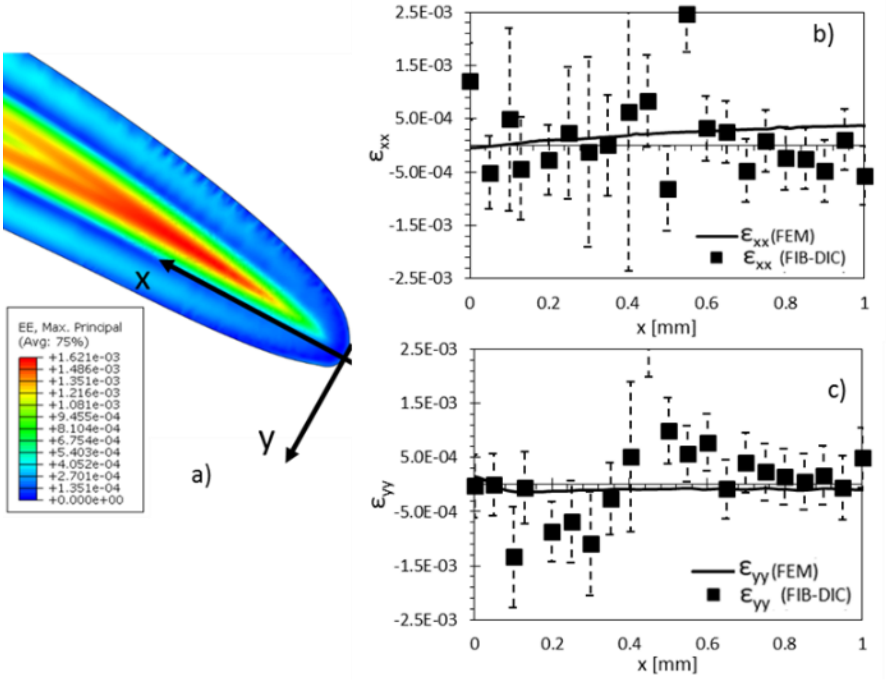

Figure 107 Residual strain distribution along the blade cross section (position ***LE1****) and comparison with eigenstrain reconstruction. (a) Max principal elastic strain contour plot. (b)* ε_{xx}*, (c)* ε_{yy}

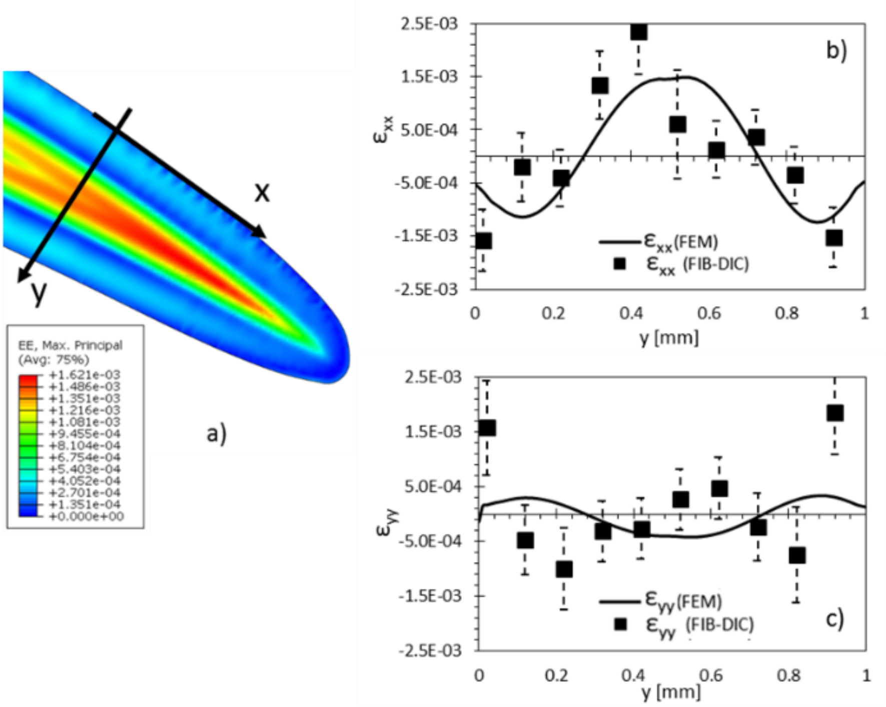

Figure 108 Residual strain distribution along the blade cross section (position ***LE2****) and comparison experiment vs. eigenstrain reconstruction. (a) Max principal elastic strain contour plot. (b)*ε_{xx} *comparison. (c)* ε_{yy} *comparison.*

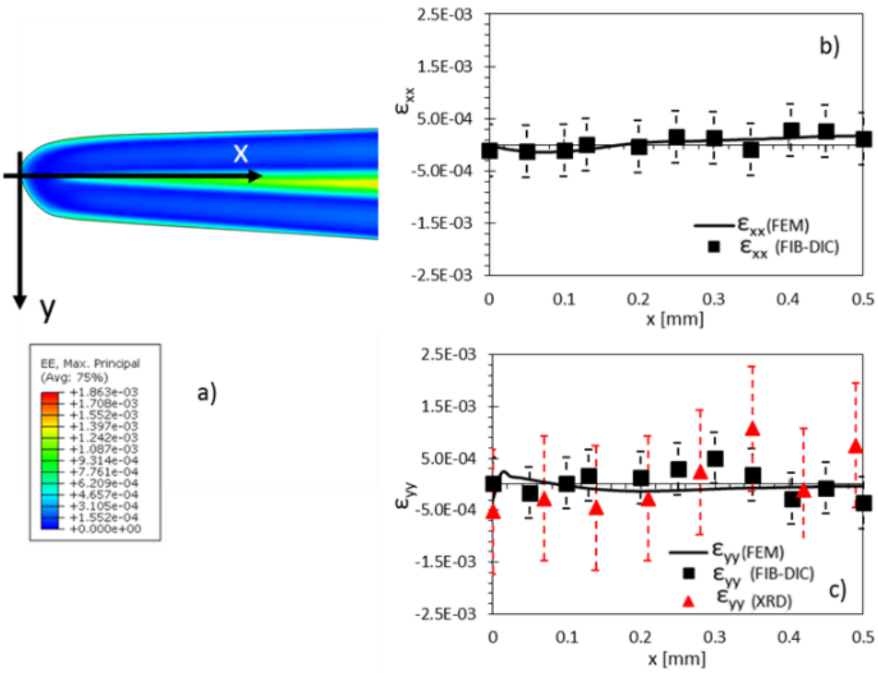

*Figure 109 Residual strain distribution along the blade cross section (position **TE**) and comparison experiment vs. eigenstrain reconstruction. (a) Max principal elastic strain contour plot. (b)ε_{xx} comparison. (c) ε_{yy} comparison.*

At the blade Leading Edge (LE), the residual strain was measured along two perpendicular lines. The first line originated at the tip of the blade in the LE position and ran along the bisector of the LE tip contour line. The results are shown in Figure 107. For this location no reliable SXRPD measurements can be reported due to the excessive graininess of diffraction patterns.

The second measurement line at the blade Leading Edge (LE) ran across the blade thickness at the location where it equals 1mm. The results are shown in Figure 108. Once again, no SXRPD measurements are reported for the same reason stated above.

The final set of measurements was collected at the blade Trailing Edge (TE). At this location the residual strain distribution was spatially resolved along a line perpendicular to the blade tip as shown in Figure 109(a). The same figure also shows the residual strain plots. Here the SXRPD are reported solely for *yy* strain component, for which the values could be seen as useful even in the presence of large errors indicated by the error bars.

However, in order to quantitatively describe the dispersion of experimental data about the FEM strain field, the root-mean-square deviation was evaluated for each set of measurements. The calculated values are reported in Table 12.

Strain	TE	LE1	LE2	MP
RMSD ε_{xx}	1.05e-04	7.59e-04	7.82e-04	6.89e-04
RMSD ε_{yy}	7.07e-04	8.23e-04	9.24e-04	9.34e-04

Table 12 Root-mean-square deviations at different locations and for the two relevant strain components

5.4.4. Discussion

A procedure for efficient description of eigenstrain distribution due to surface treatment in two-dimensional models has been successfully developed and presented. The correctness of the implementation was verified by visualising principal strain directions over the model geometry.

The problem being studied concerned shot peening (SP) process applied to compressor blade. Residual stresses arising in this situation represent the superposition and perhaps interaction between the two manufacturing processes (ALM and SP). The assessment of the residual strain profile was conducted experimentally by means of FIB-DIC and SXRPD. The eigenstrain profile induced by SP over the pre-existing ALM background was assessed, and the predicted residual elastic strain distribution compared to experimental measurements. Acceptable overall agreement was found, particularly in view of the large uncertainty associated with the ALM outcomes. Specifically, at the blade Middle position the xx component of strain (ε_{xx}) showed good agreement between experimental and numerical solutions (Figure 106(b)). Less accurate agreement between reconstruction and measurements was found for the perpendicular component of strain, ε_{yy}. In fact, this reconstructed quantity failed to match the magnitude in the central part of blade thickness, although the overall trend match is satisfactory (Figure 106(c)). It is worth noting that the mismatch was primarily observed at the central region of the profile, where the background residual stress was imposed. This disagreement may be imputed to the complex residual stress distribution produced by the manufacturing process that evidently may slightly diverge from the nominal eigenstrain distribution imposed as background.

Regarding the other two regions of the blade, it is worth reminding that the FEM simulation are the outcome of the calibration against experiments conducted at the MP. Therefore, a limited discrepancy from the experimental outcomes was expected. At the blade Leading Edge, the measurements were affected by large errors, as is evident in Figure 107(b-c). Nevertheless, the majority of experimental points are seen to lie close to the predicted eigenstrain curve. Nevertheless, the trend highlighted by the measurements was not captured satisfactorily. This divergence is thought to be due changes in the operation of both ALM and SP processes at blade tips. It is reasonable to anticipate that at the tip the effectiveness of SP may deviate significantly from parallel surface regions. Similarly, the conditions of material deposition by ALM are likely to be modified by the proximity of the sample boundary. Furthermore, local deviation between FEM prediction and FIB-DIC measurements can be caused by the presence of very small and localised pockets of porosity in the form of micron-scale clusters of solidification nano-pores. In fact, it is well known that one of the most prominent disadvantages of this manufacturing technique is the generation of undesired porosity [316]. On the other hand, good agreement was found along the line across the blade thickness at this location (Figure 108(b-c)).

Finally, the analysis at the blade Trailing Edge (TE) did not reveal high magnitudes of residual strain (Figure 109). This was confirmed by the eigenstrain reconstruction that predicted this residual elastic strain state. Low residual strain magnitudes are the results of large plastic deformation occurring almost throughout the entire blade thickness. Therefore, only a very limited amount of residual elastic strain arising to, may arise to restore the equilibrium disturbed by eigenstrain introduction.

One remark needs to be made regarding the effectiveness of SP process. It has been revealed in the present work that in the presence of tight contour radii, the effectiveness of SP process may be reduced. This implies that the induced residual strain may diverge from the expectation based on the ideal case where the local curvature radius is thought to be large. Same findings were earlier experienced by DeWald and Hill [58].

Further efforts can be addressed at implementing the presented method for the simulation of three-dimensional geometries. Full reconstruction of the residual stress contained in a three-dimensional object requires further measurements in order to capture evolution of the out-of-plane component of residual stress arising as background (arising from AL manufacturing). However, it is worth noting that shot peening is thought to introduce isotropic deformations along all the directions perpendicular to the local shot trajectory. Therefore, in principle the 3D residual stress field given by the sole shot peening could be simulated by imposing the same eigenstrain distribution along this third direction.

5.4.5. Conclusions

The proposed eigenstrain method for the in-plane strain reconstruction was successfully applied to a real case study of ALM and SP compressor blade section. The computed strain maps showed good agreement with the experimental outcomes. The application of the eigenstrain distribution to the entire geometry allowed the prediction of the strain field not only at positions where experimental evidence was available, but *everywhere within the cross section*. Furthermore, numerical simulation confirmed the consistency of the experiments in terms of stress equilibrium, strengthening the confidence in their validity. For these reasons, the proposed method can be considered as complementary to the experimental evaluation of residual elastic strains. Once the intrinsic inelastic deformation (i.e. eigenstrain) of a specific process is known (e.g., SP), the great advantage of the approach lies in the applicability of this description to 2D geometries of arbitrary shape. Therefore, the simulation of residual elastic strain arising from SP can be performed for any 2D model. One remark needs to be made regarding the effectiveness of SP process. It has been revealed in the present work that in the presence of tight contour radii, the effectiveness of SP process may be reduced. This implies that the induced residual strain may diverge from the expectation based on the ideal case where the local curvature radius is thought to be large.

6. Conclusions

In this Chapter I draw conclusions from the developments and results presented in this thesis regarding the three major areas of study reported in this work, namely:

1) FIB-DIC technique development
2) The influence of residual stress and plasticity-induced crack closure on fatigue crack growth rate (FCGR)
3) Residual stress evaluation and modelling in polycrystalline materials.

Here I pay particular attention to the limitations encountered, and offer my thoughts about the likely future developments to improve the insights that could be derived from the methodology presented.

6.1. FIB-DIC technique development

Results reported in this thesis concern the development of two aspects of the FIB-DIC technique for residual stress evaluation: quantitative evaluation of uncertainty due to the unknown underlying local crystal orientation and assessment of FIB milling induced eigenstrain and its implications in residual stress measurements. I consider these as having fundamental importance in terms of the applicability of the technique beyond the range of specific case-studies covered by this thesis. In fact, the work conducted was aimed also at highlighting *classes of problems* in which the technique could find applications both in scientific and industrial contexts, providing improved accuracy, resolution and statistical robustness compared to other approaches to date.

One aspect of the technique that appears to be worth exploring further concerns the identification of error sources and the quantification of errors and their effect on the final values. In the first instance, the effort was directed at the quantification of residual stress uncertainty due to the underlying local crystal orientation being unknown. Depending upon the degree of material elastic anisotropy, the errors arising due to the target material having poly-crystalline nature can affect the evaluation considerably. For instance, it was shown that for Ni-base superalloys the unknown crystal orientation may lead to errors up to 40% in the evaluated stress magnitude (at 95% of confidence). It is worth highlighting that even dealing with materials with low anisotropy factors, the error that arise may be not negligible, e.g. for Al alloys it amounts to ~8%.

Another potential source of error associated with this technique concerns the effect of the FIB milling itself on the deformation state of the gauge volume studied. Extensive experimental and numerical analyses were performed in order to shed some light onto the mechanism of material amorphisation and consequent development of residual stress within the layer of material affected by ion beam damage. By means of the X-ray reflectivity technique it was shown that the exposure of single crystal Si to Ga-ion beam at 10° grazing angle produced a ~23nm-thick amorphous layer with a diffuse interlayer and a density gradient as a function of the depth. The second aspect analysed concerned the quantification of inelastic strain caused by FIB milling. By exposing a stress-free Si micro-cantilever (AFM probe) to the Ga-ion beam at normal incidence (worst case scenario), it was observed that inelastic deformation took place in the affected material, giving rise to residual stress and the attendant bending. By quantifying the cantilever deflection and employing eigenstrain theory, it was then possible to evaluate the residual stress magnitude assuming half-Gaussian distribution of eigenstrain, which turned out to be of negative sign. Beside the experimental evidence, MD simulations were employed with the purpose of assessing the residual stress distribution. The eigenstrain profile abstracted from the MD simulations allowed then the simulation of the deflection due to a thin layer of eigenstrain within the AFM cantilever. The beam curvature comparison of the experimental vs. the MD simulation outcomes found good agreement, with the difference in the radius of curvature lying within ~10%.

Further FEM simulations of the entire FIB-DIC milling process within stress-free Si samples permitted the evaluation of the minimum ring-core radius allowable in order to keep the effect of FIB-induced eigenstrain negligible. It was found that these effects are insignificant provided the diameter of the central ‘island’ feature is not smaller than 1μm. The results of this study of the effect of Ga-ion irradiation is likely to be of interest not only for the specific case of FIB-DIC ring-core milling, but also in numerous applications where FIB is employed for the preparation of miniaturised samples.

6.2 Residual Stress and Plasticity induced crack closure effects in fatigue crack growth

With the help of FIB-DIC ring-core milling and other techniques such as synchrotron X-ray diffraction, advances were made in the fundamental understanding of fatigue crack propagation mechanisms. In combination with fatigue testing, the extensive amount of experimental data acquired at synchrotron facilities and using FIB-DIC was of paramount importance in validating non-linear FE modelling, and in allowing the simulation of load anomalies (overload & underload) that may occur during what is otherwise constant amplitude fatigue crack propagation. Further experimental evidence was collected by means of optical systems, such optical observation and DIC quantification of crack closure. This approach helped identify plasticity-induced crack closure. Furthermore, EBSD was used for the analysis of microstructure effects on crack path, and qualitative plastic deformation maps were obtained.

Concerning the problem of fatigue crack retardation due to the application of a single overload, it was confirmed that the presence of compressive residual stress and the alteration of crack face shape and closure in the wake of the crack play a great role in modifying the crack growth rate. Other minor effects were observed, such crack branching and crack deflection. EBSD analysis of fatigue crack propagation in an Al alloy sample revealed interesting features of the crack path that highlight the influence of grain morphology and residual compressive stress region size. Specifically, along with the crack branching effect, crack deflection was seen to arise immediately past the overload site, confirming that the crack tends to propagate along a path that is distant from the regions of high compressive stress. Additional detailed analysis of crack propagation past an overload allowed the separation of individual contributions of residual stress and crack closure to crack retardation. In turned out that crack closure effect manifested a longer lasting effect throughout the entire period of propagation where the overload consequence was still active. Moreover, it was worth noting that the effect of residual stress in crack retardation vanished when the crack had overtaken around half of the overload induced plastic region ahead of the crack tip, whilst the persistent crack retardation beyond the region of compressive residual stress was only due to contact taking place in the wake of the crack (crack closure).

In contrast with the retardation due to overload, the crack acceleration caused by an underload is mainly dependent on the loading history sequence. As shown in the experimental and numerical analyses conducted, the magnitude of the constant amplitude cycling prior to the underload largely governs the severity of the crack acceleration and its extent. Parametrical numerical simulations revealed the nature of deformation along the crack flanks and ahead of the tip during the underload occurrence, showing that this is highly dependent on the magnitude of the previous loading cycles. By considering the cyclic

J-integral as the crack driving force at the crack tip, it was shown how the crack propagation speed is affected. Optical observation and DIC analysis of crack closure revealed a substantial increase in the effective stress intensity factor (SIF) during following the underload, suggesting that this is the predominant acceleration mechanism in this case. A mild change in the residual stress level after the underload was also noted, but was not as significant as the crack closure.

6.3. Residual Stress evaluation in polycrystalline materials

A number of case studies were analysed in this section of the thesis. The evaluation of residual stress in this class of materials was performed principally by employing the tools developed in the first section, and also adopting new strategies for the residual stress numerical simulation.

The first study concerned the residual stress evaluation of Al alloy notched samples subjected to shot peening surface treatment. The key finding of this study concerned the effectiveness of the shot peening process at the roots of narrow notches. It was discovered that identical shot peening processes applied to three notches of different severity led to different compressive residual stress magnitudes in the vicinity of the free surface. It was revealed that as the fillet radius diminishes, the plastic deformation created beneath the surface by the shot peening process is reduced.

A similar effect was found in the analysis of residual stress in an aeroengine turbine airfoil manufactured by ALM and treated by shot peening. In this case, by combining experimental measurements (i.e. FIB-DIC & SXRPD) with the novel eigenstrain based model, it was possible to discern the reduction of shot peening efficacy at blade tips with small local radii of curvature. The newly developed eigenstrain procedure facilitated the simulation of residual stress fields induced by shot peening in two-dimensional geometries of arbitrary shape. This approach relied on the principle of transferability of eigenstrain, according to which the consequence of treatment (shot peening) can be expressed as a depth-dependent eigenstrain that only dependent on the process conditions (shot size and weight, speed, coverage)[297]. The main strength of this approach is the possibility of applying one-dimensional eigenstrain distribution as a function of the distance from the treated surface, enabling residual stress simulation for intricate geometries.

Further studies were addressed at the statistical analysis of residual stress across the scales. To this end, the definition of Type I, II & III residual stress associated with their corresponding length scale was revisited and re-examined. An extensive FIB-DIC residual stress measurement campaign was carried out on a 4-point-bent miniature beam, in combination with multi-scale FEM simulations of the bending process which allowed the discernment of different stress types. Macro-scale simulation of residual stress (Type I) found excellent agreement with measurements. Regarding the statistical distribution of residual stress, a CP-FEM analysis was used for the comparison with the experimental findings. A close match could not be found, with different on ~24% in terms of standard deviation persisting. This was ascribed to the combination of crystallographic texture and prior deformation history of the material. Despite the disagreement, the study presented a calculation procedure used for the prediction of the statistical distribution of residual stress in plastically deformed materials. This is of great relevance for structural integrity assessment, especially for mechanical components subject to fatigue loading where the effect of the residual stress at the grain level plays a central role.

The final problem examined concerned the characterisation of a re-cast layer generated upon EDM cutting of an Al alloy. Thanks to the improved capabilities of the FIB-DIC technique, for the first time it was possible to obtain high resolution information about the residual stress distribution through the depth of the affected layer. Material amorphisation observed in the shallowest regions (~3 microns), was associated with compressive residual stress state. Tensile residual stress was experienced in deeper layers lying beneath the interface between the while layer and the HAZ. For the first time it was possible to achieve nanometre depth resolution to capture adequately a steep near-surface stress gradient. It is important to note that previous literature results reported do not report any compressive residual stress at the EDM-machined surfaces, mainly due to the lack of spatial resolution.

6.4. Future work

In my opinion, future investigations in this field should be aimed at applying the methods developed in the thesis to a wider range of case-studies, and using the insights obtained to improve the current state-of-art in fatigue prediction models. In particular, further studies ought to be addressed at the following specific areas:

1. As thoroughly analysed in the thesis, current state-of-art models for the prediction of fatigue crack propagation under variable amplitude loading rely on semi-empirical approaches. Therefore, these

can only be employed after calibration of a number of parameters, which in most cases are not reliable due to the lack of clear physical meaning of the coefficients. To establish a new model which would be both more accurate and able to cover a wider range of load variability and materials, the separation of mechanisms affecting crack propagation is of fundamental importance. Progress made in this work will provide input for the development of improved models, with significant implications for the cost-effectiveness and safety of engineering components and assemblies.

2. Following the development of the procedure for eigenstrain prescription in 2D arbitrarily shaped models, further progress can be made to extend the method to 3D models. This would allow the complete reconstruction of residual stress in any geometry, regardless of its complexity. Moreover, a user-friendly implementation of the eigenstrain method has the potential to be employed in the industrial context, rather than solely for research applications.
3. The analysis of the statistical distribution of residual stresses in polycrystalline materials requires further efforts focused on the implementation of this with the fatigue prediction framework. Extension to a more complete description of the multi-scale residual stress state will lead to more accurate prediction of failure in engineering components, especially for high- and very high-cycle fatigue problems.

7. Appendix

7.1. Appendix 1

The total strain is the result of two contributions: eigenstrain generated by the material amorphisation, and the elastic strain generated within the material to accommodate the presence of eigenstrain, and maintain strain compatibility within the cantilever. This total strain present in beam cross section can be represented as a linear function of its thickness according to Kirchhoff's hypothesis of plane normals:

$$\varepsilon_{tot}(x) = \varepsilon^*_{eig}(x) + \varepsilon_{el}(x) = a + \frac{bx}{h} \tag{97}$$

The function describing the eigenstrain profile is assumed to have the form:

$$\varepsilon^*_{eig}(x) = \varepsilon^*_{max}\, e^{-\frac{(x-h)^2}{2W^2}} \tag{98}$$

Therefore, the elastic strain can be expressed as:

$$\varepsilon_{el} = \varepsilon_{tot} - \varepsilon^*_{eig} = a + \frac{bx}{h} - \varepsilon^*_{max}\, e^{-\frac{(x-h)^2}{2W^2}} \tag{99}$$

The conditions of Force and Moment equilibria across the beam lead to the following equations:

$$\boldsymbol{F} = \int\limits_{\boldsymbol{A}} \left(\varepsilon_{tot} - \varepsilon^*_{eig}\right) dA = \int\limits_{0}^{h}\int\limits_{0}^{f(x)} \left[a + \frac{bx}{h} - \varepsilon^*_{max}\, e^{-\frac{(x-h)^2}{2W^2}}\right] dy\, dx = 0 \tag{100}$$

$$\begin{aligned}\boldsymbol{M} &= \int\limits_{\boldsymbol{A}} \left(\varepsilon_{tot} - \varepsilon^*_{eig}\right) x\, dA \\ &= \int\limits_{0}^{h}\int\limits_{0}^{f(x)} \left[a + \frac{bx}{h} - \varepsilon^*_{max}\, e^{-\frac{(x-h)^2}{2W^2}}\right] x\, dy\, dx = 0\end{aligned} \tag{101}$$

These expressions involve integration over the domain occupied by the beam cross-section. The geometrical properties of this cross-section are known, as shown in Figure 110 and Table 13

α [mm]	β [mm]	h [mm]
0.021	0.0354	0.0020

Table 13 Cantilever cross section dimensions.

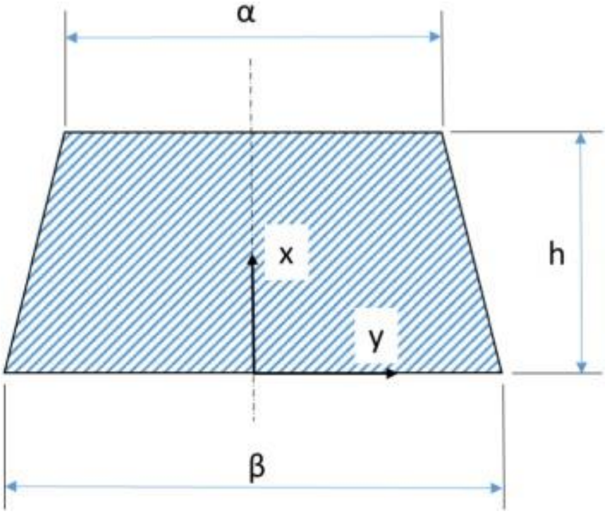

Figure 110 Cantilever cross-section representation.

The upper limit of integration in y is defined by the oblique “bevel” edge. This can be represented by the equation:

$$f(x) = \frac{x(\alpha - \beta)}{2h} + \frac{\beta}{2} \tag{102}$$

Coefficient b of the total strain equation is directly related to the beam curvature through the following relation:

$$k = \frac{b}{h} \tag{103}$$

The curvature is the inverse of the beam bending radius ρ. This was found to be equal to (40.78±21.21) mm. Hence, b can be determined as:

$$b = h\,k = \frac{h}{\rho} = \frac{0.002}{40.78} = 4.9 \times 10^{-5} \tag{104}$$

The coefficient that defines the width of the Gaussian function is also known from the literature, as noted before. Therefore, the system of Eqs.(100) and (101) can be solved numerically for the coefficients

a and $\varepsilon_{\max}$ to obtain, respectively, the values of $-1.5\times10^{-5}$and -4.1×10^{-4}, determined with the relative accuracy of ~35%.

7.2. Appendix 2

Laboratory (EBSD) coordinate system is shown in Figure 111 together with sample geometry. The loading direction corresponds to the z-axis direction (also denoted RD in the EBSD system). Schmidt factor is evaluated for loading in the z-direction for all slip systems of the $(111) < 1\bar{1}0 >$ type.

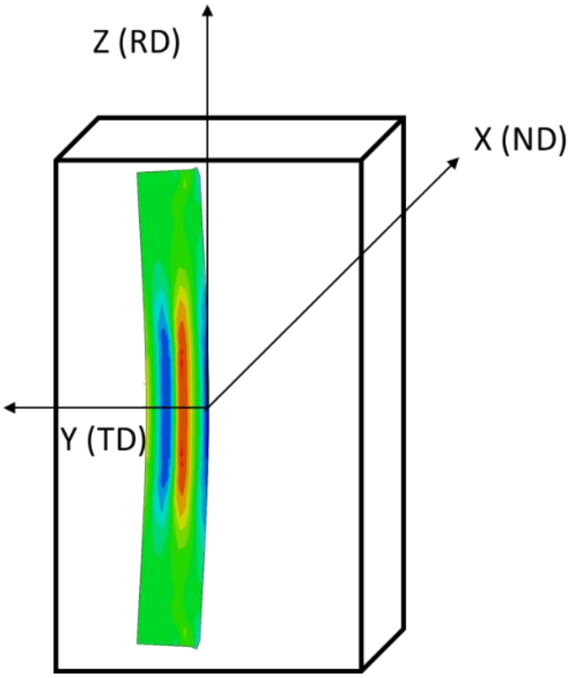

Figure 111. Sample orientation with respect to the EBSD coordinate system.

7.3. Appendix 3

The relevant steps involved in the model building process are listed below in a sequential order, that is also schematically represented in Figure 112 below.

i. 2D modelling

- The geometry shape is obtained by pre-existing model, e.g. CAD, or by contouring a real mechanical component shape (e.g. importing SEM image)
- A model containing the geometric contour is exported for Abaqus meshing, and a second model is exported as a binary mask by filling the solid part of the model with value 1, and outside with 0.

ii. Abaqus mesh generation

- The geometry is imported and meshed by refining the elements where high strain gradient is expected.

iii. Abaqus IPs extraction

- A dummy solution is run with the purpose of extracting the IPs coordinates of the meshed model.

iv. Matlab distances and angles computation

- An image format version of the model (e.g. TIFF, JPEG) is imported into Matlab and treated as matrix.
- At each position of the matrix (equivalent pixel), two new matrices are generated where the distances from all the surrounding pixels are computed in terms of the x and y differences.
- The element-wise multiplication by the binary mask representing the model geometry allows the values at positions outside the sample to be set to 0.
- A new matrix containing the distances is populated by seeking the minimum value of distance (both x and y components), and calculating the resulting vector distance.
- A matrix containing the angles is populated by calculating the angles made by the distance vector with the x axis at each pixel position.

v. Interpolation

- Matrices containing IPs coordinates are imported in Matlab
- The interpolation between the grid generated by the imported mesh (IPs) and the image pixels positions is performed. As outcome, at each IP, the distances and angles are evaluated.
- The arrays containing IPs number, distances and angles are exported

vi. Eigenstrain implementation

- The UEXTERNALDB subroutine is used for the importation of the computed values in an Abaqus script.
- The UEXPAN subroutine is then used for the assignment of the thermal expansion coefficient at each IP. This subroutine at each loop computes the eigenstrain assignment by recalling the value of the distance and angle assigned to the datum IP.

vii. Solution

- The Finite Element computation is run and the solution can be visualised in the post-processing environment of Abaqus.

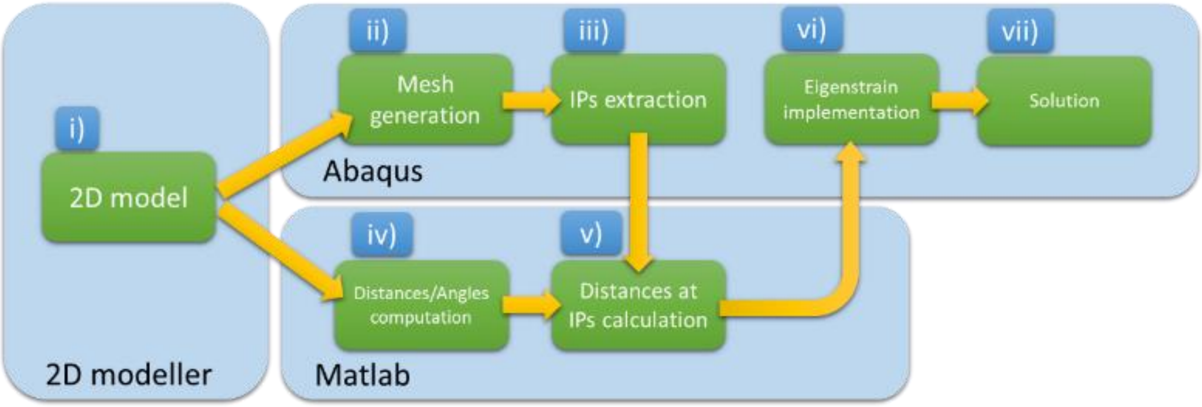

Figure 112 *Eigenstrain modelling workflow*

8. References

[1] J. Goodman, Mechanics applied to engineering, Longmans, Green & Co., London, 1899.

[2] http://www.ilfattoquotidiano.it/2013/11/12/strage-di-viareggio-comincia-il-processo-per-il-treno-di-fuoco-a-giudizio-anche-moretti/773608/, http://www.ilfattoquotidiano.it/2013/11/12/strage-di-viareggio-comincia-il-processo-per-il-treno-di-fuoco-a-giudizio-anche-moretti/773608/, (2017).

[3] http://www.repubblica.it/2006/05/gallerie/cronaca/asse-viareggio/1.html, (2017).

[4] https://it.wikipedia.org/wiki/Incidente_ferroviario_di_Viareggio (2017).

[5] D. Regazzi, S. Beretta, M. Carboni, An investigation about the influence of deep rolling on fatigue crack growth in railway axles made of a medium strength steel, Engineering Fracture Mechanics 131 (2014) 587-601.

[6] D. Radaj, P. Lazzarin, F. Berto, Generalised Neuber concept of fictitious notch rounding, International Journal of Fatigue 51 (2013) 105-115.

[7] F. Berto, P. Lazzarin, D. Radaj, Fictitious notch rounding concept applied to sharp V-notches: Evaluation of the microstructural support factor for different failure hypotheses. Part II: Microstructural support analysis, Engineering Fracture Mechanics 76(9) (2009) 1151-1175.

[8] F. Berto, P. Lazzarin, D. Radaj, Fictitious notch rounding concept applied to V-notches with root holes subjected to in-plane shear loading, Engineering Fracture Mechanics 79 (2012) 281-294.

[9] R. Tovo, P. Livieri, A numerical approach to fatigue assessment of spot weld joints, Fatigue and Fracture of Engineering Materials and Structures 34(1) (2011) 32-45.

[10] D. Radaj, C.M. Sonsino, Fatigue assessment of welded joints by local approaches, Fatigue Assessment of Welded Joints by Local Approaches (1998).

[11] Y. Du-Yi, W. De-Jun, A new approach to the prediction of fatigue notch reduction factor Kf, International Journal of Fatigue 18(2) (1996) 105-109.

[12] R. Tovo, P. Livieri, An implicit gradient application to fatigue of sharp notches and weldments, Engineering Fracture Mechanics 74(4) (2007) 515-526.

[13] P. Livieri, E. Salvati, R. Tovo, A non-linear model for the fatigue assessment of notched components under fatigue loadings, International Journal of Fatigue 82, Part 3 (2016) 624-633.

[14] F. Berto, P. Lazzarin, A review of the volume-based strain energy density approach applied to V-notches and welded structures, Theoretical and Applied Fracture Mechanics 52(3) (2009) 183-194.

[15] V. Yakovlevich Prinz, V. Alexandrovich Seleznev, A. Victorovich Prinz, A. Vladimirovich Kopylov, 3D heterostructures and systems for novel MEMS/NEMS, Science and Technology of Advanced Materials 10(3) (2009).

[16] V. Sazonova, Y. Yalsh, I. Üstünel, D. Roundy, T.A. Arlas, P.L. McEuen, A tunable carbon nanotube electrochemical oscillator, Nature 431(7006) (2004) 284-287.

[17] N.V. Lavrik, M.J. Sepaniak, P.G. Datskos, Cantilever transducers as a platform for chemical and biological sensors, Review of Scientific Instruments 75(7) (2004) 2229-2253.

[18] K.L. Ekinci, M.L. Roukes, Nanoelectromechanical systems, Review of Scientific Instruments 76(6) (2005).

[19] P.J. Withers, H.K.D.H. Bhadeshia, Residual stress part 1 - Measurement techniques, Materials Science and Technology 17(4) (2001) 355-365.

[20] X. Song, K.B. Yeap, J. Zhu, J. Belnoue, M. Sebastiani, E. Bemporad, K.Y. Zeng, A.M. Korsunsky, Residual stress measurement in thin films using the semi-destructive ring-core drilling method using Focused Ion Beam, Procedia Engineering, 2011, pp. 2190-2195.

[21] A.J.G. Lunt, A.M. Korsunsky, A review of micro-scale focused ion beam milling and digital image correlation analysis for residual stress evaluation and error estimation, Surface and Coatings Technology 283 (2015) 373-388.

[22] L.E. Lindgren, Finite element modeling and simulation of welding part 1: Increased complexity, Journal of Thermal Stresses 24(2) (2001) 141-192.

[23] D. Deng, FEM prediction of welding residual stress and distortion in carbon steel considering phase transformation effects, Materials and Design 30(2) (2009) 359-366.

[24] J. Wang, F. Liu, F. Yu, G. Zhang, Shot peening simulation based on SPH method, International Journal of Advanced Manufacturing Technology 56(5-8) (2011) 571-578.

[25] J. Wang, F. Liu, Numerical simulation for shot-peening based on sph-coupled fem, International Journal of Computational Methods 8(4) (2011) 731-745.

[26] M. Klemenz, M. Zimmermann, V. Schulze, D. Löhe, Numerical prediction of the residual stress state after shot peening, High Performance Computing in Science and Engineering 2006 - Transactions of the High Performance Computing Center Stuttgart, HLRS 2006, 2007, pp. 437-448.
[27] X. Zhao, FEM simulation on cold rolling of outer spherical bearing ring, Advanced Materials Research, 2010, pp. 1088-1092.
[28] Y.Q. Zhang, Z.L. He, X.N. Zhang, Three-dimensional elastic-plastic FEM simulation for cold rolling of plate and strip, Zhongbei Daxue Xuebao (Ziran Kexue Ban)/Journal of North University of China (Natural Science Edition) 30(4) (2009) 390-394.
[29] J. Sun, F. Du, X. Li, Fem simulation of the roll deformation of six-high cvc mill in cold strip rolling, Proceedings - 2008 International Workshop on Modelling, Simulation and Optimization, WMSO 2008, 2009, pp. 412-415.
[30] R. Bünten, K. Steinhoff, W. Rasp, R. Kopp, O. Pawelski, Development of a FEM-model for the simulation of the transfer of surface structure in cold-rolling processes, Journal of Materials Processing Technology 60(1-4) (1996) 369-376.
[31] X.J. Shao, J. Liu, Y. Liu, Z.F. Yue, FEM simulation and experimental test on residual stress of cold expansion hole of rectangular plate, Key Engineering Materials, 2007, pp. 745-748.
[32] X.J. Shao, J. Liu, Y. Liu, Z.F. Yue, Experiment and FEM simulation on residual stress of cold expansion hole, Materials Science Forum, 2007, pp. 1783-1786.
[33] X.L. Liu, Y.K. Gao, Y.T. Liu, D.F. Chen, 3D finite element simulation and experimental test on residual stress field by hole cold expansion, Hangkong Cailiao Xuebao/Journal of Aeronautical Materials 31(2) (2011) 24-27.
[34] K. Murugaratnam, S. Utili, N. Petrinic, A combined DEM-FEM numerical method for Shot Peening parameter optimisation, Advances in Engineering Software 79 (2015) 13-26.
[35] Y. Cao, Y.C. Shin, B. Wu, Parametric study on single shot and overlapping laser shock peening on various metals via modeling and experiments, Journal of Manufacturing Science and Engineering, Transactions of the ASME 132(6) (2010) 0610101-06101010.
[36] S. Xu, W. Wang, Numerical investigation on weld residual stresses in tube to tube sheet joint of a heat exchanger, International Journal of Pressure Vessels and Piping 101 (2013) 37-44.
[37] N. Kinoshita, T. Mura, EIGENSTRAIN PROBLEMS IN A FINITE ELASTIC BODY, SIAM Journal on Applied Mathematics 44(3) (1984) 524-535.
[38] R. Furuhashi, T. Mura, On the equivalent inclusion method and impotent eigenstrains, Journal of Elasticity 9(3) (1979) 263-270.
[39] X. Song, A.M. Korsunsky, Fully two-dimensional discrete inverse eigenstrain analysis of residual stresses in a railway rail head, Journal of Applied Mechanics, Transactions ASME 78(3) (2011).
[40] A.M. Korsunsky, G. Regino, D. Nowell, Residual stress analysis of welded joints by the variational eigenstrain approach, Proceedings of SPIE - The International Society for Optical Engineering, 2005, pp. 487-493.
[41] A.M. Korsunsky, On the modelling of residual stresses due to surface peening using eigenstrain distributions, Journal of Strain Analysis for Engineering Design 40(8) (2005) 817-824.
[42] A.M. Korsunsky, G.M. Regino, Residual elastic strains in autofrettaged tubes: Variational analysis by the eigenstrain finite element method, Journal of Applied Mechanics, Transactions ASME 74(4) (2007) 717-722.
[43] W.D. Callister, D.G. Rethwisch, Materials Science and Engineering: An Introduction, John Wiley and Sons (2007) 960.
[44] C.S. Shin, S.H. Hsu, On the mechanisms and behaviour of overload retardation in AISI 304 stainless steel, International Journal of Fatigue 15(3) (1993) 181-192.
[45] W.D. Musinski, D.L. McDowell, On the eigenstrain application of shot-peened residual stresses within a crystal plasticity framework: Application to Ni-base superalloy specimens, International Journal of Mechanical Sciences 100 (2015) 195-208.
[46] C. Correa, A. Gil-Santos, J.A. Porro, M. Díaz, J.L. Ocaña, Eigenstrain simulation of residual stresses induced by laser shock processing in a Ti6Al4V hip replacement, Materials & Design 79 (2015) 106-114.
[47] T.-S. Jun, A.M. Korsunsky, Evaluation of residual stresses and strains using the Eigenstrain Reconstruction Method, International Journal of Solids and Structures 47(13) (2010) 1678-1686.
[48] G.S. Shajer, Practical Residual Stress Measurement Methods, (2013) 328.

[49] D.J. Quesnel, M. Meshii, J.B. Cohen, Residual stresses in high strength low alloy steel during low cycle fatigue, Materials Science and Engineering 36(2) (1978) 207-215.
[50] Z.C. Lin, J.C. Huang, Y.C. Chao, The study of deformation and stress—strain distribution of nano-scale thin sheet copper under the biaxial tensile loads by using molecular dynamics and finite-element method, Proceedings of the Institution of Mechanical Engineers, Part C: Journal of Mechanical Engineering Science 222(6) (2008) 1097-1107.
[51] M. Soleymani, M.H. Parsa, H. Mirzadeh, Molecular dynamics simulation of stress field around edge dislocations in Aluminum, Computational Materials Science 84 (2014) 83-96.
[52] S. Shen, S.N. Atluri, Atomic-level Stress Calculation and Continuum-Molecular System Equivalence, cmes 6(1) (2004) 13.
[53] M. Zhou, A new look at the atomic level virial stress: on continuum-molecular system equivalence, Proceedings of the Royal Society of London. Series A: Mathematical, Physical and Engineering Sciences 459(2037) (2003) 2347-2392.
[54] E. Macherauch, H. Wohlfahrt, U. Wolfstieg, Zur zweckmässigen Definition von Eigenspannungen, HTM 28 (1973) 201.
[55] L. Pintschovius, V. Jung, E. Macherauch, O. Vöhringer, Residual stress measurements by means of neutron diffraction, Materials Science and Engineering 61(1) (1983) 43-50.
[56] E. Macherauch, INTRODUCTION TO RESIDUAL STRESS A2 - NIKU-LARI, A, Residual Stresses, Pergamon1987, pp. 1-36.
[57] A.M. Korsunsky, The modelling of residual stresses due to surface peening using eigenstrain distributions, The Journal of Strain Analysis for Engineering Design 40(8) (2005) 7.
[58] A.T. DeWald, M.R. Hill, Eigenstrain-based model for prediction of laser peening residual stresses in arbitrary three-dimensional bodies Part 2: Model verification, The Journal of Strain Analysis for Engineering Design 44(1) (2009) 13-27.
[59] A.M. Korsunsky, Variational eigenstrain analysis of synchrotron diffraction measurements of residual elastic strain in a bent titanium alloy bar, Journal of Mechanics of Materials and Structures 1(2) (2006) 18.
[60] M.A. Cuddihy, A. Stapleton, S. Williams, F.P.E. Dunne, On cold dwell facet fatigue in titanium alloy aero-engine components, International Journal of Fatigue 97 (2017) 177-189.
[61] S.J. Bull, A.M. Korsunsky, Mechanical properties of thin carbon overcoats, Tribology International 31(9) (1998) 547-551.
[62] Z. Nibennanoune, D. George, F. Antoni, S. Ahzi, D. Ruch, J. Gracio, Y. Remond, Improving diamond coating on Ti6Al4V substrate using a diamond like carbon interlayer: Raman residual stress evaluation and AFM analyses, Diamond and Related Materials 22 (2012) 105-112.
[63] A.M. Korsunsky, M.R. Daymond, K.E. James, The correlation between plastic strain and anisotropy strain in aluminium alloy polycrystals, Materials Science and Engineering: A 334(1–2) (2002) 41-48.
[64] S. Pratihar, M. Turski, L. Edwards, P.J. Bouchard, Neutron diffraction residual stress measurements in a 316L stainless steel bead-on-plate weld specimen, International Journal of Pressure Vessels and Piping 86(1) (2009) 13-19.
[65] A.M. Korsunsky, K.E. James, M.R. Daymond, Intergranular stresses in polycrystalline fatigue: diffraction measurement and self-consistent modelling, Engineering Fracture Mechanics 71(4–6) (2004) 805-812.
[66] A.M. Korsunsky, K.E. Wells, P.J. Withers, Mapping two-dimensional state of strain using synchroton X-ray diffraction, Scripta Materialia 39(12) (1998) 1705-1712.
[67] Y. Guo, H. Abdolvand, T.B. Britton, A.J. Wilkinson, Growth of {} twins in titanium: A combined experimental and modelling investigation of the local state of deformation, Acta Materialia 126 (2017) 221-235.
[68] T.B. Britton, A.J. Wilkinson, Measurement of residual elastic strain and lattice rotations with high resolution electron backscatter diffraction, Ultramicroscopy 111(8) (2011) 1395-1404.
[69] T.B. Britton, A.J. Wilkinson, High resolution electron backscatter diffraction measurements of elastic strain variations in the presence of larger lattice rotations, Ultramicroscopy 114 (2012) 82-95.
[70] M.E. Kartal, R. Kiwanuka, F.P.E. Dunne, Determination of sub-surface stresses at inclusions in single crystal superalloy using HR-EBSD, crystal plasticity and inverse eigenstrain analysis, International Journal of Solids and Structures 67–68 (2015) 27-39.

[71] Y. Zhang, S. Ganguly, V. Stelmukh, M.E. Fitzpatrick, L. Edwards, Validation of the Contour Method of Residual Stress Measurement in a MIG 2024 Weld by Neutron and Synchrotron X-ray Diffraction, Journal of Neutron Research 11(4) (2003) 181-185.
[72] M.R. Hill, M.D. Olson, Repeatability of the Contour Method for Residual Stress Measurement, Experimental Mechanics 54(7) (2014) 1269-1277.
[73] G.S. Schajer, B. Winiarski, P.J. Withers, Hole-Drilling Residual Stress Measurement with Artifact Correction Using Full-Field DIC, Experimental Mechanics 53(2) (2013) 255-265.
[74] S. Schuster, J. Gibmeier, Incremental Hole Drilling for Residual Stress Analysis of Strongly Textured Material States – A New Calibration Approach, Experimental Mechanics 56(3) (2016) 369-380.
[75] H. Wolf, W. Bohm, The Ring-Core Method for Measuring Residual Stresses and its Use with Turbines and Generator Shafts, Archiv. Eisenhiittenwesen 41 (1971) 5.
[76] A.M. Korsunsky, M. Sebastiani, E. Bemporad, Focused ion beam ring drilling for residual stress evaluation, Materials Letters 63(22) (2009) 1961-1963.
[77] T. Arnold, G. Böhm, R. Fechner, J. Meister, A. Nickel, F. Frost, T. Hänsel, A. Schindler, Ultra-precision surface finishing by ion beam and plasma jet techniques—status and outlook, Nuclear Instruments and Methods in Physics Research Section A: Accelerators, Spectrometers, Detectors and Associated Equipment 616(2–3) (2010) 147-156.
[78] X. Song, K.B. Yeap, J. Zhu, J. Belnoue, M. Sebastiani, E. Bemporad, K.Y. Zeng, A.M. Korsunsky, Residual stress measurement in thin films using the semi-destructive ring-core drilling method using Focused Ion Beam, Procedia Engineering 10 (2011) 2190-2195.
[79] M. Sebastiani, F. Massimi, G. Merlati, E. Bemporad, Residual micro-stress distributions in heat-pressed ceramic on zirconia and porcelain-fused to metal systems: Analysis by FIB-DIC ring-core method and correlation with fracture toughness, Dental Materials 31(11) (2015) 1396-1405.
[80] M. Sebastiani, C. Eberl, E. Bemporad, G.M. Pharr, Depth-resolved residual stress analysis of thin coatings by a new FIB-DIC method, Materials Science and Engineering A 528(27) (2011) 7901-7908.
[81] M. Sebastiani, E. Bemporad, F. Carassiti, N. Schwarzer, Residual stress measurement at the micrometer scale: Focused ion beam (FIB) milling and nanoindentation testing, Philosophical Magazine 91(7-9) (2011) 1121-1136.
[82] A.J.G. Lunt, A.M. Korsunsky, Intragranular residual stress evaluation using the semi-destructive FIB-DIC ring-core drilling method, Advanced Materials Research, 2014, pp. 8-13.
[83] A.J.G. Lunt, N. Baimpas, E. Salvati, I.P. Dolbnya, T. Sui, S. Ying, H. Zhang, A.K. Kleppe, J. Dluhoš, A.M. Korsunsky, A state-of-the-art review of micron-scale spatially resolved residual stress analysis by FIB-DIC ring-core milling and other techniques, The Journal of Strain Analysis for Engineering Design 50(7) (2015) 426-444.
[84] E. Bemporad, M. Brisotto, L.E. Depero, M. Gelfi, A.M. Korsunsky, A.J.G. Lunt, M. Sebastiani, A critical comparison between XRD and FIB residual stress measurement techniques in thin films, Thin Solid Films 572 (2014) 224-231.
[85] N. Baimpas, E. Le Bourhis, S. Eve, D. Thiaudière, C. Hardie, A.M. Korsunsky, Stress evaluation in thin films: Micro-focus synchrotron X-ray diffraction combined with focused ion beam patterning for do evaluation, Thin Solid Films 549 (2013) 245-250.
[86] G.S. Schajer, T.J. Rickert, Incremental Computation Technique for Residual Stress Calculations Using the Integral Method, Experimental Mechanics 51(7) (2011) 1217-1222.
[87] G.S. Schajer, T.J. Rickert, Incremental computation technique for residual stress calculations using the integral method, Conference Proceedings of the Society for Experimental Mechanics Series, 2011, pp. 185-191.
[88] G.S. Schajer, T.J. Rickert, Incremental computation technique for residual stress calculations using the Integral Method, Society for Experimental Mechanics - SEM Annual Conference and Exposition on Experimental and Applied Mechanics 2010, 2010, pp. 642-648.
[89] G.S. Schajer, Y. An, Inverse calculation of uniaxial stress-strain curves from bending test data, Journal of Engineering Materials and Technology, Transactions of the ASME 131(4) (2009) 0410011-0410016.
[90] G.S. Schajer, Measurement of Non-Uniform Residual Stresses Using the Hole-Drilling Method. Part II—Practical Application of the Integral Method, Journal of Engineering Materials and Technology 110(4) (1988) 344-349.

[91] M. Krottenthaler, L. Benker, M.Z. Mughal, M. Sebastiani, K. Durst, M. Göken, Effect of elastic anisotropy on strain relief and residual stress determination in cubic systems by FIB-DIC experiments, Materials and Design 112 (2016) 505-511.

[92] B. Winiarski, M. Benedetti, V. Fontanari, M. Allahkarami, J.C. Hanan, P.J. Withers, High Spatial Resolution Evaluation of Residual Stresses in Shot Peened Specimens Containing Sharp and Blunt Notches by Micro-hole Drilling, Micro-slot Cutting and Micro-X-ray Diffraction Methods, Experimental Mechanics 56(8) (2016) 1449-1463.

[93] M. Sebastiani, C. Eberl, E. Bemporad, A.M. Korsunsky, W.D. Nix, F. Carassiti, Focused ion beam four-slot milling for Poisson's ratio and residual stress evaluation at the micron scale, Surface and Coatings Technology 251 (2014) 151-161.

[94] P.K. Chu, L. Li, Characterization of amorphous and nanocrystalline carbon films, Materials Chemistry and Physics 96(2–3) (2006) 253-277.

[95] P. Barnes, Powder Diffraction., http://pd.chem.ucl.ac.uk/pdnn/diff2/kinemat2.htm (2017).

[96] A.P. Hammersley, FIT2D: An introduction an Overview, ESRF Internal Report ESRF97HA02T (1997).

[97] M.F. Toney, S. Brennan, Measurements of carbon thin films using x-ray reflectivity, Journal of Applied Physics 66(4) (1989) 1861-1863.

[98] Bruker, X-ray Reflectivity (XRR), web: https://www.bruker.com/products/x-ray-diffraction-and-elemental-analysis/x-ray-metrology/d8-fabline/metrology-knowledge/x-ray-metrology-knowledge/xrr.html (2017).

[99] R. University, EBSD: Electron BackScatter Diffraction, http://abinitio.iehk.rwth-aachen.de/glossar/?text_id=159&division=Array&scale=Array (2017).

[100] T.L. Anderson, T. Anderson, Fracture mechanics: fundamentals and applications, CRC press2005.

[101] J.R. Rice, A Path Independent Integral and the Approximate Analysis of Strain Concentration by Notches and Cracks, Journal of Applied Mechanics 35(2) (1968) 379-386.

[102] J. Rice, G.F. Rosengren, Plane strain deformation near a crack tip in a power-law hardening material, Journal of the Mechanics and Physics of Solids 16(1) (1968) 1-12.

[103] J. Hutchinson, Singular behaviour at the end of a tensile crack in a hardening material, Journal of the Mechanics and Physics of Solids 16(1) (1968) 13-31.

[104] N. Dowling, J. Begley, Fatigue Crack Growth During Gross Plasticity and the J-Integral, ASTM International (1976).

[105] P. Paris, F. Erdogan, A Critical Analysis of Crack Propagation Laws, Journal of Basic Engineering 85(4) (1963) 528-533.

[106] P.C. Paris, R.J. Bucci, E.T. Wessel, W.G. Clark Jr, T.R. Mager, EXTENSIVE STUDY OF LOW FATIGUE CRACK GROWTH RATES IN A533 AND A508 STEELS, ASTM Special Technical Publication (1972) 141-176.

[107] N.E. Dowling, Mechanical behavior of materials, Pearson2012.

[108] K.R. Dennis, Fatigue crack growth of gun tube steel under Spectrum Loading, MS Thesis (1986).

[109] J. Zhang, S. Yang, J. Lin, A nonlinear continuous damage model based on short-crack concept under variable amplitude loading, Fatigue and Fracture of Engineering Materials and Structures 39(1) (2016) 79-94.

[110] A. Ray, R. Patankar, Fatigue crack growth under variable-amplitude loading: Part I - Model formulation in state-space setting, Applied Mathematical Modelling 25(11) (2001) 979-994.

[111] H. Liu, D.G. Shang, J.Z. Liu, Z.K. Guo, Fatigue life prediction based on crack closure for 6156 Al-alloy laser welded joints under variable amplitude loading, International Journal of Fatigue 72 (2015) 11-18.

[112] L.C.H. Ricardo, C.A.J. Miranda, Crack simulation models in variable amplitude loading - a review, Frattura ed Integrita Strutturale 10(35) (2016) 456-471.

[113] W. Elber, Damage Tolerance in Aircraft Structures, Damage Tolerance in Aircraft Structures (1971) 230-242.

[114] A. Kumar, A.R. Murthy, N.R. Iyer, Crack growth prediction under variable amplitude loading considering elastic-plastic stress field ahead of crack tip, Procedia Engineering, 2014, pp. 645-652.

[115] D.J. Nicholls, THE RELATION BETWEEN CRACK BLUNTING AND FATIGUE CRACK GROWTH RATES, Fatigue & Fracture of Engineering Materials & Structures 17(4) (1994) 459-467.

[116] M.A. Meggiolaro, A.C.O. Miranda, J.T.P. Castro, L.F. Martha, Crack retardation equations for the propagation of branched fatigue cracks, International Journal of Fatigue 27(10-12) (2005) 1398-1407.

[117] S.U. Khan, R.C. Alderliesten, R. Benedictus, Delamination growth in Fibre Metal Laminates under variable amplitude loading, Composites Science and Technology 69(15-16) (2009) 2604-2615.

[118] R.O. Ritchie, Mechanisms of fatigue-crack propagation in ductile and brittle solids, International Journal of Fracture 100(1) (1999) 55-83.

[119] M.N. James, C.J. Christopher, Y. Lu, E.A. Patterson, Local crack plasticity and its influences on the global elastic stress field, International Journal of Fatigue 46 (2013) 4-15.

[120] R.E. Jones, Fatigue crack growth retardation after single-cycle peak overload in Ti-6Al-4V titanium alloy, Engineering Fracture Mechanics 5(3) (1973) 585-588,IN13-IN16,589-604.

[121] R.C. Rice, R.I. Stephens, OVERLOAD EFFECTS ON SUBCRITICAL CRACK GROWTH IN AUSTENITIC MANGANESE STEEL, ASTM Special Technical Publication (1972) 95-114.

[122] R.L. Carlson, G.A. Kardomateas, P.R. Bates, The effects of overloads in fatigue crack growth, International Journal of Fatigue 13(6) (1991) 453-460.

[123] S.Y. Lee, P.K. Liaw, H. Choo, R.B. Rogge, A study on fatigue crack growth behavior subjected to a single tensile overload: Part I. An overload-induced transient crack growth micromechanism, Acta Materialia 59(2) (2011) 485-494.

[124] K. Sadananda, A.K. Vasudevan, R.L. Holtz, E.U. Lee, Analysis of overload effects and related phenomena, International Journal of Fatigue 21(SUPPL. 1) (1999) S233-S246.

[125] R. Sunder, A. Andronik, A. Biakov, A. Eremin, S. Panin, A. Savkin, Combined action of crack closure and residual stress under periodic overloads: A fractographic analysis, International Journal of Fatigue xxx (2015) xxx–xxx International Journal of Fatigue (2015).

[126] J.M. Vasco-Olmo, F.A. Díaz, E.A. Patterson, Experimental evaluation of shielding effect on growing fatigue cracks under overloads using ESPI, International Journal of Fatigue xxx xxx–xxx (2015).

[127] W. Elber, FATIGUE CRACK CLOSURE UNDER CYCLIC TENSION, Engineering Fracture Mechanics 2(1) (1970) 37-45.

[128] A.M. Korsunsky, X. Song, J. Belnoue, T. Jun, F. Hofmann, P.F.P. De Matos, D. Nowell, D. Dini, O. Aparicio-Blanco, M.J. Walsh, Crack tip deformation fields and fatigue crack growth rates in Ti-6Al-4V, International Journal of Fatigue 31(11-12) (2009) 1771-1779.

[129] P. Lopez-Crespo, A. Steuwer, T. Buslaps, Y.H. Tai, A. Lopez-Moreno, J.R. Yates, P.J. Withers, Measuring overload effects during fatigue crack growth in bainitic steel by synchrotron X-ray diffraction, International Journal of Fatigue 71 (2015) 11-16.

[130] A. Steuwer, M. Rahman, A. Shterenlikht, M.E. Fitzpatrick, L. Edwards, P.J. Withers, The evolution of crack-tip stresses during a fatigue overload event, Acta Materialia 58(11) (2010) 4039-4052.

[131] V. Tvergaard, Effect of underloads or overloads in fatigue crack growth by crack-tip blunting, Engineering Fracture Mechanics 73(7) (2006) 869-879.

[132] D.G. Pavlou, N.V. Vlachakis, M.G. Pavlou, V.N. Vlachakis, Estimation of fatigue crack growth retardation due to crack branching, Computational Materials Science 29(4) (2004) 446-452.

[133] L. Lawson, E.Y. Chen, M. Meshii, Near-threshold fatigue: A review, International Journal of Fatigue 21(SUPPL. 1) (1999) S15-S34.

[134] M.T. Yu, T.H. Topper, P. Au, EFFECTS OF STRESS RATIO, COMPRESSIVE LOAD AND UNDERLOAD ON THE THRESHOLD BEHAVIOUR OF A 2024-T351 ALUMINUM ALLOY, 1984, pp. 179-190.

[135] F.S. Silva, Fatigue crack propagation after overloading and underloading at negative stress ratios, International Journal of Fatigue 29(9-11) (2007) 1757-1771.

[136] R.L. Carlson, G.A. Kardomateas, Effects of compressive load excursions on fatigue crack growth, International Journal of Fatigue 16(2) (1994) 141-146.

[137] M. Yu, W. Chen, R. Kania, G. Van Boven, J. Been, Underload-induced crack growth behaviour of minor cycles of pipeline steel in near-neutral pH environment, Fatigue and Fracture of Engineering Materials and Structures 38(6) (2015) 681-692.

[138] M. Hassanipour, Y. Verreman, J. Lanteigne, J.Q. Chen, Effect of periodic underloads on fatigue crack growth in three steels used in hydraulic turbine runners, International Journal of Fatigue 85 (2016) 40-48.

[139] L. Ma, A.M. Korsunsky, The principle of equivalent eigenstrain for inhomogeneous inclusion problems, International Journal of Solids and Structures 51(25–26) (2014) 4477-4484.

[140] S.A. Faghidian, A smoothed inverse eigenstrain method for reconstruction of the regularized residual fields, International Journal of Solids and Structures 51(25–26) (2014) 4427-4434.

[141] T. Mura, Micromechanics of Defects in Solids, (1987).

[142] A.M. Korsunsky, Residual elastic strain due to laser shock peening: Modelling by eigenstrain distribution, The Journal of Strain Analysis for Engineering Design 41(3) (2006) 195-204.

[143] J.D. Eshelby, The Determination of the Elastic Field of an Ellipsoidal Inclusion, and Related Problems, Proceedings of the Royal Society of London. Series A. Mathematical and Physical Sciences 241(1226) (1957) 376-396.

[144] X. Song, W.C. Liu, J.P. Belnoue, J. Dong, G.H. Wu, W.J. Ding, S.A.J. Kimber, T. Buslaps, A.J.G. Lunt, A.M. Korsunsky, An eigenstrain-based finite element model and the evolution of shot peening residual stresses during fatigue of GW103 magnesium alloy, International Journal of Fatigue 42 (2012) 284-295.

[145] T.S. Jun, K. Dragnevski, A.M. Korsunsky, Microstructure, residual strain, and eigenstrain analysis of dissimilar friction stir welds, Materials & Design 31, Supplement 1 (2010) S121-S125.

[146] T. Hensl, U. Mühlich, M. Budnitzki, M. Kuna, An eigenstrain approach to predict phase transformation and self-accommodation in partially stabilized zirconia, Acta Materialia 86 (2015) 361-373.

[147] E.C. Oliver, M.R. Daymond, P.J. Withers, Interphase and intergranular stress generation in carbon steels, Acta Materialia 52(7) (2004) 1937-1951.

[148] A.M. Korsunsky, K.E. James, M.R. Daymond, Intergranular stresses in polycrystalline fatigue: Diffraction measurement and self-consistent modelling, Engineering Fracture Mechanics 71(4-6) (2004) 805-812.

[149] B. Clausen, T. Lorentzen, T. Leffers, Self-consistent modelling of the plastic deformation of F.C.C. polycrstals and its implications for diffraction measurements of internal stresses, Acta Materialia 46(9) (1998) 3087-3098.

[150] A.M. Korsunsky, M. Sebastiani, E. Bemporad, Residual stress evaluation at the micrometer scale: Analysis of thin coatings by FIB milling and digital image correlation, Surface and Coatings Technology 205(7) (2010) 2393-2403.

[151] C. Zener, Elasticity and Anelasticity of Metals (1948).

[152] H.J. Bunge, Texture analysis in materials science, Math. Methods (1969).

[153] A. Constantinescu, A. Korsunsky, Elasticity with Mathematica (2007).

[154] E. Salvati, A.J.G. Lunt, T. Sui, A.M. Korsunsky, An Investigation of Residual Stress Gradient Effects in FIB-DIC Micro-Ring-Core Analysis, (2015).

[155] T.M. Holden, R.A. Holt, A.P. Clarke, Intergranular strains in Inconel-600 and the impact on interpreting stress fields in bent steam-generator tubing, Materials Science and Engineering A 246(1-2) (1998) 180-198.

[156] W. Tayon, R. Shenoy, R. Bird, Hafley, M. Redding, Texture-induced anisotropy in an inconel 718 alloy deposited using electron beam freeform fabrication, International Conference on Texture of Materials (2014).

[157] T.H. Courtney, Mechanical Behavior of Materials (1990).

[158] J.W. Hutchinson, Elastic- plastic behavior of polycrystalline metals and composites, Proc Roy Soc Ser A Math Phys Sci 319(1537) (1970) 247-272.

[159] M. Fukuhara, A. Sanpei, Elastic moduli and internal frictions of Inconel 718 and Ti-6Al-4V as a function of temperature, Journal of Materials Science Letters 12(14) (1993) 1122-1124.

[160] M.A. Hopcroft, W.D. Nix, T.W. Kenny, What is the Young's modulus of silicon?, Journal of Microelectromechanical Systems 19(2) (2010) 229-238.

[161] K. Topolski, P. Wieciński, Z. Szulc, A. Gałka, H. Garbacz, Progress in the characterization of explosively joined Ti/Ni bimetals, Materials and Design 63 (2014) 479-487.

[162] J.M. Glasko, R.G. Elliman, J. Zou, D.J.H. Cockayne, J.D. Fitz Gerald, Strain and defect microstructure in ion-irradiated GeSi/Si strained layers as a function of annealing temperature, Applied Physics Letters 73(6) (1998) 838-840.

[163] S. Decoster, A. Vantomme, Implantation-induced damage in Ge: Strain and disorder profiles during defect accumulation and recovery, Journal of Physics D: Applied Physics 42(16) (2009).

[164] J.F. Ziegler, Handbook of stopping cross-sections for energetic ions in all elements, The Stopping and Ranges of Ions in Matter 5 (1980).

[165] C.L. Liu, S.J. Plimpton, Molecular dynamics simulations of grain boundary diffusion in A1 using embedded atom method potentials, Journal of Materials Research 10(7) (1995) 1589-1592.

[166] L. Pelaz, L.A. Marqús, J. Barbolla, Ion-beam-induced amorphization and recrystallization in silicon, Journal of Applied Physics 96(11) (2004) 5947-5976.

[167] M.F. Russo Jr, M. Maazouz, L.A. Giannuzzi, C. Chandler, M. Utlaut, B.J. Garrison, Gallium-induced milling of silicon: A computational investigation of focused ion beams, Microscopy and Microanalysis 14(4) (2008) 315-320.

[168] P. Roediger, H.D. Wanzenboeck, S. Waid, G. Hochleitner, E. Bertagnolli, Focused-ion-beam-inflicted surface amorphization and gallium implantation-new insights and removal by focused-electron-beam-induced etching, Nanotechnology 22(23) (2011).

[169] J.P. McCaffrey, M.W. Phaneuf, L.D. Madsen, Surface damage formation during ion-beam thinning of samples for transmission electron microscopy, Ultramicroscopy 87(3) (2001) 97-104.

[170] V. Delaye, F. Andrieu, F. Aussenac, C. Carabasse, In-line FIB TEM sample preparation induced effects on advanced fully depleted silicon on insulator transistors, Proc. EMC 2008 (2008) 659-660.

[171] O.V. Kuzmin, Y.T. Pei, J.T.M. De Hosson, Nanopillar fabrication with focused ion beam cutting, Microscopy and Microanalysis 20(5) (2014) 1581-1584.

[172] N.L. Okamoto, M. Inomoto, H. Adachi, H. Takebayashi, H. Inui, Micropillar compression deformation of single crystals of the intermetallic compound ς-FeZn13, Acta Materialia 65 (2014) 229-239.

[173] D. Kiener, C. Motz, M. Rester, M. Jenko, G. Dehm, FIB damage of Cu and possible consequences for miniaturized mechanical tests, Materials Science and Engineering A 459(1-2) (2007) 262-272.

[174] J.A. El-Awady, C. Woodward, D.M. Dimiduk, N.M. Ghoniem, Effects of focused ion beam induced damage on the plasticity of micropillars, Physical Review B - Condensed Matter and Materials Physics 80(10) (2009).

[175] B.J. Inkson, D. Leclere, F. Elfallagh, B. Derby, The effect of focused ion beam machining on residual stress and crack morphologies in alumina, Journal of Physics: Conference Series 26(1) (2006) 219-222.

[176] P.K. Chu, L. Li, Characterization of amorphous and nanocrystalline carbon films, Materials Chemistry and Physics 96(2-3) (2006) 253-277.

[177] M.F. Toney, S. Brennan, Measurements of carbon thin films using x-ray reflectivity, Journal of Applied Physics 66(4) (1989) 1861-1863.

[178] Y.-c. Wang, D.-g. Xie, X.-h. Ning, Z.-w. Shan, Thermal treatment-induced ductile-to-brittle transition of submicron-sized Si pillars fabricated by focused ion beam, Applied Physics Letters 106(8) (2015) 081905.

[179] A.M. Korsunsky, J. Guénolé, E. Salvati, T. Sui, M. Mousavi, A. Prakash, E. Bitzek, Quantifying eigenstrain distributions induced by focused ion beam damage in silicon, Materials Letters 185 (2016) 47-49.

[180] A.M. Korsunsky, S. Cherian, R. Raiteri, R. Berger, On the micromechanics of micro-cantilever sensors: Property analysis and eigenstrain modeling, Sensors and Actuators, A: Physical 139(1-2 SPEC. ISS.) (2007) 70-77.

[181] R. Schöngrundner, R. Treml, T. Antretter, D. Kozic, W. Ecker, D. Kiener, R. Brunner, Critical assessment of the determination of residual stress profiles in thin films by means of the ion beam layer removal method, Thin Solid Films 564 (2014) 321-330.

[182] L.M. Jiang, J. Peng, Y.G. Liao, Y.C. Zhou, J. Liang, H.X. Hao, C. Lu, A modified layer-removal method for residual stress measurement in electrodeposited nickel films, Thin Solid Films 519(10) (2011) 3249-3253.

[183] S.H. Kim, Mismatch strain and residual stress of freestanding electroplated Ni thin film, Japanese Journal of Applied Physics 49(1 Part 1) (2010).

[184] A.M. Korsunsky, Residual elastic strain due to laser shock peening: Modelling by eigenstrain distribution, J. Strain Analysis 41(3) (2006) 195-204.

[185] L. Pastewka, R. Salzer, A. Graff, F. Altmann, M. Moseler, Surface amorphization, sputter rate, and intrinsic stresses of silicon during low energy Ga+ focused-ion beam milling, Nuclear Instruments and Methods in Physics Research, Section B: Beam Interactions with Materials and Atoms 267(18) (2009) 3072-3075.

[186] K. Saitoh, Nakao, H. Setsuo Niwa, Surface swelling of MeV Si ion implanted silicon, Ion Implantation Technology Proceedings (1998).

[187] A. Battaglia, F. Priolo, E. Rimini, Influence of doping on ion-induced growth and shrinkage of partial damage in silicon, Nuclear Inst. and Methods in Physics Research, B 59-60(PART 1) (1991) 382-385.

[188] X. Zhu, Z. Wang, Nanoinstabilities as revealed by shrinkage of nanocavities in silicon during irradiation, International Journal of Nanotechnology 3(4) (2006) 492-516.

[189] A.P. Thompson, S.J. Plimpton, W. Mattson, General formulation of pressure and stress tensor for arbitrary many-body interaction potentials under periodic boundary conditions, Journal of Chemical Physics 131(15) (2009).

[190] N.C. Admal, E.B. Tadmor, A unified interpretation of stress in molecular systems, Journal of Elasticity 100(1-2) (2010) 63-143.

[191] J. Guénolé, A. Prakash, E. Bitzek, (2016).

[192] L. Pizzagalli, J. Godet, J. Guénolé, S. Brochard, E. Holmstrom, K. Nordlund, T. Albaret, A new parametrization of the Stillinger-Weber potential for an improved description of defects and plasticity of silicon, Journal of Physics Condensed Matter 25(5) (2013).

[193] H.J.C. Berendsen, J.P.M. Postma, W.F. Van Gunsteren, A. Dinola, J.R. Haak, Molecular dynamics with coupling to an external bath, The Journal of Chemical Physics 81(8) (1984) 3684-3690.

[194] L.B. Freund, S. Suresh, Thin Film Materials (2003).

[195] F. Hofmann, B. Abbey, L. Connor, N. Baimpas, X. Song, S. Keegan, A.M. Korsunsky, Imaging of grain-level orientation and strain in thicker metallic polycrystals by high energy transmission micro-beam Laue (HETL) diffraction techniques, International Journal of Materials Research 103(2) (2012) 192-199.

[196] A.M. Korsunsky, M.R. Daymond, K.E. James, The correlation between plastic strain and anisotropy strain in aluminium alloy polycrystals, Materials Science and Engineering A 334(1-2) (2002) 41-48.

[197] Y. Murakami, Stress Intensity Factors Handbook (1987).

[198] G.R. Irwin, Fracture, in: S. Flügge (Ed.), Elasticity and Plasticity / Elastizität und Plastizität, Springer Berlin Heidelberg, Berlin, Heidelberg, 1958, pp. 551-590.

[199] K.T. Venkateswara Rao, R.O. Ritchie, Mechanisms for the retardation of fatigue cracks following single tensile overloads: behavior in aluminum-lithium alloys, Acta Metallurgica 36(10) (1988) 2849-2862.

[200] T. Zhang, R. Bao, B. Fei, Load effects on macroscopic scale fatigue crack growth path in 2324-T39 aluminium alloy thin plates, International Journal of Fatigue 58 (2014) 193-201.

[201] J. Zuidema, P.J.M. Mense, R.A.H. Edwards, Environmental dependence of fatigue crack growth retardation following a single overload in 2024-Al alloy, Engineering Fracture Mechanics 26(6) (1987) 927-935.

[202] X. Song, F. Hofmann, A.M. Korsunsky, Dislocation-based plasticity model and micro-beam Laue diffraction analysis of polycrystalline Ni foil: A forward prediction, Philosophical Magazine 90(30) (2010) 3999-4011.

[203] F. Hofmann, D. Nguyen-Manh, M.R. Gilbert, C.E. Beck, J.K. Eliason, A.A. Maznev, W. Liu, D.E.J. Armstrong, K.A. Nelson, S.L. Dudarev, Lattice swelling and modulus change in a helium-implanted tungsten alloy: X-ray micro-diffraction, surface acoustic wave measurements, and multiscale modelling, Acta Materialia 89 (2015) 352-363.

[204] S.I. Wright, M.M. Nowell, D.P. Field, A Review of Strain Analysis Using Electron Backscatter Diffraction, Microscopy and Microanalysis 17(3) (2011) 316-329.

[205] L. Brewer, M. Othon, A. T., Characterizing local strain variations around crack tips using EBSD mapping, Application note (2017).

[206] H. Wang, F.G. Buchholz, H.A. Richard, S. Jägg, B. Scholtes, Numerical and experimental analysis of residual stresses for fatigue crack growth, Computational Materials Science 16(1–4) (1999) 104-112.
[207] L. Xiao, D. Ye, C. Chen, J. Liu, L. Zhang, Instrumented indentation measurements of residual stresses around a crack tip under single tensile overloads, International Journal of Mechanical Sciences 78 (2014) 44-51.
[208] Y. Onuki, S. Fujieda, R. Ukai, S. Sato, M. Sato, K. Kajiwara, S. Suzuki, Local stress development in polycrystalline Fe-17mol%Ga alloy under tensile loading - In situ measurement using synchrotron X-ray micro-beam, Journal of Alloys and Compounds 653 (2015) 195-201.
[209] F. Hofmann, X. Song, B. Abbey, T.-S. Jun, A.M. Korsunsky, High-energy transmission Laue micro-beam X-ray diffraction: a probe for intra-granular lattice orientation and elastic strain in thicker samples, Journal of Synchrotron Radiation 19(3) (2012) 307-318.
[210] C.R. Chen, S.X. Li, Distribution of stresses and elastic strain energy in an ideal multicrystal model, Materials Science and Engineering: A 257(2) (1998) 312-321.
[211] M. Croft, V. Shukla, N.M. Jisrawi, Z. Zhong, R.K. Sadangi, R.L. Holtz, P.S. Pao, K. Horvath, K. Sadananda, A. Ignatov, J. Skaritka, T. Tsakalakos, Mapping and load response of overload strain fields: Synchrotron X-ray measurements, International Journal of Fatigue 31(11-12) (2009) 1669-1677.
[212] K. Walker, The effect of stress ratio during crack propagation and fatigue for 2024-T3 and 7075-T6 aluminum, ASTM STP 462 (1970) 1-14.
[213] I.H. Onn, N. Ahmad, M.N. Tamin, Fatigue characteristics of dual-phase steel sheets, Journal of Mechanical Science and Technology 29(1) (2015) 51-57.
[214] P. Livieri, E. Salvati, R. Tovo, A non-linear model for the fatigue assessment of notched components under fatigue loadings, International Journal of Fatigue 82 (2016) 624-633.
[215] N.E. Dowling, C.A. Calhoun, A. Arcari, Mean stress effects in stress-life fatigue and the Walker equation, Fatigue and Fracture of Engineering Materials and Structures 32(3) (2009) 163-179.
[216] J. Zheng, B.E. Powell, A method to reduce the scatter in fatigue crack growth rate data, Fatigue and Fracture of Engineering Materials and Structures 20(9) (1997) 1341-1350.
[217] J.A.R. Duran, R.M. Boloy, R.R. Leoni, Some remarks on the engineering application of the fatigue crack growth approach under nonzero mean loads, Frontiers of Mechanical Engineering 10(3) (2015) 255-262.
[218] D. Nowell, P.F.P. De Matos, Application of digital image correlation to the investigation of crack closure following overloads, Procedia Engineering, 2010, pp. 1035-1043.
[219] C. Eberl, Digital Image Correlation and Tracking, Digital Image Correlation and Tracking (2010).
[220] B. Lê Minh, M.H. Maitournam, V. Doquet, A cyclic steady-state method for fatigue crack propagation: Evaluation of plasticity-induced crack closure in 3D, International Journal of Solids and Structures 49(17) (2012) 2301-2313.
[221] P.F.P. de Matos, D. Nowell, Experimental and numerical investigation of thickness effects in plasticity-induced fatigue crack closure, International Journal of Fatigue 31(11-12) (2009) 1795-1804.
[222] J.P. Belnoue, T.S. Jun, F. Hofmann, B. Abbey, A.M. Korsunsky, Evaluation of the overload effect on fatigue crack growth with the help of synchrotron XRD strain mapping, Engineering Fracture Mechanics 77(16) (2010) 3216-3226.
[223] M.C. Croft, N.M. Jisrawi, Z. Zhong, R.L. Holtz, K. Sadananda, J.R. Skaritka, T. Tsakalakos, Fatigue history and in-situ loading studies of the overload effect using high resolution X-ray strain profiling, International Journal of Fatigue 29(9-11) (2007) 1726-1736.
[224] S. Ishihara, A.J. McEvily, T. Goshima, S. Nishino, M. Sato, The effect of the R value on the number of delay cycles following an overload, International Journal of Fatigue 30(10-11) (2008) 1737-1742.
[225] L.P. Borrego, J.M. Ferreira, J.M. Pinho da Cruz, J.M. Costa, Evaluation of overload effects on fatigue crack growth and closure, Engineering Fracture Mechanics 70(11) (2003) 1379-1397.
[226] H. Tsukuda, H. Ogiyama, T. Shiraishi, FATIGUE CRACK GROWTH AND CLOSURE AT HIGH STRESS RATIOS, Fatigue & Fracture of Engineering Materials & Structures 18(4) (1995) 503-514.
[227] M.L. Zhu, F.Z. Xuan, S.T. Tu, Effect of load ratio on fatigue crack growth in the near-threshold regime: A literature review, and a combined crack closure and driving force approach, Engineering Fracture Mechanics 141 (2015) 57-77.

[228] D.F. Martelo, M.D. Chapetti, Analysis of the importance of the crack closure in the driving force, for the fatigue crack growth in metastable austenitic stainless steels, Procedia Mater. Sci. 9 (2015) 387-395.
[229] R. Sunder, A unified model of fatigue kinetics based on crack driving force and material resistance, International Journal of Fatigue 29(9-11) (2007) 1681-1696.
[230] I.R. Wallhead, L. Edwards, P. Poole, A study of crack closure using the optical method of caustics and consequences for the use of ΔKeff as a fatigue crack driving force, Engineering Fracture Mechanics 60(3) (1998) 291-302.
[231] X. Huang, M. Torgeir, W. Cui, An engineering model of fatigue crack growth under variable amplitude loading, International Journal of Fatigue 30(1) (2008) 2-10.
[232] B.K.C. Yuen, F. Taheri, Proposed modifications to the Wheeler retardation model for multiple overloading fatigue life prediction, International Journal of Fatigue 28(12) (2006) 1803-1819.
[233] O.E. Wheeler, Spectrum Loading and Crack Growth, Journal of Basic Engineering 94(1) (1972) 181-186.
[234] M. Mehrzadi, F. Taheri, A material sensitive modified wheeler model for predicting the retardation in fatigue response of AM60B due to an overload, International Journal of Fatigue 55 (2013) 220-229.
[235] D. Nowell, R.J.H. Paynter, P.F.P. De Matos, Optical methods for measurement of fatigue crack closure: Moiré interferometry and digital image correlation, Fatigue and Fracture of Engineering Materials and Structures 33(12) (2010) 778-790.
[236] D. Nowell, M.E. Kartal, P.F.P. De Matos, Digital image correlation measurement of near-tip fatigue crack displacement fields: constant amplitude loading and load history effects, Fatigue & Fracture of Engineering Materials & Structures 36(1) (2013) 3-13.
[237] X. Song, M. Xie, F. Hofmann, T.S. Jun, T. Connolley, C. Reinhard, R.C. Atwood, L. Connor, M. Drakopoulos, S. Harding, A.M. Korsunsky, Residual stresses in Linear Friction Welding of aluminium alloys, Materials and Design 50 (2013) 360-369.
[238] N. Schalk, J. Keckes, C. Czettl, M. Burghammer, M. Penoy, C. Michotte, C. Mitterer, Investigation of the origin of compressive residual stress in CVD TiB2 hard coatings using synchrotron X-ray nanodiffraction, Surface and Coatings Technology 258 (2014) 121-126.
[239] A.M. Korsunsky, X. Song, F. Hofmann, B. Abbey, M. Xie, T. Connolley, C. Reinhard, R.C. Atwood, L. Connor, M. Drakopoulos, Polycrystal deformation analysis by high energy synchrotron X-ray diffraction on the I12 JEEP beamline at Diamond Light Source, Materials Letters 64(15) (2010) 1724-1727.
[240] K.S. Fong, M.J. Tan, B.W. Chua, D. Atsushi, Enabling Wider Use of Magnesium Alloys for Lightweight Applications by Improving the Formability by Groove Pressing, Procedia CIRP 26 (2015) 449-454.
[241] K.S. Fong, D. Atsushi, T.M. Jen, B.W. Chua, Effect of Deformation and Temperature Paths in Severe Plastic Deformation Using Groove Pressing on Microstructure, Texture, and Mechanical Properties of AZ31-O, Journal of Manufacturing Science and Engineering 137(5) (2015) 051004-051004-16.
[242] S. Zheng, Q. Yu, Z. Gao, Y. Jiang, Loading history effect on fatigue crack growth of extruded AZ31B magnesium alloy, Engineering Fracture Mechanics 114 (2013) 42-54.
[243] J.L. Chaboche, K.D. Van, G. Cordier, MODELIZATION OF THE STRAIN MEMORY EFFECT ON THE CYCLIC HARDENING OF 316 STAINLESS STEEL, Transactions of the International Conference on Structural Mechanics in Reactor Technology L (1981).
[244] J. Lemaitre, J.L. Chaboche, Mechanics of Solid Materials (1990).
[245] P.J. Armstrong, C.O. Frederick, A mathematical representation of the multiaxial bauscinger effect, CEGB Report No. RD/B/N 731 (1966).
[246] T. Vojtek, J. Pokluda, J. Horníková, P. Šandera, K. Slámečka, Description of Fatigue Crack Growth under Modes II, III and II+III in Terms of J-integral, Procedia Materials Science 3 (2014) 835-840.
[247] A. Ktari, N. Haddar, F. Rezai-Aria, H.F. Ayedi, On the assessment of train crankshafts fatigue life based on LCF tests and 2D-FE evaluation of J-integral, Engineering Failure Analysis 66 (2016) 354-364.

[248] D. Carka, C.M. Landis, On the Path-Dependence of the J-Integral Near a Stationary Crack in an Elastic-Plastic Material, Journal of Applied Mechanics 78(1) (2010) 011006-011006-6.
[249] M. Metzger, T. Seifert, C. Schweizer, Does the cyclic J-integral δJ describe the crack-tip opening displacement in the presence of crack closure?, Engineering Fracture Mechanics 134 (2015) 459-473.
[250] F. Yusof, P. Lopez-Crespo, P.J. Withers, Effect of overload on crack closure in thick and thin specimens via digital image correlation, International Journal of Fatigue 56 (2013) 17-24.
[251] M.A. Sutton, W. Zhao, S.R. McNeill, J.D. Helm, R.S. Riddell, ASTM STP 1343 (1999) 145.
[252] S. Beretta, S. Rabbolini, A. Di-Bello, Frattura ed Integrità Strutturale 33 (2015) 174.
[253] C. Eberl, Digital Image Correlation and Tracking (Software) (2015).
[254] S.Y. Lee, (2009).
[255] X. Zhang, D. Liu, G. Gao, Effect of shot peening factors on fretting fatigue resistance of Ti811 titanium alloy at elevated temperature, Xiyou Jinshu Cailiao Yu Gongcheng/Rare Metal Materials and Engineering 34(12) (2005) 1985-1989.
[256] M. Guagliano, L. Vergani, An approach for prediction of fatigue strength of shot peened components, Engineering Fracture Mechanics 71(4-6) (2004) 501-512.
[257] M. Benedetti, V. Fontanari, B.D. Monelli, Plain fatigue resistance of shot peened high strength aluminium alloys: Effect of loading ratio, Procedia Engineering 2(1) (2010) 397-406.
[258] X. Song, S.Y. Zhang, D. Dini, A.M. Korsunsky, Finite element modelling and diffraction measurement of elastic strains during tensile deformation of HCP polycrystals, Computational Materials Science 44(1) (2008) 131-137.
[259] A.M. Korsunsky, D. Dini, F.P.E. Dunne, M.J. Walsh, Comparative assessment of dissipated energy and other fatigue criteria, International Journal of Fatigue 29(9–11) (2007) 1990-1995.
[260] Simulia, ABAQUS User Manual, (2015).
[261] A. Zeghadi, F. N'Guyen, S. Forest, A.F. Gourgues, O. Bouaziz, Ensemble averaging stress-strain fields in polycrystalline aggregates with a constrained surface microstructure-part 1: Anisotropic elastic behaviour, Philosophical Magazine 87(8-9) (2007) 1401-1424.
[262] H. Lim, J.D. Carroll, C.C. Battaile, T.E. Buchheit, B.L. Boyce, C.R. Weinberger, Grain-scale experimental validation of crystal plasticity finite element simulations of tantalum oligocrystals, International Journal of Plasticity 60 (2014) 1-18.
[263] A. Chernatynskiy, S.R. Phillpot, R. Lesar, Uncertainty quantification in multiscale simulation of materials: A prospective, Annual Review of Materials Research, 2013, pp. 157-182.
[264] A. Saai, I. Westermann, S. Dumoulin, O.S. Hopperstad, Crystal plasticity finite element simulations of pure bending of aluminium alloy AA7108, International Journal of Material Forming 9(4) (2016) 457-469.
[265] E. Salvati, T. Sui, A.M. Korsunsky, Uncertainty quantification of residual stress evaluation by the FIB-DIC ring-core method due to elastic anisotropy effects, International Journal of Solids and Structures 87 (2016) 61-69.
[266] H. Zhao, B.P. Wynne, E.J. Palmiere, Effect of austenite grain size on the bainitic ferrite morphology and grain refinement of a pipeline steel after continuous cooling, Materials Characterization 123 (2017) 128-136.
[267] Y. Li, Q.L. Bai, J.C. Liu, H.X. Li, Q. Du, J.S. Zhang, L.Z. Zhuang, The Influences of Grain Size and Morphology on the Hot Tearing Susceptibility, Contraction, and Load Behaviors of AA7050 Alloy Inoculated with Al-5Ti-1B Master Alloy, Metallurgical and Materials Transactions A: Physical Metallurgy and Materials Science 47(8) (2016) 4024-4037.
[268] V.V.C. Wan, M.A. Cuddihy, J. Jiang, D.W. Maclachlan, F.P.E. Dunne, An HR-EBSD and computational crystal plasticity investigation of microstructural stress distributions and fatigue hotspots in polycrystalline copper, Acta Materialia 115 (2016) 45-57.
[269] J. Jiang, T.B. Britton, A.J. Wilkinson, Mapping type III intragranular residual stress distributions in deformed copper polycrystals, Acta Materialia 61(15) (2013) 5895-5904.
[270] A. Zeghadi, S. Forest, A.F. Gourgues, O. Bouaziz, Ensemble averaging stress–strain fields in polycrystalline aggregates with a constrained surface microstructure – Part 2: crystal plasticity, Philosophical Magazine 87(8-9) (2007) 1425-1446.
[271] D. Welling, Results of Surface Integrity and Fatigue Study of Wire-EDM Compared to Broaching and Grinding for Demanding Jet Engine Components Made of Inconel 718, Procedia CIRP 13 (2014) 339-344.

[272] J.G. LÓPez, P. Verleysen, J. Degrieck, Effect of fatigue damage on static and dynamic tensile behaviour of electro-discharge machined Ti-6Al-4V, Fatigue & Fracture of Engineering Materials & Structures 35(12) (2012) 1120-1132.
[273] A. Hasçalık, U. Çaydaş, Electrical discharge machining of titanium alloy (Ti–6Al–4V), Applied Surface Science 253(22) (2007) 9007-9016.
[274] G. Cusanelli, A. Hessler-Wyser, F. Bobard, R. Demellayer, R. Perez, R. Flükiger, Microstructure at submicron scale of the white layer produced by EDM technique, Journal of Materials Processing Technology 149(1–3) (2004) 289-295.
[275] M. Ramulu, G. Paul, J. Patel, EDM surface effects on the fatigue strength of a 15 vol% SiCp/Al metal matrix composite material, Composite Structures 54(1) (2001) 79-86.
[276] F. Ghanem, H. Sidhom, C. Braham, M.E. Fitzpatrick, Effect of near-surface residual stress and microstructure modification from machining on the fatigue endurance of a tool steel, Journal of Materials Engineering and Performance 11(6) (2002) 631-639.
[277] V. Yadav, V.K. Jain, P.M. Dixit, Thermal stresses due to electrical discharge machining, International Journal of Machine Tools and Manufacture 42(8) (2002) 877-888.
[278] H.T. Lee, T.Y. Tai, Relationship between EDM parameters and surface crack formation, Journal of Materials Processing Technology 142(3) (2003) 676-683.
[279] B. Ekmekci, Residual stresses and white layer in electric discharge machining (EDM), Applied Surface Science 253(23) (2007) 9234-9240.
[280] A.G. Mamalis, G.C. Vosniakos, N.M. Vacevanidis, X. Junzhe, Residual Stress Distribution and Structural Phenomena of High-Strength Steel Surfaces Due to EDM and Ball-Drop Forming, CIRP Annals - Manufacturing Technology 37(1) (1988) 531-535.
[281] P. Srinivasa Rao, K. Ramji, B. Satyanarayana, Effect of wire EDM conditions on generation of residual stresses in machining of aluminum 2014 T6 alloy, Alexandria Engineering Journal 55(2) (2016) 1077-1084.
[282] S.S. Sidhu, A. Batish, S. Kumar, Analysis of residual stresses in particulate reinforced aluminium matrix composite after EDM, Materials Science and Technology 31(15) (2015) 1850-1859.
[283] M. Shabgard, S.N.B. Oliaei, M. Seyedzavvar, A. Najadebrahimi, Experimental investigation and 3D finite element prediction of the white layer thickness, heat affected zone, and surface roughness in EDM process, Journal of Mechanical Science and Technology 25(12) (2011) 3173-3183.
[284] L. Paul, L.V. Korah, Effect of Power Source in ECDM Process with FEM Modeling, Procedia Technology 25 (2016) 1175-1181.
[285] J.F. Liu, Y.B. Guo, Modeling of White Layer Formation in Electric Discharge Machining (EDM) by Incorporating Massive Random Discharge Characteristics, Procedia CIRP 42 (2016) 697-702.
[286] B. Ekmekci, A.E. Tekkaya, A. Erden, A semi-empirical approach for residual stresses in electric discharge machining (EDM), International Journal of Machine Tools and Manufacture 46(7–8) (2006) 858-868.
[287] X. Yang, X. Han, F. Zhou, M. Kunieda, Molecular Dynamics Simulation of Residual Stress Generated in EDM, Procedia CIRP 6 (2013) 432-437.
[288] J.F. Liu, L. Li, Y.B. Guo, Surface integrity evolution from main cut mode to finish trim cut mode in W-EDM of shape memory alloy, Applied Surface Science 308 (2014) 253-260.
[289] C.A. Huang, F.Y. Hsu, S.J. Yao, Microstructure analysis of the martensitic stainless steel surface fine-cut by the wire electrode discharge machining (WEDM), Materials Science and Engineering: A 371(1–2) (2004) 119-126.
[290] T.M. Quick, EDM and the resulting hydrogen embrittlement of maraging steel, JOM 45(10) (1993) 52-55.
[291] C.H. Fu, J.F. Liu, Y.B. Guo, Q.Z. Zhao, A Comparative Study on White Layer Properties by Laser Cutting vs. Electrical Discharge Machining of Nitinol Shape Memory Alloy, Procedia CIRP 42 (2016) 246-251.
[292] J.F. Liu, Y.B. Guo, T.M. Butler, M.L. Weaver, Crystallography, compositions, and properties of white layer by wire electrical discharge machining of nitinol shape memory alloy, Materials & Design 109 (2016) 1-9.
[293] F. Klocke, L. Hensgen, A. Klink, L. Ehle, A. Schwedt, Structure and Composition of the White Layer in the Wire-EDM Process, Procedia CIRP 42 (2016) 673-678.

[294] A. Kromm, T. Kannengiesser, J. Gibmeier, In Situ Studies of Phase Transformation and Residual Stresses in LTT Alloys During Welding Using Synchrotron Radiation, in: T. Kannengiesser, S.S. Babu, Y.-i. Komizo, A.J. Ramirez (Eds.), In-situ Studies with Photons, Neutrons and Electrons Scattering, Springer Berlin Heidelberg, Berlin, Heidelberg, 2010, pp. 13-26.
[295] T.S. Jun, A.M. Korsunsky, Evaluation of residual stresses and strains using the Eigenstrain Reconstruction Method, International Journal of Solids and Structures 47(13) (2010) 1678-1686.
[296] E. Salvati, M. Benedetti, T. Sui, A.M. Korsunsky, Residual stress measurement on shot peened samples using FIB-DIC, Conference Proceedings of the Society for Experimental Mechanics Series, 2016, pp. 275-283.
[297] T.S. Jun, A.M. Venter, A.M. Korsunsky, Inverse Eigenstrain Analysis of the Effect of Non-uniform Sample Shape on the Residual Stress Due to Shot Peening, Experimental Mechanics 51(2) (2011) 165-174.
[298] E. Salvati, H. Zhang, K.S. Fong, X. Song, A.M. Korsunsky, Separating plasticity-induced closure and residual stress contributions to fatigue crack retardation following an overload, Journal of the Mechanics and Physics of Solids 98 (2017) 222-235.
[299] E. Salvati, T. Sui, H. Zhang, A.J.G. Lunt, K.S. Fong, X. Song, A.M. Korsunsky, Elucidating the Mechanism of Fatigue Crack Acceleration Following the Occurrence of an Underload Advanced Engineering Material, (2016).
[300] B. Lin, S. Zabeen, J. Tong, M. Preuss, P.J. Withers, Residual stresses due to foreign object damage in laser-shock peened aerofoils: Simulation and measurement, Mechanics of Materials 82 (2015) 78-90.
[301] M.K. Khan, M.E. Fitzpatrick, S.V. Hainsworth, A.D. Evans, L. Edwards, Application of synchrotron X-ray diffraction and nanoindentation for the determination of residual stress fields around scratches, Acta Materialia 59(20) (2011) 7508-7520.
[302] R. Zhu, H. Xie, X. Dai, J. Zhu, A. Jin, Residual stress measurement in thin films using a slitting method with geometric phase analysis under a dual beam (FIB/SEM) system, Measurement Science and Technology 25(9) (2014).
[303] B. Winiarski, P.J. Withers, Mapping residual stress profiles at the micron scale using FIB micro-hole drilling, Applied Mechanics and Materials, 2010, pp. 267-272.
[304] B. Winiarski, M. Benedetti, V. Fontanari, M. Allahkarami, J.C. Hanan, G.S. Schajer, P.J. Withers, Comparative analysis of shot-peened residual stresses using micro-hole drilling, micro-slot cutting, X-ray diffraction methods and finite-element modelling, Conference Proceedings of the Society for Experimental Mechanics Series, 2016, pp. 215-223.
[305] Q. Wang, H. Xie, Z. Liu, X. Lou, J. Wang, K. Xu, Z. Zhang, J. Liao, C. Gu, Residual stress assessment of interconnects by slot milling with FIB and geometric phase analysis, Optics and Lasers in Engineering 48(11) (2010) 1113-1118.
[306] L.E. Murr, S.M. Gaytan, D.A. Ramirez, E. Martinez, J. Hernandez, K.N. Amato, P.W. Shindo, F.R. Medina, R.B. Wicker, Metal Fabrication by Additive Manufacturing Using Laser and Electron Beam Melting Technologies, Journal of Materials Science & Technology 28(1) (2012) 1-14.
[307] O. Ivanova, C. Williams, T. Campbell, Additive manufacturing (AM) and nanotechnology: Promises and challenges, Rapid Prototyping Journal 19(5) (2013) 353-364.
[308] A. Hinojos, J. Mireles, A. Reichardt, P. Frigola, P. Hosemann, L.E. Murr, R.B. Wicker, Joining of Inconel 718 and 316 Stainless Steel using electron beam melting additive manufacturing technology, Materials & Design 94 (2016) 17-27.
[309] I. Kelbassa, P. Albus, J. Dietrich, J.I. Wilkes, Manufacture and repair of aero engine components using laser technology, (2008).
[310] J. Jones, P. McNutt, R. Tosi, C. Perry, D. Wimpenny, Remanufacture of turbine blades by laser cladding, machining and in-process scanning in a single machine, 23rd Annual International Solid Freeform Fabrication Symposium - An Additive Manufacturing Conference, SFF 2012, 2012, pp. 821-827.
[311] G. Bi, A. Gasser, Restoration of Nickel-Base Turbine Blade Knife-Edges with Controlled Laser Aided Additive Manufacturing, Physics Procedia 12, Part A (2011) 402-409.
[312] X. Zhou, D. Wang, X. Liu, D. Zhang, S. Qu, J. Ma, G. London, Z. Shen, W. Liu, 3D-imaging of selective laser melting defects in a Co-Cr-Mo alloy by synchrotron radiation micro-CT, Acta Materialia 98 (2015) 1-16.

[313] R.S. Khmyrov, C.E. Protasov, S.N. Grigoriev, A.V. Gusarov, Crack-free selective laser melting of silica glass: single beads and monolayers on the substrate of the same material, International Journal of Advanced Manufacturing Technology 85(5-8) (2016) 1461-1469.
[314] H. Liu, Sparks T., F. Liou, Residual Stress and Deformation Modelling for Metal Additive Manufacturing Processes, Proceedings of the World Congress on Mechanical, Chemical, and Material Engineering (MCM 2015) Barcelona, Spain – July 20 - 21, 2015 (2015) Paper No. 245.
[315] Y. Watanabe, Simulation of Residual Stress Distribution on Shot Peening, Journal of the Society of Materials Science, Japan 44(496) (1995) 110-115.
[316] G. Tapia, A.H. Elwany, H. Sang, Prediction of porosity in metal-based additive manufacturing using spatial Gaussian process models, Additive Manufacturing 12, Part B (2016) 282-290.